Analysis and Application of Passive Gait Rehabilitation Methods

by

Ismet Handžić

A dissertation submitted in partial fulfillment
of the requirements for the degree of
Doctor of Philosophy in Mechanical Engineering
Department of Mechanical Engineering
College of Engineering
University of South Florida

Major Professor: Kyle B. Reed, Ph.D.
Craig Lusk, Ph.D.
Jose Porteiro, Ph.D.
Rajiv Dubey, Ph.D.
Luther Palmer, Ph.D.
Seok Hun Kim, PT, Ph.D.

Date of Approval:
July 3, 2014

Keywords: Gait Enhancing Mobile Shoe, Passive Dynamics and Synchronization, Kinetic
Shapes, Roll-Over Shapes, Gait Perception

"I do not think there is any thrill that can go through the human heart like that felt by the inventor as he sees some creation of the brain unfolding to success... Such emotions make a man forget food, sleep, friends, love, everything."

- Nikola Tesla

Dedication

I dedicate this dissertation to my mother who has never taken herself before anyone else and who has always perpetually and lovingly supported and encouraged me any way possible. This dissertation reflects all her creativity, cleverness, originality, intellect, and attention to detail. It is because of her that I am the creative and understanding man I am today.

I dedicate this dissertation to my father who lead our family through terrors of war and horrors of genocide, showing unimaginable strength. It was he who guided our family to twice reestablish our lives in two different countries from nothing after losing everything. It is because of him that I am the vigorous and focused man I am today.

I dedicate this dissertation to my older sister who never abandoned her protective and supportive instincts towards her younger brother. It was she who initially pioneered and guided me through the unknown and foreign American education system we were thrown into.

I dedicate this dissertation to my country of birth and heritage, Bosnia and Herzegovina. It is this sense of culture and pride that forms a solid foundation of my identity and establishment to achieve more.

Finally, I dedicate this work to the scientific community and scientific advancement. I hope that someone somewhere will use, build upon, or benefit form any of my theories, models, analyses, explanations, and innovations I am presenting in this dissertation.

Acknowledgments

First, I tremendously would like to thank my advisor and mentor Dr Kyle B. Reed for teaching me invaluable and diverse lessons in becoming a great researcher, problem solver, and professional. He greatly broadened and refined my understanding of engineering, while molding me into an efficient and competitive researcher. I greatly appreciate him setting up a productive environment, giving me the freedom, tools, and understanding to express my creativity and imagination in the laboratory, while keeping me focused on broader goals.

I thank all my lab mates who I had the privilege working hard with while having the benefit of goofing off with. I hope I was and continue to be as good of an influence in your lives as you were in mine. Thank you Craig, John, Sam, Ahmed, Tyagi, Nellie, Woody, Neven, and all who over the years worked and interacted with me in our laboratory. I particularly like to thank Haris Muratagić for his help during the acute home stretch of this dissertation work.

I thank Jonathan Gaines and John Dixon, who have given me great freedom as a teaching assistant at USF Mechanical Engineering Department. This position has instilled a great sense and passion for teaching in me.

I thank the National Institute of Health for financially supporting my work during the first years of my research.

I lastly thank the United States of America for giving me the opportunities and nurturing the environment to get me to this point and hopefully much further. My academic experiences in this remarkable country truly resonate the quote: *"Education, then, beyond all other devices of human origin, is the great equalizer of the conditions of men, - the balance-wheel of the social machinery"* - Horace Mann.

Table of Contents

List of Tables

List of Figures

Abstract

Human gait is elegant and efficient in propelling the body forward. While a healthy human gait is symmetric, any deviation from symmetry can cause inefficiencies to the entire body. Such asymmetries may present themselves in hemiplegic patients, prosthetic users, lower limb injuries, limb height and weight discrepancies, or abnormal overground foot rolling. In this dissertation, practical passive methods to alleviate such asymmetric walking dynamics are presented. The novel concepts presented in this manuscript can all be related and applied to passive gait rehabilitation, that is, the rehabilitation of a person's gait through methods that do not require external power.

One of the passive rehabilitation solutions for asymmetric gait is the the Gait Enhancing Mobile Shoe (GEMS). The GEMS is designed to mimic the motions of a split-belt treadmill, which is commonly used for asymmetric gait rehabilitation. Two iterations of the GEMS prototype are presented. While the first development design of the GEMS was too bulky, it showed controlled and constant backward motion. The second fully mechanical design was tested on healthy participants and was successful in producing spatial and temporal aftereffects similar to those seen in split-belt treadmill gait studies.

In order to more accurately define the dynamics of the GEMS wheel as an individual steps on the shoe, mathematical models that predict the static and dynamic behavior of irregularly shaped curves on a flat plane as a weight is applied are derived and verified. While this *kinetic shape* concept can be applied to rolling irregularly shaped wheels, it can also be utilized to predict and manipulate roll-over motions of human feet, prosthetic feet, or even robotic biped feet. This kinetic shape concept was applied to develop a force dependent musical string instrument, transportation device, a more efficient walking crutch for controlled crutch walking, and a unique form of force mathematics.

The asymmetric kinematics of dissimilar human limbs can be synchronized for symmetry with a generalized passive kinematic synchronization technique that can match the motion of two or more dissimilar and uncoupled rotating systems. This kinematic synchronization technique introduced in this dissertation can be applied to duplicate the motion of swinging human limbs with dissimilar masses and mass distributions, which allows for the passive synchronization and rehabilitation of human limbs such as swinging arms and legs during walking. This technique also allows for the synchronization of mechanical systems such as pendulums, propellers, or rotating cams.

Finally, a detailed derivation of a two and three link passive dynamic walker (PDW) model with and without variable radius feet is presented. While PDW models have been studied and derived for decades, this dissertation offers a clear and complete guide on how to derive the kinematics and kinetics of the simplest compass gait, three-link point-foot, and for the first time, a variable radius foot PDW model, where the roll-over foot shape of the PDW can be dependent on its position or other kinematic variables. This advancement in the PDW model allows for the systematic evaluation of the change of various gait parameters such as foot roll-over shape or robotic foot dynamics.

This numerical biped model was compared to human gait parameters. This comparison included normal walking, tied- and split-belt treadmill walking, and GEMS walking. This model was also used to analyze the dynamic effects of changing the foot roll-over parameters such as foot roll radius and foot shape curvature. In addition, the PDW model was employed to investigate the perception of normal and pathological gait. The PDW model was systematically manipulated to produce walking patterns that showed a degree of abnormality in spatial and temporal gait parameters. This analysis showed that certain gait parameters may be asymmetrically changed to some extent without causing an abnormal perception.

Chapter 1: Introduction

The goals of this work are to understand and formulate methods to help in the rehabilitation of individuals with asymmetric gait impairments. The specific topics include the design and devlopment of a Gait Enhancing Mobile Shoe, mathematical modeling of the statics and dynamics of irregularly shaped objects, and passive dynamics as it relates to gait. While these topics can seem distinct in nature and broadly applicable, they all can specifically be applied to passive gait rehabilitation.

1.1   Gait Enhancing Mobile Shoe (GEMS)

Individuals with a prosthesis, stroke, or other types of central nervous system damage can develop an asymmetric walking gait, preventing them from moving around normally in everyday life. Such individuals are unable to continuously perform a correct symmetric gait cycle. In these hemiplegic patients, one leg lags the other, not traveling far enough backwards to effectively push the individual forward during walking. This creates an asymmetry that can strain the individual's healthy limb and affecting the entire body.

Previous asymmetric gait research has shown that using a split belt treadmill with asymmetric belt speed velocity ratios allowed individuals to adapt their walking gait to the asymmetric belt speeds showing trained aftereffects. When the split-belt treadmill is returned back to a 1:1 ratio, the individuals walk with an altered gait. This altered walking pattern, however, vanishes after a short period of time walking on a 1:1 ratio treadmill or over ground, and the individual's initial spatial and temporal gait parameters are regained.

This concept inspired the development of the Gait Enhancing Mobile Shoe (GEMS). This portable GEMS imitates the same relative foot motion experienced in previous split-belt treadmill

gait rehabilitation methods, except that individuals move over ground as compared to walking on a stationary split-belt treadmill. In other words, as one leg completes one whole step, the other leg covers only a fraction of the distance covered by the first leg, hence, mimicking an asymmetric split-belt treadmill. However, unlike a split-belt treadmill, the GEMS is completely passive and does not utilize any motors or actuators, but only uses the user's weight as its moving force.

Other advantages of this portable rehabilitation device are that it can be worn in different environments including one's own home over an extended period of time and at more regular sessions. Given such regular and longer gait rehabilitation sessions, the corrected gait is predicted to persist longer than the gait correction from a split-belt treadmill. Moreover, the ability to wear the GEMS for longer periods of time increases the probability of producing positive gait rehabilitation effects.

This dissertation shows the design, construction, and testing of two GEMS prototypes. While the first GEMS design pushed the user's foot backwards in a controlled manner, it was too heavy and tall to be used for clinical examination. Wearing the second GEMS redesign on one leg produced significant spatial asymmetries, while wearing two opposing GEMS shoes only generated a temporal asymmetry in double support.

1.2   Kinetic Shapes

It is easily demonstrated that a perfectly circular shape does not roll on a perfectly flat surface, but only rolls when placed onto a decline. By straightforward dynamic analysis of a circular shape, it is obvious that when placed on a decline the sum of moments does not equal zero, hence the shape will roll. It can also be demonstrated that a smooth shape with a non-constant/irregular radius will try to roll on a flat surface around the instantaneous point of contact and toward a decreasing radius. Both of these situations can create the same instantaneous dynamic rolling effect.

The rolling of a circular object down a decline is definitely not novel, but the rolling of an irregularly curved shape on a level surface, such as a rolling spiral curve, is useful and has not

received much research attention. In this manuscript, I will show how to derive two- and three-dimensional shapes that, when placed on a flat plane and loaded with a known weight at the axle point, will produce a desired ground reaction force parallel to the flat plane. This derived shape with known force parameters can in turn be used in static and dynamic applications some of which include, but are not limited to, self-stabilization, material hardness testing, robotic control, human locomotion, musical string instruments, and passive gait manipulation.

This dissertation defines and validates applications of two- and three-dimensional shapes that have a predictable kinetic and kinematic profile across their perimeter surface. Due to their predictive kinetic parameter, these shapes are known as *kinetic shapes*.

Kinetic shapes can be used to derive an exact wheel shape for the GEMS and can also be used to find the shape over which the foot rolls while walking. Foot roll-over shapes are essential in human walking and balance, while also playing a key role in lower limb prosthetic design. The kinetic shape concept can be an essential tool for passive rehabilitation in that it can be applied to shoes or walking crutches modifying their fundamental rolling dynamics.

1.3   Passive Kinematic Synchronization

Passive dynamics is dynamics without any energy input. This dissertation focuses on the description of passive dynamic methods and numerical models that can be used to manipulate, rehabilitate, or analyze human gait.

Human legs can be viewed as two rotating systems swinging with symmetric dynamics that are 180 degrees out of sync. In this dissertation, I will present a generalized kinematics synchronization technique that can model and synchronize human limbs that are asymmetric in mass, mass distribution, lengths, or compliance.

Kinematic synchronization of systems is the matching of motion between two moving systems. The synchronization of any two rotating systems can be as simple as placing a joining spring or damper between the systems or may require sophisticated controllers. I will focus on the question of how two *dissimilar* rotating systems can be synchronized *without* coupling the

systems. This passive kinematic matching technique allows two separate systems to generate the same motion without any system coupling or control law. To validate this method, this synchronization technique is applied to two open-ended rotating kinematic chains: single- and double- link pendulums with different masses and mass distributions. Even though double-link pendulums are nonlinear systems that are sensitive to changes in parameters, this matching technique enables the same generated motion on dissimilar double-link pendulums.

The practical application of such a passive synchronization technique is the flexibility in mechanical design as one is able to describe the same kinematics with a variety of parameters (i.e., lengths, masses, and mass distributions). In essence, one can decouple the mass and the first and second moments of inertia so systems with dissimilar masses and mass distributions will have the same motion. For example, the motion of a double-link pendulum modeled as two links with one mass per link can only be described by one unique combination of masses and mass locations along the links. However, having two masses per link allows the kinematics to be described with an infinite number of distinct systems that all have the same motion. In fact, the minimum number of masses per rotating link to describe any arbitrary rotational kinematics is two masses, yet many models only include one mass. Using only one mass per link inherently couples the moments of inertia so that any change in the location of the mass necessarily affects both the first and second moments of inertia.

The proposed matching technique can be used to simplify complicated kinematics problems that yield identical results. For example, the rotation of a fan blade can be represented with two masses distributed as specified using this method instead of finding detailed masses, mass distributions, or moments of inertias of the continuous system. In turn, using this matching technique, it is possible to design a second completely different rotating system that moves identically. Such a method can be useful in the simplification of a kinematic system model, in the manipulation of human or robotic limb movement, and in prosthesis design. The only requirements for passive kinematic synchronization are: identical degrees of freedom, initial conditions, and torques applied

to the systems. These same requirements are also needed to cause two identical systems to have the same motion.

Examples are provided which show proof and application of this passive matching method by mathematically and experimentally analyzing three dissimilar one-degree-of-freedom systems and also two dissimilar two-degree-of-freedom systems.

1.4 Passive Dynamic Walking

There are significant advantages of using numerical models to test hypotheses of how gait abnormalities and the altering of gait parameters affect the kinematics and kinetics of walking. For instance, a limitation of human subject clinical testing is that precise characteristics of gait vary from subject to subject and by the severity and cause of the gait disability. Over time, individuals with the same impairment develop different strategies to compensate, which results in different gait patterns. Thus, using a computer model that excludes sensorimotor control can be advantageous in the development and analysis of gait rehabilitation.

This dissertation includes the derivation of a comprehensive passive dynamic walker (PDW) model with variable curved feet. A PDW is a biped that walks down a decline solely by the force of gravity. In contrast to humanoid robots, the PDW shows a repeatable human-like gait, walking with a near energy optimal gait. An important characteristic of PDWs is that the focus is on the dynamic effects of a gait, excluding the cognitive aspects that can vary among individuals.

The derivation of this model in this manuscript is uniquely clear and descriptive such that it may be more replicable and applicable. This PDW model can be utilized to determine how variation of gait dynamics affect a gait so that rehabilitation methods can be approximated and evaluated prior to clinical trials. In this work, I compare the passive dynamics to humans walking in four environments: Over ground, on a tied-belt treadmill, on a split-belt treadmill, and on the Gait Enhancing Mobile Shoe (GEMS). For a rational comparison, the PDW model parameters used for this analysis are extracted from an anthropomorphic model and proportionally sized such that

the masses and mass distributions are relatively sized down from an individual. While this walking model has limitations, it does give further insight into gait and gait rehabilitation.

This PDW model is further used to understand the extent of the perception of altered gait. A healthy human body with a human-like shape and movements is perceived as normal, healthy, and familiar. Also, an exaggerated unrealistic caricature animation of a human body and its movements can be accepted as normal and familiar as we expect the caricature to be un-human-like. However, human-like objects, models, robots, or dolls often are designed to mimic normal human body parts, motions, or gestures that almost look normal, but cause a repulsion or abhorrence. This psychological reaction to the almost human-like is known as the uncanny valley and is recognized in the fields of cinematography, biomedical technology, and neurological conditions. The uncanny valley can sometimes be described as the perception of something that is familiar, yet incongruous, creating a repulsive effect. The uncanny valley is the decent of the plot between human likeness and my familiarity. Although the notion of the uncanny valley is widely known, the depths and edges of it are still fuzzy and open for study.

As we approach the uncanny valley from the left (low human likeness), we encounter it with lifeless objects, models, and movements such as industrial robots, stuffed puppets, or humanoid robots. However, approaching the uncanny valley from the right (high human likeness), that is, coming from the perception of a normal and healthy person, we encounter it with lively computer generated and/or realistic features and motions. In this dissertation, I will particularly focus on the edge of the right side of the uncanny valley. Specifically, I will examine the perception of human walking and the limits to which gait will continue to be perceived as normal in the presence of slight abnormalities of gait. My hypothesis is that gait can appear human-like even when it deviates from perfect temporal and spatial symmetry. Appearance is a major concern for individuals with a disability. These results could guide physical therapists in their treatments and would benefit individuals with disabilities that affect gait by determining and aiming for the gait patterns that minimize the perception of abnormal gait.

6

Since there are many gait patterns that can provoke uncanny feelings in an observer, the PDW allows for a systematic alteration in gait parameters such as knee height or joint stiffness. The results from the research presented in this dissertation allow for the characterization of the decent into the uncanny valley from the right hand side using various altered PDW walking models, comparing normal healthy gait to variations in gait.

Chapter 2: Background

My dissertation focuses on rehabilitation, modification, and analysis of human gait. Specifically, my work focuses on the design, construction, and development of devices, computational models, and analytical methods, which can be used for gait rehabilitation, gait analysis, or related fields. The following sections outline the background information needed to have a thorough comprehension of my work presented in this dissertation. This generally includes the literature review of human walking, walking rehabilitation, passive dynamics, and rolling dynamics.

2.1 Gait

An understanding of human walking, or gait, and its functions is essential to understanding the broad impact and specifics of this dissertation. I will use this section to briefly describe, characterize, and explain the functions of normal human gait, while also outlining pathological walking (particularly hemiparetic gait) and the rehabilitation and analysis. Note that I am only presenting human gait terminology and background that is relevant to my dissertation, an extensive review of human gait can be found in [153, 208]. I will also proceed to discuss the field of passive dynamics and the perception of normal, modified, or impaired human gait. Please note that as I am writing of human gait, I am referring to forward locomotion as opposed to backward locomotion gait.

2.1.1 Normal Human Gait

Normal walking in healthy and unimpaired individuals is naturally elegant and combines complex balancing, shock absorbing, and propelling dynamics along with central nervous system signals to generate efficient locomotion. In a healthy gait pattern, both legs move symmetrically

and mirror all dynamics 180 degrees out of phase. As opposed to running, individuals retain ground contact throughout the gait cycle, while both feet have simultaneous ground contact (double support) for about 10% of the gait cycle as body weight is transfered from left leg to right leg [153, 208] (Figure 2.1). *The repeating gait cycle can be subdivided into two periods (stance and swing), eight phases (heel strike, loading response, mid stance, terminal stance, toe-off, initial swing, mid swing, and terminal swing), or three tasks (weight acceptance, single limb support, and limb swing)* [153, 208]. These subdivisions of normal gait can be seen in Figure 2.2. The upper body, which includes head, neck, trunk, and arms, moves along as a unit and is considered the passenger unit to the locomotor system, which consists of the legs [153]. While step and stride are sometimes used interchangablly, it is important to differentiate between the two. One *step* is the heel to heel distance of subsequent left-right foot placements. One *stride* is the heel to heel distance of subsequent foot placements of the same foot. This difference is shown in Figure 2.3.

Normal healthy walking is symmetric in left-right step length distance, leg swing time, internal joint forces, and external ground reaction forces. The concept of gait symmetry in able-bodied human beings is still an on-going debate [173]. While many studies exist that assume gait symmetry for the sake of simplicity in data collection analysis, other studies assume gait symmetries if no statistical differences are noted on parameters (kinematics or kinetics) measured
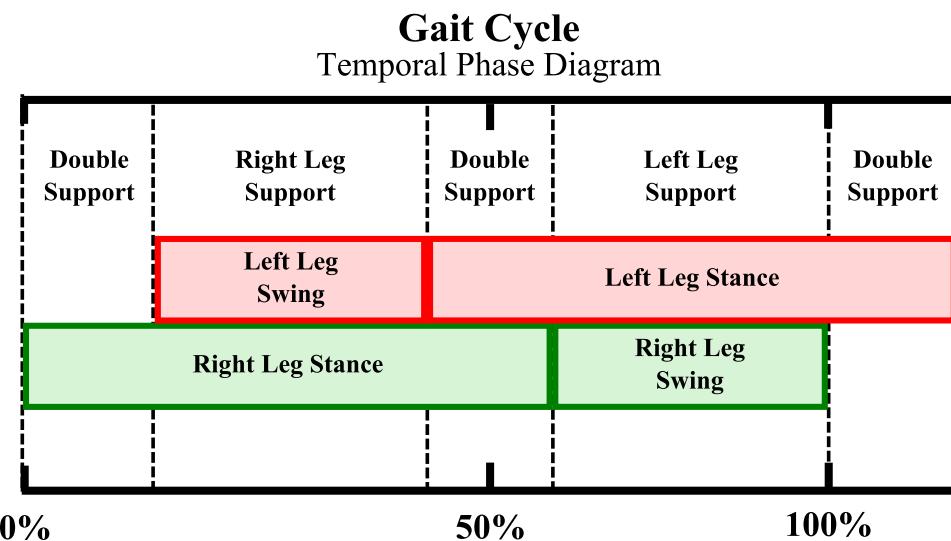
Figure 2.1: Normal human gait cycle temporal phase diagram

9
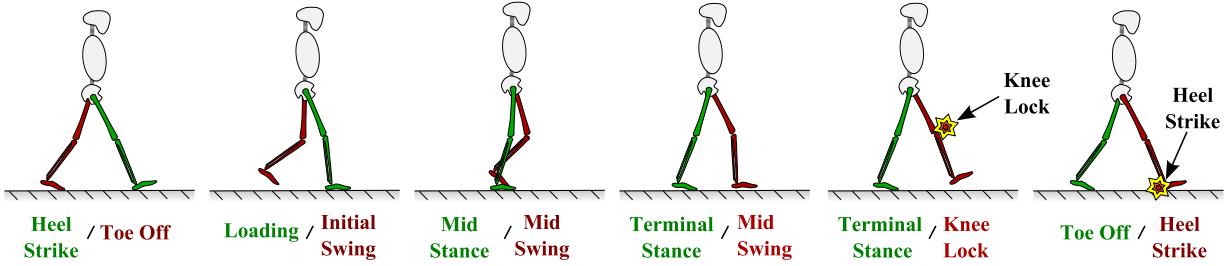
Figure 2.2: Normal human gait and its gait phases

between limbs. Most able-bodied individuals inherently have some small and unnoticeable spatial and temporal gait asymmetries due to limb dominance or frequent and demanding movements such as in sports [173]. It is interesting to note that gait symmetry does not change between walking barefoot and walking with shoes [123]. However, throughout my dissertation I will define asymmetry between any left and right parameter (i.e. step length, swing time, ground reaction force, limb length, etc) in terms of percent difference with Equation 6.77.

$$Asymmetry\ (\%) = \left(\frac{abs(Left - Right)}{(Left + Right)/2} \right) \tag{2.1}$$

In normal and healthy individuals, the vertical and horizontal *ground reaction forces (GRF)* exchanged between the ground and each foot throughout the gait cycle are shown in Figure 2.4. During the mid-stance phase, a slightly variable vertical GRF (weight) is applied, while the horizontal GRF (ground friction) switches from backward (resisting) to forward (assisting) at the around 30% gait cycle, accelerating the body forward before toe-off.
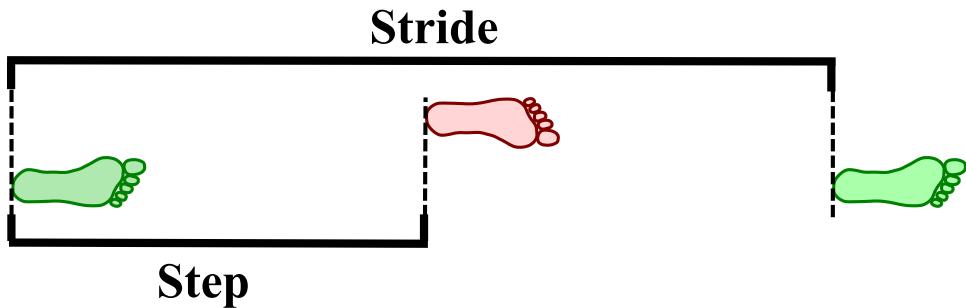
Figure 2.3: Distinction between step and stride in gait

10
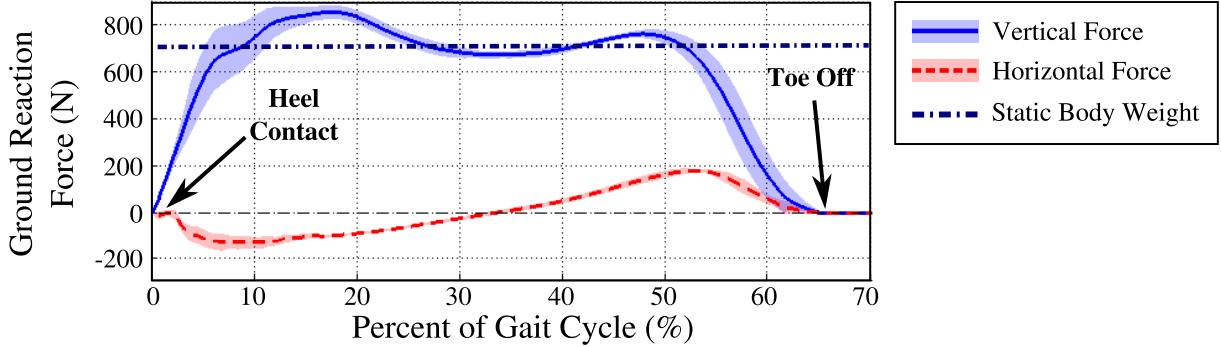
Figure 2.4: Measured normal gait ground reaction forces. One person weighing 71kg (690 N) stepping onto a force plate (AMTI model OR6-5 biomechanics platform) seven times. Shading represents one standard deviation in measurements. Forces were recorded during the stance phase during steady walking.

While the kinetics and kinematics of the human gait are straight forward to quantify, it also has a psychological side to it. Walking involves context awareness (or location awareness). *Context awareness* is a human's ability to automatically and unconsciously account for perturbations to the physical body while preparing and adjusting for such disturbances [208]. The human body is a learning machine, which adapts to external perturbations with conscious and unconscious anticipations, reactions, and balancing forces. A good example of gait context awareness is the "broken escalator" phenomenon that occurs when someone is about to step onto a non-moving escalator when anticipating a moving escalator. The person's body automatically adjusts muscle tension and aligns its center of gravity anticipating escalator movement, however in turn awkwardly loses balance as they step onto the non-moving (broken) escalator [22, 25, 26, 150, 163, 197]. During walking if a repeated perturbation is anticipated, an individual adapts their walking pattern in an unconscious and automatic manner. This effect can also be provoked by manipulating an individual's sensory input, particularly visual/optic flow, and so influencing their gait [47, 182]

2.1.2 Pathological Human Gait and Rehabilitation

As I've mentioned in the previous section, gait asymmetry can be subjective to the measuring technique and metric, however excessive gait asymmetry can became pathological due to various reasons. Gait asymmetry generating factors can include, but are not exclusive to:

11

- *Leg Footedness/Dominance/Bias* [173, 174]

- *Leg Length Discrepancy* [14, 57, 102]

- *Limb mass and mass distribution / Mass Loading* [43, 65, 128, 181]

- *Continuous or sudden perturbation* - Post-fracture leg cast [213], split-belt treadmill [157, 158, 201], balance training [105, 190], etc

- *Injury* - Muscle or ligament sprain [209], ankle fracture [12], etc.

- *Lower Limb Prosthetics* [129, 145]

- *Neurological Disease* - Stroke [151, 152], Parkinsons [217], cerebral palsy [181], etc.

Most survivors of stroke, persons suffering from traumatic brain injury, paraplegia, tetraplegia, multiple sclerosis, cerebral palsy, or hydrocephalus are known to suffer from motor deficits, including hemiparesis. *Hemiparesis* in the lower limb leads to hemiparetic gait, which is characterized by an asymmetric walking pattern, which may be caused by muscle weakness or paralysis [21, 206]. Hemiparetic gait typically includes asymmetries in walking coordination measures, such as step length, swing time, and double support. In other words, the placement and timing of each foot are not equal on the two sides. Hemiparesis patients often develop *drop foot*, which causes them to drag their forefoot along the ground due to foot weakness caused by nerve damage or paralysis [188]. This inability to raise their toes greatly inhibits forward progression and causes gait asymmetry. The general rehabilitation techniques used for hemiparetic patients can be categorized as one of the following:

- *Classic gait Rehabilitation (Neurophysiological and Motor Learning)* - Currently, the most common gait rehabilitation techniques are classic methods, but robotic devices are gaining acceptance [13]. Classic gait rehabilitation mainly includes preparatory and patient customized exercises, such as calisthenics, mild stretching, range of motion exercises [199,

200], and guidance/assistance of the limb position while walking over even ground in conjunction with a physical therapist. It is suggested that a combination of methods, such as the use of body weight supported treadmill training [140], is a more effective approach [97].

- *Robotic Devices* - Classic gait rehabilitation methods alone are unable to restore a normal walking pattern in many stroke patients [41] and are progressively used in conjunction with robotic devices such as exoskeletons [33, 106], pedaling devices [99, 118, 157], or split-belt treadmills [31, 159, 161]. There are several advantages in the use of robotic devices for gait rehabilitation: reduction of physical assistance and therapy cost, data acquisition, measurement and assessment, and repeatability [63]. Studies indicate that introducing robotic devices into gait rehabilitation results in improved endurance, lower-limb balance, functional balance, gait symmetry, double stance support, and stride length [10, 18, 164].

- *Functional Electrical Stimulation* - Functional Electrical Simulation (FES) is the stimulation of muscle tissue by electric current delivery. FES has been a rehabilitation method since the mid-twentieth century and was most commonly used for the rehabilitation of dropfoot and control of dorsiflexion of the foot [16]. Studies have indicated that regular use of multichannel FES is a suitable treatment for hemiplegic subjects [17, 189], however it is unclear if improvements were maintained after FES was removed. Further, the combination of FES to other techniques such as treadmill walking with body weight support yields a vast improvement in gait pattern.

As stated, walking on a *split-belt treadmill*, which has two belts that can drive each leg at different speeds (Figure 2.5), changes the coordination between legs (interlimb coordination) in adult humans [30, 38, 39, 115, 158, 205] and other animals [110, 122] and is often used in clinics for hemiparesis rehabilitation. Following a period of split-belt walking, when the treads are returned to the same speed ('tied-belts'), this altered interlimb coordination is retained, demonstrating that individuals learned and stored a new walking pattern. It has been shown that split-belt

training can alter normal gait and improve abnormal coordination in individuals with hemiparetic gait [115, 116, 139, 158, 159], suggesting that this is useful as a gait rehabilitation device.

However, these beneficial asymmetry correcting effects are only retained for a few minutes and more permanent effects are only seen with regular training over several weeks [185]. Moreover, the improved coordination only transfers partially to everyday walking over ground [161]. These are both issues that could limit the therapeutic potential of the split-belt treadmill in rehabilitation.

This transference problem may be due to context awareness discussed previously in Section 2.1.1. Unconsciously anticipating and adjusting to perturbations through vision plays a dominant role in the conditioning of a walking gait and in turn the adaptation of symmetric gait in hemiplegic patients. It is this context awareness that is hypothesized to be an integrating factor in the inability to store the previously described feed forward motion learned in split-belt gait manipulation research. While after-effects can be achieved, as subjects adapt to the asymmetric treadmill speed and are set out to walk over ground, the learned gait motion disappears within seconds.

Further, the continuous and persistent motions of the split-belt treadmill onto hemiparesis patients is still unknown, because split-belt rehabilitation training is usually performed on patients
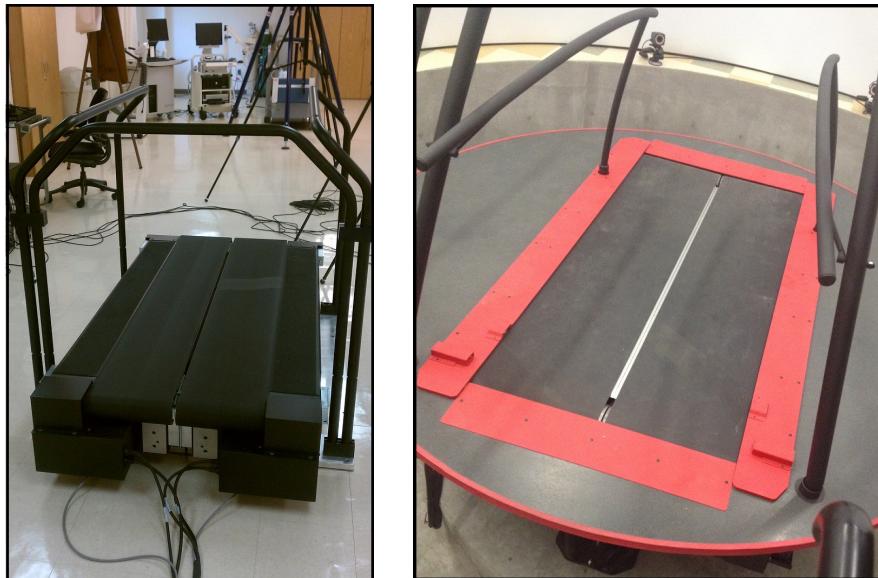
Figure 2.5: Split-belt treadmills commonly used for asymmetric gait rehabilitation

on limited occasions per week for less than half an hour per session. Due to the stationary nature of the split-belt treadmill, learned and altered gait on the split-belt treadmill does not transfer well to overground walking and the altered gait is lost in less than a minute.

It is important to state that although the kinematics of walking on a treadmill and the act of walking over ground seem identical, the visual cues and kinetics are different [166, 183, 207]. The effect of standardizing visual/optic flow during treadmill walking by adding virtual reality has been shown to minimize the differences between treadmill walking and overground walking [52, 182]. It is important to note that although treadmill and overground walking are biomechanically similar, the metabolic cost of treadmill walking is higher [149].

While all rehabilitation techniques, including utilizing a split-belt treadmill, have shown at least some rehabilitative benefits to patients, it is clear that the conjunction of multiple techniques promises optimal results. Also, the more and earlier after their traumatic event a person with a traumatic brain injury, such as stroke, is able to practice, the better their motor relearning will be [88]. However, patients are dissatisfied with their options for training after they are discharged from the rehabilitation hospital/clinic [203], and 85% of patients would prefer a home-based rehabilitation solution [63]. The ability to train at home means individuals can train more often, which leads to better results in motor relearning [135] and can maintain individuals' ability to perform activities of daily living [119, 172]. These studies indicate that appropriate methods need to be further developed to enable home-based rehabilitation to improve functional ability after discharge.

As explained in the previous Section 2.1.1, context awareness plays a large role in walking and the locomotor learning process. Hence, rehbilitative gait training on a stationary split-belt treadmill is percieved different than applying the same motions overground while walking. Person's walking over ground after split-belt locomotor adaptation experience a disconnect in context awareness. A very innovative attempt to solve this context awareness problem when altering and rehabilitating human gait is the *Gait Enhancing Mobile Shoe (GEMS)* [37]. GEMS makes it possible to adjust an asymmetric walking gait so that both legs move at a relatively symmetric

speed over ground. It alters the wearers walking gait by forcing each foot backwards during the stance phase, operating solely by mechanical and passive motions, transferring the wearer's downward force into a horizontal backwards motion. Recreating the split-belt treadmill effect over ground by using the GEMS will potentially enable testing long term effects of a corrected gait, which is impossible using a split-belt treadmill. Also, with the GEMS, it is possible to apply rehabilitative motions in different environments such as in one's own home. As part of this dissertation, I have developed and tested subsequent versions of the GEMS, which will be discussed later in Chapter 3.

2.1.3   Perception of Gait

Humans are quite good at recognizing and analyzing human-like movements such as identifying themselves and others others [11, 35], differentiating gender [109], or recognizing and analyzing movement in the sagital/side plane viewpoint [36]. Recognition of such healthy human movement with a human-like shape and movements is perceived as normal, healthy, and familiar. Also, an exaggerated caricature animation of a human body and its movements can be perceived and accepted as normal and familiar as we expect the caricature to be un-human-like. However, human-like objects, models, robots, or dolls often are designed to mimic normal human body parts, motions, or gestures that almost look normal, but cause a repulsion or abhorrence. This psychological reaction to the almost human-like is known as the uncanny valley and is recognized in the fields of cinematography, biomedical technology, and neurological conditions [49, 96, 138]. The *uncanny valley* can sometimes be described as the perception of something that is familiar, yet incongruous, creating a repulsive effect. As shown in Figure 2.6, the uncanny valley is the decent of the plot between human likeness (horizontal axis) and our familiarity (vertical axis) [138]. Although the notion of the uncanny valley is widely known, the depths and edges of it are still fuzzy and open for study. As we approach the uncanny valley from the left (low human likeness), we encounter it with lifeless objects, models, and movements such as industrial robots, stuffed puppets, or humanoid robots. The left side of the valley is characterized by motions and attributes

Figure 2.6: The uncanny valley of still and moving objects. As human likeness increases, so does the observer's familiarity up until a sudden decrease in familiarity into the uncanny valley where familiarity becomes abnormal, perceived with an uneasy or eerie feeling.

that we know not to be human. However, approaching the uncanny valley from the right (high human likeness), that is, coming from the perception of a normal and healthy person, we encounter it with lively computer generated and/or realistic features and motions. This side of the valley is populated by things that are very human-like, however may show some traits that are perceived as not exactly normal. In my dissertation I focus on the edge of the right side of the uncanny valley. *Specifically, I will examine the perception of human walking and the limits to which gait will continue to be perceived as normal in the presence of slight abnormalities.*

Previous studies have aimed to cross the uncanny valley [44, 202], but this proposed research is coming from the opposite direction and examining what changes cause a human-like gait to begin to appear uncanny. *My hypothesis is that gait can appear human-like even when it deviates from perfect temporal and spatial symmetry.* These results could guide physical therapists

17

in their treatments and would benefit individuals with disabilities that affect gait by determining the gait patterns that minimize the perception that their gait is impaired. Appearance is a major concern for individuals with a disability [19, 20].

Humans are keenly aware of walking motions that are close, but not exactly the same as a human makes. To other human observers, a normal healthy gait does not draw any attention and is usually dismissed as ordinary. However, as normal and healthy walking becomes unhealthy or impaired, it starts to raise attention and sometimes uneasy feelings, hence falling into the uncanny valley of gait mechanics. At an extreme end, this uncanny feeling can be provoked when observing the gait of extremely walking-impaired individuals suffering from neurological movement disorders such as athetoid cerebral palsy or dystonia, resulting in involuntary muscle contractions, repetitive movements, or abnormal postures. However, even smaller alterations from normal healthy gait may be easily recognizable and viewed as abnormal or unfamiliar. Pathological human gait, such as a slightly limping leg or sprained ankle, can be viewed as human-like and normal, yet the impairment will be quickly identified.

In healthy humans, the two sides of the body are mostly symmetric with regards to mass and strength; thus, it makes biomechanical sense to have both knees at the same location [195]. However, when wearing a transfemoral prosthesis, the mass and strength of the two legs are no longer equal and the biomechanical reasons to keep the same prosthetic knee location no longer exist. Moving the knee location adds a degree of freedom in the prosthesis design process that allows the gait dynamics to be adjusted to a desired gait pattern. However, changing the knee location depends on the answer to an essential question: what amount of knee location asymmetry can be considered normal or human-like?

Note that in this dissertation I am only concerned with the bio-mechanical movements of leg limbs and how these movements are perceived. I am not investigating the effects of limb thickness or texture perception, such as wearing a Flex-Foot Cheetah prosthetic blade foot [60].

2.2 Rolling Dynamics

In this section I will examine rolling dynamics of shapes over flat surfaces, which is consequential to human gait, gait rehabilitation (foot over ground rolling), and the related innovations discussed later in my dissertation. I will also explain the concept of roll-over shapes (ROS) and as they affect human walking.

2.2.1 Shape Rolling

It is easily demonstrated that a perfectly circular shape does not roll on a flat surface, but only rolls when placed onto a decline. By straightforward dynamic analysis of a circular shape, it is obvious that when placed on a decline the sum of moments does not equal zero, hence the shape will roll. It can also be demonstrated that a smooth two-dimensional polar shape with a non-constant radius will roll on a flat surface around the instantaneous point of contact. It will roll toward the decreasing radius with respect to angle when a vertical force is applied to its axle. Both of these situations create the same instantaneous dynamic rolling effect, illustrated in Figure 2.7.

The rolling of a circular wheel is definitely not novel, but the rolling of an irregularly curved shape, such as a spiral rolling on a flat surface, is useful and has not received much research attention.

Two centuries B.C., astronomer and mathematician Conon of Samos was the first to study conic sections, which are curves created by the intersections of cones. His work greatly inspired
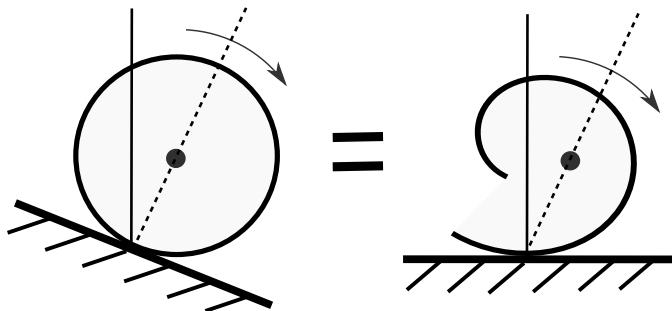
Figure 2.7: A circular wheel on a decline and a shape with a negatively changing radius are instantaneously equivalent in rolling dynamics

19

a colleague, Archimedes, to further study a special two dimensional curve now known as the Archimedean spiral (AS) [6]. The AS is given by Equation (2.2),

$$R(\theta) = a + b\,\theta, \tag{2.2}$$

where *a* and *b* are arbitrary spiral constants. While there are many variations of such a curve (e.g., Logarithmic Spiral, Corte's Spiral, etc.), the AS is defined in polar coordinates as a curve that increases at a steady rate in radius as the angle increases. This shape is particularly interesting in its physical form, in that it rolls by itself on a flat surface and closely mimics a circular wheel rolling down a hill. While the physical form of the AS is applicable in many disciplines, such as fluid compression [177] or microbiology [55], it is found to be attractive to mechanical designs where passive rolling or force redirection is desired.

Similarly, a deformable crawling and jumping soft robot [192] can use this rolling principle where the initial circular shape is mechanically deformed, which causes it to roll on a flat surface and it can even roll up a slope. This circular robot progresses forward by shortening and lengthening internal chords that are attached to an outside rim. As the rim is systematically deformed by the chords, the robot rolls forward or backward. This crawling robot used the same principle to construct a sphere that can roll [192]. This study of a crawling and jumping deformable soft robot only addresses the hardware, software, and motion energy analysis, but is missing an explanation of the rolling kinetics and an analytical description of the motion. *In this thesis I will proceed to solve for a complete and analytical description of irregular shape statics and shape rolling dynamics.*

A static version of a spiral shape is used in rock climbing equipment. The safety equipment known as a spring-loaded camming device (SLCD) [95] is commonly used by rock climbers to secure their rope into a rock crack while climbing. The SLCD utilizes two freely spinning spiral-shaped cams facing opposite directions. When the climber falls and applies a sudden force between the spiral cams and the rock surface, the cams are pushed outwards increasing friction between the cams and rock surface and providing enough force to resist the falling climber. This static force

redirection is similar, but opposite rolling robot in that it directs horizontally applied force into a perpendicular force. While this climbing innovation has been on the market for decades, I am not aware and could not find any significant analysis/research that has been published regarding the variation of forces along the cam perimeter and optimization of its logarithmic spiral shape. *In this dissertation I will proceed to solve for a complete and analytical description of two and three dimensional shapes/curves that are able to exert the exact and known forces when a force is applied to its axle*, such as in a SLCD.

Spiral-shaped wheels have a resemblance to objects with an eccentric rotation point, such as cams [28, 46]. Research on cam design focuses on the transfer of kinematics of two or more entities, generally rotary motion (the cam) into linear motion (the follower). While research on camming generally focuses on kinematics and tribology, it does not have free or forced rolling dynamics or force redirection of continuous irregular shapes.

The study of belt drives [180] and gearing [154] generally focuses on torque, rotational velocities, and normal forces between gear tooth surfaces. This includes the kinematics of circular and non-circular (elliptical) belt pulleys [221] and gears [148], and the kinematics of rack and pinion type of mechanisms [37]. Again, I found little in this area for free rolling and force redirection of irregular shapes. One related study derived a square wheel with matching roads (a type of rack and pinion) [66] that showed some insight into irregular shape rolling kinematics, but kinetics and static equilibrium of these shapes are not addressed.

One study considered the geometry of 2D circular, non-circular, and logarithmic shape rolling [15]. However, it did not consider any kinetics and strictly focused on the traces of curves (roulettes) created when rolling over various surfaces.

Spiral patterns are also possible in 3D, such as a rhumb line (loxodrome). I am including helix type spirals in my definition of 3D spirals, which have no change in radius, only in the depth dimension. I wasn not able to find literature that defines the kinetic or kinematic behavior of such shapes (or curves) during static conditions, free, or forced rolling dynamics. However, such research is needed for gait correction and rehabilitation.

2.2.2 Roll Over Shapes in Gait

An important aspect of the human gait is the *roll-over shape (ROS)* that the foot effectively follows when completing the stance phase during the gait cycle. ROS are foot rocker shapes that the foot rolls over when completing the stance phase during the gait cycle. The ROS is the curve created by the center of pressure ground contact described in a coordinate frame attached to the shank. An example of a ROS during the stance phase and an explanation is presented in Figure 2.8.

ROS have enormous effects on gait dynamics [1–3, 82, 134, 141], foot pressure [23], balance [117] and metabolic cost [1, 2, 80]. ROS can be used to train the body and alter lower limb muscle strength with *rocker bottom shoes* such as the Masai Barefoot Technology (MBT) shoe [82, 144, 191], while being greatly important in prosthetic foot design [34, 78, 79, 187], effecting limb dynamics and the forces exerted by the prosthetic onto the user's stump, which is a traditional issue for prosthetic users. Unwanted walking forces exerted on a foot can cause severe damage and discomfort such as in persons with diabetic peripheral neuropathy, foot calluses, leg joint paint, or by a prosthetic limb, however these can be manipulated or even diminished if the ROS is modified properly [3, 165].

Despite the importance of ROS, current gait studies have not been able to analytically predict the behavior of ROS and most ROS research relies on high level cut and try design and observational analysis. Addressing this need for a clear and analytic definition of ROS, Hanson
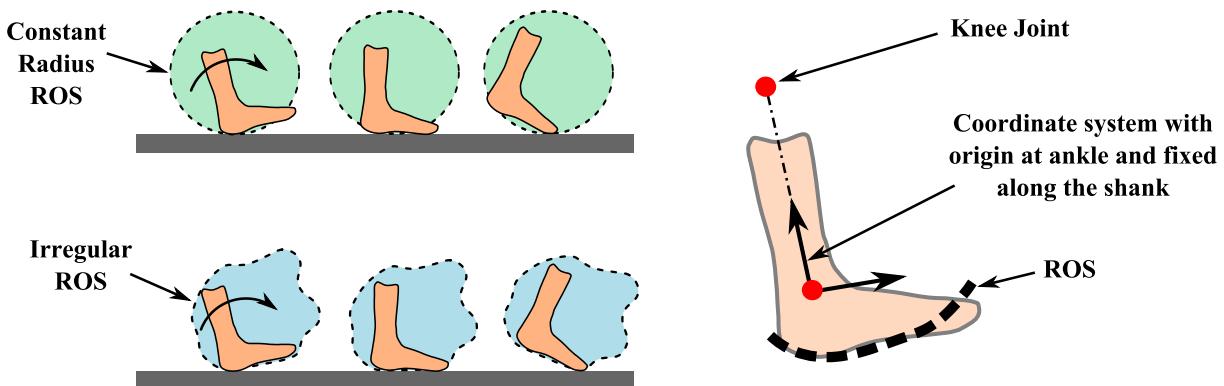
Figure 2.8: Foot roll-over shape (ROS) during stance phase in gait

et al. [79] states *"A better understanding [of ROS] could be used to develop improved prostheses, perhaps improving balance and balance confidence, and reducing the occurrence of falling in lower limb prosthesis users"*.

Besides prosthetic design, orthotic therapy, and gait rehabilitation, using specially-designed shoe soles can benefit patients of diseases such as cerebral palsy, parkinson's, and stroke [168], and increase muscle activity of selected foot muscles [117].

ROS also play a crucial role in the design of passive dynamic walkers (PDW) (discussed in the next section), which can be used to predict normal and pathological human gait [71]. Through design trials, McGeer indicates a most effective foot rocker radius to be 1/3 of total leg length constant radius [132], exactly matching the most efficient human ROS radius [1]. Although PDW ROS are a key component to the dynamics and stability of PDWs, I am not aware of any literature that clearly defines the size or shape of effective PDW ROS specifications.

2.3   Passive Dynamics

A *passive system* consumes energy or holds a constant total energy (potential plus kinetic energy). In terms of macroscopic classical mechanics, a passive system produces negative work. For example, a pendulum pivoting on a friction bearing released from a certain height is considered a passive system. Once released from a set height, the pendulum can not swing higher than its set height, only lower, hence a friction torque is being applied against its motion (negative work). In contrast, an *active system* produces energy, increasing its total energy by producing positive work. Released from a set height, an active pendulum with an actuator at its pivot point would be able to swing higher past its release height as the actuator produces torque in the direction of motion (positive work). In my dissertation I will only focus on passive systems such as the passive dynamic walker (PDW), and I will present a novel method with which two or more passive rotating dissimilar systems can be kinematically matched.

2.3.1 Passive Dynamic Walkers

A *passive dynamic walker (PDW)* is an entirely mechanical device that is able to exhibit a steady and stable gait down an declined slope purely due to gravitational forces and no other energy input. The energy gained by its progression down a slope due to gravity is lost during inelastic collision events such as knee strike (knee lock) or the heel strike. Its total energy remains constant throughout its gait cycle, hence it is completely passive.

An attractive aspect of a PDW to the field of gait analysis is that it allows us to separate the purely mechanical attributes of walking from the cognitive controls of the human body. This characteristic is advantageous when it is desired only to study the physical parameters of human gait such as step length, swing time, gait asymmetries, etc.

It is quite different from humanoid robots in its dynamics. All humanoid robots either follow a quasi-static pattern and/or require controllers to model feedback laws. Neither approach is analogous to human gait since human walking is dynamically stable and robot controllers do not yet adequately model the human sensorimotor system. A dynamically stable passive model is more realistic of the natural human gait dynamics and can predict the motions from altered dynamics. Toyota's ASIMO [176], Aldebaran Robotics's NAO [5], and Albert-HUBO [146] robots are statically stable robots that are able to simulate a slow and careful walking pattern while always keeping their center of gravity above their support base. Humans can walk this way, but rarely do. While more elegant and proficient in its gait, Google's/Boston Dynamics's Atlas [155] is an anthropomorphically correct biped able to mimic gait very similar to humans. Atlas is able to skillfully navigate across obstacles such as stairs and withstand moderate perturbations during gait. However, in contrast to Atlas, PDWs are much simpler, and versatile, while retaining human-like dynamics while Atlas follows highly controlled dynamic algorithms. The mentioned humanoid robots can be seen in Figure 2.9

The two-dimensional PDW concept was pioneered by analyzing a rimless wheel progressing down a slope, then developed into a inverted double pendulum model (compass gait). The *compass gait* PDW model is represented by two straight legs progressing down a decline.

24
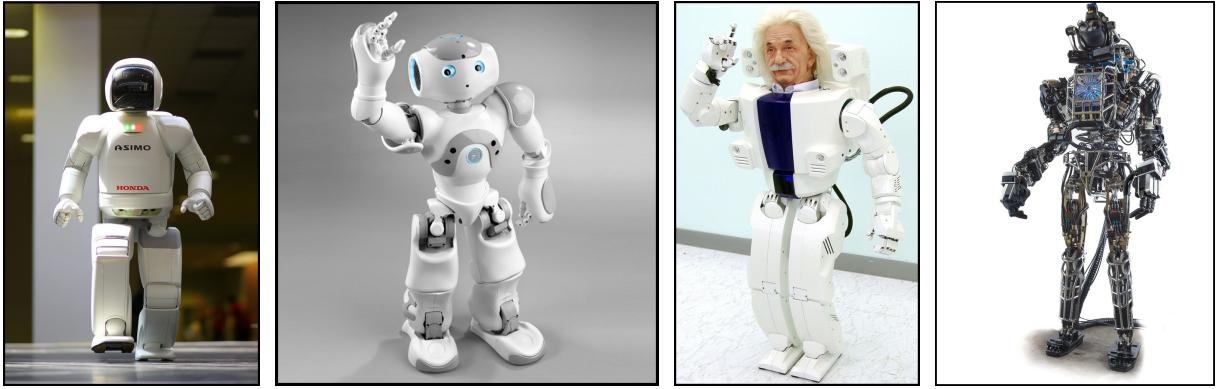
Figure 2.9: Modern humanoid robots. (Left-Right) Toyota ASIMO, Aldebaran Robotics's NAO, Albert-HUBO, and Google's (Boston Dynamics) Atlas. (All images in public domain)

Subsequently, that model was advanced into a kneed walker modeled by two system phases during limb swing. By differentiating left and right legs and varying leg mass and mass distribution, Honeycutt et al. [87] enabled an asymmetric PDW while also adding additional masses to the PDW model. Two or more masses per link allows the first and second moment of inertia to be uncoupled, which yields more versatility in distributing the lumped masses along the link. These evolutionary steps in PDW development were modeled with one or no masses per link as seen in Figure 2.10)

As previously discussed, roll over shapes (ROS) have a great impact on gait dynamics, balance, and control. Constant radius ROS have also been included into PDW models, playing a crucial role in the design of passive dynamic walkers (PDW). Through design trials, McGeer indicates a most effective foot rocker radius to be 1/3 of total leg length [132], exactly matching

| (a) | (b) | (c) | (d) |
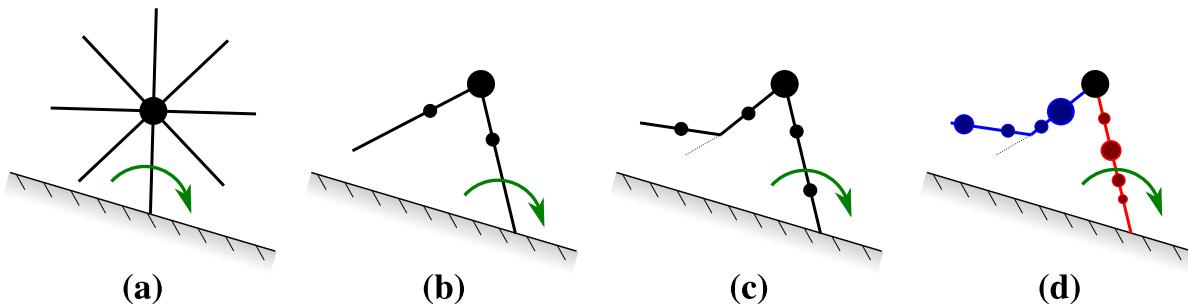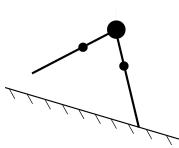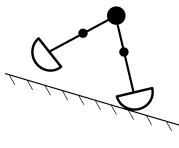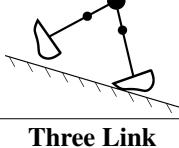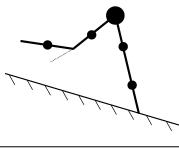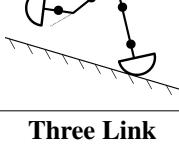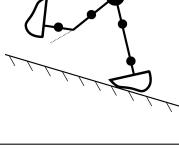
Figure 2.10: PDW evolution. (a) Rimless wheel (b) Compass Gait (c) Three-link (Kneed) walker (d) Asymmetric 9-mass walker

25

the most efficient human ROS radius [1]. Wu et al. [215] used a method of trial-and-error to design the curved feet of a PDW ROS, while emphasizing the importance of ROS in the design of PDWs, stating: *"More information is needed about the effect of the foot roll-over shape on the allowable size of the disturbances"*. Although PDW ROS are a key component to the dynamics and stability of PDWs, currently I am not aware of any literature that specifically studies and specifies the size or shape of PDW ROS. Also, I was not able to find any research which studies the effect of asymmetric ROS feet or ROS with given continuous functions (step, trigonometric, etc.). I was only able to find one study which uses a compass gait PDW, modeling its ROS in a discrete and numerical mannor and deviding the ROS into two sections, fore foot and back foot [124]. Due to the fact that PDWs do not exhibit ankle action/push-off (dorsiflexsion), *I hypothesis that this drawback can be aliviated by shaping the ROS so that it is able to push the walker forward similar to dorsiflexsion.*

For decades, PDWs have been constructed and mathematically analyzed, ameliorating and varying their physical designs and analytical models. Because of the diversity and range of past PDW research, I am not able to discuss every single permutations and combinations of past research in this field. Therefore I am presenting all past research of two dimensional passive (un-actuated) dynamic walking I was able to find in Table 2.1.

Note that my summary of past research in Table 2.1 shows much capacity for further exploration in this field. No one single PDW model or PDW study exists that encompasses all, or even most of the areas presented in Table 2.1. Although much has been acomplished in the area of PDWs, noone was able to encompass and progress current designs. A large part of my dissertation will concentrate on filling these unexplored areas and will be discussed in later sections. The highlighted areas in Table 2.1 are able to be filled with my developed PDW model, discussed in a later chapter.

Table 2.1: Two Dimensional Passive Dynamic Walker Research

	Plain Walker	Antrop. Mass Distribution	Dissimilar Sides	Ground Kinetics	Joint Siff. or Damp.	Human Gait Research
Compass Gait Point Feet	[111] [59] [58] [53] [186] [220] [125] [127] [175] [51] [113] [215] [204]	*None*	*None*	[53] [204]	*None*	[111] [53] [127] [204]
Compass Gait Const. R. Feet	[64] [111] [198] [210] [212] [211] [81] [108] [132] [131] [8] [9] [7] [1] [2]	*None*	*None*	*None*	[64]	[1] [2]
Compass Gait Var. R. Feet	[124] [114]* [121]* [89]*	*None*	*None*	*None*	*None*	*None*
Three Link Point Feet	[220] [219] [29] [167] [195] [76] [71] [4] [214] [167] [218]	[195] [76] [71]	[195] [76] [71]	[71]	*None*	[195] [76] [71]
Three Link Const. R. Feet	[196] [32] [211] [94] [170] [132] [131] [1] [112]	*None*	*None*	*None*	[196]	[1] [112]
Three Link Var. R. Feet	*None*	*None*	*None*	*None*	*None*	*None*

* Flat foot PDW model that includes a toe-down collision event.
Highlight - Areas that will be addressed with my PDW model.

2.3.2 Kinematic Synchronization

Kinematic synchronization of systems is the matching of motion between two moving systems. The synchronization of any two rotating systems can be as simple as placing a joining spring or damper between the systems or may require sophisticated controllers. In my dissertation, I am focusing on the question of how two *dissimilar* rotating systems, such as swinging limbs, can be synchronized *without* coupling the systems.

2.3.2.1 Coupled Synchronization

In 1657, in the quest to improve nautical navigation, Dutch mathematician Christiaan Huygenes invented the first pendulum clock [27]. Pendulum clocks were astounding mechanisms of their day. An interesting aspect is that they tend to synchronize and operate in phase or anti-phase when hung on the same wall with another pendulum clock. He deduced that the clocks were coupled by their common supporting structures which transferred small movements between clocks. This clock can be considered the first observation of a synchronized coupled oscillator.

The kinematic synchronization of two or more coupled mechanical systems such as Huygen's clock has been extensively studied since the time of Huygen himself. More recent such studies include the synchronization of coupled nonlinear oscillators [40], analysis of coupled multi-pendulum systems [48], and synchronization of double pendulums under the effects of external forces [104]. Osipov et al. [147] published a thorough review on synchronization in oscillatory networks, which mainly discusses different aspects of synchronization in chains and lattices of interconnected oscillatory elements.

As part of the rise of faster computing power came the ability to actively synchronize coupled mechanical systems with linear, nonlinear, passivity-based, or active control laws. There are hundreds of publications which demonstrate such control laws, some of these publications are on controlled motion synchronization for dual-cylinder electrohydraulic lift systems [193], inverted pendulum systems [142], and non-linear systems [194].

2.3.2.2   Uncoupled Synchronization

Passive kinematic synchronization of uncoupled systems has been studied significantly less and the authors were only able to find two examples of uncoupled passive mechanical synchronization, both of which are rooted in sports science.

A golfer's technique as well as familiar equipment play an essential role in a golfer's performance. It is for this reason that all golf clubs in a set are matched (synchronized) statically and dynamically, so when swung, each club behaves and feels the same to the golfer [24]. Statically a golf club is matched by simply balancing it on a fulcrum, however dynamically matching the golf club can be achieved by matching the moment of inertia for each club in the set about the swinging axis [45]. Jorgensen presents a golf club dynamic synchronization technique by modeling the swing arm and golf club and matching overall moments of inertia about the wrist axis [98]. In these examples the kinematics of each uncoupled system (golf club) is synchronized given the same input torque. While this technique of golf club matching is practical in its specific application, it lacks generalization and flexibility to apply to other rotating systems.

Although very little can be found in the field of passive synchronization of uncoupled systems, this method has practical implications for locomotion robotics, lower limb gait analysis, and prosthetics. For instance, an individual's walk can largely be modeled as two inverted pendulums (left and right step) rotating about the stance foot and progressing down a decline with gravity as the only source of energy [113]. Such models are the previously discussed passive dynamic walkers (PDW) and have been shown to predict certain aspects of human gait dynamics [53, 71, 76]. Honeycutt et. al [87] used a brute force search through a numerical PDW model to show that asymmetric limbs can have symmetric kinematics, and moving a prosthetic knee joint lower while lowering the prosthetic mass can result in a spatially symmetric gait. Gregg [61, 62] examined symmetry from the other point of view by finding symmetric PDW parameters that yielded asymmetric kinematics. A motion matching technique for PDWs and individuals can be helpful to design and implement devices and methods which either even out gait asymmetries [54],

or intentionally exaggerate gait asymmetries for rehabilitation [157]. These gait asymmetries can also arise from the asymmetric size and weight of a prosthetic limb [86].

2.3.2.3   String Vibration

In 1637, French mathematician and music theorist Marin Mersenne, who is often referred to as the "father of acoustics", used a sonometer [91] to derive formulas that predicted the lowest (fundamental) frequency of oscillation of a taut (stretched without sag) string [136]. These formulas, which relate string vibration frequency, mass per unit length, and tension, are refereed to as Mersenne's laws and are essential for the fabrication and operation of plucked, strummed, or bowed string instruments such as the guitar, chelo, piano, or harp. Marsenne's laws can be united as one formula that relates taut string vibration parameters and predicts a string's fundamental oscillation frequency (Equation 2.3).

$$f = \left(\frac{1}{2L}\right) \sqrt{\frac{TL}{\mu}} \tag{2.3}$$

In Equation 2.3, L is the length of the vibrating string, T is the string tension, and μ is the mass per unit length of the string.

It is apparent that Marsenne's laws can be applied to produce different string vibration frequencies (pitch) by altering the string length, mass per unit length, or tension. That is, one can alter the vibration of an oscillating string by altering:

1. *String Length (L):* Holding all other factors constant, shorter strings will produce a higher vibration frequency, while longer strings will produce lower frequencies.

2. *String Linear Density (μ):* A uniformly thicker string will move slower and so produce a lower frequency, while a thinner string will produce a higher frequency.

3. *String Tension (T):* Stretching a string with a higher force (tighter) will produce a higher frequency, while loosening the string will produce a lower frequency.
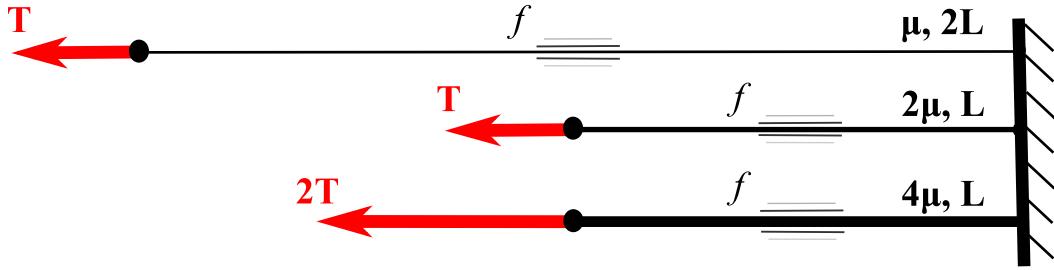
Figure 2.11: Three methods of changing string vibration frequency. By Marsenne's laws, dissimilar combinations of taut string length, tension, and mass per unit length parameter can produce the same vibration frequency. Each of the strings shown will produce the same tone.

For example, all three strings depicted in Figure 2.11 will produce the same vibration frequency. In practice, however, the one parameter most used to vary string vibration frequencies is string length (L) and linear density (μ).

Creating a variation of frequencies on one string by varying string length can be found on the guitar, violin, or chelo, where the player is able to produce different tones on one string by changing the length of the string by fretting it against the instrument [169]. The traditional japanese kato (similar to zheng, yatga, or gayageum) [92] produces a variation of string vibration frequencies as the player changes string length by manually moving string supports (bridges).

Commonly, different notes can be produced by playing different gage (thickness) strings present on the same instrument, such as in the piano [83]. Usually preset string thicknesses are set on the instrument and do not actively change.

Although the string pitch may be altered by stretching, or "bending", the string in stringed instruments such as the guitar, which increases string tension, it is not the explicit way to play these instruments. String tension in stringed instruments is usually adjusted to calibrate, or fine tune, the instrument to a preset and unchanging tension.

The authors were only able to find one instrument that exclusively changes string vibration frequency by changing string tension. The bhapang [92] (Figure 2.12), is an Indian single stringed percussion instrument. The string, which is tightened or loosened by the player with a handle, passes through the drum head absorbing the drum's vibration as the drum is struck. The player can

tighten or loosen the string to produce a continuous variation of sounds. Because of this continuous tension transition of the string, the pitch ramps up or down continuously.

It is also possible to automate and control a stringed musical instrument. This is not new concept and many mechatronic devices have been constructed to do so, which includes automating the piano [85] or violin [179]. A regularly performing thirteen piece robot musician band was developed that included seven guitars, two drum sets, two violins, and a cello, all controlled by electronic actuators [184]. In contrast, anthropomorphic robots have also been constructed and programmed to play instruments [100, 101].

A useful analytical application of the taut vibrating string concept is presented in geotechnical and civil engineering applications as vibrating strain gages [84, 90]. These gages are placed into a soil, concrete, or onto structural members to measure deformations. As deformation occurs the tension in a taut wire is altered and, thus, the wire's oscillation frequency changes which is measured by a sensor.

Taut string vibration frequency as a function of tension can also be of great interest outside musical practices such as in mechanical analysis of medical equipment [171]. The Ilizarov apparatus is an external fixation device that is used to lengthen, reshape, or align bones. The Ilizarov apparatus frame is adjusted by tightening external tensioned wires. As guiding bone growth is a

Figure 2.12: The bhapang is played by altering the string vibration frequency by tightening or loosening a string that is attached to a drum head

delicate process and misalignments can become permanent, the tensioned wires need to have exact specified tensions. These wire tensions can be found by wire vibration frequencies when plucked [171]. It was also found that after a few cycles of dynamic loading, pre-tension of these wires settle to a steady state tension [162].

Chapter 3: Gait Enhancing Mobile Shoe

In this chapter, I will describe the concept of the gait enhancing mobile shoe (GEMS) for asymmetric gait rehabilitation. I then will review the first and previously developed GEMS, after which I will present my design, development, and testing of the second, and third generation of the GEMS prototype shown in Figure 3.1.

Prototype 1	**Prototype 2**	**Prototype 3**
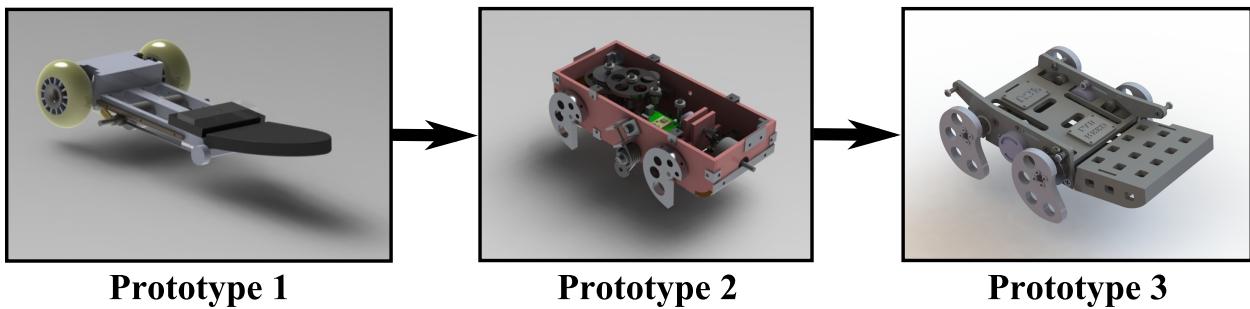
Figure 3.1: GEMS design evolution. My work includes the design and development of the second and third prototype

3.1 GEMS Concept

As discussed in the background/literature review Section 2.1.2, persons with hemiparetic gait, sometimes develop an asymmetric walking patterns where one leg does not fully swing backward. This uneven gait hinders these individuals in properly and efficiently moving through everyday life. Previous research in individuals with hemiparetic gait has introduced a split-belt treadmill to analyze possible rehabilitation, which can recreate a correct gait pattern by altering the speed of each track. While the corrective motions of a split-belt treadmill are beneficial, there is a large context awareness disconnect from the time spent on the split-belt treadmill to over ground walking. The GEMS is an innovative device that alleviates this context awareness problem as it recreates the same rehabilitative motions a split-belt treadmill produces, but in a locomotive

Foot with GEMS

GEMS Travel Distance
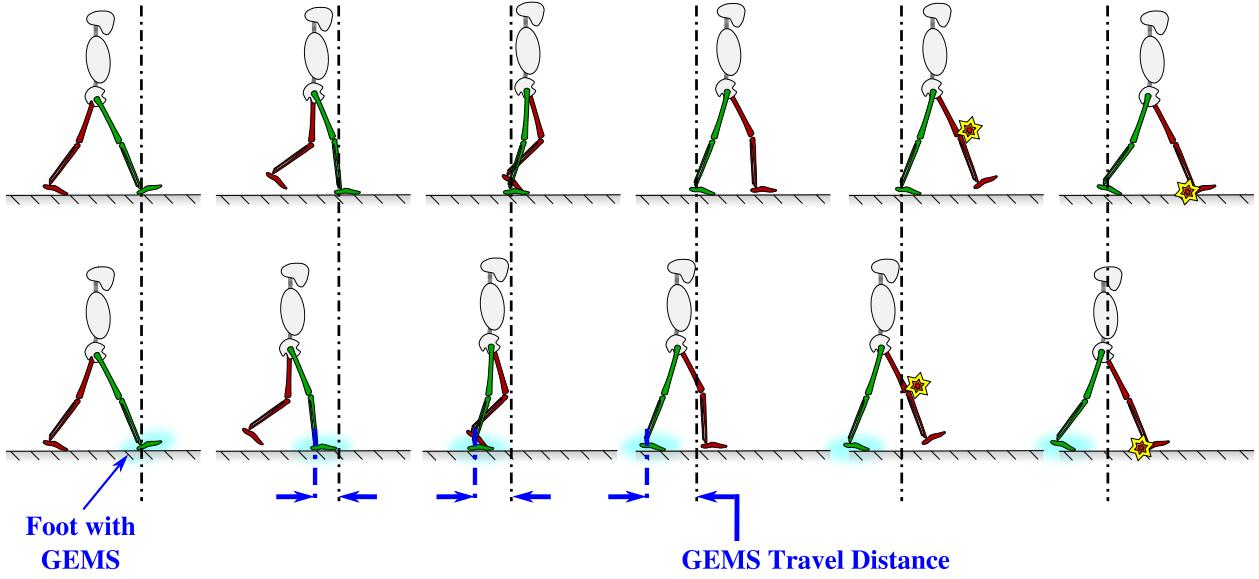
Figure 3.2: Gait Enhancing Mobile Shoe Concept. Rehabilitation method for asymmetric gait based on exaggeration where the GEMS is worn on lagging leg. The lagging leg is pushed backward motivating individual to perform a healthier toe off.

situation. As opposed to a split-belt treadmill, this allows a GEMS user to train their gait over various environments and over a pre-longed amount of time.

The method by which long-term effects would be trained is through motion exaggeration. By letting a patient wear the shoe on the weak leg, limits the forward motion of the healthy leg. This motivates the individual to lengthen the forward distance where the initial heel contact point is. Just like a split-belt treadmill, the GEMS exaggeration method pushes the impaired leg backwards simulating a correct gait (Figure 3.2). It is hypothesized that prolonged wearing of the GEMS will have positive after-effects helping asymmetric walking patients adapt a more normal walking gait over a longer period of wearing the GEMS. This application of the GEMS also has a potential to increase muscle impedance through the external perturbations, resulting in an altered walking gait.

Even if no long term and permanent aftereffects are found to be present, the GEMS can still be used to correct asymmetric walking patterns by wearing the shoe on the strong leg and letting it swing past the stance phase, limiting forward progression, and letting individuals toe off with that leg. As a result both legs will push the individual forward by similar distances, evening out the asymmetric gait. This is important considering that post-stroke patients do not bring one

leg back far enough, causing a limp. The result is the shortening of the stance phase, causing an unsuccessful toe off to efficiently propel them forward.

3.2   GEMS Prototype One

The existing GEMS prototype [37], shown in Figure 3.3, was previously developed and successfully generated the desired backward motion simulating a split-belt treadmill with a near 2:1 track velocity ratio. However, large variations from step to step were observed, which is hypothesized to prevent the user from fully adapting to the motion.

This prototype consists of a rear wheel at the user's heel, a middle roller, and a rubber piece to use for toe off. The rear wheel's axle is attached to the geared rack which when a downward force is applied the wheel will cause a backward motion. Figure 3.3 shows this geared rack in closer detail.

The middle roller is coupled with a rail moving forward as the shoe moves backwards, providing a constant two point contact between the shoe and the ground until toe off is initiated. Figure 3.4 shows the kinematics of the shoe as the stance phase is initiated until toe off is complete.

The front surface of the existing shoe consists of a free roller and a rubber surface to increase friction during toe off. The rubber surface is just like any other shoe surface and is relatively flexible allowing the wearer to bend this surface when pushing oneself forward.

Figure 3.3: GEMS Prototype One (left) with the geared rear wheel (right)

Heel Strike
Back wheel touches down immediately pusshing user's foot backward

Mid Stance
Back wheel and spur gear roll down geared rack. Middle and front wheel touch down

Terminal Stance
Back wheel raises off ground. Middle and front wheel remain in ground contact.

Toe Off
Middle wheel raises off ground. User pushes off with with rubber front. Geared rack raises into position.

Figure 3.4: As a wearer steps on the GEMS, it slides the user's foot backward

This version of the GEMS worked as intended and slid the user's foot backward by a total of 10in (25cm) on most steps. The GEMS initial prototype yielded similar results as the 2:1 ratio split belt treadmill, while wearing the shoe. However, only minor aftereffects were observed. In other words, only very short-term aftereffects of two steps were noted.

This inconsistency from step to step is thought to be caused by the large variation in dynamics from step to step using the GEMS, where the user has to consciously go through the motions of walking compared to the reliable and even dynamics of a split-belt treadmill generating a constant and predictable velocity profile.

Although this previous design was able to move the wearer's foot backwards, it performed the motion in a jerky, uncontrolled, and unnatural manner. Also instead of pushing the wearer's foot backwards, it acted as if the wearer was slipping on ice or a slippery surface. It is assumed that this uncontrolled motion activates the bodies balancing and recovery reflexes, thus hindering

37

a positive adaptation of an altered walking pattern. Such a recovery reflex is not present in the locomotor adapation and rehabilitation of split-belt treadmill walking.

In addition, as a result of the previous model's large horizontal backward motion of 10 in (25cm), the walking speed was decreased. A huge limitation of this GEMS prototype was that it had little adjustability and little control in backward motion velocity and travel distance. There was also a variation of backward stepping distance in each step observed to be caused in the variation of applied user force and walking speed. The next section will discuss how these limitations will be overcome in the controlled version of the second version of the GEMS which I designed and constructed.

3.3 GEMS Prototype Two

While the broad concept of this version of the GEMS stems from the previous version, this version is my complete redesign utilizing different mechanical concepts while alleviating some of the previous version's issues. This GEMS design aims to smooth out the transitions between phases in a human gait by regulating the horizontal backward motion of the foot. This controlled motion makes the redesigned GEMS similar to the foot motion experienced when walking on a split belt treadmill. This version still acts in a passive manner in that it utilizes the wearer's vertical downward motion to create horizontal backward motion and not any motors or actuators, it is only
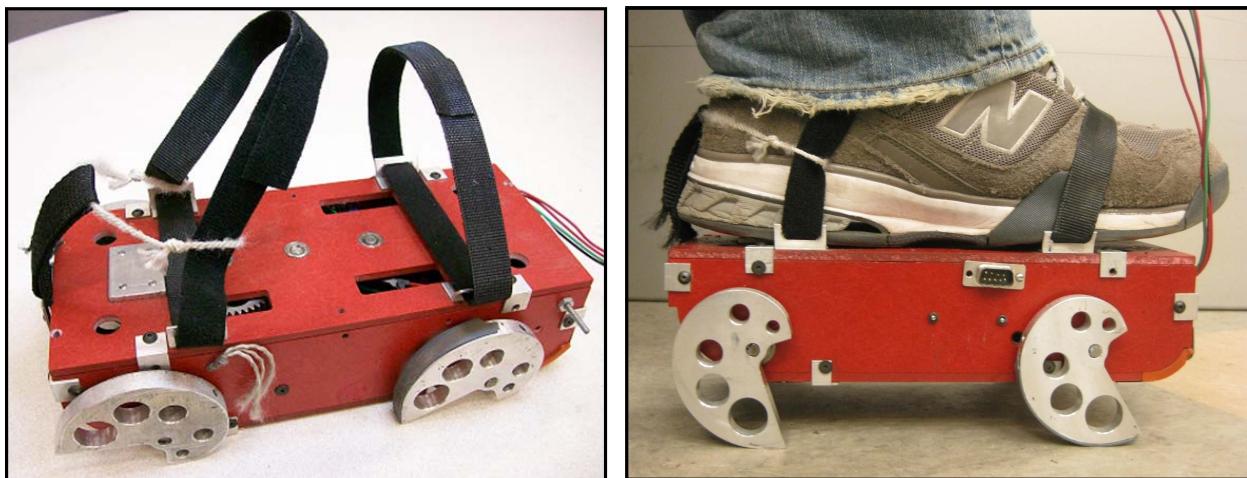
Figure 3.5: Second GEMS prototype

Heel Strike
Back wheel touches down immediately pusshing user's foot backward

Mid Stance
Front wheel touches down. User foot is pushed back with a steady motion

Terminal Stance
User foot is pushed back with a steady motion

Toe Off
Front wheel bottoms out. User pushes off with rubber front. Back wheel rotates into initial orientation.
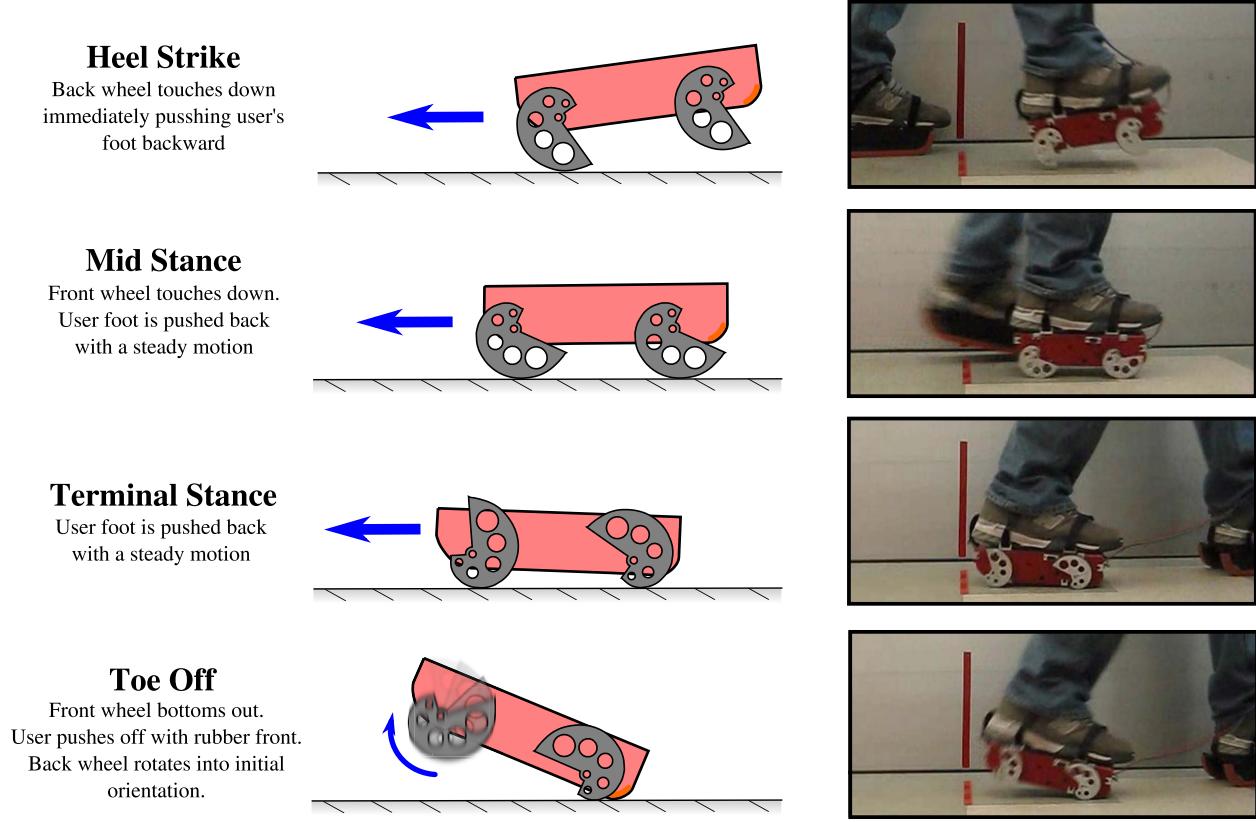
Figure 3.6: Second GEMS function. As a wearer steps on the GEMS, it slides the pushes the user's foot backward. The motion is smooth and controlled.

controlled by a programmable braking system. The complete second GEMS prototype is depicted in Figure 3.5, while the function of this GEMS prototype is shown in Figure 3.6. Detailed computer aided drafting (CAD) drawings, anatomy, and electrical diagram of this version of the GEMS can be viewed in Appendix A.1.

3.3.1 Design

3.3.1.1 Wheel Design

This version of the GEMS utilizes the concept of an Archimedean spiral-shaped wheel to passively push the user's foot backwards with only the user's weight as energy input. The description of the Archimedean spiral wheel in polar coordinates is defined in Equation 3.2.

$$R(\theta) = R(\theta_i) + C \; \theta^{1/n} \tag{3.1}$$

Here, θ is the polar angle around the wheel's origin, $R(\theta_i)$ is the initial wheel radius, and n and C are arbitrary constants that determine the wheel radius change. The rolling distance can be described by the arc length (perimeter) of the Archimedean spiral from initial angle θ_i to final angle θ_f. Note that a Archimedean spiral wheel rolls over from the largest radius, $R(\theta_f)$, to the smallest radius, $R(\theta_i)$.

As I've mentioned in the background Section 2.2.1, this non-constant Archimedean spiral wheel shape rolls on level ground just as a circular-shaped wheel rolls down a decline. A spiral wheel such as the Archimedean spiral wheel pushed onto a level surface by an axle at wheel origin will produce a rotation motion about ground contact and in the direction of decreasing radius. This is due to the fact that the applied weight at the axle/rotation point does not align with ground contact point as shown in Figure 3.7.

Because of the passive nature of the GEMS, in that it rolls on its own weight due to an asymmetric nature of the wheel, the Archimedean spiral is utilized in creating a passive GEMS to where the user applies their own weight to create the shoe's backward motion. With this spiral wheel the GEMS wearer applies a vertical force during the stance phase that can be directly related to the instantaneous horizontal backward reaction force through Equation 3.2.

$$F_h(\theta) = F_v \left(\frac{d(\theta)}{R(\theta)} \right) \tag{3.2}$$
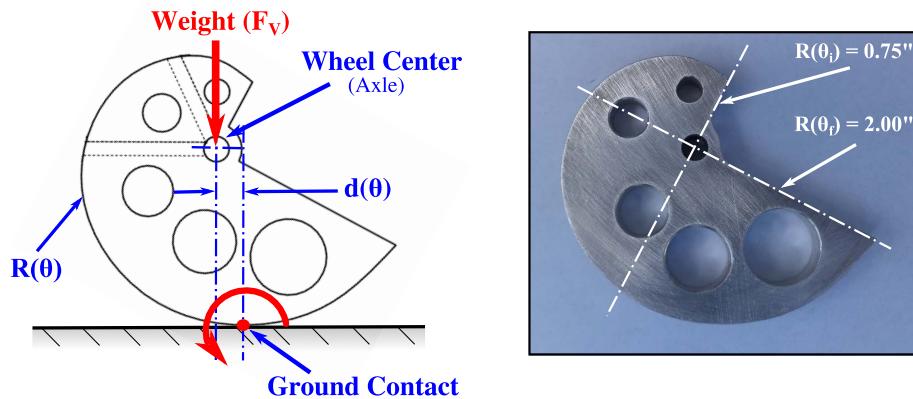
Figure 3.7: GEMS 2 spiral wheel rolls around ground contact as weight is applied to the axle

Here, $d(\theta)$ is the instantaneous perpendicular distance between the wheel center and the ground contact point and $R(\theta)$ is the distance between the ground and wheel center or axle attachment. Converting the wheel radius, $R(\theta)$ into cartisian coordinates allows me to find the distance $d(\theta)$ to relate the wheel radius to the horizontal backward ground reaction force, $F_h(\theta)$.

It is important for me to mention that at the time I was designing and constructing this GEMS prototype, I had invented the kinetic shape concept defined in the subsequent chapter, hence it was not available for more specification and optimization of the GEMS wheel, but used a numerical approximation to define wheel reaction forces.

Using a numerical trial-and-error method I used Equations 3.2 and 3.2 to create a GEMS wheel that will produces enough rolling force to overcome horizontal ground reaction forces during the stance phase. The average horizontal force that is exerted by the GEMS wheel can be approximated using Equation 3.3.

$$F_{h.Avg} = \frac{1}{\theta_i - \theta_f} \int_{\theta_i}^{\theta_f} F_h(\theta) \, d\theta \qquad (3.3)$$

Considering the GEMS size, stance ground reaction force exerted on the foot, and travel distance, the wheel shape for the second GEMS prototype was chosen with parameters shown in Table 3.1. These parameters will produce the wheel shape shown in Figure 3.7.

As shown in Figure 2.4 in the background Section 2.1.1 , a maximum 170N (38lbf) horizontal force is applied slightly after the person makes heel contact in the backward direction and slightly before a person initiates toe off in the forward direction (assisting). The average backward

Table 3.1: GEMS Prototype 2 Archimedean Spiral Wheel Parameters

Shortest Radius, $R(\theta_i)$	0.75 in (1.90cm)
Longest Radius, $R(\theta_f)$	2.00 in (5.08cm)
Archimedean Spiral Constant, C	0.006
Archimedean Spiral Constant, n	1.0475
Arc Length / Rolling Distance (0 - 270°)	6.71in (17.04cm)
Average Horizontal Force, $F_{h_{Avg}}$, at 800 N (180 lbf)	270N (60lbf)

force of 270N (60lbf) exerted by the wheel shape in the horizontal direction easily overcomes the initial horizontal force exerted by a person's foot after heel contact. Overcompensating for the wheel's backward reaction force is intended to prevent the user from slipping forward after heel contact and to compensate for the internal shoe mechanism friction.

A single wheel (of four total) experiences a average moment of 2.3N-m (20lbf-in) at the wheel axle throughout the stance phase. Considering this and that the GEMS weight is to minimized, the wheels were fabricated of 0.4in (1.0cm) thick aluminum. To minimize weight even further holes were cut out of the wheels. The fabrication of the wheels was done using a computer numerical control (CNC) mill. The wheels were mounted on the shoe's axles using two 0.25in (0.64cm) diameter course thread set screws. The wheel axle was 0.25in (0.64cm) in diameter and made of plain carbon steel with flats at wheel attachment points.

3.3.1.2   Motion Control via Magnetic Particle Brake and Gear Train

My design for the second prototype of the GEMS alleviates the largest deficiency of the previous shoe: the large motion variability generated and the jerkiness during each step. To overcome this limitation, the angular velocity of the wheels in this design can be controlled by a braking system. This braking system consists of a gear train and a 0–24V small magnetic particle brake (Figure 3.8), which both need to be strong enough to resist any motion as a person is stepping on the shoe while also allowing me to implement a known resistance to the GEMS backward motion. The magnetic particle brake is essentially a voltage actuated clutch; the more voltage is applied, the harder two internal plates push together to impede shaft rotation. The strength of the gear train and brake is strong enough to hold any position as a 180lb (800N) person is standing on the shoe.

As shown in Figure 3.8, the front axle is mated to the rear axle with a chain and sprockets. As the wearer applies a vertical downward force onto any or all of the four wheels, the combined torque is fed from the rear axle through the gear train and to the brake. The torque exerted by the

42
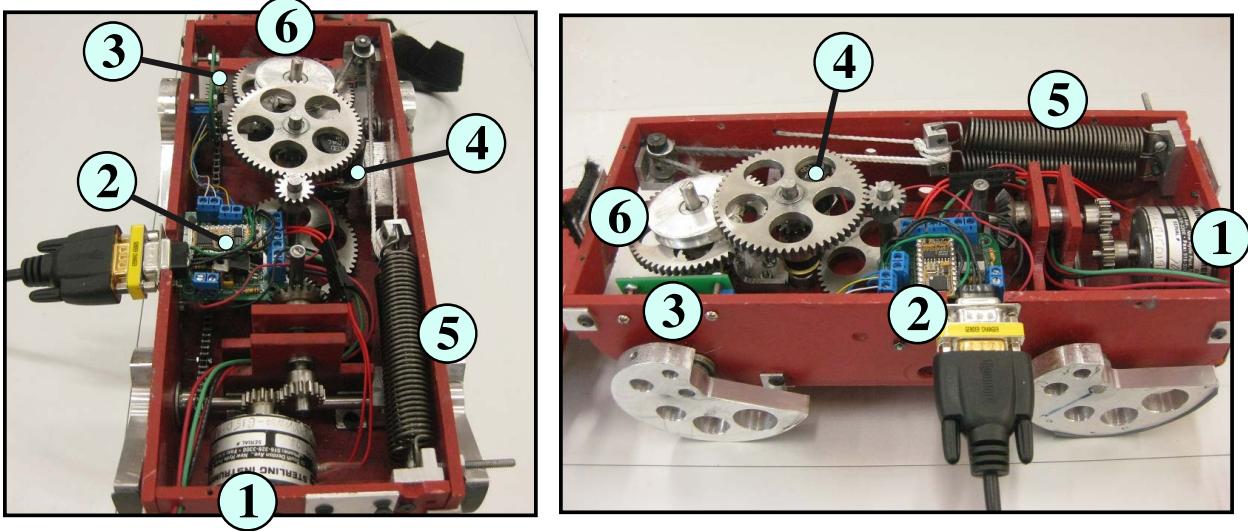
Figure 3.8: Second GEMS internal components. (1) Magnetic particle brake (2) Microcontroller circuit (3) Accelerometer (4) Potentiometer (5) Two extension springs (6) Reset pulley

wheels onto the rear axle can be estimated using Equation 3.3 combined with Equation 3.4.

$$T_{Avg} = F_{h.Avg} \, R(\theta_f) \tag{3.4}$$

Two sets of steel Miter gears were used to redirect the gear train for a space efficient fit. Three spur gear sets with 4:1 gear reductions each were used to reduce the torque applied by the GEMS wheels by a factor of 64. A 1 lb-in magnetic particle brake (S90MPA-B15D19S) was selected to apply resistance to the gear train reduced torque. During the brake selection the friction resistance forces and resistance forces of the spring actuated wheel reset mechanism was also taken into account. Note that I chose to use a brake only since the horizontal force is generated by the redirected downward force through the GEMS wheel, a motor capable of generating the necessary torque would require too much power and weight. The magnetic particle brake weighs 2.2lb (1kg). More details on the gear train and the magnetic particle brake is presented in Appendix A.1.

3.3.1.3 Wheel Reset Mechanism

In order for the shoe dynamics to be identical every step, the GEMS resets the wheel position using the spring mechanism shown in Figure 3.8. This reset mechanism consists of two

extension springs, non-elastic nylon strings, and a pulley which is attached to a gear axle. As the wearer applies a vertical downward force on the wheels during the stance phase, the rotation of the wheels causes the pulley to rotate, pulling the two extension springs apart. This potential energy stored in the extension springs is released during the swing phase as the wearer GEMS is lifted off the ground so that the wheels are rotated back to their initial position and ready for a subsequent step.

The springs were selected so their force can overcome all internal friction of the system while having a sufficient stretch length and stiffness. Selecting the extension spring which can overcome this torque is an iterative process that accounts for several factors: Free/nominal spring length, maximum extension spring selection, stiffness, force at extension lengths, availability, and the consideration of combinations of springs in parallel and in series.

Combined internal static and dynamic frictional forces are complex and hard to predict and so to correctly account for all the spring force required to rotate the whole mechanism back to its initial position against all frictional and damping forces, I utilized a simple setup as depicted in Figure 3.9. I tied a string around the circumference of a pulley with a known diameter that was attached to the GEMS axle. Weights were added to the string end until the pulley and so the whole mechanism started rotating. Knowing this pulley radius and the applied weight, I found that it takes a torque of 1.2N-m (10.5lbf-in) to reset the entire mechanism. This torque is required to
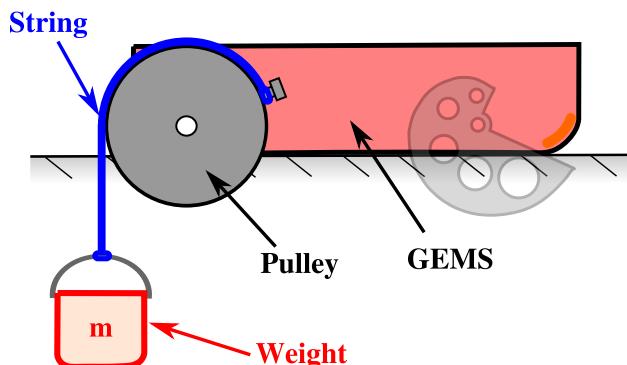
Figure 3.9: Setup used to determine how much torque it takes to reset the GEMS mechanism

overcome all internal static friction and damping of the GEMS and rotate the wheel to its initial position.

As there are three spur gear readuction with a 4:1 gear ratio, winding the system back at the first gear axle would require 1.2N-m (10.5lbf-in) of torque, at the second gear axle it would require 0.30N-m (2.6lbf-in) of torque, and on the third gear axle it would require 0.075N-m (0.65lbf-in) of torque. However, in turn as I move down the gear train, the number of rotations per reset increases by a factor of four. Further, the diameter of a reset pulley used to apply the resetting torque to the system factors into how much torque is applied, what spring stiffness is required, and how far the string can extend off its nominal length. So the position and size of the reset pulley dictates the extension length of the spring, in that as the reset pulley moves further down the gear train, more rotations are required to reset the wheels and the greater the circumference the reset pulley is, the longer distance the spring is eventually extended.

Given these design constraints and spring availability, two extension springs were placed in parallel with the reset pulley placed on the first rotation shaft of the gear train. I selected two parallel springs with a sufficient stretch, pre-tension, and a maximum force at max stretch length so that when applied to a reset pulley of 1.0in (2.54cm) on top of the first gear train axle, would adequately cover the needed 10.5lb-in (1.2N-m) torque to completely reset the shoe. For sufficient stretch of the spring, a redirect pulley was placed in the upper back corner of the GEMS frame, which guided the nylon string from the extension spring onto the reset pulley. To reset the GEMS mechanism, each extension spring had a stiffness of 4.40N/m (2.5 lbf/in), free/nominal length of 3.50in (8.89cm), a stretched length of 9.50in (24.13cm), and a spring outside diameter of 0.50in (1.27cm).

A nylon string was used to pull the extension springs apart. While wires and ropes were either inflexible or too thick, the nylon string was very low friction, strong, and very flexible, however by itself was too weak to withstand the extension spring set force when extended to the maximum, hence, the nylon string was doubled, cutting the tension in each chord by half.
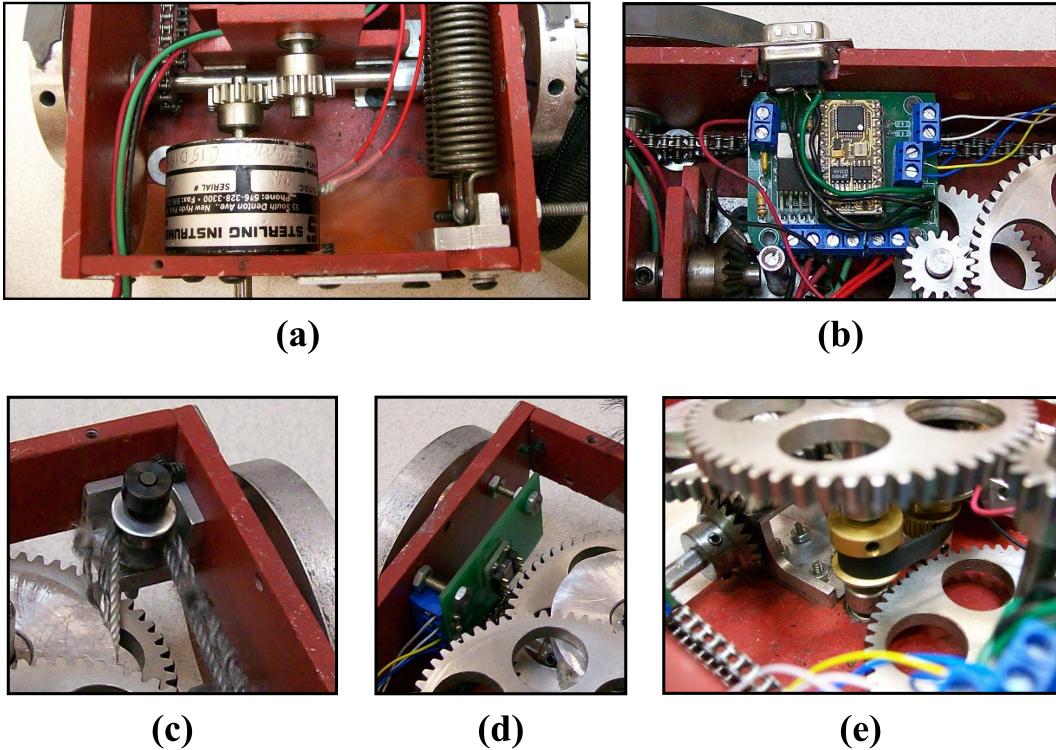
Figure 3.10: Second GEMS specific parts. (a) GEMS 2 magnetic particle brake. (b) Microcontroller circuit (c) Redirect pulley (d) Accelerometer (e) Potentiometer coupled to gear train axle

3.3.1.4 GEMS Control Electronics

The GEMS varies the motion resistance through the magnetic particle brake using an op-amp circuit in conjunction with a programmable microprocessor (Parallax® BS2p24, 20Mhz) located on the inside wall of the GEMS (Figure 3.8 and 3.10b).

Depending on what point in the gait cycle the wearer is, variable resistance is applied to the GEMS via magnetic particle brake. Instances in the gait cycle are identified by using a rotational potentiometer (10 turn, 10kΩ) coupled to the second gear train axle and an accelerometer (Parallax® MX2125) attached to the GEMS frame. The accelerometer is shown in Figure 3.10d and the rotational potentiometer is seen in Figure 3.10e. While the potentiometer recognizes the wheel rotation, the accelerometer recognizes when heel contact and toe off occur. Heel contact is measured by the sudden acceleration (jerk) applied to the wheel and frame of the GEMS while the wheel is in its neutral position. Toe off is determined when the accelerometer detects a sudden
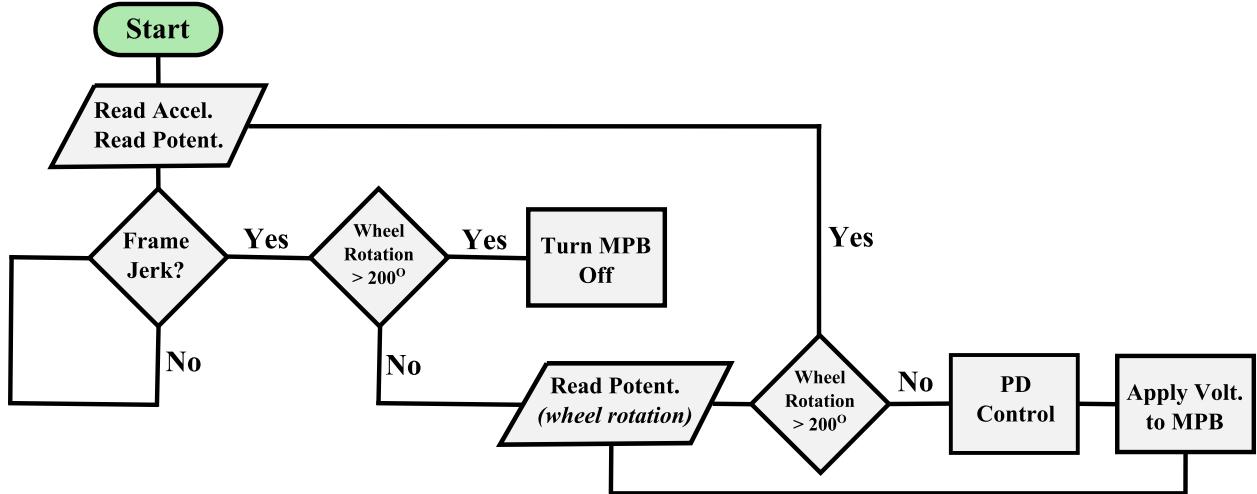
Figure 3.11: GEMS 2 microcontroller progrm flow diagram

acceleration while wheel rotation passes 200 degrees. The microprocessor logic is shown in Figure 3.11

The microcontroller reads the wheel rotation from the potentiometer and sudden movements from the accelerometer. It then controls the timing and resistance of the magnetic particle brake and so the GEMS backward movement. During the stance phase as the magnetic particle brake is actuated it is controlled by a position and derivative (PD) controller algorithm. In order to easily reprogram the on-board microprocessor, an external RS232 connection was mounted outside the side of the GEMS. All electronics are powered by a small battery pack, which the user wears on their hip. The electrical diagram for the combined GEMS electronics can be viewed in Appendix A.1.

The electrical components of the GEMS all require power at various voltages which are provided by a battery pack which the user wears by the hip. This rechargeable battery pack consists of a 24VDC (500mAH, Ni-Cd) battery pack which feeds into the op-amp circuit that power the magnetic particle brake (0.085A, 2.0W), a 7.5VDC (5 x 1.5VDC AA) battery pack which powers the microprocessor (0.04A, 0.02W) with the accelerometer (0.0005A, 0.003W), and a -3VDC (2 x 1.5VDC AA) power pack which also feeds into the op-amp. With this battery pack the GEMS

<center>(a)   (b)</center>

<center>Figure 3.12: (a) GEMS 2 battery pack (b) Opposite foot support platform</center>

is able to support 5.5 hours of uninterrupted operation. The battery pack is shown in Figure 3.12 while the shoe's electrical diagram is shown in Appendix A.1 Figure A.4.

3.3.1.5   Frame and Straps

The GEMS symmetric frame shape was chosen so it could be used in both directions as the wheels can be repositioned. It is made out of light and strong $3/16''$ (0.5 cm) fiberglass and held together with various aluminum brackets. Two rubber pieces were added to the lower front and back corner of the shoe so the wearer could effectively create a solid heel contact and toe off. While the GEMS frame itself is important to the general operation of the GEMS, it was designed around other design requirements, which included the size of the gear train, the size and shape of the wheels, and the size of the magnetic particle brake. The simplest shape was chosen for the frame design, a rectangular box with rounded rubber pieces at the lower front and back corners. The general dimensions of the GEMS frame is shown in Appendix A.1.

During usage, the wearer's shoe is strapped down to the top of the GEMS. These straps were designed after a traditional sandal design, rigidly supporting the whole foot with minimal straps. Velcro straps were utilized for quick strapping and unstrapping of the wearer's shoe to the GEMS.

3.3.1.6   Opposite Leg Support Platform

Because the GEMS is $2in$ (5 cm) off the ground, a supporting platform of equal height and weight for the opposite foot was constructed. The platform was constructed to roughly form

a similar roll over shape as rolling over the GEMS. However, an exact shape of this supporting platform is unclear. The kinetic shape concept could be applied to produce the correct support platform.

The support platform was designed to be the exact same dimensions, weight, and fastening style to eliminate any unnecessary asymmetries. This platform was made with a thick rubber sole to maximize friction and stepping smoothness. This compensatory platform on worn on the opposite foot is seen in Figure 3.12.

3.3.1.7 Results and Discussion

This functional motion controlled GEMS prototype design resulted in a total shoe dimension of $10.5 in$ x 4.5 x $2 in$ and a total weight of 4.5 lb (2 kg). Most of the total GEMS height and weight comes from the gear train and the magnetic particle brake responsible for controlling the wheel rotation. Considering that the average walking sneaker weighs about 1.5–2 lb, this final weight is on the high side of the acceptable range for a shoe of this purpose. As addressed in the third GEMS prototype, in the forthcoming section, optimizing the wheel shape, spring forces, and reset mechanism can help to reduce the overall weight and most likely reduce the overall height of the shoe.

The motion controlled GEMS successfully applied a horizontal backward motion to the user's foot during the stance phase. The total backward motion distance averaged $6 in$ (15.2 cm) per step. This motion, which is shown Figure 3.13, was observed to be continuous and smooth. The horizontal backward motion was comparable to the natural smoothness of a split-belt treadmill.

While the previous GEMS design [37] successfully slid the wearer's foot backwards 10in (25cm), much of the backward motion was similar to a sliding motion. Using the Archimedean spiral wheel shape design, the new GEMS continues to utilize the wearer's vertical downward force due to the wearer's weight in the stance phase and converts it into a horizontal backward motion that can be controlled.

Another interesting observation is that the large displacement distance from the previous GEMS resulted in a slowed down total walking speed. Since the motion is only a $6\,in$ $(15.2\,cm)$ with a smooth displacement, a second shoe pushing in the opposite direction will enable the desired difference between the feet. Since one foot moves forward and the other backward, the net progression of the individual will be the same as walking without any GEM shoes.

This sudden and large displacement in the previous GEMS also has a tendency to activate the wearer's natural instincts to restore balance making the walking pattern somewhat unnatural. This again has been corrected in the new GEMS design, allowing a shorter and smoother backward foot displacement as shown in Figure 3.13. The backward displacement of the foot in the new GEMS follows a constant and smooth $7.92\,in/sec$ $(20.12\,cm/sec)$ velocity.

Although the previous version of the GEMS effectively showed some after-effects in the wearer's gait comparable to previous split belt rehabilitation studies, it was unnaturally jerky pushing the wearer's foot back in a sudden motion analogous to slipping on ice. This type of sudden motion triggers a person's recovery and balancing instincts, thus producing an unnatural feel. This unnatural motion was greatly reduced in this version of the motion controlled GEMS model. My improved model is easily adjustable to different horizontal push length, force, speed and direction by simply adjusting the wheel size, wheel shape, and magnetic particle brake resistance. This adjustability in behavior of the GEMS makes testing for various situations possible.
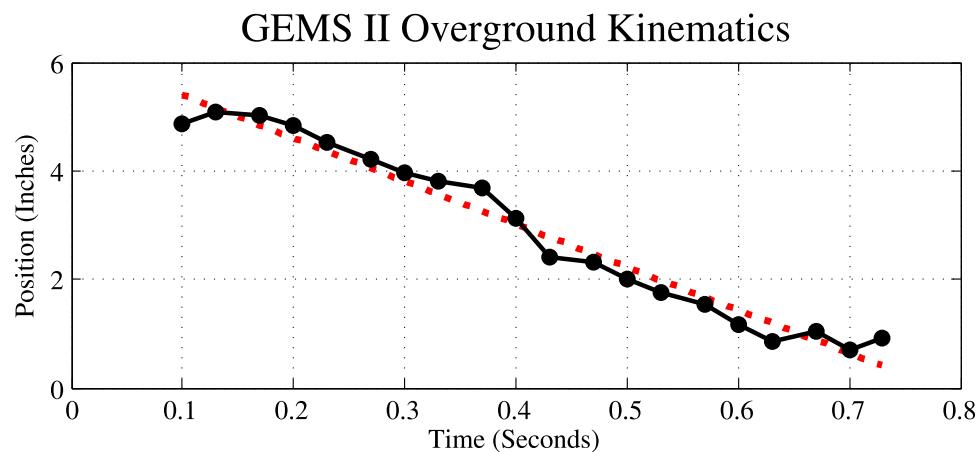
Figure 3.13: GEMS 2 backward motion during the stance phase and across the ground

While this design of the GEMS is promising and is a step forward from the previous GEMS design, room for optimization are plentiful. These optimizations include, but are not limited to, material selection, wheel shape design, control shoe resistance design, or reset mechanism design. Furthermore, during the design and assembly process of this new GEMS many practical and technical missteps were taken from which valuable GEMS design skills were acquired for proceeding versions of the GEMS. These missteps range anywhere from machining practices to design approach strategies.

3.4 GEMS Prototype Three

The first GEMS prototype (Section 3.2) was passive and had no control of the backward sliding motion of the foot during stance – this resulted in a jerky and unpredictable perturbation comparable to slipping on a slippery surface, like ice. The second prototype (Section 3.3) eliminated the problem of jerkiness and provided a smooth and controlled horizontal motion, however the various motion controls caused the second version to be too high off the ground and too heavy for actual subject testing.
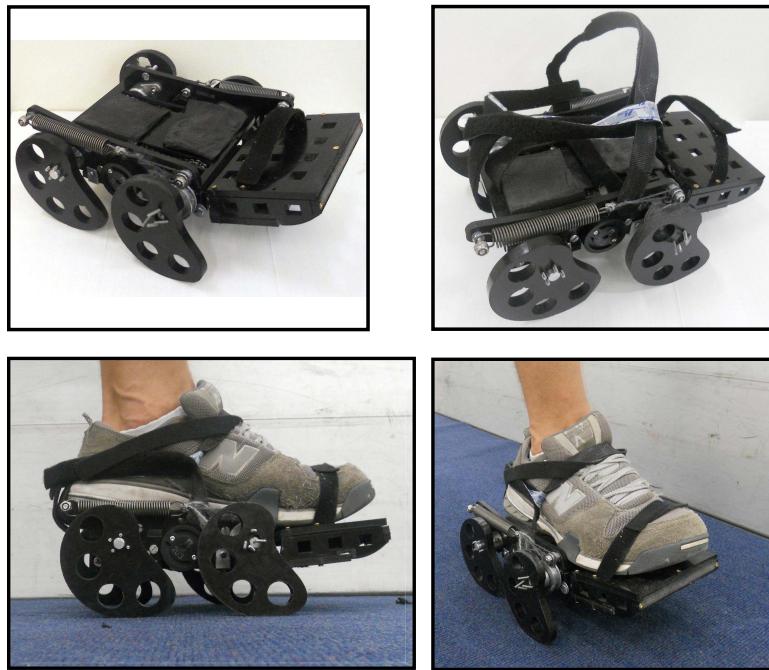
Figure 3.14: Third gait enhancing mobile shoe prototype

Heel Strike
Back wheel touches down immediately pusshing user's foot backward

Mid Stance
Front wheel touches down. User foot is pushed back with a steady motion

Terminal Stance
User foot is pushed back with a steady motion. Front toe touches ground.

Toe Off
Front wheel bottoms out. User pushes off with rubber front. Springs resets GEMS.
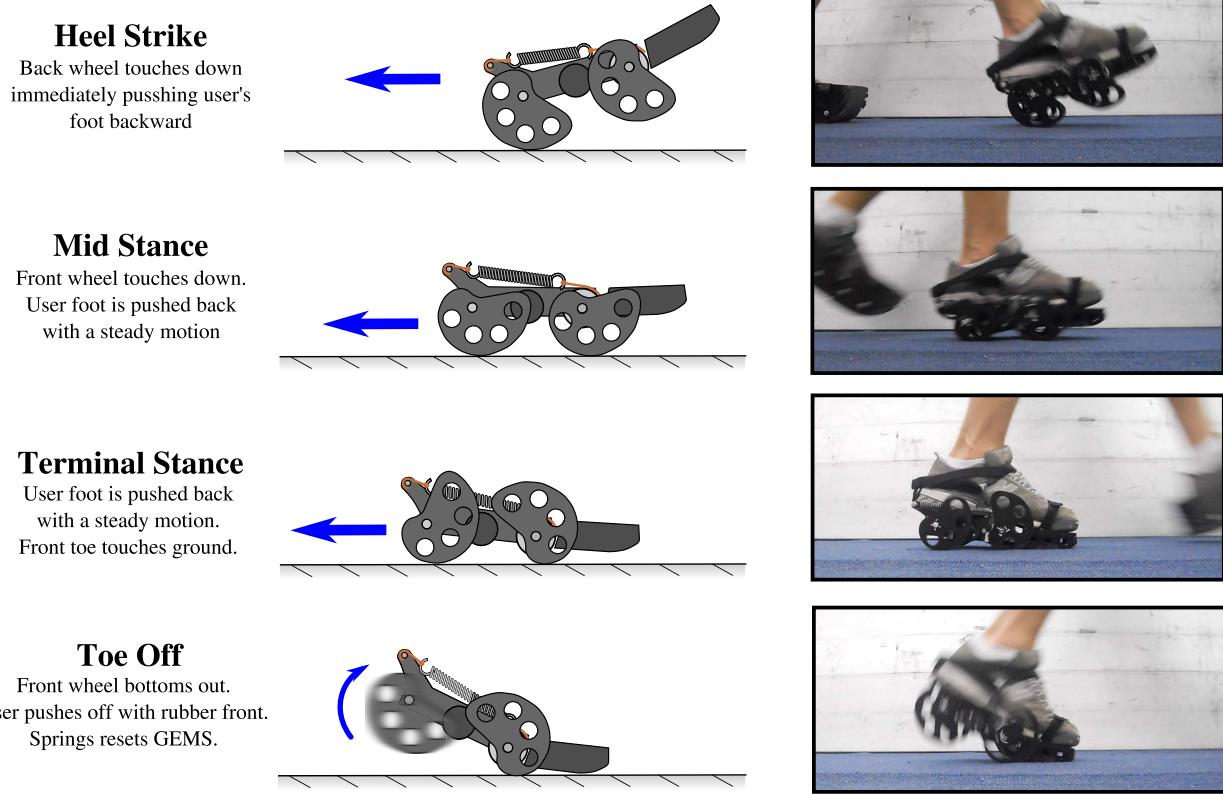
Figure 3.15: Third GEMS function. The third GEMS prototype controls backward motion via unidirectional rotary damper coupled to spiral shape wheels

The third GEMS is a balance between the first version, which was too simple and unpredictable, and the second version, which was complicated and unreliable. The third prototype of the GEMS is "just right" in that it is low to the ground, completely passive, and provides sufficient damping for a consistent shoe motion. Instead of an electronic braking system, this prototype utilizes a specially a set of seized uni-directional rotational damper, impeding the backward motion produced by Archimedean spiral wheels. This makes this prototype very as reliable and predicable as a split-belt treadmill is. The third prototype GEMS is depicted in Figure 3.14.

This version is also reliable enough to allow for at least one hour of continuous training. Additionally, this design was adapted so the shoe could either push the wearer's foot backward or forward. Compared to the second GEMS it is more reliable while allowing for longer training without maintenance. This design flexibility makes it possible to use two shoes simultaneously,

allowing one foot to be moved backward and the other to be moved forward during the respective stance phases in order to increase the applied perturbation. This motion is shown in Figure 3.15.

Two human trial experiments were conducted with healthy individuals using this GEMS prototype. As in split-belt research, healthy participants are used to show if the GEMS produces any gait asymmetry after-effects. If indeed the GEMS can produce gait asymmetry in healthy individuals, it should be able to even the gait of people with asymmetric walking pattern. In the first experiment with this version, participants wore the GEMS on one foot, while in the second experiment participants wore two GEMS, one pushing one foot forward and another pushing the other foot backward.

3.4.1 Design

3.4.1.1 Wheel Design

As with the second prototype of the GEMS in Section 3.3.1, this prototype again utilizes the Archimedean spiral shape wheel as a means to forcing/pushing the GEMS backward. When attached to an axle, this type of wheel shape redirects the wearer's weight during the stance phase into a horizontal backward or forward motion depending on the direction of the wheel slope. The Archimedean spiral shape wheel is explained in greater detail in the previous GEMS design section. The size of the wheel shape and the horizontal reaction force is determined by Equation 3.2 and 3.3 in the previous section, respectively.

The parameters of the GEMS wheels are defined in Table 3.2 and Figure 3.16. For the preliminary tests reported here, I have designed the wheels to change linearly with the radius. However, changing the slope at different points will allow for a numerical optimization of the force generated during each instant during the stance phase.

As with the previous GEMS prototype, it is important for me to mention that at the time I was designing and constructing this GEMS prototype, I had not invented the kinetic shape concept presented in the subsequent Chapter, hence it was not available for more specification and optimization of the GEMS wheel.

53

Table 3.2: GEMS Prototype 3 Archimedean Spiral Wheel Parameters

Shortest Radius, $R(\theta_i)$	1.00 in (2.54cm)
Longest Radius, $R(\theta_f)$	2.75 in (7.00cm)
Archimedean Spiral Constant, C	0.0325
Archimedean Spiral Constant, n	1.4
Arc Length / Rolling Distance (0 - 270°)	9.82in (24.94cm)
Average Horizontal Force, $F_{h_{Avg}}$, at 800 N (180 lbf)	160N (36lbf)

I have chosen the wheel parameters for this experiment such that the wheel produces sufficient backward push force to overcome heel contact. Because this GEMS version does not have as much internal mechanical impedance due to non-conservative forces such as friction, the force exerted by the wheel did not have to be overcompensated. This wheel was chosen such that its arc length is maximized for a longer backward travel/push of the foot wearing the GEMS.

I cut the wheel form a 0.375in (0.952cm) thick polyoxymethylene (POM) plastic (a.k.a. acetal, polyacetal, or Delrin®). The plastic was cut using a Universal® Laser Systems 60W laser cutter. I also fabricated aluminum hubs that joined the plastic wheel to the GEMS axle via two set screws. This wheel hub can be seen in Figure 3.16 and in Appendix A.2.

3.4.1.2 Motion Control via Rotary Damper and Wheel Reset

The GEMS uses one unidirectional damper that prevents a swift and jerky backward progression once the user steps on the shoe. The damper has an over-running clutch (or a free-wheel
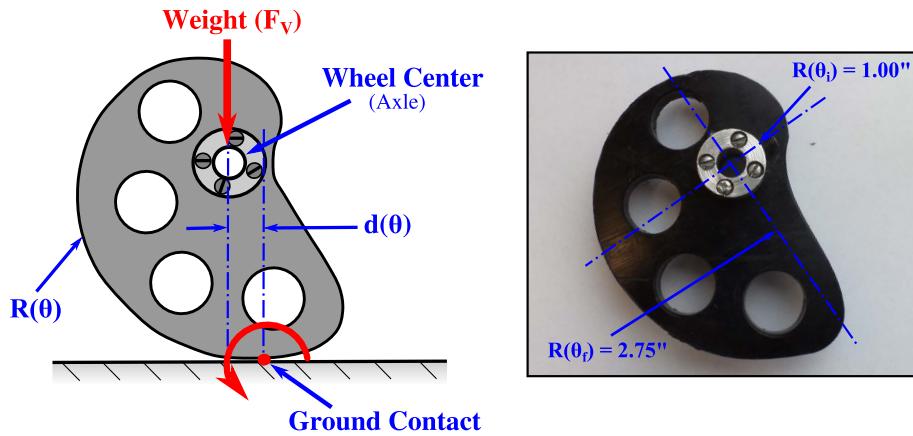
Figure 3.16: GEMS 3 spiral wheel rolls around ground contact as weight is applied to the axle
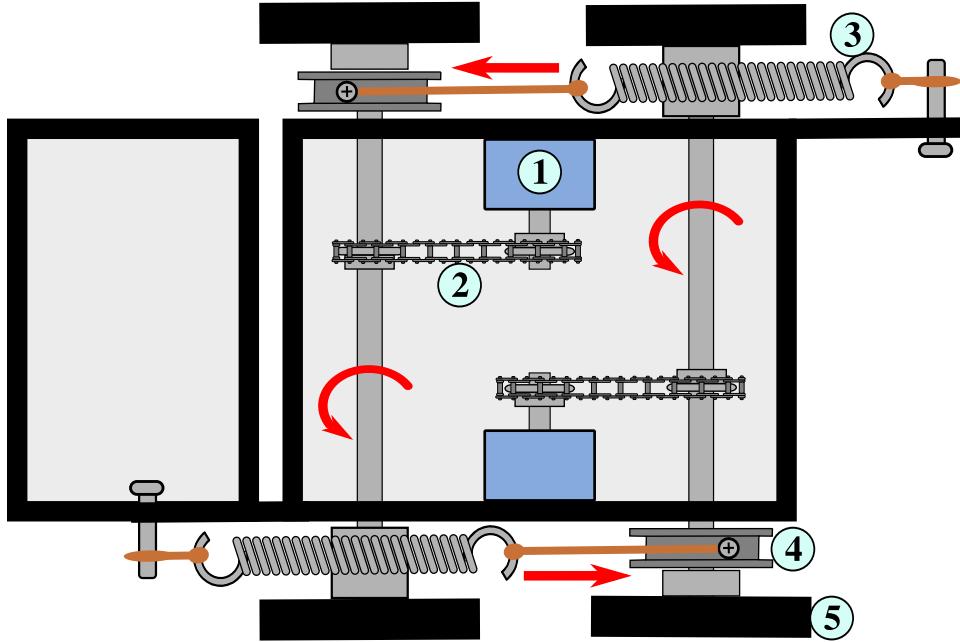
Figure 3.17: Third backward GEMS mechanism. Top view of damping and spring reset mechanism. (1) Unidirectional damper (2) Steel chain (3) Extension spring (4) Reset pulley (5) GEMS wheel

clutch) that exerts a damping force in only one direction of wheel rotation, but does not damp the mechanism when the shoe is resetting back to its initial state in preparation for another step. An over-running clutch acts similar to a continuous ratchet mechanism; it allows rotation in one direction and limits rotation in the opposite direction. Based on the torque exerted by the wheels, the damper was sized to 1.9 N-m, which provides sufficient damping to decrease the velocity of the motion to a comfortable and natural velocity magnitude. The damping torque works for wearers with a weight in the range of 68 kg to 86 kg and can be adjusted as needed for other wearers. In order to keep the GEMS velocity steady for users out of this weight range, the damper must be replaced by a weaker damper for lighter wearers or a stronger one for heavier wearers. Whereas the generated horizontal force scales with the wearer's weight, the damper force is independent of the weight. The damper is coupled to the axle of the GEMS with a chain and two sprockets, one on the axle and one on the damper, as illustrated in Figure 3.17. As the wearer steps onto the shoe, the wheels apply a torque onto both axels, one of which is coupled to the damper.

Once the shoe reaches the limit of its motion at toe off and the foot is lifted off the ground, the spring mechanism resets the wheels to their original positions to prepare for the next step starting at heel contact. The spring reset mechanism works by extending a spring, which is located on the side of the shoe, as the wheels of the GEMS rotate. As the wearer toes off into the swing phase, the spring pulls the wheels back to their initial positions. To reset the GEMS mechanism the GEMS has one extension spring per axle. Each extension spring had a stiffness of 4.40N/m (2.5 lbf/in), free/nominal length of 3.50in (8.89cm), a stretched length of 9.50in (24.13cm), and a spring outside diameter of 0.50in (1.27cm).

3.4.1.3 Frame Structure and Straps

Just like the GEMS wheel, the shoe frame structure is fabricated completely from poly-oxymethylene (POM) plastic, which I cut using a 60W laser printer. Using plastic for the frame allowed for a light and strong frame and a more rapid fabrication process. The ability to use the laser cutter also enabled unnecessary material to be extracted from certain regions of the frame, thus reducing the weight. The plastic pieces of the frame were cut such that it can snap together with certain parts being screwed together.

The frame consists of a front half and a back half connected by a hinge, which is placed near the ball of the wearer's foot and is able to angle up to thirty degrees upward. Unlike previous GEMS, this version has a more natural feel to it by letting it deform with the shoe as the user toes off and the two hinged parts angle toward each other. When the user first initiates heel contact, the wearer's shoe bottom sits 3.4in (8.6cm) off the ground. Then as the wheels are bottomed out at the end of the stance phase, the wearer's shoe bottom sits 1.5in (3.8cm) off the ground. Also unlike the second GEMS design this version is a lot lighter at 3.3lb (1.5kg). The overall dimension of the GEMS are 11.0in (28.0cm) long, 7.9in (20.0cm) wide, and 2.0in (5.0cm). More detailed dimensions can be viewed in Appendix A.2.

During usage, the wearer's shoe is strapped down to the top of the GEMS. Identical to the first and second GEMS design, these straps were designed after a traditional sandal design, rigidly

supporting the whole foot with minimal straps, this ensured minimal movement of the foot relative to the GEMS. Velcro straps were utilized for quick strapping and unstrapping of the wearer's shoe to the GEMS.

3.4.1.4 Second Direction GEMS

My design of this third iteration of the GEMS is flexible in that the shoe can redirect the downward forces to either a forward or backward motion by turning its spiral wheels around so the slope goes in the opposite direction. This is beneficial since a configuration in which one foot moves forward and one foot moves backward during the respective stance phases would generate the greatest motion differential between both feet. One GEMS was measured to move the foot back an average of 17.8 cm during each stance phase. Adding a forward-GEMS to the other foot should create twice the differential between the feet during waking.

The forward moving shoe is opposite; in the backward moving shoe, the unidirectional dampers are flipped, damping in the opposite moving direction. The forces applied to the forward shoe are initially in the direction of the desired motion; at initial heel contact, the shoe generates a forward motion and the user is pushing forward, thus the damper is engaged to slow the large motion. As the user transitions to the middle and end of the stance phase, the forces are pushing backward, but the shoe will continue to generate a forward motion since the forces from the wheel are strong enough to overcome the horizontal pushing force and the damper will no longer be affecting the motion.

As stated before, the forces involved are currently linear and constant and are based on the simple shape of the Archimedean spiral. The interaction of these forces can be optimized to generate a large range of different force profiles that could be used in several different ways. One alternative application is to use two shoes that propel a person forward during both steps to increase their natural walking speed. Does the increase in forward progression make up for the extra weight and slight increase in the height of the shoe? The answer is unclear at the moment. Another use of these shoes is to test walking perturbations where the force in the shoe could be customized or

remotely actuated to generate a sudden force to measure how people recover from unexpected foot motions.

3.4.2 Backward GEMS Experiment

3.4.2.1 Kinematic Measurements

Measurements for walking with the GEMS were taken by a 3D VICON motion capture system infrared camera at 120 Hz at the University of South Florida. Measurements were taken in the sagittal plane. The recorded individual had markers placed on the left and right ilium of the hip bone and on the lowest point on the back of the subject's sneaker of both feet, including the GEMS on the right foot. I numerically integrated the position of the markers while applying a first order low pass Butterworth filter to the velocity data. The recorded subject was age 26, male, 6ft and 1in (1.85 m) in height, with a weight of 200lb (90.7 kg).

As seen in Figure 3.18, The GEMS pushed the wearer's foot back an average of 7.0in (17.8cm) backward in a continuous, steady, and non-jerky motion. The shoe enables the wearer
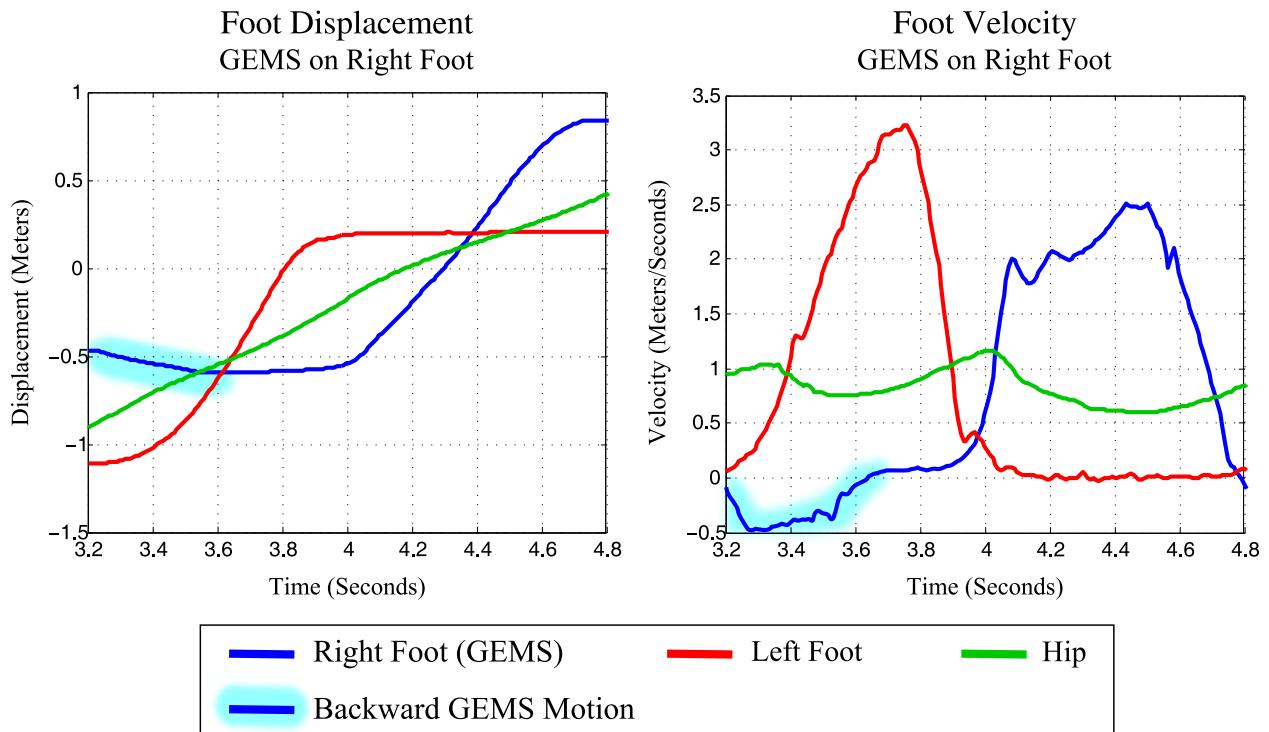
Figure 3.18: Foot kinematics of a person wearing the GEMS on their right foot

to toe off correctly for a smooth transition into the swing phase due to its deformability. Every step was very consistent and there was little variation, much like a split-belt treadmill. This low variation from step to step is important since it is our goal to mimic the motion of a split-belt treadmill.

3.4.2.2 Experimental Protocol

Subject testing consisted of three healthy subjects with no gait impairment who were all males (aged 20.7 ± 1.24 years), with normal walking patterns in a study approved by the University of South Florida Institutional Review Board. All three subjects were measured on their baseline walking pattern before walking on the GEMS. Temporal and spatial variables of gait were evaluated using the GAITRite® Walkway System (CIR Systems, Inc., PA), which is a 2.0ft (0.6m) by 16.0ft (4.9m) walkway consisting of pressure sensors that are able to accurately monitor each step position. Since I ultimately am aiming to even out asymmetric gait patterns, this experimental study emphasizes the change in step length between the baseline and immediately post-training, which is most relevant to the purpose of this study. The subjects were all healthy and start with only a negligible and normal asymmetric gait. The experimental protocol for the first GEMS study is outlined in Figure 3.19.

For baseline measurement, each subject walked on the GAITRite® Walkway System five separate times. The average step length of all five trials was taken and later compared to post-training step length. The baseline readings were analyzed for any initial and substantial asymmetry of the subject's gait before the *GEMS was strapped to the foot with the shorter step length (if present)*. This was done because an individual with an asymmetric gait such as a stroke patient would have a shorter step length on the hemiplegic side, so in essence, the GEMS was attached to the "hemiplegic" leg of the healthy subject in order to increase the step length although the asymmetry was very small or nonexistent. In order to compensate for the height and weight of the GEM shoe, an adjustable and flexible platform was worn on the opposite foot. This adjustable

platform also was made out of a rubber sole with hook-and-loop (Valcro®) straps. The feel of both shoes is similar with the exception of the generated backward motion.

With the GEMS, the subject proceeded to walk back and forth on a 48ft (14.6m) thin carpet walkway for approximately 15 minutes. The shoe was tested on a thin carpet surface in order to increase the friction between the smoothly cut plastic wheels and the ground, which prevented the shoe from slipping. During GEMS gait training, the subjects were observed and encouraged to take normal heel-to-toe steps in order to keep a consistent gait during the training process and between subjects.

After 15 minutes of gait training on the GEMS, the subject was seated in a rolling chair and the GEMS and support platform were removed. The subject was then rolled to the close-by GAITRite walkway system in order to capture the initial steps. The subject proceeded to walk five separate times on the walkway system where each trial was recorded for later comparison to the average baseline step length.

A retention test was also performed in order to observe if any after-effects persisted over a longer time period. This was done by letting the subject walk around at a comfortable pace without stopping for ten additional minutes. After the subject has walked ten minutes, the subject walked

Baseline	**Adaptation**	**Post Adaptation**	**Retention**
Subject's gait parameters were measured prior to GEMS gait training	Subject walked 15 minutes with the GEMS on the right foot.	Immediately after wearing the GEMS, subject's gait parameters were recorded.	After 10 minutes of walking, subject's gait parameters were recorded again.
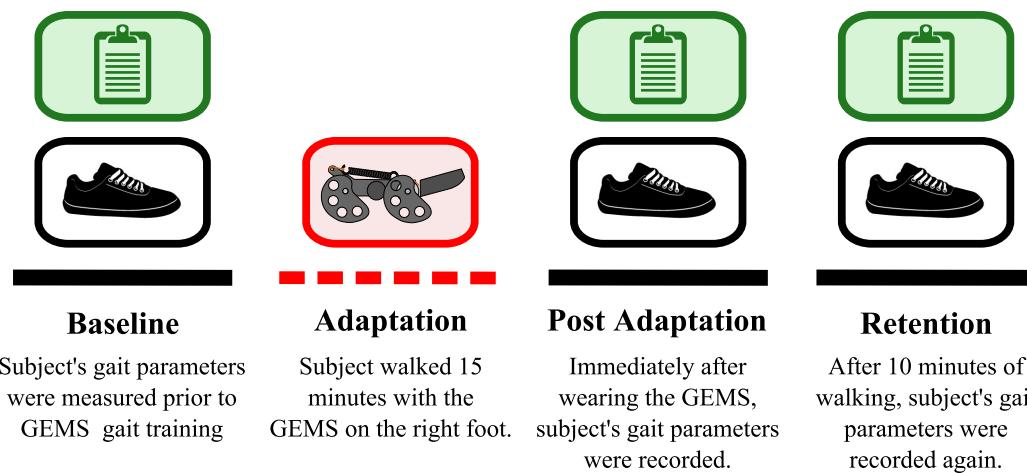
Figure 3.19: First GEMS experimental protocol. Experimental paradigm for healthy unimpaired subjects wearing the GEMS on one foot. Solid lines show periods that were recorded. Dashed line (adaptation) was not recorded. Subjects wore the GEMS during the periods marked red, while walking in normal sneakers/shoes for the periods marked black.

on the GAITrite mat five more times and an average retention step length was recorded for later analysis.

3.4.2.3 Results and Discussion

As mentioned before, the GEMS closely mimics a split-belt treadmill, however, unlike the split-belt treadmill which has a tread speed ratio of 2:1, this third prototype version of the GEMS has a foot speed ratio of 4:3. Because of this difference we expect the after-effects to be smaller than the split-belt treadmill.

The difference in step length between the foot with the GEMS and the foot without are shown in Figure 3.20 for the baseline average, post training five trials of walking 16ft (4.9m), and retention average. Note that two out of the three subjects (subject 2 and 3) showed an increase in the asymmetry in the direction that we expected – the leg that wore the shoe developed a longer step length in the post-training trials. This implies that the GEMS was able to cause an adaptation in the gait patterns. The subject who had the opposite pattern also had the highest variability in step symmetry during baseline and retention testing, so there may be other effects affecting this subject's adaptation. The post-training average step length difference for subjects 2 and 3 increased 0.67in (1.72cm) and 0.94in (2.38cm), respectively. For both subjects 2 and 3, the retention after a ten minute walking period was negligible, which is expected in healthy subjects.

Test subject 1 showed no average difference in step length increase, but rather a slight decrease of 0.36in (0.92cm) in the reverse direction. Further looking at Figure 3.20, it becomes a little more apparent that the post training step length difference fluctuated around zero. The results for subject 1 become more interesting as they show that the average retention difference in step length has a magnitude of 1.10in (2.77cm) from baseline average in the reverse direction from the other two subjects. This deviation from our hypothesis can possibly be explained by the walking style of subject 1. While subjects 2 and 3 comfortably walked in a correct gait when wearing the GEMS, subject 1 swung the leg with the GEMS around the side to compensate for the loss in step
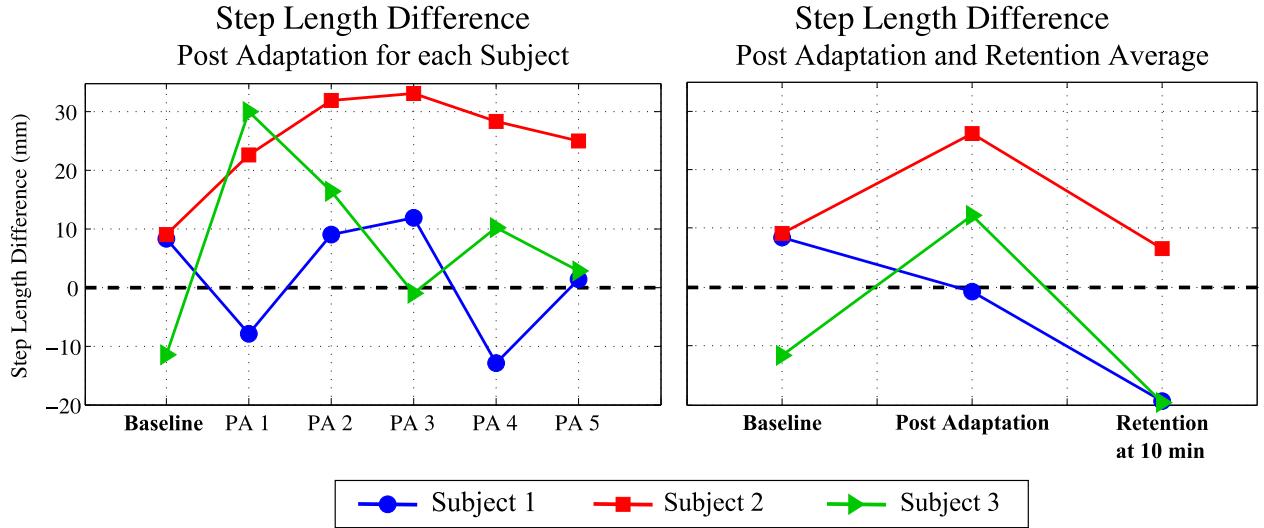
Figure 3.20: Third GEMS Experimental Results. *(Left)* Difference in step length for average base line and each five walking trials in post adaptation. *(Right)* Difference in step length for average base line, post adaptation, and retention of non-stop walking for three subjects

length, thus conditioning separate leg muscles. This indicates that training is dependent upon the wearer continuing to walk with a similar gait as they typically do.

The baseline average and all five post-training trials are shown in Figure 3.20. Again, test subject 2 and 3 validate the hypothesis and show post training after-effects. Compared to their baseline difference in step length, these after-effects are very strong in subject 2 and subject 3, although with slight differences. As subject 2 kept the after-effect over all five post-training trials, subject 3 diminishes some of the after-effect at trial 3, regains some at trial 4, and then again diminishes at trial 5.

The GEMS was found to demonstrate functional outcomes in its ability to alter normal gait patterns. In the experimental study completed with this prototype, two out of three subjects validated our hypothesis and changed their post training difference in step length. This gives reason to further investigate the effects of the shoe.

These results are very promising in the area of asymmetric gait rehabilitation. However, further investigation is needed to completely validate the effectiveness of the GEMS. A larger study with a single GEMS shoe is needed to validate these results.

3.4.3 Backward and Forward GEMS Experiment

3.4.3.1 Kinematic Measurements

As with the single GEMS kinematic measurements, analysis for walking with the GEMS were taken by a 3D VICON motion capture system infrared camera at $120\,\text{Hz}$ at the University of South Florida. Measurements were taken in the sagittal plane. The recorded individual had markers placed on the left and right ilium of the hip bone and on the lowest point on the back of the subject's sneaker of both feet, including the GEMS on the right foot. I numerically integrated the position of the markers while applying a first order low pass Butterworth filter to the velocity data. The recorded subject was age 26, male, 6ft and 1in ($1.85\,\text{m}$) in height, with a weight of 200lb ($90.7\,\text{kg}$).

As seen in Figure 3.21, the GEMS moving backward pushed the wearer's foot back an average of 7.0in (17.8cm) at a continuous, steady, and non-jerky motion of 0.40m/s. The forward moving GEMS pushed the wearer's foot forward a average distance of 7.1in(19.1cm) with a
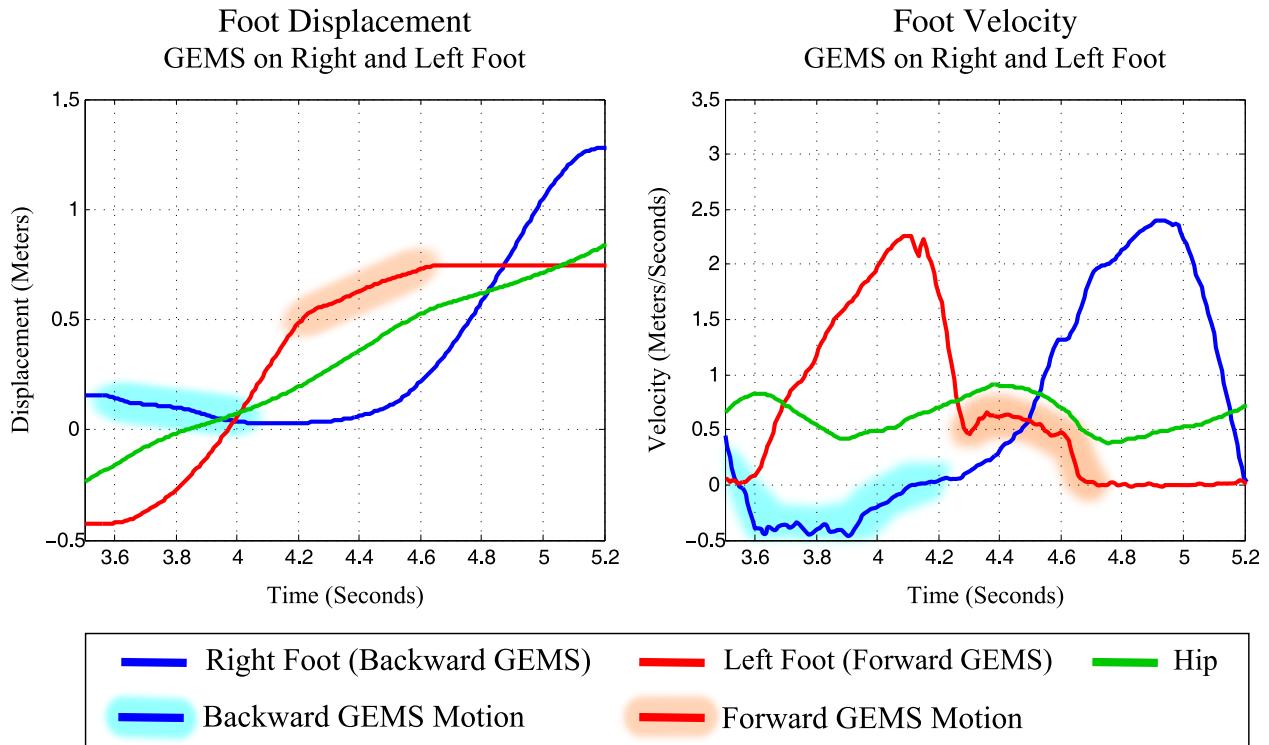
Figure 3.21: Foot kinematics of a person wearing one backward moving GEMS on their right foot while wearing the other GEMS on their left foot

velocity of 0.5m/s. The exaggerated step difference between the two feet was approximately 14in (35.5cm). However, the absolute overground translation measured at the hip was 0.2m/s less then just wearing one GEMS in the previous experiment in Section 3.4.2. This may be because the GEMS user was more careful walking with both GEMS pushing in opposite directions.

3.4.3.2 Experimental Protocol

Three healthy females (aged 22.4 ± 0.08 years), free from neurological or musculoskeletal impairment, participated in this study. All participants gave informed written consent prior to participating and the experimental protocols were approved by the Einstein Healthcare Network Institutional Review Board. This experiment was conducted at MossRehab Stroke and Neurological Disease Center in Philadelphia, Pennsylvania.

Kinematic data was collected using the CODAmotion® active marker system (Charmwood Dynamics, Leicestershire, UK) at 100 Hz. Infrared-emitting markers were placed bilaterally over the toe (fifth metatarsal head), ankle (lateral malleolus), knee (intra-joint space), hip (greater trochanter), pelvis (iliac crest), and shoulder (acromion process). Walking was recorded while subjects walked along a 21.3ft (6.5m) path over ground. Each experiment began with 10 baseline trials (one trial = one pass on walking path = approximately 8-12 strides), in which participants were instructed to walk at a comfortable pace in their own athletic sneakers (Figure 3.22).

Immediately following the baseline trials, the two GEMS were strapped on the participant's feet with the forward-rolling GEMS attached to the subject's dominant foot (the right foot, for these three subjects), and the backward-rolling GEMS attached to the non-dominant foot. Once the two GEMS were secured, 10 trials were recorded ("Early Adaptation"). Then subjects proceeded to walk for an additional 10min while wearing the two GEMS in order to adapt. During this 10min, subjects continued walking at their preferred speed, as established during the Early Adaptation period, along the same path used in the recorded trials. The number of steps during adaptation ranged from 252 to 366 (group mean 309.3 ± 56.5 steps). At the end of this period, an additional 10 trials while wearing the GEMS were recorded ("Late Adaptation"). The subjects were then
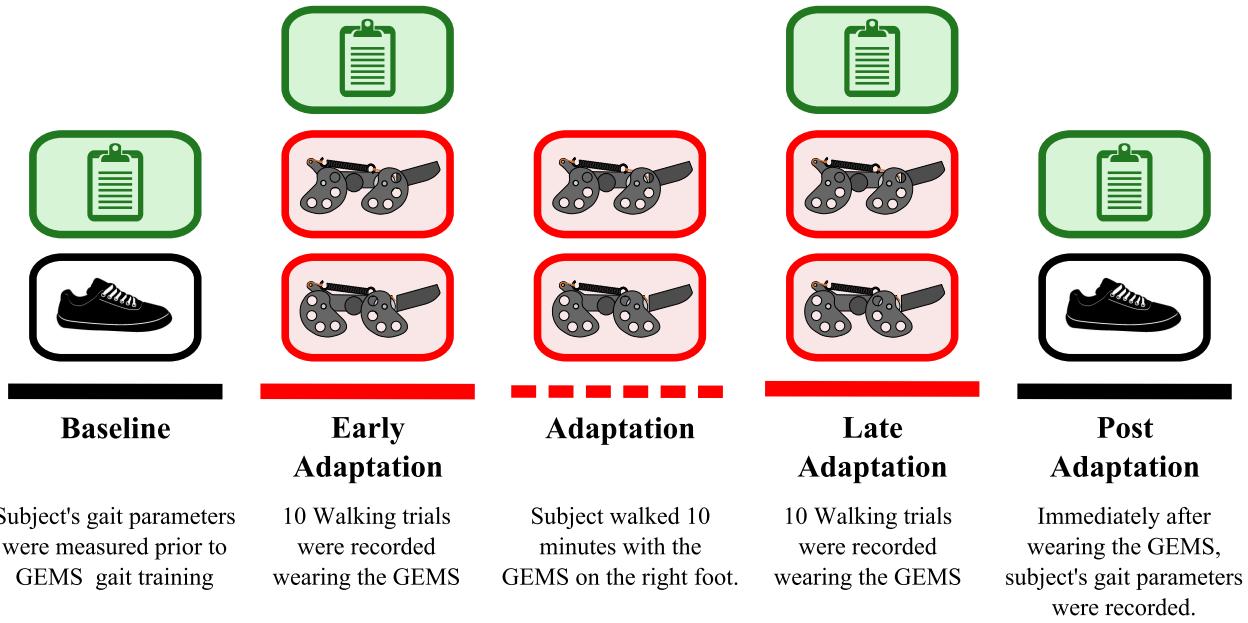
Figure 3.22: Experimental paradigm for healthy unimpaired subjects wearing one backward moving GEMS one one foot and one forward moving GEMS on the other foot. Solid lines show periods that were recorded. Dashed line (adaptation) was not recorded. Subjects wore the GEMS during the periods marked red, while walking in normal sneakers/shoes for the periods marked black. A trial was equivalent to 1 pass across the over ground walking path, which took 8-12 steps. The un-recorded adaptation period (dashed line) lasted 10 min, which was equivalent to 309.3 ± 56.5 steps (mean $\pm$ SD).

instructed to sit down to remove the GEMS, and then complete 10 additional walking trials wearing their own athletic sneakers ("Post-Adaptation"). This Post-Adaptation period allowed us to assess if the GEMS caused subjects to learn a new walking pattern.

3.4.3.3 Results and Discussion

To assess walking symmetry during Baseline, Early Adaptation, Late Adaptation, and Post-Adaptation periods, I examined two different measures: step length difference and double-support time difference. Step length was calculated as the antero-posterior distance between malleolus markers of each limb at heel strike, and was defined as "right" or "left" depending on which leg is leading. Note that step length is calculated at the instant of heel contact. We calculated a difference in step lengths (left-right) in order to assess whether steps were the same size (i.e., symmetric gait) or whether they were different (i.e., asymmetric gait). A second measure to quantify walking

symmetry was based on the difference in the duration of double support periods during gait. Double support was calculated as a percentage of time during the stride cycle that two feet were on the ground at the same time – right double support occurred at the end of right side stance phase and likewise for left double support. Difference in double support was equal to the percent double support on the right side subtracted from that on the left. A difference close to zero would indicate near-symmetric gait. Note that the weight of the GEMS shoes is different than the weight of the baseline testing with sneakers, but the weight is changed equally on both feet. The change in weight is likely to have a slight symmetric effect on the step lengths, but the measures used here are all based on the differences between the legs, which will not be significantly affected by the testing procedures.

Figures 3.23 (Top Left) and 3.23 (Bottom Left) show step length difference and double support difference, respectively, from each of the three subjects for the Baseline, Early Adaptation, Late Adaptation, and Post-Adaptation periods. Averages within subjects were calculated for the entire Baseline period (approximately 30 steps), the first five steps of Early Adaptation, and the entire Late Adaptation and Post-Adaptation periods. Wearing the GEMS did not appear to change the step length difference in a consistent manner across subjects (compare Early and Late Adaptation to Baseline in Figure 3.23 (Top Left). My preliminary results showed that the difference between Post-Adaptation, when subjects returned to walking in normal shoes, and Baseline was $8.85 \pm 14.35\,\mathrm{mm}$ (Figure 3.23 (Top Right)). A power analysis was performed to estimate the number of subjects required to show a significant effect (based on paired t-tests between baseline and Post-Adaptation). A moderate effect size of 0.68 was found. With power set to 0.8, we estimated my sample size to be 18 subjects, which is similar to those tested in previous studies of split-belt adaptation. If the trend presented here continues, this would indicate that the GEMS was capable of modifying step length symmetry in control subjects.

The experiment showed that the effect of wearing the GEMS on double-support time difference was greater than the effect on step length difference. In particular, subjects 1 and 2 showed altered double support durations between Baseline and Early Adaptation in the positive
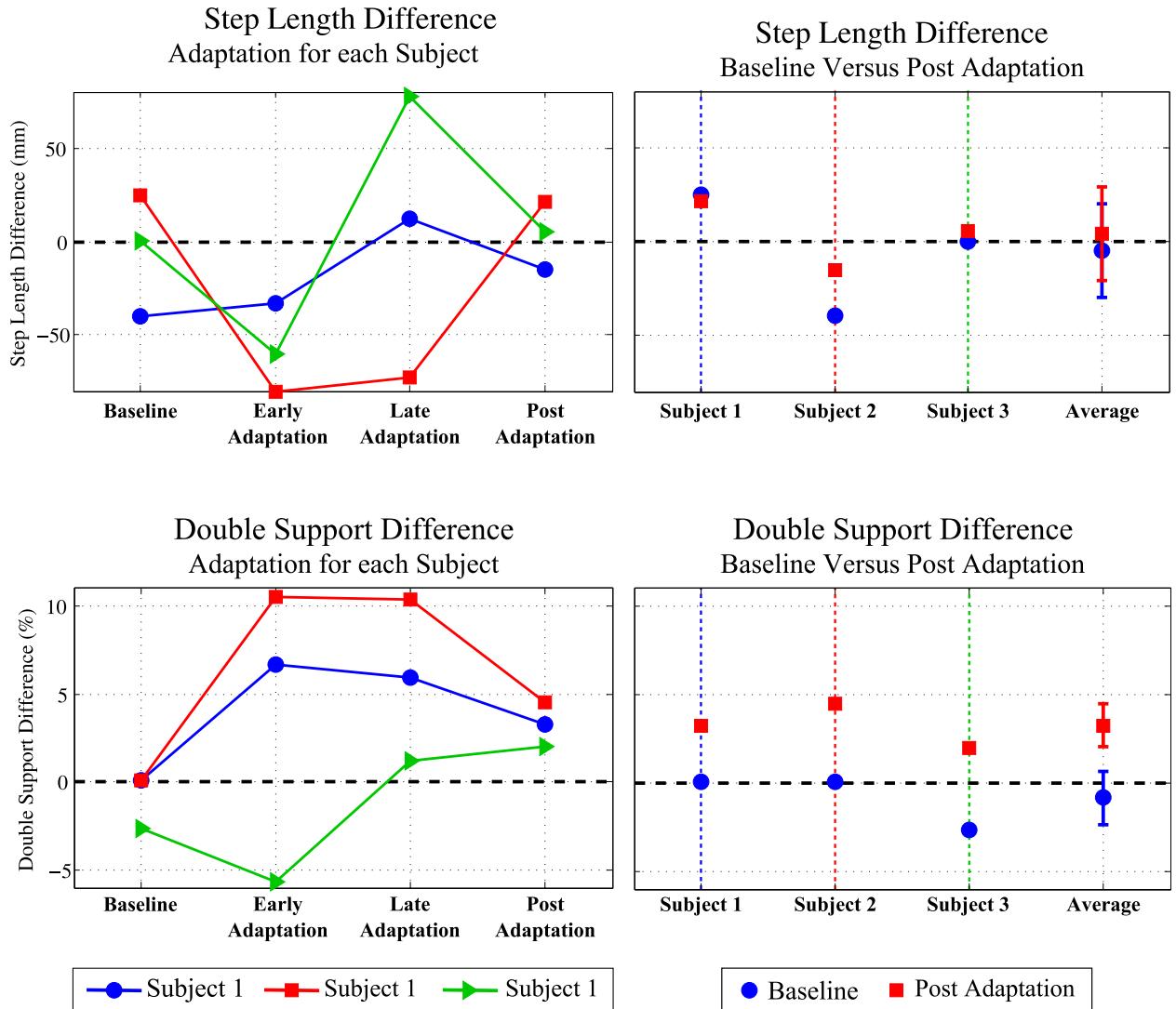
Figure 3.23: GEMS 3 experimental results. *(Top Left)* Single-subject data showing the average difference in step length (right-left; ± standard deviation), during baseline (BL), early adaptation (EA), late adaptation (LA), and post-adaptation (PA). *(Top-Right)* Summary of single-subject and group-averaged differences in double support time between baseline and post-adaptation *(Bottom Left)* Single-subject differences in double support duration. Double support difference was calculated by subtracting the duration of right double support time (expressed as a percent of stride cycle) from the duration of left double support. *(Bottom-Right)* Summary of single-subject and group-averaged differences in step length between baseline (blue diamonds) and post-adaptation (red squares). Error bars show 1 standard deviation

direction, indicating that the GEMS caused the left (backward-GEMS) double-support phase to be longer than that on the right (forward-GEMS). Note that this is what we had predicted, as previously discussed. While double-support difference in subject 3 changed in the negative direction

during Early Adaptation, by Late Adaptation the change was positive and similar to the trend in the other subjects. The mean change between Baseline and Post-Adaptation for all subjects was 4.08 ± 0.78 (units = % total stride time), shown in Figures 3.23 (Bottom Left) and (Bottom Right), which indicates that they learned a new double-support relationship between the legs while walking with the GEMS. This effect size was very large (5.23) leading to an estimated sample size of 3 (power = 0.8). Since double support is a measure of temporal interlimb coordination (i.e., determined by "when" the limb is placed during gait), our preliminary data suggest that the GEMS shows promise in changing temporal relationships between the legs.

This study found that the GEMS was able to perturb temporal (double support duration), but not spatial coordination (step length). Adaptation to the perturbation in temporal coordination was characterized by a lengthening of the double support phase on the left side (wearing the backward GEMS) as compared to the right side (wearing the forward GEMS). This asymmetry in double support continued even when the GEMS were removed and subjects resumed walking with normal shoes (Figure 3.23 (Bottom Right)). This indicates that a new coordination was learned and stored following a period of walking with the GEMS.

Adaptation reflects a re-calibration of motor commands in response to changes in the environment (e.g., icy surfaces) or in oneself (e.g., injury) [126, 158, 178]. It is a form of short-term learning that occurs on a time scale of minutes to hours and is likely a precursor to more permanent forms of motor learning. Recently, it has been suggested that adaptation training on a split-belt treadmill, which also perturbs interlimb coordination, may help to improve abnormal gait coordination in individuals who have had a stroke [158, 160, 161]. However, these effects were short-lived unless training occurred over the course of weeks [160], and the improved coordination did not transfer completely to normal walking over ground [161]. These issues may limit the feasibility of using the split-belt treadmill as a rehabilitation device.

In summary, I have successfully developed a Gait Enhancing Mobile Shoe (GEMS), which is able to generate a smooth and consistent backward and/or forward motion. The GEMS outlined in this study is the successor of previous models and builds upon previous design concepts. This

current design of the GEMS resulted in a lighter, smoother shoe that was lower to the ground. While the shoe provides similar motions to a split-belt treadmill in a completely passive way, it exhibits various benefits, which include gait training in different environments and locations, and gait training over a longer period of time. These benefits will allow for further investigation of the long-term after-effects of extended training sessions, which I hypothesize will lead to prolonged retention of the corrected gait in individuals with asymmetric gaits.

Chapter 4: Kinetic Shapes

As discussed in the Background Section 2.2.1, rolling of a circular wheel is definitely not novel, but the rolling of an irregularly curved shape, such as a spiral rolling on a flat surface, is useful and has not received much research attention. In my work, I derived definitions for two- and three-dimensional shapes that, when placed on a flat plane and loaded with a known weight at the axle point, will produce a desired ground reaction force parallel to the flat plane. My derivation also allows for the exact prediction of shape kinematics. *Due to their predictive kinetic parameter, I have named my definition/solution of these shapes, kinetic shapes (KS).* KS can be used in static and dynamic applications some of which include, but are not limited to, gait rehabilitation, walking assistance, self-stabilization, material hardness testing, and mechanical robotic control.

In this chapter, I will present my static and dynamic solutions of two- and three-dimensional kinetic shapes, while also demonstrating physical verification of kinetic shape examples. I will also put forth my innovative and practical application ideas utilizing the KS.

4.1   Static Mathematic Derivation

In this section I will present my derivations of a two- and three- dimensional kinetic shape in static equilibrium (restrained and not rolling).

4.1.1   Two-Dimensional Kinetic Shape

A curved and continuous arbitrarily 2D shape that is pressed onto a flat plane at its axle point tends to rotate towards the decreasing radius. This rotation is because the applied weight is not vertically in line with the point of ground contact, which creates unmatched moment couples

with the radial ground reaction force (RGRF). Hence, the shape is not in static equilibrium and will roll.

However, if the rolling motion of this shape is restrained by a horizontal force at the axle point so that the shape is in static equilibrium, the sum of all forces and moments must equal zero (Figure 4.1(a)). For this to happen, the moment couple created by the RGRF (friction) and the equal and opposite restraining force has to be equal to the moment couple created by the applied weight and the equal and opposite vertical ground reaction force, $F_v(\theta)$. Because the shape varies in radius, the RGRF component pushing away from the axis, $F_r(\theta)$, must vary as well.

I will assume that the friction force between the ground and the shape is large enough for the shape not to slip. It is also assumed that there is no deformation of the shape or ground. This analysis is also only valid when the applied force at the shape axle is much greater than the combined gravitational forces applied at the center of mass of the shape or if the center of mass coincides with the shape axle.

I will derive a general formulation to create a shape that will generate a desired RGRF given a known applied weight at the axle (rotation) point. I will begin by adding the two moment couples acting on a general 2D shape under static equilibrium

$$\sum M_z = F_v(\theta)L(\theta) - F_r(\theta)H(\theta) = 0 \tag{4.1}$$

where $L(\theta)$ and $H(\theta)$ are shown in Figure 4.1(a), and defined as

$$H(\theta) = R(\theta)\sin(\psi(\theta)), \tag{4.2}$$

$$L(\theta) = R(\theta)\cos(\psi(\theta)), \tag{4.3}$$

and $\psi(\theta)$ is defined in Figure 4.1(a). Substitution of Equation 4.2 and Equation 4.3 into the statics equilibrium Equation 4.1 yields

$$F_v(\theta)[R(\theta)\cos(\psi(\theta))] = F_r(\theta)[R(\theta)\sin(\psi(\theta))]. \tag{4.4}$$
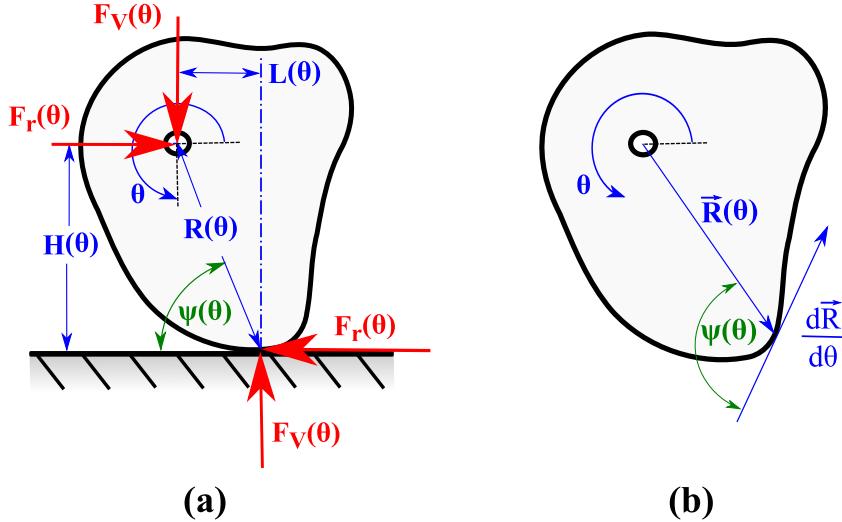
Figure 4.1: 2D shape diagram. (a) 2D shape in static equilibrium. (b) Polar tangential angle of a 2D shape [216]

Dividing out $R(\theta)$ in Equation 4.4 and applying appropriate trigonometric identity redefinitions results in

$$\psi(\theta) = \tan^{-1}\left(\frac{F_v(\theta)}{F_r(\theta)}\right).$$

(4.5)

Equation 4.5 defines the angle $\psi(\theta)$ along the perimeter of the shape. $\psi(\theta)$ relates the weight applied at the shape axle and the RGRF at ground contact.

Commonly, $\psi(\theta)$ can also be defined as the angle at the point of ground contact between the ground vector (shape tangent), $dR/d\theta$, and the radial vector (axle to ground contact point), $R(\theta)$, as shown in Figure 4.1(b) [216]. This relation is defined as

$$\psi(\theta) = \tan^{-1}\left(\frac{\overrightarrow{R}(\theta)}{d\overrightarrow{R}/d\theta}\right)$$

(4.6)

and is a frequent definition known as the *polar tangential angle* of a curve [216]. It is now apparent that it is possible to equate and reorder Equations. 4.5 and 4.6 to form a first order ordinary differential equation.

$$\frac{dR}{d\theta} = \frac{R(\theta)F_r(\theta)}{F_v(\theta)}$$

(4.7)

72

One might attempt to solve Equation 4.7 for the exact shape radius solution, $R(\theta)$, by substituting assumed curve definitions, however the resulting solutions do not yield correct definitions. That is, substituting polar radius functions, $R(\theta)$, of the logarithmic spiral, Cortes's spiral, Archimedean spiral, or an involute circle does not yield a valid exact solution that can be verified by plugging it in back into Equation 4.4.

However, Equation 4.7 can be solved using the method of separation of variables by first rearranging,

$$\left(\frac{1}{R(\theta)}\right) dR = \left(\frac{F_r(\theta)}{F_v(\theta)}\right) d\theta \, , \tag{4.8}$$

then integrating both sides of the equation to solve for the shape radius.

$$R(\theta) = \exp\left[\int \frac{F_r(\theta)}{F_v(\theta)} d\theta + \text{Constant}\right] \tag{4.9}$$

The integration constant can be solved for by applying one initial condition, which is the initial radius of the shape, $R(\theta_i)$, and when solved will produce Equation 4.10.

$$R(\theta) = R(\theta_i) \, exp\left[\int \frac{F_r(\theta)}{F_v(\theta)} d\theta\right] \tag{4.10}$$

Equation 4.10 is used to derive a 2D kinetic shape that produces a RGRF, $F_r(\theta)$, when a load perpendicular to the ground at axle point, $F_v(\theta)$, is applied. In the following section I will show how Equation 4.10 is used to design a shape and experimentally verify several force profiles.

My derivation of the kinetic shape can be checked to determine if it produces the desired reaction forces when loaded by taking the obtained shape $R(\theta)$ and finding $\psi(\theta)$ in Equation 4.6, then inputting it back into Equation 4.5. The resulting forces should match the initial input forces. This also enables one to find the kinetic profile of any irregular curved 2D shape.

The 2D KS equation, Equation 4.10, yields a unitless radius value. This indicates that it only depends on the force ratio rather than the size of the shape. Thus, when loaded with a fixed weight, the same kinetic shape with different scaling factors will produce the same RGRF.

For example, a KS for a constant $800\,\text{N}$ applied weight and constant $200\,\text{N}$ RGRF input will behave the exact same as a kinetic shape for a constant $4\,\text{mN}$ vertical and constant $1\,\text{mN}$ RGRF input regardless of its scaled dimensions. Theoretically, the behavior of the kinetic shape does not depend on the radius size, but on the change in radius.

In practice it may be desirable to reverse this definition. That is, it may be advantageous to know what RGRF response a given shape may provide when a weight is applied. Thus, if a two-dimensional shape, $R(\theta)$, is given, known, provided, or approximated, Equation 4.7 can be rearranged to predict the shape's ground reaction response, $F_r(\theta)$, when a known applied vertical force $F_v(\theta)$ is applied to the shape rotation axle. This auxiliary equation is Equation 4.11.

$$F_r(\theta) = \frac{F_v(\theta)\frac{dR(\theta)}{d\theta}}{R(\theta)} \tag{4.11}$$

Note that my derivation can in turn be rearranged so that when the shape function and RGRF is given, one can find the applied weight that is being applied to generate the RGRF at that specific angle.

Further, it is interesting and important for me to note that if the 2D kinetic shape, $R(\theta)$, is to be continuous around itself from initial kinetic shape radius, $R(\theta_i)$, to final kinetic shape radius, $R(\theta_f)$. Equation 4.12 must be satisfied.

$$\int_{\theta_i}^{\theta_f} \frac{F_r(\theta)}{F_v(\theta)} d\theta = 0 \tag{4.12}$$

Here, θ_i is the initial shape angle and θ_f is the final kinetic shape angle.

I have written a computer program in Matlab® that is able to generate a two dimensional kinetic shape given specified radial and vertical force functions. *This programming code is available in Appendix B.1.*

4.1.1.1 Examples

To demonstrate a few examples of two dimensional kinetic shapes defined using Equation 4.10, I have chosen three different desired radial ground reaction force (RGRF) functions with constant applied vertical weight. The three radial force functions are constant, sinusoidal with an offset, and Fourier series expanded non-smooth. Each derived kinetic shape assumed a constant vertical force of 800 N. The magnitude of all these force functions were chosen for the convenience of experimentation. However, as explained in the previous Section 4.1.1, it is possible to apply a variable weight with respect to the angle around the kinetic shape. Although the analysis can be expanded to kinetic shapes that revolve more than once, I will focus on shapes that range from zero to 2π rads.

I verified all three 2D kinetic shapes with the setup shown in Figure 4.2. The weight was applied to the shape axle and the reaction forces exerted by the shape axle are simultaneously measured with a pair of load cell sensors (Omega LC703) placed in line with the forces. The load cell that measured the radial ground reaction force was supported by a small platform to minimize any cable tension force due to the sensor weight. This platform was adjustable in height. The signal from both force sensors was read by a Phidgets® force sensor interface board. The interface board was connected to a desktop computer, acquiring data with a C++ program. To prevent the kinetic shape from slipping, I placed two-sided course grade sandpaper at the point the kinetic shape was touching the ground. As the applied weight was gradually loaded, the RGRF increased as well.

The tested kinetic shapes were loaded at $\pi/6$ rads intervals from zero to 2π rads. Some perimeter points, such as the lowest radii on a spiral shape, were omitted because the ground contact could not physically reach that particular perimeter point due to other parts of the kinetic shape touching the ground, however this usually was only one kinetic shape orientation angle.

The reaction load for each perimeter point was recorded with a mass of 7.9 kg to 18.0 kg at four even intervals applied to the shape axle. The mean and standard deviation for each point
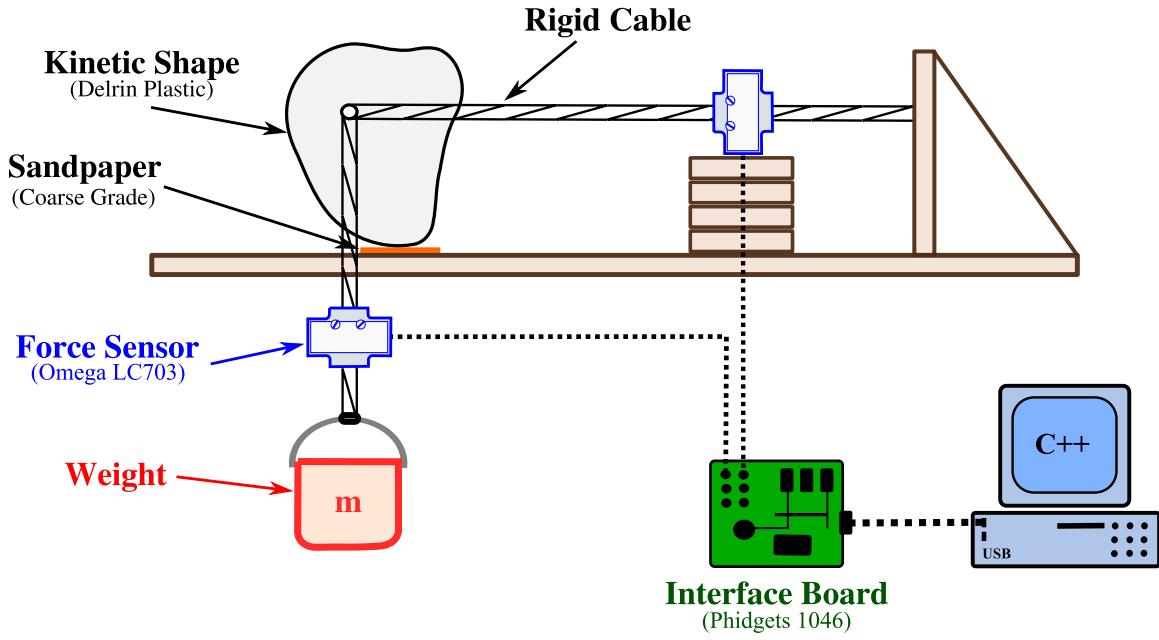
Figure 4.2: Schematic of test structure for 2D kinetic shape examples

was calculated in terms of percent force transfer $(100 * F_r(\theta)/F_r(\theta))$, which was then multiplied by $800\,N$.

The three 2D kinetic shapes examples chosen for verification were laser cut from tough $0.25\,in$ ($0.64\,cm$) thick Acetal Resin (Delrin®) plastic. The laser cutter used to cut test shapes was a 60 Watt Universal Laser System® VLS4.60.

4.1.1.1.1   2D Shape Example 1: Constant RGRF.   To introduce the KS design concept, I will start with a shape defined by a constant force function and a constant applied weight function. Equation 4.13 and Equation 4.14 describe the input force functions used to derive the first 2D kinetic shape. The kinetic shape was started with an initial shape radius of $2.5\,in$ ($6.35\,cm$) and ends with a $5.46\,in$ ($13.86\,cm$) radius.

$$F_v(\theta) = 800\,N \tag{4.13}$$

$$F_r(\theta) = 100\,N \tag{4.14}$$

Plugging in these force functions and the value for initial radius, Equation 4.10 becomes the following Equation 4.15.
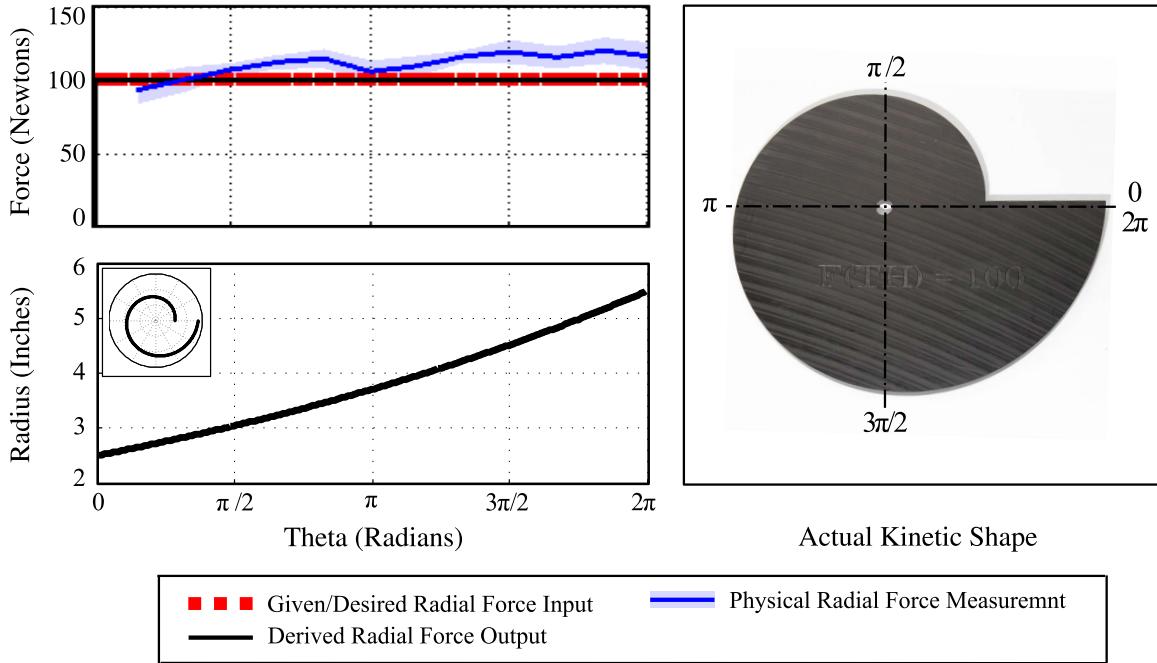
Figure 4.3: 2D kinetic shape example 1. 2D example kinetic shape 1 forms a spiral with a monotonically increasing radius. Theoretical and measured RGRF are in good agreement.

$$R(\theta) = 2.5 \, \exp \left[\frac{100}{800} \, \theta \right]_{\theta=0}^{\theta=2\pi} \tag{4.15}$$

As an 800 N force is applied at the shape axle, the shape will react with a 100 N force regardless of the rotation angle. As seen in Figure 4.3, the gradual and slight exponential increase in shape radius, $dR/d\theta$, statically produces a constant force at any perimeter point around the shape, creating a spiral KS. Note that the units, and thus the scaled size, are irrelevant and this KS would behave the same if scaled up or down, the shape radius change is established by the ratio between the the applied weight and the RGRF.

As seen in Figure 4.3, the physical measurements are in good agreement with theoretical values. Although the force profile standard deviation is not always within predicted theoretical range, the trend is relatively constant. There are some variations; however, these can be accounted for by shape surface and test setup imperfections, hence an overall larger kinetic shape may be more resistant to surface imperfections.
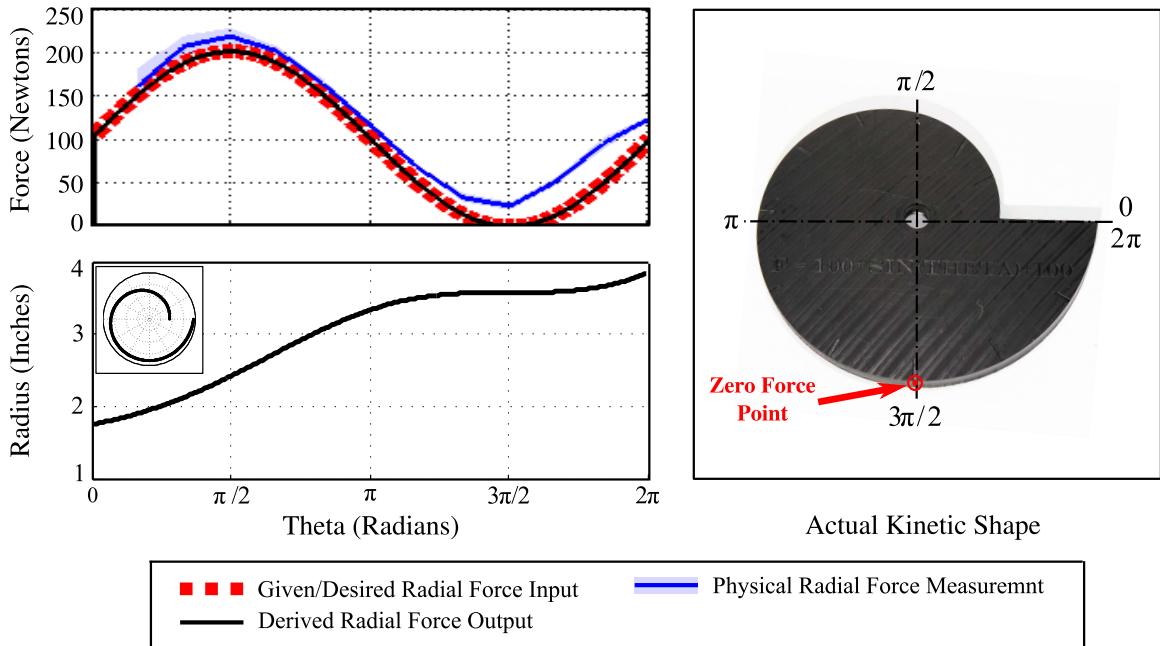
Figure 4.4: 2D kinetic shape example 2. 2D Shape 2 forms a monotonically increasing radius spiral, however when a constant weight is applied, it reacts with a sinusoidal RGRF around its perimeter.

4.1.1.1.2 2D Shape Example 2: Sinusoidal RGRF.
A kinetic shape can also be derived using a more complicated sinusoidal force function with a constant offset. Equations 4.16 and 4.17 describe the input functions that define this 2D kinetic shape.

$$F_v(\theta) = 800N \tag{4.16}$$

$$F_r(\theta) = 100\sin(\theta) + 100N \tag{4.17}$$

With these forces, Equation 4.10 then becomes Equation 4.18.

$$R(\theta) = 1.75 \exp\left[\frac{1}{8}[\theta - \cos(\theta)]\right]_{\theta=0}^{\theta=2\pi}. \tag{4.18}$$

Unlike in the previous example that produces a constant RGRF, this shape creates a varying sinusoidal force throughout the rotation. In this example it is clear that the reaction force is dependent on $dR/d\theta$ of the shape. As the sinusoidal force reaches a maximum at $\theta = \pi/2$ radians, radius change, $dR/d\theta$, is steepest and so produces the highest RGRF. Likewise, as the
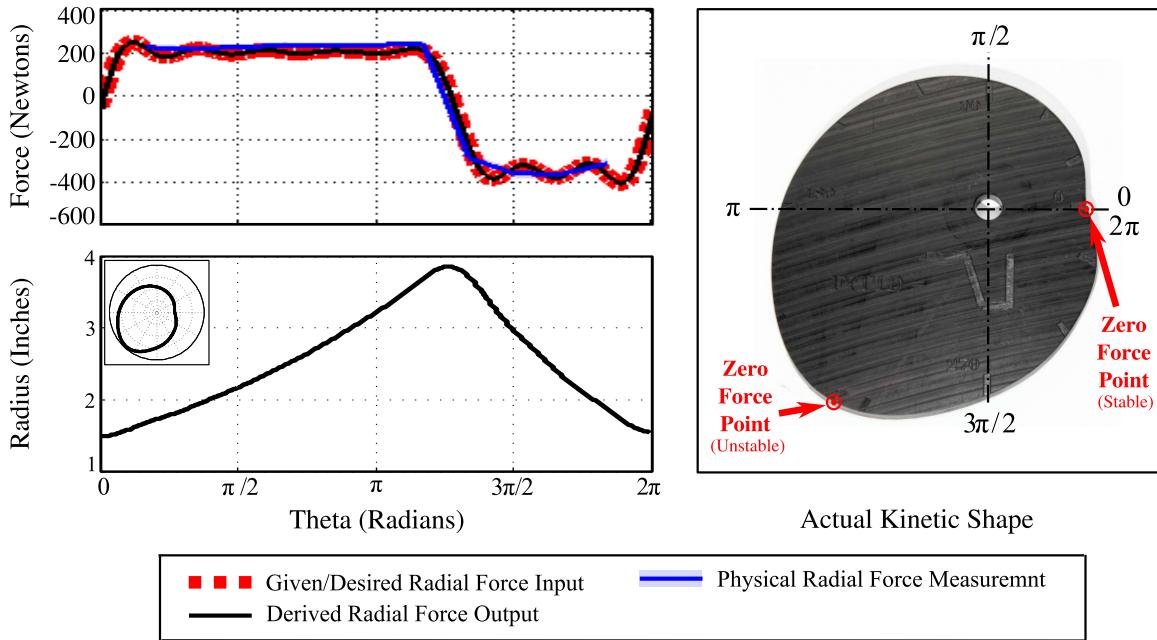
Figure 4.5: 2D kinetic shape example 3. The shape forms a continuous shape because, when a constant weight input is applied, it initially reacts with a positive reaction force and then switches directions to form a negative RGRF. All physical measurements are in good agreement.

input force reaches a minimum of zero at $\theta = 3\pi/2$, $dR/d\theta$ is zero as well. At $\theta = 3\pi/2$ the KS instantaneously behaves as a circular wheel would, and, like a circular wheel, it does not produce a RGRF when vertically loaded at its axle.

This kinetic shape assumes a spiral shape with a starting radius of 1.75 in (4.44 cm) and a final radius of 3.82 in (9.70 cm). The shape again resembles a spiral due to the fact that the sum of force around the shape perimeter is non-zero as defined by Equation 4.12. The physically measured force profile for this 2D kinetic shape, shown in Figure 4.4, was slightly higher than predicted, however the sinusoidal trend was in good agreement with theoretical.

4.1.1.1.3 2D Shape Example 3: Fourier Expanded Piecewise Force. It is clear now that a kinetic shape can be designed with any input force function. I will now expand my analysis to a piecewise force function that has been expanded using a ten term Fourier series to demonstrate that nearly any force profile can be created. This piecewise force function is defined by Equations 4.19 and 4.20.

$$F_v(\theta) = 800\,N \tag{4.19}$$

$$F_r(\theta) = \begin{cases} 200\,N, & 0 \le \theta \le 3.8 \\ 4380 - 1100\,\theta\,N, & 3.8 < \theta < 4.3 \\ -350\,N, & 4.3 \le \theta < 2\pi \end{cases} \tag{4.20}$$

Note that this time the RGRF function crosses zero at $\theta = 4.1$ *radians* (Figure 4.5). This point is an unstable maxima of the shape radius function. At exactly this point, the shape produces no force, while any slight deviation off this point will cause RGRF. At exactly $\theta = 0/2\pi$ *rads* the shape radius is at its global minima with a RGRF equal to zero. This point is a stable point of the kinetic shape. This shape does not form a spiral, but is continuous around its perimeter, starting and ending at the same radius, hence Equation 4.12 is satisfied.

Measurements on the physical shape verified the predicted values. As seen in Figure 4.5, physical data falls well within theoretical values. Note that the standard deviation of measurements increases where the force profile fluctuates the most. Note that no measurements are possible at exactly $\theta = 0/2\pi$ *rads*

4.1.2 Three-Dimensional Kinetic Shape

In this section, I am expanding my analysis into the third dimension by deriving and analyzing a 3D KS. The concept and behavior of a 3D KS can sometimes become hard to visualize. While a 2D KS produces only one radial ground reaction force (RGRF) that pushes radially away from the shape's axle, a 3D KS can theoretically produce two force components: the same RGRF pushing radially away from the axle point and a tangential ground reaction force (TGRF) pushing *around* the vector of weight application that is orthogonal to the ground plane.

To visualize the TGRF, imagine a cylinder sitting on a flat plane (e.g., a cup on a table) as shown in Figure 4.6. If the cylinder is tipped over, the ground experiences only a RGRF to keep it from slipping. However, if the cylinder's sides are not uniform in length around its perimeter,
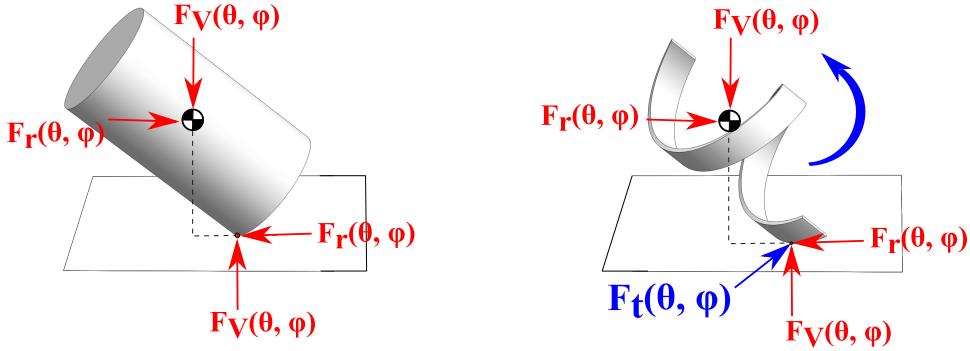
Figure 4.6: 3D kinetic shape tangential force example. While a cylinder (left) only produces a RGRF force to keep it from slipping, a helix curve (right) produces an additional TGRF for sideways rolling

such as in a helix curve, the tipped helix will tend to push and roll around the vertical axis which runs through the center of mass and is perpendicular to the ground. This rolling motion is caused by the TGRF acting on the cylinder's rim at ground contact. This TGRF could also be generated if a 2D KS is wrapped around a vertical axis with a non-constant radius and is defined as the ground contact force acting parallel to the curve and tangent to the ground contact point.

In this section I will derive a set of equations that allows me to construct a shape that produces a known radial RGRF and TGRF when vertically loaded. In this scenario, the vertical load always acts orthogonal to the ground plane. Similar methods and assumptions utilized to derive a 2D KS are used to produce an analytical model of a 3D KS. *It is important to note that the 3D kinetic shape formulation describes a curve. This curve represents the accessible path of ground contact.*

I begin by examining a 3D shape/curve in static equilibrium, shown in Figure 4.7(a). Note that the rotating of the vertical force application vector is held orthogonal with an additional moment, M_r. The summation of all moment couples about the ground contact point and in the radial plane (Figure 4.7(b)) and about the vertical vector in the ground plane (Figure 4.7(c)) yields the following Equation 4.22 and Equation 4.23, respectively. Note that the force vectors are decomposed into cartisian coordinates, which are the vertical, radial, and tangential directions.

81
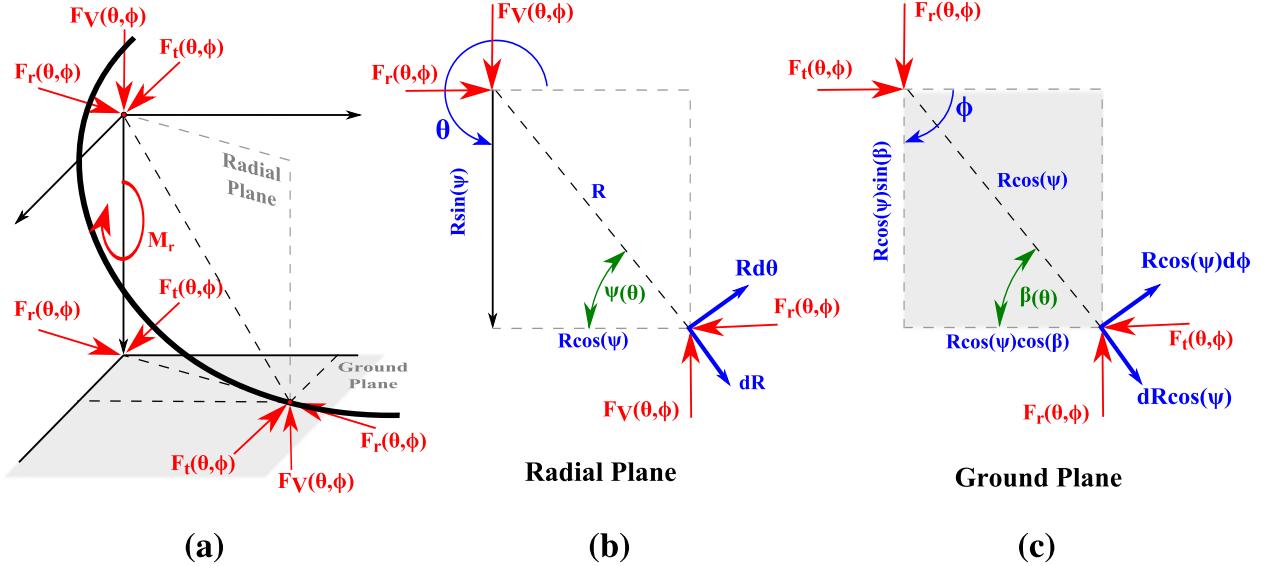
Figure 4.7: 3D kinetic shape kinetic diagram. (a) Kinetic diagram of a 3D kinetic shape in static equilibrium. (b) Radial and tangential geometric parameter relation.

The tangential and radial force vectors are perpendicular.

$$\sum M_r = F_v(\theta,\phi)R(\theta,\phi)\cos[\psi(\theta)] \dots \qquad (4.21)$$
$$-F_r(\theta,\phi)R(\theta,\phi)\sin[\psi(\theta)] = 0$$

$$\sum M_g = F_t(\theta,\phi)\left[R(\theta,\phi)\cos[\psi(\theta)]\sin[\beta(\phi)]\right] \dots \qquad (4.22)$$
$$-F_r(\theta,\phi)\left[R(\theta,\phi)\cos[\psi(\theta)]\cos[\beta(\phi)]\right] = 0$$

As before in the derivation of the two-dimensional kinetic shape in Section 3.1.1, these kinetic equilibrium equations are simplified, rearranged, and related to the geometric parameters shown in Figure 4.7(b) and Figure 4.7(c).

$$\tan[\psi(\theta)] = \frac{F_v(\theta,\phi)}{F_r(\theta,\phi)} = \frac{R(\theta,\phi)}{dR/d\theta} \qquad (4.23)$$

$$\tan[\beta(\phi)] = \frac{F_r(\theta,\phi)}{F_t(\theta,\phi)} = \frac{R(\theta,\phi)}{dR/d\phi} \qquad (4.24)$$

Angle $\psi(\theta)$ again relates forces in the radial plane while also relating the radial vector to the ground plane. Angle $\beta(\phi)$ relates the TGRF to the RGRF, while also relating the geometric parameters shown in Figure 4.7(b). Note that both, $\psi(\theta)$ and $\beta(\phi)$ define the curvature offset of the 3D curve with the elevation and azimuth angle.

After rearranging terms, I am left with two first order ordinary differential equations.

$$\left(\frac{1}{R(\theta,\phi)}\right) dR = \left(\frac{F_r(\theta,\phi)}{F_v\theta,\phi)}\right) d\theta \tag{4.25}$$

$$\left(\frac{1}{R(\theta,\phi)}\right) dR = \left(\frac{F_t(\theta,\phi)}{F_r\theta,\phi)}\right) d\phi \tag{4.26}$$

These two differential equations can be solved by the method of separation of variables, yielding a solution for the shape radius, $R(\theta,\phi)$, in spherical coordinates.

$$R_r(\theta,\phi) = \exp\left[\int \frac{F_r(\theta,\phi)}{F_v(\theta,\phi)} d\theta + \text{Constant}\right] \tag{4.27}$$

$$R_t(\theta,\phi) = \exp\left[\int \frac{F_t(\theta,\phi)}{F_r(\theta,\phi)} d\phi + \text{Constant}\right] \tag{4.28}$$

The integration constant in each equation is dependent on the initial radius of the shape and can be solved for by applying the initial radius, $R(\theta_i,\phi_i)$, of the kinetic shape. Once solved the final 3D kinetic shape equations are Equations 4.29 and 4.29.

$$R_r(\theta,\phi) = R_r(\theta_i,\phi_i) \, exp\left[\int \frac{F_r(\theta,\phi)}{F_v(\theta,\phi)} d\theta\right] \tag{4.29}$$

$$R_t(\theta,\phi) = R_t(\theta_i,\phi_i) \, exp\left[\int \frac{F_t(\theta,\phi)}{F_r(\theta,\phi)} d\phi\right] \tag{4.30}$$

Equations 4.29 and 4.30 jointly describe a 3D KS curve that relates an applied weight, RGRF ($F_r(\theta,\phi)$), and TGRF ($F_t(\theta,\phi)$). These radius equations describe the shape in the radial and tangential direction, respectively. That is, this curve depends on the integration path through the specified force functions. As before, a radial force is produced by the change in radius with

elevation angle, θ, in the radial direction, while TGRF is produced by a change in azimuth angle, ϕ in the tangential direction.

It is important for me to note that there cannot be a tangential ground reaction force without a radial ground reaction force, just as there can not be a radial ground reaction force without a vertically applied force at the axle point. In other words, examining Equations 4.29 and 4.30, a TGRF, $(F_t(\theta, \phi))$, requires RGRF $(F_r(\theta, \phi))$, which in turn RGRF $(F_r(\theta, \phi))$ requires a vertical force (orthogonal to ground) applied at the axle/rotation point.

In the absence of a twisting TGRF, Equation 4.29 is Equation 4.10, and forms a 2D kinetic shape. This is made clear when examining Equation 4.30, where as the force ratio diminishes, the radius does not change in the tangential direction. Also, as the force ratio increases, the shape increases exponentially in the tangential direction radius.

Further, in absence of the TGRF *and* integrating across the elevation angle, θ, and azimuth angle, ϕ, Equation 4.29 can describe a 3D shape that only produces a RGRF, or a force that only acts away from the axle/rotation point, however ranges in three dimensions.

The 3D kinetic shape described by Equations 4.29 and 4.30 will produce a three dimensional object that produces ground reaction forces specified at each point coordinate on the object. Depending on the specified RGRF and TGRF some points may be inaccessible. However, in practice one could derive a curve rather than a 3D object, specifying the integration path along the curve. This is precisely how I am going to exemplify the 3D shape in the upcoming section.

As before with the 2D KS, it may be beneficial to predict ground reaction forces when the shape radius function is given or approximated and the applied vertical force is known. Adjusting Equation 4.23 for the radial direction yields the previously defined Equation 4.31, describing the RGRF of the 3D KS.

$$F_r(\theta, \phi) = \frac{F_v(\theta, \phi)\frac{dR(\theta, \phi)}{d\theta}}{R(\theta, \phi)} \tag{4.31}$$

Further, the definition of the TGRF is available by redefining Equation 4.24 and substituting Equation 4.31, yielding the complementary Equation 4.32.

$$F_t(\theta, \phi) = \frac{F_v(\theta, \phi) \frac{dR(\theta, \phi)}{d\phi}}{\frac{dR(\theta, \phi)}{d\theta}} \tag{4.32}$$

Granted a given or approximate radius function of a function onto which a known vertical force is applied, my derived equations are able to predict the ground reaction forces in the radial and tangential direction for a 3D shape or curve.

Unlike the 2D shape where there is only one direction to integrate over angular position, θ, the 3D kinetic shape is defined by two variables, angular position elevation angle, θ, and angular position azimuth angle, ϕ. Hence the continuity of the 3D kinetic shape depends on the path of integration over these two variable. For a 3D kinetic shape to be continuous about itself from initial kinetic shape radius, $R(\theta_i, \phi_i)$, to final kinetic shape radius, $R(\theta_f, \phi_f)$, Equation 4.33 must be satisfied.

$$\int_{\theta_i}^{\theta_f} \int_{\phi_i}^{\phi_f} \frac{F_r(\theta, \phi)}{F_v(\theta, \phi)} + \frac{F_t(\theta, \phi)}{F_r(\theta, \phi)} \, d\phi d\theta = 0 \tag{4.33}$$

Supplemental to this derivation, I present a computer program in Matlab® that is able to generate a three dimensional kinetic shape given specified radial and vertical force functions. *My programming code is available in Appendix B.2.*

4.1.2.1 Examples

In this section I will present two examples of the the application of my three- dimensional kinetic shape equations. As opposed to the two dimensional kinetic shape, the three dimensional shape is more difficult to fabricate and examine. While the theoretical results of the 3D kinetic shape definitions are sound, the construction of these shapes presents a challenge that is open for future research and development. Therefore, in this section I am only presenting two theoretical examples for the 3D kinetic shape derived by Equations 4.29 and 4.30.

4.1.2.1.1 3D Shape Example 1   I will begin by defining the force functions for this first three dimensional kinetic shape. Equation 4.34 defines the applied force orthogonal to the flat ground surface, this force function is held as a constant. Equation 4.35 is the radial ground reaction force at ground contact and is a repeating sinusoidal force function with period of 2π. The tangential ground reaction force acting around the vertical force vector is defined in Equation 4.36. This tangential force is held at a constant value. Note that the tangential function always has to be less than the radial force function, just as the radial function has to less than the vertical applied force. The radial and tangential ground reaction force with respect to the elevation angle, θ, and azimuth angle, ϕ, is shown in Figure 4.8. The initial radius for this example shape is $R(\theta_i)$=1.0cm.

$$F_v(\theta,\phi) = 1000 \ N \tag{4.34}$$

$$F_r(\theta,\phi) = 200\sin(\theta) \ N \tag{4.35}$$

$$F_t(\theta,\phi) = 15 \ N \tag{4.36}$$

Inserting these force definition into Equations 4.29 and 4.30 produces the three dimensional kinetic shape radius definition. In this example, the radial function of the kinetic shape is defined by Equations 4.37 and 4.38.

$$R_r(\theta,\phi) = 1.0 \ \exp\left[-\frac{\cos(\theta)}{5}\right] \ cm \tag{4.37}$$

$$R_t(\theta,\phi) = 1.0 \ \exp\left[-\frac{15\phi}{200\sin(\theta)}\right] \ cm \tag{4.38}$$

As previously stated, this kinetic shape definition in three dimensions depends on the integration path and not only on the initial and final angles. As seen on the bottom of Figure 4.8, changing the path across the two dimensions (θ and ϕ) will alter the resulting kinetic shape. As seen, if the integration path is strictly across the azimuth angle, ϕ, the shape radius definition will only occur in the tangential direction with Equation 4.38. Similarly, if the integration is strictly across the elevation angle, θ, the shape radius definition will only occur in the radial direction with Equation 4.37.
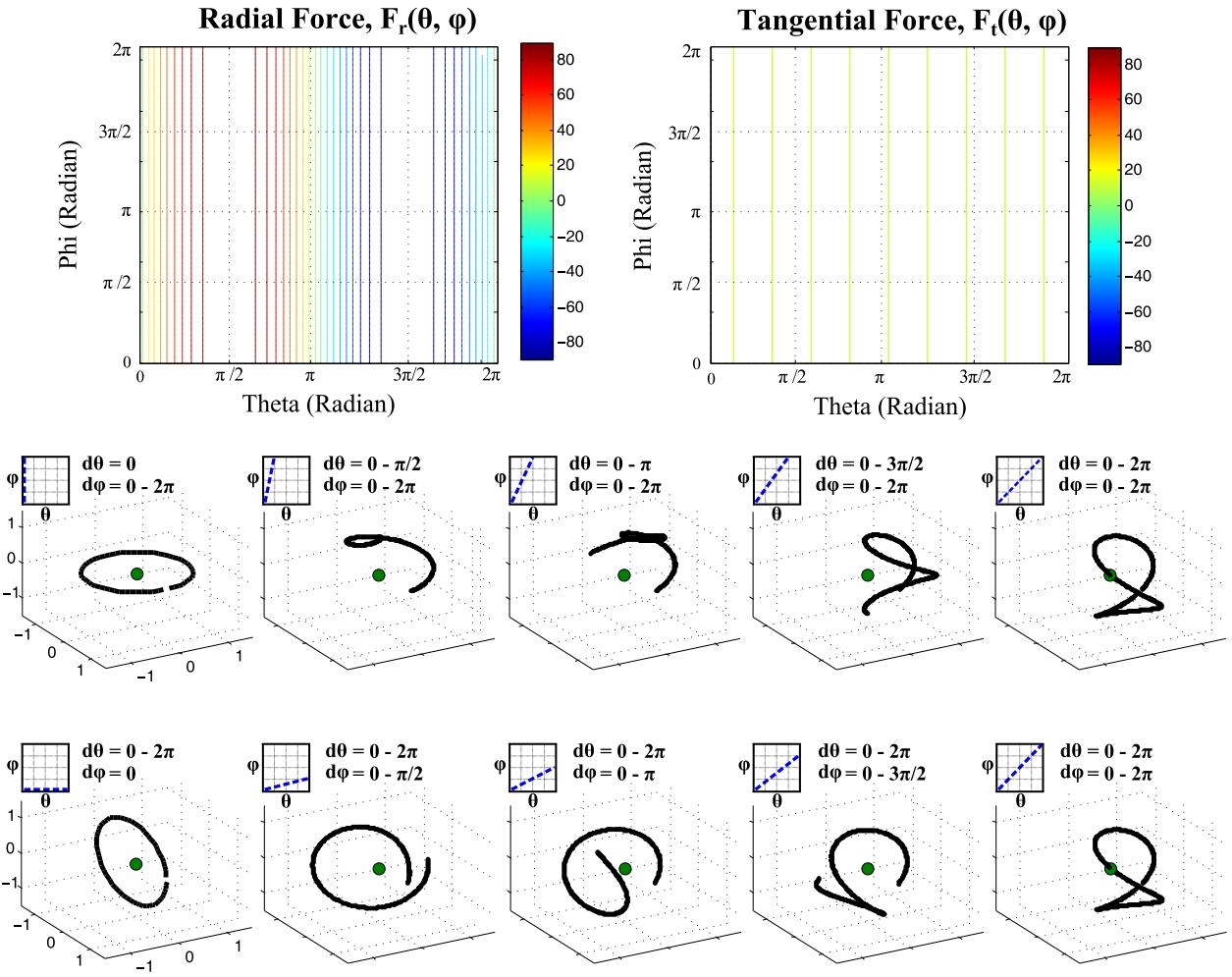
Figure 4.8: 3D kinetic shape example 1 results. The 3D kinetic shape is a curve which depends on the integration path across the elevation and azimuth angles.

In this example the integration path across angle dimensions is one line, however the integration path may be chosen as any type of curve. The integration direction could also be chosen to be the direction of least force (i.e. least resistance). This type of path of least resistance may be desirable when free rolling comes into play.

4.1.2.1.2 3D Shape Example 2   In this example I will be discussing more complex force functions that define the three dimensional kinetic shape. The applied vertical force function is again be defined as a constant (Equation 4.39). The radial ground reaction force definition in this example is now dependent on both angles, θ and ϕ (Equation 4.40). Further, unlike the first example, the tangential force definition is now dependent on the azimuth angle, ϕ (Equation 4.41). These force
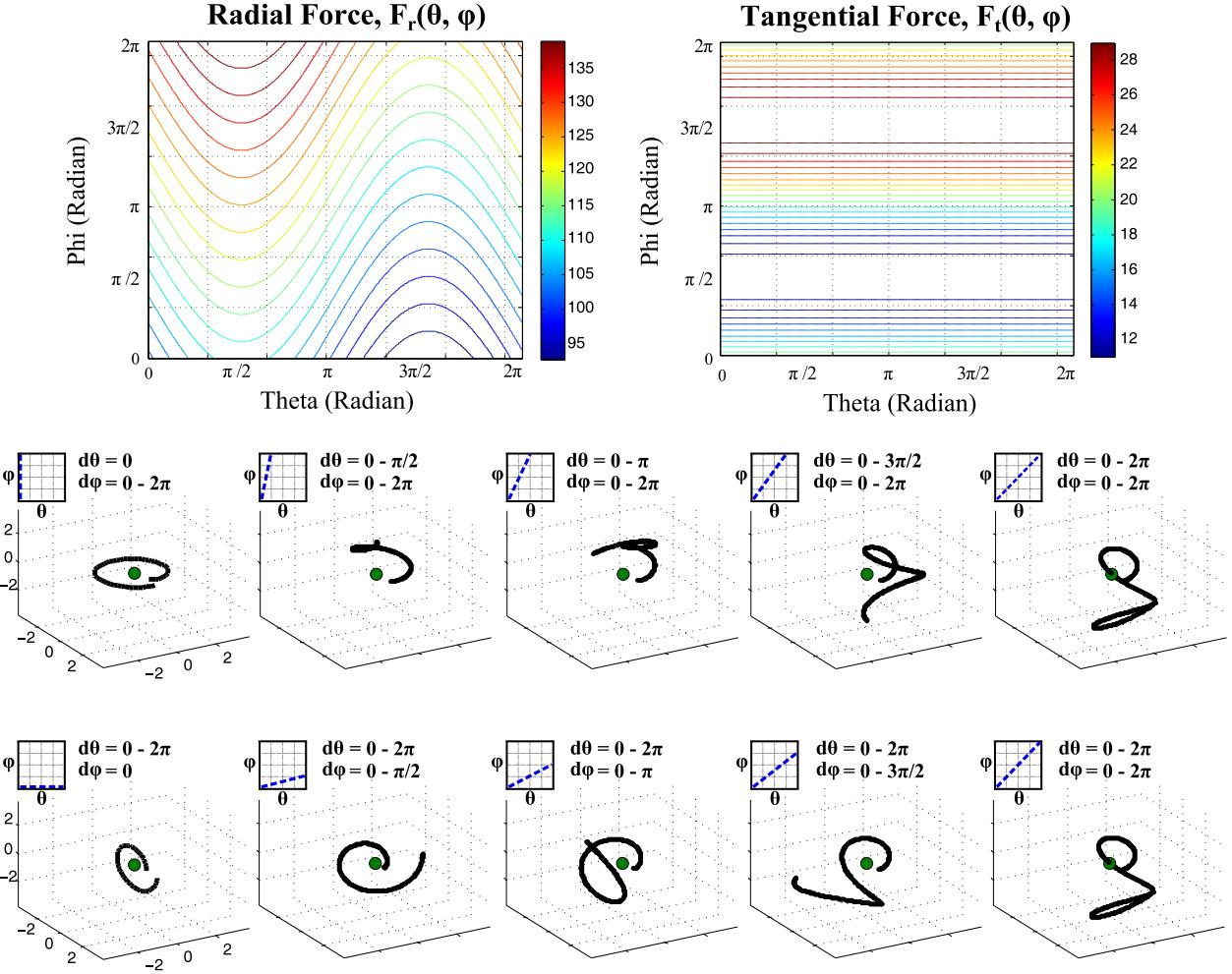
Figure 4.9: Three dimensional kinetic shape example 2 results

definition can be seen in Figure 4.9. The initial radius is again defined as $R(\theta_i)$=1.0cm.

$$F_v(\theta, \phi) = 1000 \, N \tag{4.39}$$

$$F_r(\theta, \phi) = 100 + 5\phi + 10\sin(\theta) \, N \tag{4.40}$$

$$F_t(\theta, \phi) = 20 - \sin(\phi) \, N \tag{4.41}$$

Again, inserting these force definitions into Equations 4.29 and 4.30 produces the three dimensional kinetic shape radius definition. The radial function of the kinetic shape is defined by Equations 4.42 and 4.44.

$$R_r(\theta, \phi) = 1.0 \, \exp\left[\frac{\phi\theta}{200} + \frac{\theta}{10} - \frac{\cos(\theta)}{100}\right] \, cm \tag{4.42}$$

$$R_t(\theta,\phi) = 1.0 \ (\phi + 2\sin(\theta) + 20)^4 \ \exp[\ 2\sin(2\sin(\theta) + 20) \ \dots \tag{4.43}$$

$$Ci(\phi + 2\sin(\theta) + 20) - 2\cos(2\sin(\theta) + 20) \ Si(\phi + 2\sin(\theta) + 20)] \ cm$$

Here, *Ci* and *Si* are the cosine integral and sine integral functions, respectively. Although the shape radius definition in the tangential direction, (ϕ) direction is long and complicated, it is still exact and valid.

As seen in Figure 4.9, as the path of integration is strictly defined along ϕ, the kinetic shape still has a slight offset as it follows a path from $\phi_i = 0$ to $\phi_f = 2\pi$. This makes sense since Equation 4.44 returns a minute value at this range and $\theta_i = \theta_f = 0$. In this example it is also worth mentioning that as the shape definition is strictly in the elevation angle range and not in the azimuth range, the kinetic shape assumes that of a two dimensional kinetic shape, setting all ϕ to zero.

4.2 Dynamic Mathematic Derivation

Here I am presenting my derivation for the two- and three- dimensional kinetic shapes when not in static equilibrium. That is, when the shape is rolling as a vertical force is applied to the axle point (origin) of the kinetic shape and orthogonal to level ground. Particularly, I will derive equations that can predict the kinematics of the kinetic shape. These formulations only apply if a kinetic shape polar function is already known or is approximated/fitted. Further this dynamic analysis is not exclusive to kinetic shapes, but can predict the motions of any shape/curve rolling across level ground as an orthogonal force is applied to the axle point.

4.2.1 Two-Dimensional Kinetic Shape

As discussed previously in Section 3.1, when a curved and continuous arbitrary 2D shape is pressed onto a flat plane at its axle point, a moment is generated. However, now I will consider the case where the shape is not restrained, where the moments are not matched and the sum of all moments does not diminish, hence the shape will freely rotate about the ground contact point. This setup can be seen in Figure 4.11(a).

As before, I will assume that the friction force between the ground and the shape is large enough for the shape not to slip. It is also assumed that there is no deformation of the shape or ground. In a vertical setup this analysis is also only valid when the applied force at the shape axle is much greater than the combined gravitational forces applied at the center of mass of the shape or if the center of mass coincides with the shape axle. Note that in the forthcoming derivation $R(\theta)$ is the 2D shape radius defined in polar coordinates and is a function of θ.

To derive the dynamics formulation for a two dimensional kinetic shape, I will begin by stating Isaac Newton's 2nd law [143] for rotational rigid body dynamics in plane motion for the 2D shape (Equation 4.44).

$$\sum M = J_G(R, \theta) \frac{d^2\theta}{dt^2} \tag{4.44}$$

Here the polar mass moment of inertia of the kinetic shape about the ground contact point is defined as $J_G(R, \theta)$ and $d^2\theta/dt^2$ is the angular acceleration of the shape rolling over the ground contact point. As an irregular kinetic shape rolls, the polar moment of inertia changes with shape orientation with respect to ground contact. Thus, it is important for me to formulate the polar mass moment of inertia so that it accounts for this reorientation. I will start by defining Equation 4.45 as the polar mass moment of inertia of a kinetic shape of variable thickness and heterogeneous material about the shape origin ($R = 0, \theta = 0$).

$$J_O(R, \theta) = \int_A R(\theta)^2 \, \rho(R, \theta) \, t(R, \theta) \, dA \tag{4.45}$$

Here, $\rho(R, \theta)$ is the continuous density across the kinetic shape and $t(R, \theta)$ is the continuous thickness throughout the kinetic shape. The differential area, dA, of the shape can be defined by the infinitesimal change in radius and arc length as seen in Figure 4.10. This definition of the shape area yields Equation 4.46.

$$J_O(R, \theta) = \int_{\theta_i}^{\theta_f} \int_{R_i}^{R_f} R(\theta)^2 \, \rho(R, \theta) \, t(R, \theta) \, R(\theta) dR \, d\theta \tag{4.46}$$

θ_i and θ_f are the initial and final angles of the shape definition, while R_i and R_f are the initial
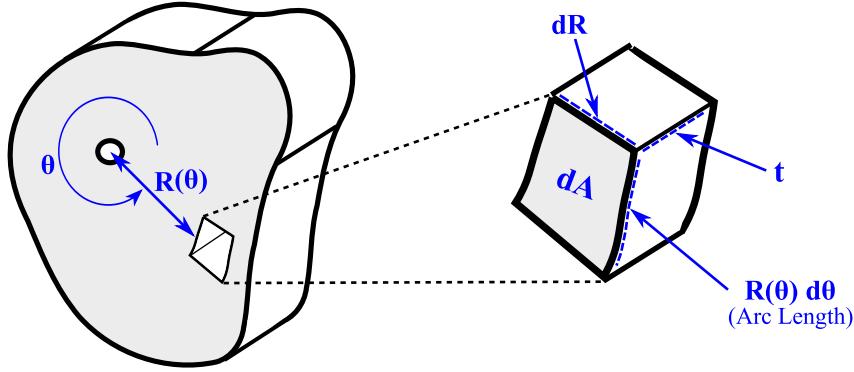
Figure 4.10: Differential (Infinitesimal) kinetic shape surface area element with finite thickness

and final radii of kinetic shape radius function $R(\theta)$. It is possiblethe define the polar mass moment of inertia with a variable thickness and heterogeneous shape density, however due to later explained kinetic shape applications, I will consider the 2D kinetic shape to be of uniform density and thickness. This consideration produces Equation 4.47.

$$J_O(\theta) = \rho\, t\, \int_{\theta_i}^{\theta_f} \int_{R_i}^{R_f} R(\theta)^3\, dR\, d\theta \tag{4.47}$$

Integrating accross the radial variable, I obtain Equation 4.48. Notice that I am assuming no gaps in the radial direction, hence integrating from origin ($R_i = 0$) to shape edge, ($R_f = R(\theta)$). However, one could integrate across any specified radial range within the shape parameter to define holes and gaps within the kinetic shape.

$$J_O(\theta) = \frac{\rho t}{4} \int_{\theta_i}^{\theta_f} R(\theta)^4\, d\theta \tag{4.48}$$

Equation 4.48 describes the polar mass moment of inertia of the 2D kinetic shape about its axle point as the shape rotates about its axle. If the shape rolls about the contact point, it is required to calculate the moment of inertia of the 2D KS around the contact point. Applying the parallel axis theorem defined in Equation 4.49 will shift the rotation point to ground contact to obtain Equation 4.50, the polar mass moment of inertia of the 2D kinetic shape about the ground contact point. Note, modifying Equation 4.48 into Equation 4.50 is only required if the shape *rolls over*

itself, that is, rolls over ground.

$$J_G(\theta) = J_O(\theta) + m_{KS}R(\theta)^2 \qquad (4.49)$$

$$J_G(\theta) = \frac{\rho t}{4} \int_{\theta_i}^{\theta_f} R(\theta)^4 \, d\theta + m_{KS}R(\theta)^2 \qquad (4.50)$$

Here, m_{KS} is the mass of the entire shape and $R(\theta)$ is the distance from shape axle to ground contact. The mass of a 2D shape with non-constant density and thickness is defined by Equation 4.51.

$$m = \int_A \rho(R,\theta) \, t(R,\theta) \, dA \qquad (4.51)$$

Density, $\rho(R,\theta)$, and shape thickness, $t(R,\theta)$, can again be assumed tobe constant, in which case, as before, it is moved outside the integrals.

$$m = \rho t \int_A dA \qquad (4.52)$$

As before in my derivation for the polar mass moment of inertia, the differential area, dA, in Equation 4.52 is redefined to yield Equation 4.53.

$$m = \rho t \int_{\theta_1}^{\theta_2} \int_{R_1}^{R_2} R(\theta) \, dr \, d\theta \qquad (4.53)$$

Finally, integrating over the radial coordinate results in the final definition of the total two dimensional shape mass in Equation 4.53.

$$m = \frac{\rho t}{2} \int_{\theta_1}^{\theta_2} R(\theta)^2 \, d\theta \qquad (4.54)$$

Now that I solved for the polar mass moment of inertia of the kinetic shape, I'll continue in deriving for the kinematics. Summing all moments shown in Figure 4.11(a) about the shape ground
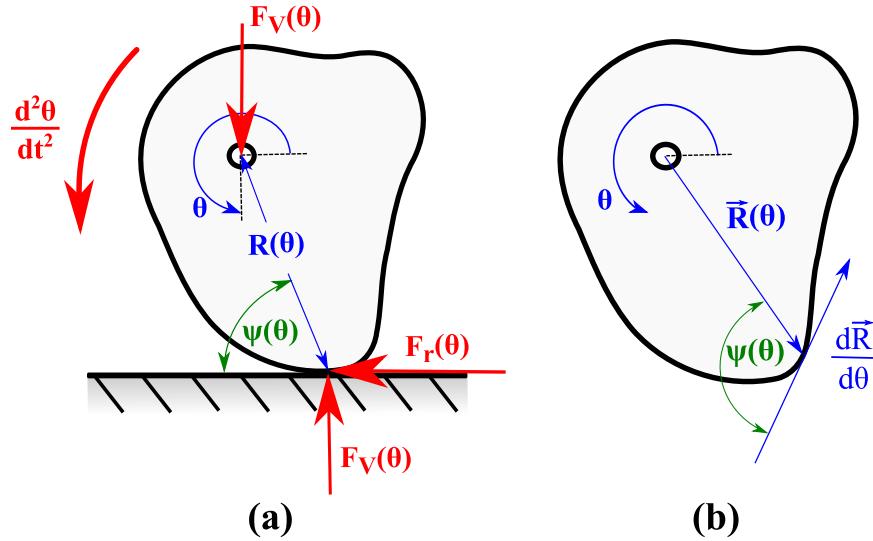
Figure 4.11: Rolling 2D kinetic shape. (a) 2D shape kinetic diagram. (c) Polar tangential angle of a 2D shape

contact using Equation 4.44 and inserting Equation 4.50, yields the following Equation 4.55.

$$F_v(\theta) \, R(\theta) \, cos[\psi(\theta)] = J_G(\theta) \, \frac{d^2\theta}{dt^2} \qquad (4.55)$$

Here, $F_v(\theta)$ is the vertical force function applied at shape axle and $R(\theta)$ is the radial distance form shape axle to ground contact point. As before, I will define the polar tangential angle, $\psi(\theta)$, of the polar curve that is the shape in Equation 4.56.

$$\psi(\theta) = \tan^{-1}\left(\frac{R(\theta)}{dR/d\theta}\right) \qquad (4.56)$$

Previous Equation 4.55 can be rearranged to define the angular acceleration of the kinetic shape as a vertical force is applied to its axle.

$$\ddot{\theta} = \frac{d^2\theta}{dt^2} = \frac{F_v(\theta)R(\theta)cos[\psi(\theta)]}{J_G(\theta)} \qquad (4.57)$$

The velocity and position of the two dimensional kinetic shape can also be solved for by integrating Equation 4.57 with respect to the time variable. Equation 4.58 represents the angular velocity of

the kinetic shape with time, while Equation 4.59 defines the kinetic shape angular position.

$$\dot{\theta} = \frac{d\theta}{dt} = \mathbf{t}\,\frac{F_v(\theta)R(\theta)\cos\left[\psi(\theta)\right]}{J_G(\theta)} + C_1 \tag{4.58}$$

$$\theta = \mathbf{t}^2\,\frac{F_v(\theta)R(\theta)\cos\left[\psi(\theta)\right]}{2\,J_G(\theta)} + \mathbf{t}\,C_1 + C_2 \tag{4.59}$$

Here, C_1 and C_2 are constants of integration and can be solved for by applying initial conditions. With two constants to solve for, only two initial conditions are needed, namely, the initial angular velocity $(\omega(0))$ and angular position $(\theta(0))$ of the kinetic shape at $t = 0$.

If I rearange Equation 4.55 once again, I am able to predict how much applied vertical force, $F_v(\theta)$, is needed to achieve a specified angular acceleration, $d^2\theta/dt^2$, of a given 2D shape, $R(\theta)$. This definition of the applied vertical force is shown in Equation 4.60.

$$F_v(\theta) = \frac{J_G(\theta)\,\frac{d^2\theta}{dt^2}}{R(\theta)\,\cos\left[\psi(\theta)\right]} \tag{4.60}$$

It is also possible to redefine the sum of moments in Equation 4.55 in terms of the radial ground reaction force, $F_r(\theta)$, instead of the applied vertical force, $F_v(\theta)$. The redefinition may be useful if one needs to find the kinetic shape kinematics if the vertically applied force is unknown and the ground reaction forces are available. This substitution of terms will define the previous equations in terms of the radial ground reaction force, utilized if the radial ground reaction force, $F_r(\theta)$, is available. Notice that the *cosine* trigonometric function in the numerator turns into a *sine*.

$$\ddot{\theta} = \frac{d^2\theta}{dt^2} = \frac{F_r(\theta)\,R(\theta)\sin\left[\psi(\theta)\right]}{J_G(\theta)} \tag{4.61}$$

$$\dot{\theta} = \frac{d\theta}{dt} = t\,\frac{F_r(\theta)\,R(\theta)\sin\left[\psi(\theta)\right]}{J_G(\theta)} + C_1 \tag{4.62}$$

$$\theta = t^2\,\frac{F_r(\theta)\,R(\theta)\sin\left[\psi(\theta)\right]}{2\,J_G(\theta)} + t\,C_1 + C_2 \tag{4.63}$$

94

Of course if both, vertically applied force and radial applied force are available, Equations 4.57 and Equations 4.61 can be added if they follow the same rotation direction and subtracted if they are applied in the opposite rotation direction, this is shown in Equation 4.64.

$$\ddot{\theta} = \frac{d^2\theta}{dt^2} = \frac{R(\theta)\left[F_v(\theta)\cos[\psi(\theta)] + F_r(\theta)\sin[\psi(\theta)]\right]}{J_G(\theta)} \tag{4.64}$$

Solving the original Equation 4.55 for the shape radius function, $R(\theta)$, would be very useful in that one could specify vertically applied force, $F_v(\theta)$, the desired radial ground reaction force, $F_r(\theta)$, and a desired angular acceleration function over time, $d^2\theta/dt^2$ that the kinetic shape will produce. However, if $d^2\theta/dt^2$ is considered to be a non-constant, Equation 4.55 yields a second order non-linear partial differential equation dependent on variables angle θ and time t. When I consider angular acceleration to be a constant ($d^2\theta/dt^2 = Constant$), I am confronted with the problem of isolating and solving for the shape radius, $R(\theta)$, embedded in the trigonometric functions. Both assumptions cannot be solved analytically, however could be solved using numerical methods.

Yet, my kinetic shape dynamics equations can be used to define the motion of a kinetic shape as it is pressed onto flat ground. These equations may be more useful in that one may approximate the radial shape form, $R(\theta)$, and predict how the shape will roll.

The available Matlab® computer program in Appendix B.1 is able to generate a 2D kinetic shape, while also predicting its exact rolling kinematics from rest position. This code is also able to account for non-conservative forces during shape kinematics.

4.2.1.1   2D Dynamic Kinetic Shape Examples

In this Section I will exhibit two examples of a two dimensional kinetic shape in motion as a force is applied to it. To confirm my dynamic kinetic shape equations, which are derived and outlined in the previous section, I have chosen two distinctly different kinetic shapes defined by different desired radial ground reaction force (RGRF) functions, $F_r(\theta)$, and with constant
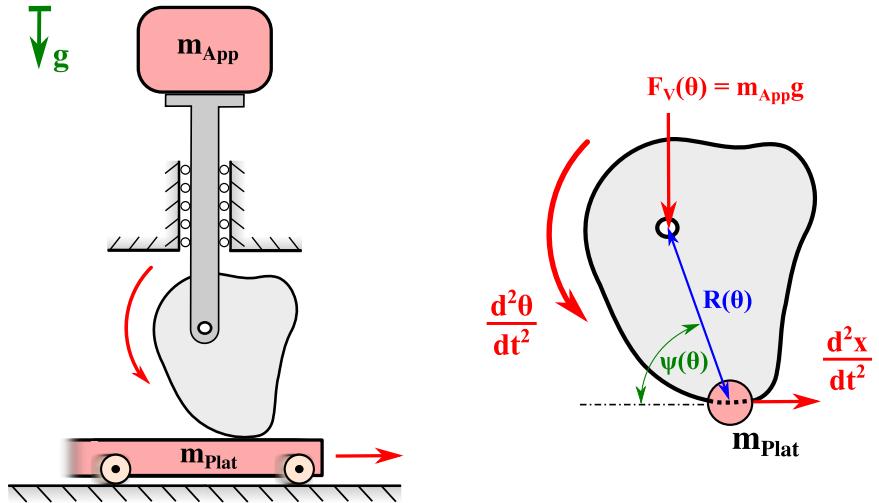
Figure 4.12: Schematic and dynamic representation of the setup used to verify kinetic shape dynamics equations

applied vertical weight, $F_v(\theta)$. The magnitude of all these force functions were chosen for the convenience of experimentation. The kinematics of the kinetic shapes were indirectly recorded with the experimental setup seen in Figure 4.12. As the kinetic shape is pressed onto a flat platform, it pushes/dispenses a flat platform linearly. *This setup both verifies the my kinetic shape dynamics equations, while introducing an extension for practical a application of the kinetic shape.*

4.2.1.1.1 Dynamic Kinetic Shape Equation Modification and Expansion
This experimental setup requires some modification to my kinetic shape dynamics equation, Equations 4.57, 4.58, and 4.59. Here the kinetic shape does not roll over itself as it would over a firm ground, but instead rolls over its rotation axle at the shape origin as the plat form is ejects from underneath the shape as seen in Figure 4.12. Hence, it is not necessary to move the rotation point to ground contact with the parallel axis theorem in Equation 4.49, nor is it necessary to compute the total mass of the shape with Equation 4.51. However, it is essential that the mass of the dispensed platform is taken into account. Instantaneously the platform moving underneath the kinetic shape can be modeled as a point mass attached at the shape at the ground contact point and moving perfectly tangent to the kinetic shape definition $R(\theta)$, as seen in Figure 4.12. The polar mass moment of inertia of a
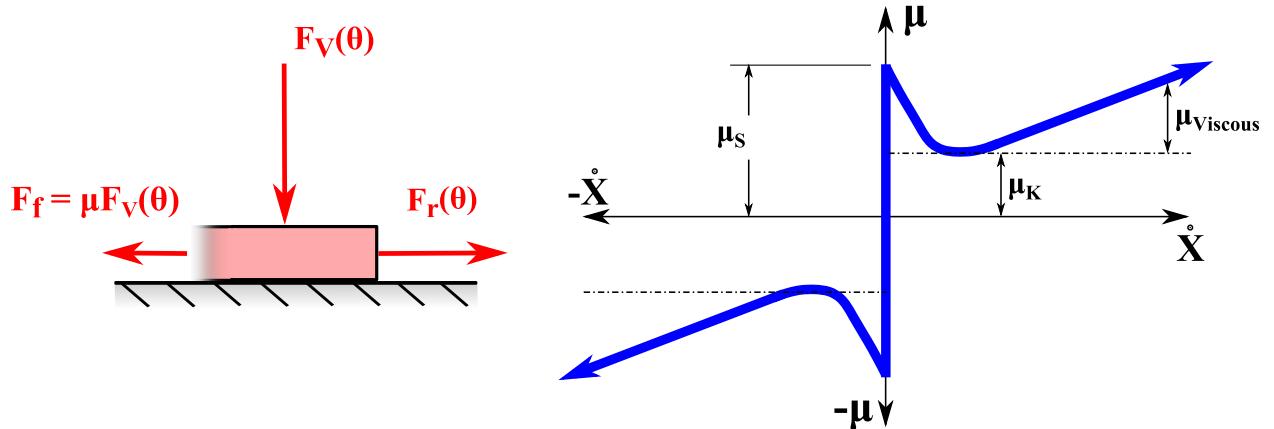
Figure 4.13: Friction model for the dispensed platform as it moves relative to ground. The friction is dependent on the applied load and velocity of the platform.

point mass at a radial distance form rotation point is given in Equation 4.65.

$$J_{Point}(\theta) = mR(\theta)^2 \tag{4.65}$$

This is true as long as the instantaneous velocity is exactly tangential to the rotation point. However, the dispensed platform is moving tangential to ground contact and not the shape origin, which requires that the perpendicular distance from the kinetic shape origin to the platform motion vector is used. This yields the correct definition of the polar mass moment of inertia for the moving platform in Equation 4.66.

$$J_{Plat}(\theta) = m_{Plat}R(\theta)^2 \, sin[\psi(\theta)] \tag{4.66}$$

Here, m_{Plat} is the mass of the entire moving platform. The total polar mass moment of inertia for a kinetic shape ejecting a flat platform is described in Equation 4.67.

$$J_O(\theta) = \frac{\rho t}{4} \int_{\theta_i}^{\theta_f} R(\theta)^4 \, d\theta \, + \, m_{Plat}R(\theta)^2 sin[\psi(\theta)] \tag{4.67}$$

In mechanical systems some non-conservative forces such as friction in rolling or sliding between components are inevitable. Friction forces in my experimental system are accounted for by defining a friction model that determines the translational friction between the dispensed platform and the ground. The friction between the platform and the ground is dependent on

the force applied to the platform by the kinetic shape and towards the ground, which in this situation is $F_v(\theta)$. It is also dependent on the velocity of the platform relative to the ground, $\dot{x}$. The friction model, which defines the coefficient of friction, μ, I will assume to be the sum of the Stribeck, Coulomb, and viscous friction forces. This friction model is defined by Equation 4.68, while also shown in Figure 4.13.

$$\mu(\dot{x}) = sign(\dot{x}) \left[\mu_K + (\mu_S - \mu_K)e^{-C_f|\dot{x}|} \right] + \mu_K \dot{x} \tag{4.68}$$

In this equation, $sign(\dot{x})$ is the sign, or signum function which holds the value of the sign (-1, 0, or 1) of the linear velocity, μ_K is the coefficient of kinematic, or Coulomb, friction, μ_S is the coefficient of static friction, and C_f is the exponential decay coefficient that describes the rate at which the friction function decays from static to kinematic friction. Notice that the viscous friction constant in my model is simply taken to be the kinematic friction multiplied by the linear velocity. Note that the friction model could also be defined with respect to and a function of position, x, that is, friction may vary at different ranges of motion. The force which the moving platform experiences due to friction is defined by Equation 4.69.

$$F_f(\theta) = \mu F_v(\theta) \tag{4.69}$$

Combining Equations 4.44, Equations 4.67, and Equations 4.69 and simplifying yields the kinematic equations which describe the linear motion of a platform moving beneath a two dimensional kinetic shape as it is pressed onto it. The linear acceleration, velocity, and position of the platform are defined by Equations 4.70, Equations 4.71, and Equations 4.72, respectively.

$$\ddot{x} = \frac{d^2x}{dt^2} = \frac{F_v(\theta)R(\theta)^2 sin[\psi(\theta)](cos[\psi(\theta)] - \mu(\dot{x})sin[\psi(\theta)])}{J_O(\theta)} \tag{4.70}$$

$$\dot{x} = \frac{dx}{dt} = t\,\frac{F_v(\theta)R(\theta)^2 sin[\psi(\theta)](cos[\psi(\theta)] - \mu(\dot{x})sin[\psi(\theta)])}{J_O(\theta)} + C_1 \tag{4.71}$$

$$x = t^2\,\frac{F_v(\theta)R(\theta)^2 sin[\psi(\theta)](cos[\psi(\theta)] - \mu(\dot{x})sin[\psi(\theta)])}{2\,J_O(\theta)} + t\,C_1 + C_2 \tag{4.72}$$

As before the integration constants are found by applying the initial conditions. Also, these linear kinematic equations can be expressed in terms of the radial ground reaction force, $F_r(\theta)$, instead of the applied weight, $F_v(\theta)$.

On my kinetic shape setup, the applied force $F_v(\theta)$ is constant for both tested shapes and is defined as $m_{App}g$, where m_{App} is the mass hung at the shape axle and g is the gravitational constant.

4.2.1.1.2 Experimental Setup The actual experimental device can be seen in Figure 4.14. I chose the kinetic shapes in this experiment to have substantial arc length yielding a longer rolling time which enables me to capture the dynamics of this setup with higher recording resolution. Because the tested shapes were relatively large in size, I paper printed the kinetic shapes using a 1:1 scale, dividing the shape outline into smaller sections that fit onto standard printer paper, which I subsequently cut out assembled with adhesive tape. This kinetic shape template was traced onto a 0.625in (1.59cm) thick pine wood material and cut out with a jigsaw. All rough edges were carefully sanded down, avoiding irregularities around the shape perimeter.

The kinetic shape was attached to a carrier via a roller bearing. The roller bearing was carried by a 0.5in (1.27cm) steel rod axle that was pressed through the carrier. While the kinetic shape was attached on one side of the carrier, a barbell with a known weight was hung onto the other side of the steel rod axle. The two steel rod rails on which the carrier traveled on were firmly pressed vertically into the base platform. To ensure low friciton between these rails and the kinetic shape carrier's acrylic plastic bearings, the rails were lubricated with lithium grease. It is important for me to note that the entire carrier itself weighs 2.0lb (0.91kg), which needs to be added to any barbell weight hung from the carrier.

This apparatus has one roller track directly beneath the kinetic shape which caries a moving platform. The platform traveling on the roller track is a 2in (5cm) x 3in (7.6cm) x 64in (162cm) long and is of pine wood material and had a weight of 5.50lb (2.50kg). The roller track consisted of rollers below the platform and also supporting the platform from the sides. Plastic rollers rolling on steel bolts were were used to minimize friction between the moving platform and the base,
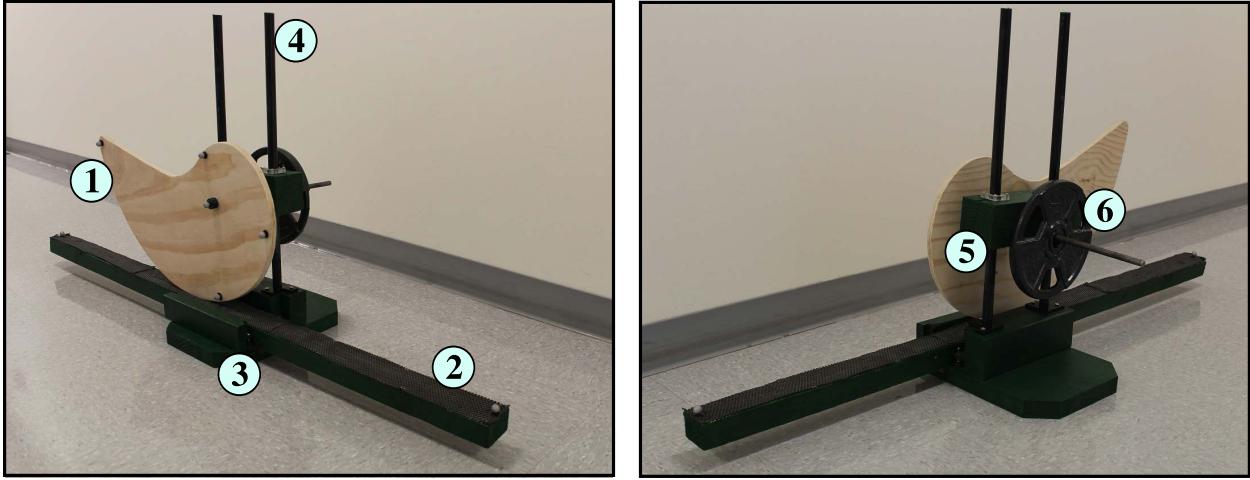
Figure 4.14: Actual setup used to measure the dynamics of the kinetic shape pushing a flat platform. (1) Wooden kinetic shape with ball bearing at axle (2) Moving/dispensed platform (3) Base with guiding rollers (4) Vertical rails (5) Kinetic shape and barbell weight carrier (6) Barbell weight

while to maximize the friction between the kinetic shape and the moving platform, thin rubber was stapled onto the surface of the dispensed platform.

Static friction, μ_S and kinematic friction, μ_K, between the moving platform and the roller track was measured by placing known weights of 10lb (4.5kg), 20lb (9.0lb), and 25lb (11.3kg) on top of the platform and above the roller bearings, while pulling one end of the platform with an analog fishscale. From three applied weights, I approximated the average static and kinematic coefficient of friction using Equation 4.69 and found them to be $\mu_S = 0.350$ and $\mu_K = 0.125$. I defined the exponential decay coefficient, C_f, for my friction model to be 9.0.

4.2.1.1.3 Motion Capture The two kinetic shapes examined were recorded using a VICON® motion tracker infrared camera system in part of the Computer Assisted Rehabilitation ENviroment (CAREN) system by Motek®. The motion tracker system is equipped with ten VICON® Bonita B10 cameras set to record at 100 Hz. The motion capture system was powered by VICON® Nexus® software. The infrared markers that I used were 14mm in diameter and were placed onto the rotating kinetic shape around its perimeter at 90° intervals and on the moving platform at the very front and very back. This recording setup can be seen in Figure 4.15. The dynamics of each

kinetic shape setup was recorded three times, particularly recording the movement of the moving platform. The infrared position data was numerically differentiated (finite difference formula) for linear velocity which in turn was filtered using a first order butterworth low pass filter with a normalized cutoff frequency of 0.05 (10 Hz). The filtered velocity was then again numerically differentiated for linear acceleration. All post processing was completed in Matlab®.

4.2.1.1.4 Computer Simulation   The dynamic motions of the proposed kinetic shape setup was simulated for direct comparison to physical measurement. The simulation evaluated the linear acceleration of the platform described in Equation 4.70, while numerically integrating for linear velocity and displacement. The simulation was evaluated at 400Hz with a 0.002 radian step size around the kinetic shape definition.

4.2.1.1.5 2D Dynamic Kinetic Shape Example 1   I will begin by defining the first kinetic shape with a sinusoidal radial ground reaction force with a constant offset, and a constant applied
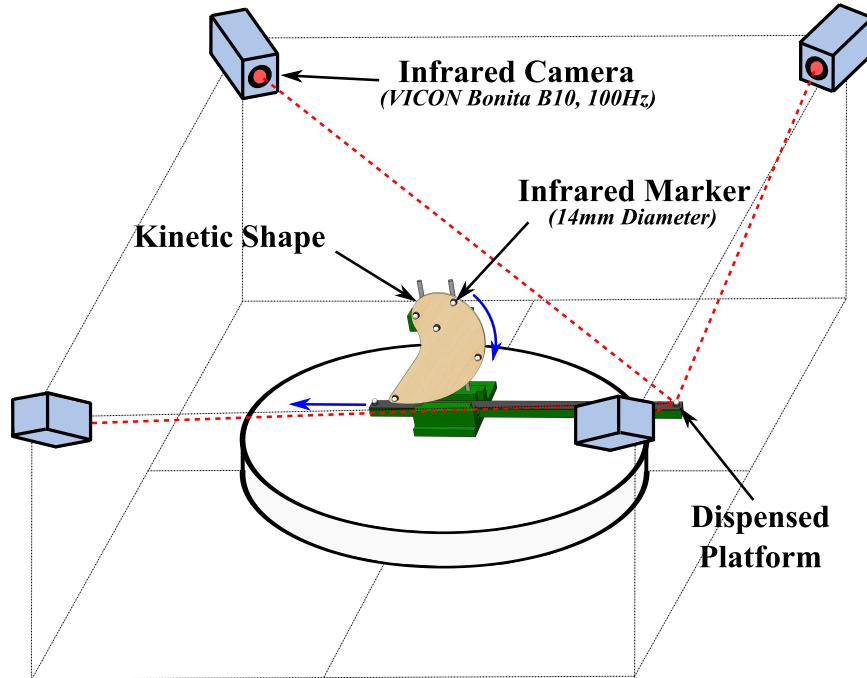
Figure 4.15: Infrared marker motion capture setup used to record the kinematics of the kinetic shape and the platform moving beneath the kinetic shape
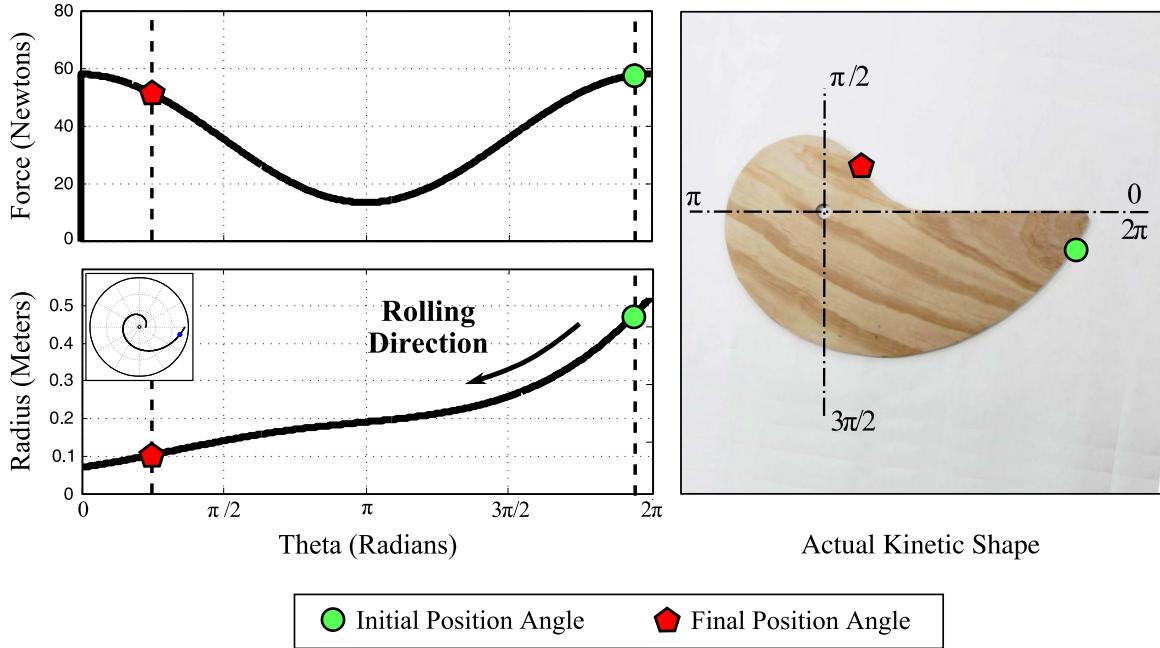
Figure 4.16: The first kinetic shape dynamic analysis

weight function. Equation 4.74 and Equation 4.74 describe these input force functions used to derive the first 2D kinetic shape and can be seen in Figure 4.16.

$$F_v(\theta) = 111 \ N \tag{4.73}$$

$$F_r(\theta) = 22.25 \cos(\theta) + 35.6 \ N \tag{4.74}$$

Using my kinetic shape Equation 4.10 in Section 4.1.1 yields the definition of the kinetic shape in Equation 4.75.

$$R(\theta) = 8.0 \ \exp\left[0.32\theta + 0.2 sin(\theta)\right]_{\theta=0}^{\theta=2\pi} \tag{4.75}$$

The kinetic shape starts with an initial shape radius of R(0) = 2.75in (7.00cm) and ends with a radius of R(2π) = 20.51in (52.1cm). The maximum dimension of this kinetic shape from $\theta = 0$ to $\theta = \pi$ was 28in (71.2cm). Using material density and thickness approximations the total weight of the kinetic shape was derived to be 3.94lb (1.79kg) while measured to be 3.7lb (1.7kg). The polar moment of inertia was derived to be 24,478in^4 (1.02 x 10^{6}cm^4). This first kinetic shape

can be seen in Figure 4.16. It shows the force exerted by the kinetic shape onto the platform, linear acceleration of the dispensed platform, and radius definition around the kinetic shape.

Now that I have the defined the shape, any vertical force can be applied onto the kinetic shape. This vertical force does not necessary have to be the same vertical force specified in the kinetic shape definition. The vertical force specified in Equation 4.75 is only used to define a shape that will yield a desired radial ground reaction force when that vertically applied force in is used. For this kinetic shape I chose to apply a vertical force of 14.5lb (6.58kg /64.5 N), which includes the kinetic shape carrier on the experimental apparatus and is directly inserted into the platform linear acceleration, Equation 4.70. That is, I hung a 12.5lb (5.67kg) at the kinetic shape axle to press it onto the moving platform underneath the kinetic shape.

The results of the recorded kinematics and the computer simulated kinematics for the dispensed platform are shown in Figure 4.17. The kinetic shape was placed onto the platform at an orientation of 6.1 radians (345°) and as the weight was applied, it rolled to a position of $\pi/4$ radians (45°). It stopped rolling as the beginning end of the shape at 2π radians hit the ground plane. All three, displacement, velocity, and acceleration of the simulation model predicted results were in close proximity to the recorded values. While not always aligned, the simulated data always followed the same trend the recorded data did. The recorded kinetic shape rolled for approximately 1.4 seconds, as it did in my simulation.

Notice that the linear acceleration of the pushed platform in the simulated model jumps to around 7m/s^2 while the recorded data raises to 5m/s^2 gradually. This difference can be explained by the friction model that was used. The friction model that was used (Figure 4.13) assumes a high stiction value after which it diminishes kinematic friction. Considering that the experimental apparatus was not ideal with room of much improvement for a smoother and more aligned setup, my kinetic shape simulation model was able to forecast recorded values.

4.2.1.1.6   2D Dynamic Kinetic Shape Example 2   In this next example, I will again define a two dimensional kinetic shape with a sinusoidal radial ground reaction force function and a con-

103

Kinetic Shape 1 : Platform Linear Kinematics
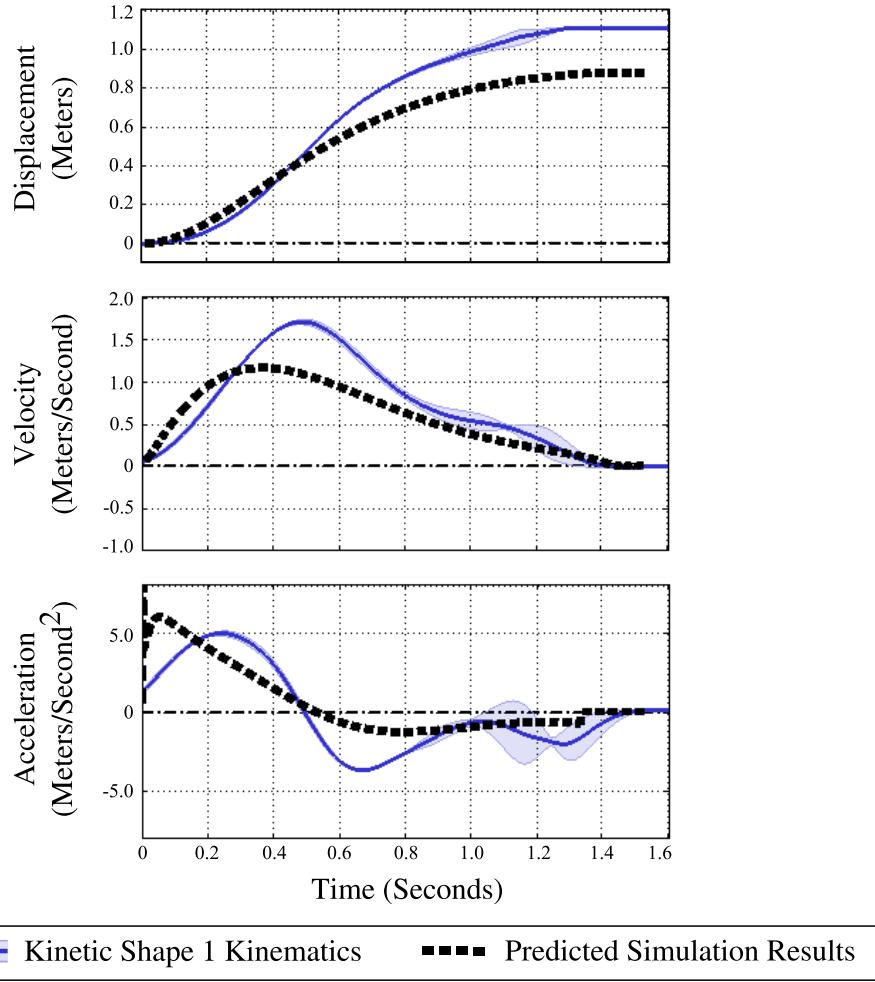
Figure 4.17: The second kinetic shape dynamic analysis

stant vertically applied force. However, in this example the radial ground reaction force function does not have a constant offset. The following Equations 4.74 and 4.74 describe the radial ground reaction force and the vertically applied force around the kinetic shape.

$$F_v(\theta) = 111 \ N \tag{4.76}$$

$$F_r(\theta) = 77.9 \sin(\theta) \ N \tag{4.77}$$
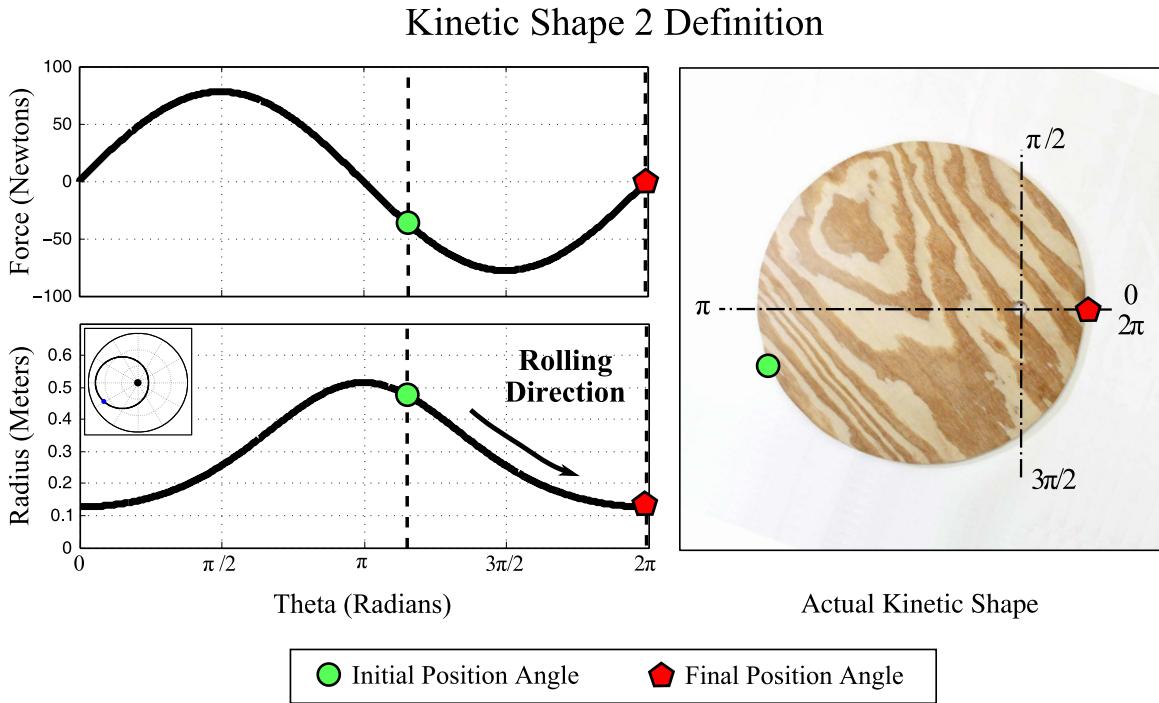
Figure 4.18: The second kinetic shape selected for dynamic analysis

Once again using Equation 4.10 in Section 4.1.1 yields the radius definition of this kinetic shape in Equation 4.75.

$$R(\theta) = 8.0 \, \exp\left[-0.71 cos(\theta)\right]_{\theta=0}^{\theta=2\pi} \tag{4.78}$$

This second kinetic shape starts with an initial shape radius of R(0) = 5.00in (12.7cm) and since the shape is defined by a only sinusoidal function, it ends also with the same radius of R(2π) = 5.00in (12.7cm). The maximum dimension of this kinetic shape from $\theta = 0$ to $\theta = \pi$ was 25.3in (64.2cm). The shape was calculated to have a total mass of 7.10lb (3.21kg) and measured to be 6.83lb (3.10kg). The polar mass moment of inertia was found to be 67,117in^4 (2.79 x 10^{6}cm^4). For the kinematic simulation and measured physical apparatus I have chosen an applied vertical weight of 27lb (12.3kg / 120N), that is a 25lb (11.3kg / 111N) barbell with the 2lb (0.91 kg / 9N) kinetic shape carrier.

The measurements of the linear kinematics of the dispensed platform as the weight was applied can be seen in Figure 4.19. The recorded dynamics lasted for about 1.4 seconds, before the system came to a halt. The position of the actual measurements and modeled predictions oscillated

Kinetic Shape 2 : Platform Linear Kinematics
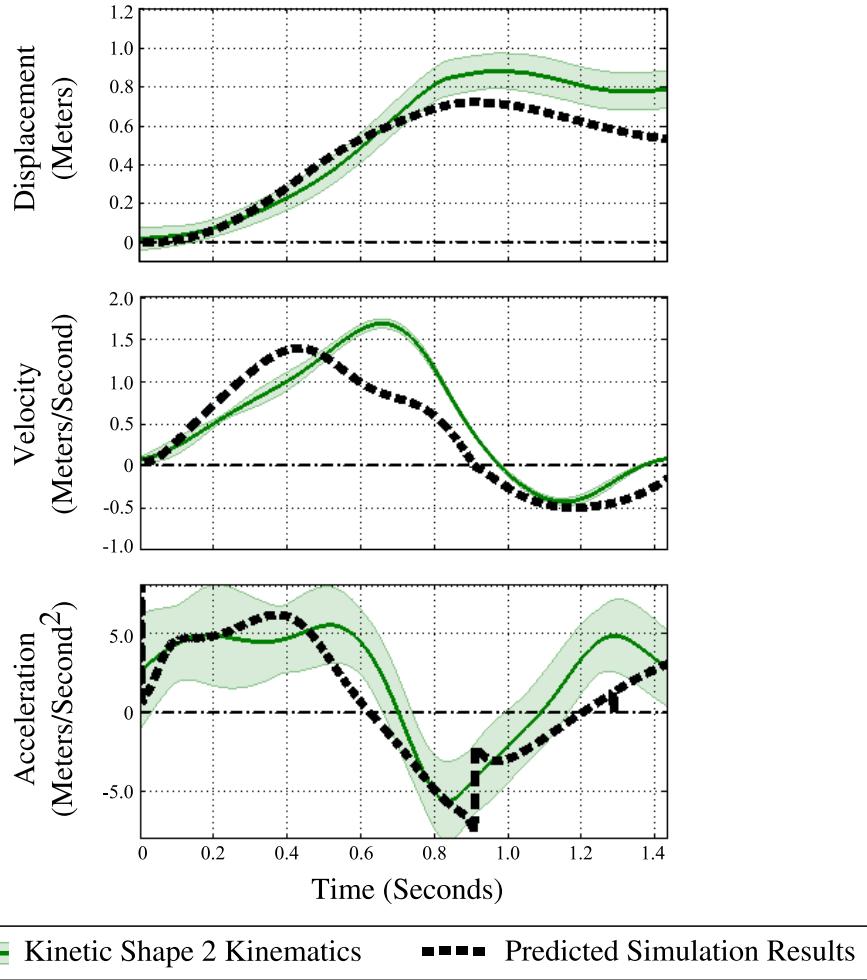
Figure 4.19: The second kinetic shape selected for dynamic analysis

around one position, which was when the kinetic shape rolled around 0 radians (or 2π radians) on the shape. As in the first example, the predicted values are in close proximity to the recorded values. The platform was found to move back and forth around 0.7m as a result of kinetic shape definition in Figure 4.18, where the measured radial ground reaction force for the shape switches around this position.

Notice that as the velocity crosses zero and the platform instantaneously comes to a halt at 0.9 seconds, the predicted model experiences a drastic increase in linear acceleration. This jump is due to the friction increasing exponentially until it reaches the static friction value (Figure 4.13). Although more continuous, this was precisely what happens to the recorded data. This suggests

that the friction model I have chosen for this application was too elementary in nature and that the actual friction affecting this apparatus is much more complicated. Complication in friction can be the result of imperfect alignment throughout the motion or a non-linear and complex cumulative friction characteristics throughout the entire system that may be difficult to model.

Nevertheless, this experiment proved that my dynamic model is valid to be used as a prediction of kinetic shape rolling over ground, or rolling while pushing a platform out, for kinetic shapes or arbitrary shapes for which the radial function, $R(\theta)$, is known or approximated.

4.2.2 Three-Dimensional Kinetic Shape

As in the previous static kinetic shape case, in this section I am expanding my analysis and derivation of kinetic shape kinematics into the third dimension. For the case of the dynamic 3D kinetic shape, the shape perimeter curve is pressed onto a flat surface by a vertically applied force that is orthogonal to the level ground plane. While the sum of moments does not diminish to zero (unrestrained) about the vertical axis, the three dimensional shape curve creates rolling dynamics in the in the tangential direction (across the azimuth angle) and over the ground plane around the vector of vertical force application. In this case, there is no rolling away from the origin (elevation direction), the radial rolling of the three dimensional shape curve will results in redefinition of the entire system, hence I am only defining the rolling dynamics around the kinetic shape and not away from the center. An example of this rolling about vertical force vector is described in Section 4.1.2 and the supplementary Figure 4.6. It is also shown in Figure 4.20, as a helix is pressed onto a plane resulting in a tangential rotation.

It is essential to note that the rolling of the 3D kinetic shape occurs across and on the path/curve that is described by the shape equations. In that sense one may call this a kinetic curve, however for its functionality and for consistency I am still naming it a kinetic shape.

Again, it is assumed that the friction force between the ground and the shape is large enough for the shape not to slip. It is also assumed that there is no deformation of the shape or ground while rolling. Additionally, this analysis is only valid when the applied force at the shape axle is

107
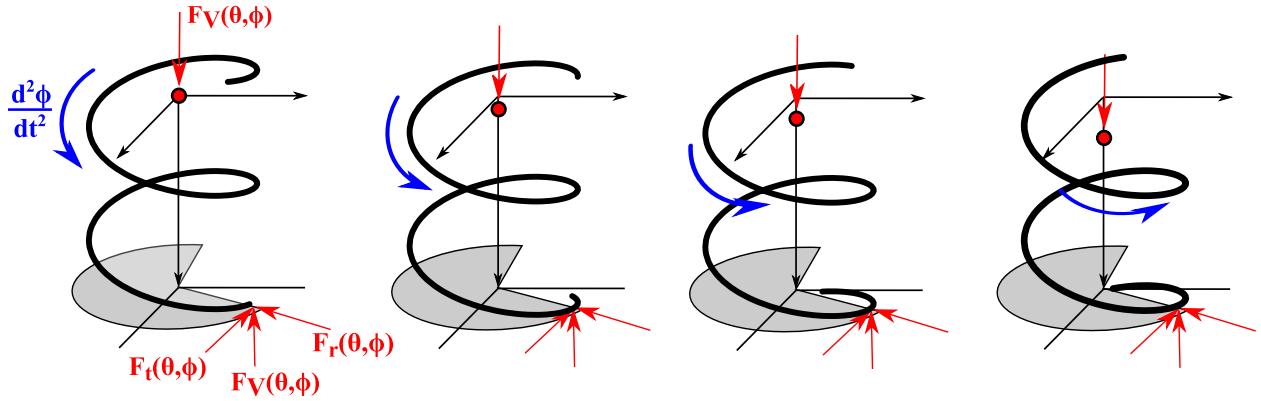
Figure 4.20: As a curve is pressed onto the ground plane it will roll about the vector of vertical force application

much greater than the combined gravitational forces applied at the center of mass of the shape or if a center of mass coincides with the 3D shape axle/rotation point. In the forthcoming derivation $R(\theta, \phi)$ is the 3D kinetic shape radius defined in spherical coordinates and as a function of elevation angle, θ, and azimuth angle, ϕ. I will begin to formulate the rolling dynamics of a kinetic shape overground and about the vertical vector that is orthogonal to the ground and runs through the shape orign.

For this formulation I will proceed in a similar manor as described in the previous Section 4.2.1. Isaac Newton's 2nd law [143] of classical physics for rotational rigid body dynamics for the 3D shape object over ground and along angle, ϕ (Equation 4.79).

$$\sum M_G = J(R, \theta, \phi) \frac{d^2 \phi}{dt^2} \tag{4.79}$$

Here, the polar mass moment of inertia of the kinetic shape around ground contact point in the azimuth angle direction, ϕ, is $J(R, \theta, \phi)$. $\frac{d^2 \phi}{dt^2}$ is the angular accelerations around the force vector orthogonal to the level ground plane and through the shape origin.

As the kinetic shape rolls over ground, naturally the polar mass moment of inertia changes with shape orientation. The formulation of this instantaneous polar mass moment of inertia which accounts for this reorientation of the object is described in Equation 4.80. This equation describes
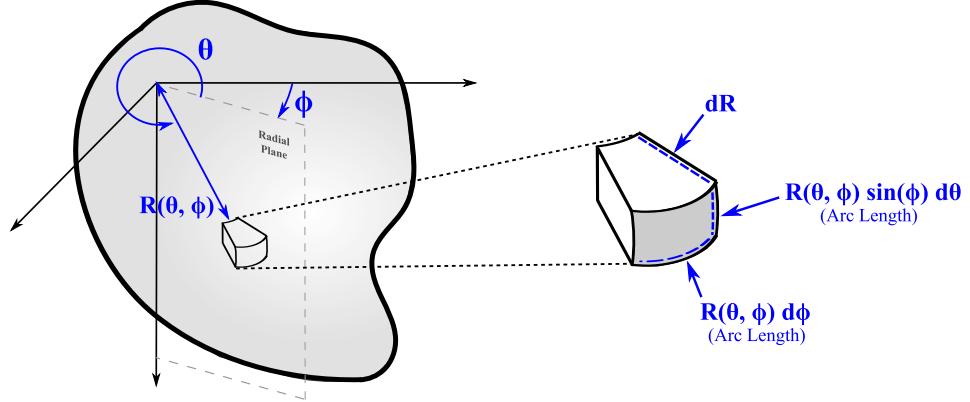
Figure 4.21: Differential (Infinitesimal) 3D kinetic shape volume element

the polar mass moment of inertia of a heterogeneous and non-uniform kinetic shape volume.

$$J_O(R,\theta,\phi) = \int_V R(\theta,\phi)^2 \, \rho(R,\theta,\phi) \, dV \qquad (4.80)$$

In this equation, $\rho(R,\theta,\phi)$ is the continuous density across the kinetic shape rolling curve. The differential shape object volume, dV, can be defined by the infinitesimal/differential change in volume spacial parameters shown in Figure 4.21. This redefinition of the shape volume according to Figure 4.21 produces Equation 4.81.

$$J_O(R,\theta,\phi) = \int_{\theta_i}^{\theta_f} \int_{\phi_i}^{\phi_f} \int_{R_i}^{R_f} R(\theta,\phi)^2 \, \rho(R,\theta,\phi) \, R(\theta,\phi)^2 sin(\phi) dR \, d\phi \, d\theta \qquad (4.81)$$

Here, θ_i and θ_f are the initial and final elevation angles, ϕ_i and ϕ_f are the initial and final azimuth angles, and R_i and R_f are the initial and final radii of kinetic shape radius function $R(\theta,\phi)$. It is possible to define the polar moment of inertia with a variable heterogeneous shape density, however for simplicity and clarity, the 3D kinetic shape will be considered to be of uniform density. This consideration produces Equation 4.82.

$$J_O(\theta,\phi) = \rho \int_{\theta_i}^{\theta_f} \int_{\phi_i}^{\phi_f} \int_{R_i}^{R_f} R(\theta,\phi)^4 \, sin(\phi) \, dR \, d\phi \, d\theta \qquad (4.82)$$
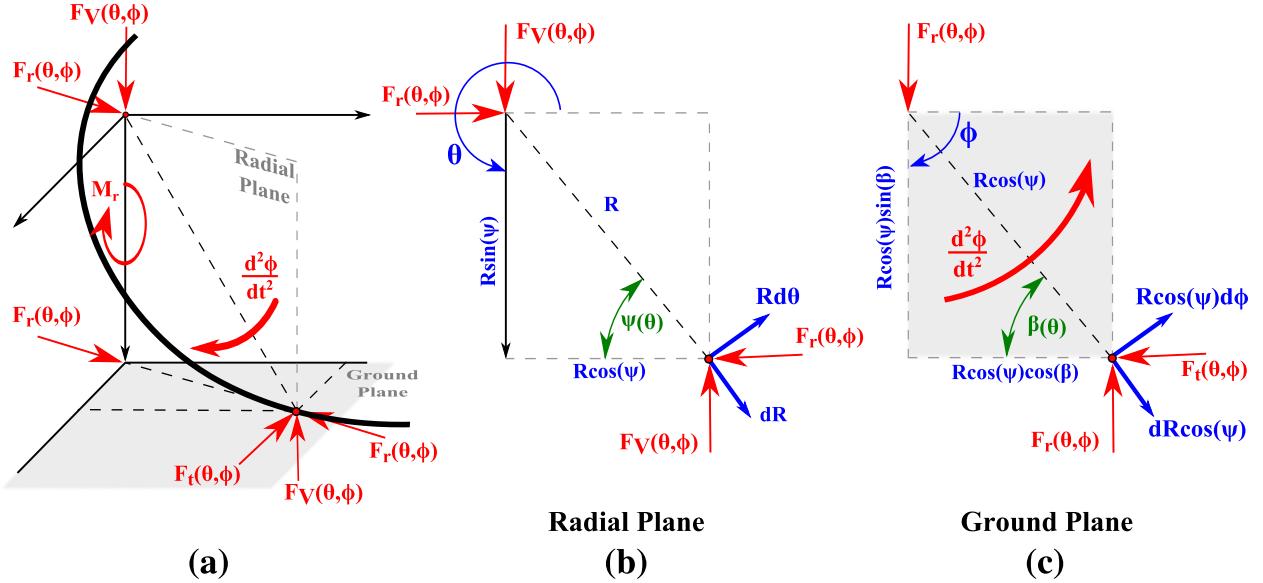
Figure 4.22: 3D kinetic shape dynamic diagram. (a) 3D kinetic shape rolling around its center. (b) 3D kinetic shape and geometric parameters in the radial plane. (c) 3D kinetic shape and geometric parameters in the ground plane

Integrating across the radial variable, Equation 4.83 is obtained.

$$J_O(\theta, \phi) = \frac{\rho}{5} \int_{\theta_i}^{\theta_f} \int_{\phi_i}^{\phi_f} R(\theta, \phi)^5 \, d\phi \, d\theta \tag{4.83}$$

Notice that I am assuming no gaps in the radial direction, hence integrating from origin ($R_i = 0$) to shape edge, ($R_f = R(\theta, \phi)$). However, one could easily integrate across any specified radial range or multiple ranges within shape parameter to define holes and gaps in the kinetic shape. Equation 4.83 describes the polar mass moment of inertia of the 2D kinetic shape about its axle.

Following up with Equation 4.79 and summing all moments about the vertically applied force vector, which results in Equation 4.84. These parameters can be seen in Figure 4.22(a and c).

$$F_r(\theta, \phi) \, R(\theta, \phi) \, \cos[\psi(\theta, \phi)] \, \cos[\beta(\theta, \phi)] = J_O(\theta, \phi) \frac{d^2\phi}{dt^2} \tag{4.84}$$

Here the $\beta(\theta, \phi)$ is the polar tangential angle in the ground plane, which is defined by Equation 4.85, while $\psi(\theta, \phi)$ is the polar tangential angle in the radial plane and is defined by Equation 4.86.

$$\beta(\theta, \phi) = \tan^{-1}\left(\frac{R(\theta, \phi)}{dR/d\phi}\right) \tag{4.85}$$

110

$$\psi(\theta,\phi) = \tan^{-1}\left(\frac{R(\theta,\phi)}{dR/d\theta}\right) \tag{4.86}$$

Rearranging the Equation 4.84 for angular acceleration gives Equation 4.87. This equation may be integrated to obtain angular velocity and position for the kinetic shape rolling about axis r-r as Equation 4.88 and 4.89, respectively.

$$\ddot{\phi} = \frac{d^2\phi}{dt^2} = \frac{F_r(\theta,\phi)\, R(\theta,\phi)\, \cos[\psi(\theta,\phi)]\, \cos[\beta(\theta,\phi)]}{J_O(\theta,\phi)} \tag{4.87}$$

$$\dot{\phi} = \frac{d\phi}{dt} = t\, \frac{F_r(\theta,\phi)\, R(\theta,\phi)\, \cos[\psi(\theta,\phi)]\, \cos[\beta(\theta,\phi)]}{J_O(\theta,\phi)} + C_1 \tag{4.88}$$

$$\phi = t^2\, \frac{F_r(\theta,\phi)\, R(\theta,\phi)\, \cos[\psi(\theta,\phi)]\, \cos[\beta(\theta,\phi)]}{2\, J_O(\theta,\phi)} + t\, C_1 + C_2 \tag{4.89}$$

The integration constants, C_1 and C_2, can be solved for by inserting the shape's initial rotational velocity and position at $t = 0$. As with the two dimensional dynamic kinetic shape, these three kinematic definitions can be rearranged to define the applied forces needed to achieve a certain kinematic of a given or approximated kinetic shape.

Notice that for tangential rolling, it is essential to have a restrictive radial ground reaction force, $F_r(\theta,\phi)$, pushing from the the origin outward. When this radial force vanishes, so does any kinematics around the vertical axis.

Similar to the 2D kinetic shape dynamic equations, Equations 4.87, 4.88, and 4.89 can be derived in terms of the tangential ground reaction force, $F_t(\theta,\phi)$, instead of the orthogonally applied force at the shape axle, $F_v(\theta,\phi)$. Further, if the shape definition, $R(\theta,\phi)$, is given or approximated, these equations may also inversely describe what forces are needed to obtain a desired rotation kinematics.

4.3   Kinetic Shape Systems

A force applied to one two dimensional kinetic shape, results in a ground reaction force parallel to the ground and radially away from its center. As discussed before, the applied force

Pushing Interaction **Pulling Interaction**
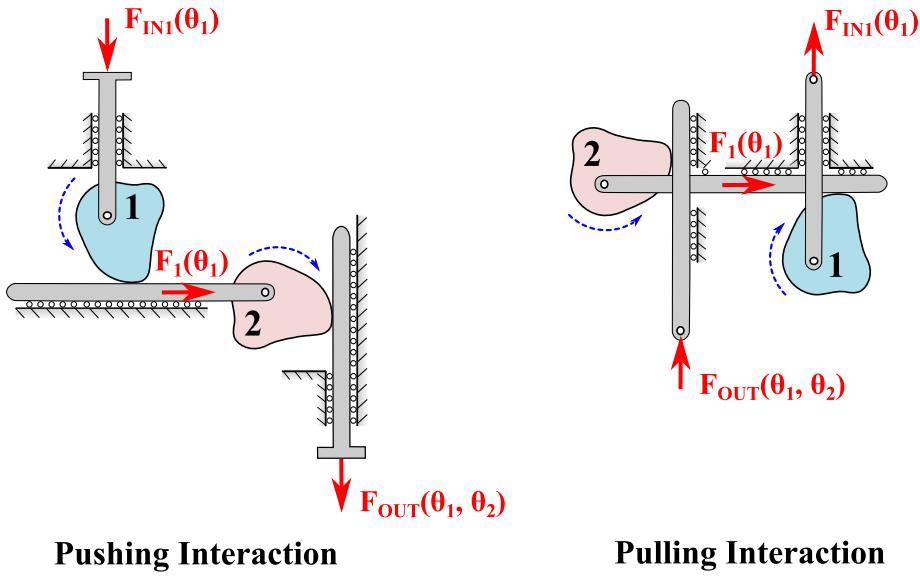
Figure 4.23: Multiple kinetic shapes in series are able to redirect and modify a force (or motion) input and output a finer resolution and degree of force (or motion) output

to the kinetic shape and the force with which the kinetic shape reacts can be specified to derive a shape function that will produce these forces (Equation 4.10). However, what will happen if two or many kinetic shapes interact in series or in other arrangements. That is, one kinetic shape pushes on a platform which holds a second kinetic shape that in turn pushes on a second platform. Given a force input into such a system, what type of output may one expect? In this section, I will present and discuss my novel development and analysis of the interaction between kinetic shapes and how different arrangements of interacting kinetic shapes can cause customized forces to be outputted from a kinetic shape system. *Hereafter, I am naming formations or arrangements of kinetic shapes kinetically interacting and affecting one other as kinetic shape systems.*

A kinetic shape system involving two kinetic shapes is shown in Figure 4.23. Here, two kinetic shapes within the kinetic shape system interact by pushing or pulling. As a force is inputted into the kinetic shape system and applied to the first shape, this first kinetic shape reacts by applying its reaction force onto the second shape. The second kinetic shape in turn reacts by creating the system output force. Because a kinetic shape reaction forces depends on the shape's orientation, the output force is dependent on the orientation of both kinetic shapes in the system. Hence, the first kinetic shape may react with a specified reaction force profile, $F_1(\theta_1)$ ($F_r(\theta)$ in my original

112

2D kinetic shape equation), and the second kinetic shape may react with a different reaction force profile, $F_2(\theta_2)$, while the interaction of both will produce a certain output force profile that is dependent on both kinetic shapes' reaction force profiles and their orientation, that is, $F_{OUT}(\theta_1, \theta_2)$. I will call a kinetic system of a second degree the interaction of two kinetic shapes in a kinetic shape system. A *kinetic shape system degree* is the number of kinetic shapes included in the system. For example, a kinetic shape system of a fifth degree is created by five kinetic shapes interacting.

It is important for me to mention that kinetic shape systems are not exclusive to the two dimensional kinetic shape, it is also possible to apply these systems outlined in this section with the three dimensional kinetic shape. In the case of the three dimensional kinetic shape, an additional tangential force is present in conjunction with the radial ground reaction force. However, for clarity I am only going to outline the nature of my kinetic shape system concept for the two dimensional kinetic shape.

4.3.1 Dependent and Independent Kinetic Shapes

As stated, a kinetic shapes can share and distribute forces with other kinetic shapes in a kinetic shape system. In a second degree kinetic shape system producing two force divisions where the first kinetic shape (1) produces a reaction force profile, $F_1(\theta_1)$, which it then applies to the second kinetic shape (2). The second shape (2) in turn uses that force and reacts with a modified/divided force profile, $F_2(\theta_2)$. It is possible to define the form of the second shape (2) such that it is defined by the output of the first shape (1). In essence, it is possible to define the second shape (2) with my kinetic shape equation in Section 4.1 (Equation 4.10), such that the vertically applied force term, $F_v(\theta)$, is defined as the first kinetic shape's (1) radial ground reaction force, $F_r(\theta)$. This situation may be described using Equation 4.90 for the first kinetic shape and Equation 4.91 for the second kinetic shape. This type of inter-definition of kinetic shapes I will refer to *dependent sets*, while two kinetic shapes defined by unrelated force functions I will refer

to as *independent sets*. Equations 4.90 and 4.91 define two kinetic shapes that are dependent.

$$R(\theta_1) = R(\theta_{1i}) \; exp \left[\int \frac{F_1(\theta_1)}{F_{IN1}(\theta_1)} d\theta_1 \right] \tag{4.90}$$

$$R(\theta_1, \theta_2) = R(\theta_{2i}) \; exp \left[\int \int \frac{F_2(\theta_2)}{F_1(\theta_1)} d\theta_2 \, d\theta_1 \right] \tag{4.91}$$

In these equations, subscript 1 refers to the first kinetic shape in the kinetic line, while subscript 2 represents the second kinetic shape in line. Hereafter, I will refer to a kinetic shape that is exerting a force onto another kinetic shape as a *donor kinetic shape*, while a kinetic shape that is accepting forces, I will refer to a *receiver kinetic shape*. Note that these previous equations describe a set of two dependent kinetic shapes. Larger sets of dependent shapes are possible, however may yield to more complicated kinetic shape definitions. Subscript *IN* refers to the force function that is received by a kinetic shape. Notice that in Equation 4.91 the denominator of the force function of the receiver shape is the numerator of the donor shape. Further, it is important to note that the ratio between the applied (denominator) and reaction force (numerator) is proportional to the radius change of the resulting shape. Hence, if the applied force to the receiver shape from the donor shape is close to zero or zero, the resulting shape will become extremely large or infinity. Careful consideration is to be taken when specifying the definition forces in a dependent set.

Independent sets of kinetic shapes within the kinetic shape system are defined by Equations 4.92 and 4.93.

$$R(\theta_1) = R(\theta_{1i}) \; exp \left[\int \frac{F_1(\theta_1)}{F_{IN1}(\theta_1)} d\theta_1 \right] \tag{4.92}$$

$$R(\theta_2) = R(\theta_{2i}) \; exp \left[\int \frac{F_2(\theta_2)}{F_{IN2}(\theta_2)} d\theta_2 \right] \tag{4.93}$$

Here the two shape definitions are not related to one other. If the donor kinetic shape, 1, applies a force onto the receiver kinetic shape, 2, the receiver shape will react by its own definition, however scaling its output force proportional to the donor output. In this setup, it is irrelevant to the second shape form if the donor shape's reaction force is defined as zero.

These are the basic shape definitions of two kinetic shapes interacting within a kinetic shape system, where one kinetic shape reaction force is affecting the subsequent kinetic shape's definition forces. In summary, there are three methods to define the kinetic shapes in a kinetic shape system:

1. *Interaction Dependent Shape Definition:* This first method is to define all kinetic shape radial functions that will provide the specified force functions throughout the kinetic shape system. That is, to provide all expected forces which in turn derive the kinetic shape as they are interacting with Equations 4.90 and 4.91.

2. *Interaction Independent Shape Definition:* This second method is the reverse of the first method. In this case the kinetic shape radii are individually and independently defined or approximated radius beforehand and then inserted into the kinetic shape system. The reverse definition of shape radius when a kinetic shape radius function is known is described by Equations 4.92 and 4.93.

3. *Mixture of Method One and Two:* The third way is a mixture of the first and second method. Some kinetic shapes may be independently pre-defined or approximated while others are defined by specified interacting forces in the kinetic shape system.

4.3.2 Kinetic Shape System Operations

My discovery of kinetic shapes and kinetic shape systems becomes more interesting as kinetic shape systems may become more complex in the number of kinetic shapes and the arrangements of these shapes. With different kinetic shape arrangements in a system I am able to manipulate the final output force from the system with a higher degree as opposed to only using one kinetic shape. I have been able to find a number of kinetic arithmetical and conditional operations that are achieved with a certain kinetic shape system. These discoveries have led me to develop a kinetic shape system notation, with which a kinetic shape system may be defined more easily. *My kinetic shape system notation with description can be viewed in the Appendix C.*

115

4.3.2.1 Normal Division and Multiplication

Normal division of forces is achieved by using one kinetic shape. That is, a kinetic shape system of the first degree. This may not be a kinetic shape system by definition, however the application of one kinetic shape is essentially used to divide a force by a value greater than one. The force transfer equation for simple kinetic shape division is Equation 4.94

$$F_{OUT}(\theta_1) = F_{IN1}(\theta_1)\frac{F_1(\theta_1)}{F_{IN1}(\theta_1)} \tag{4.94}$$

In this equation, $F_{IN1}(\theta_1)$ is the input into the kinetic shape system that is dependent on the orientation, θ_1, of this first kinetic shape, while $F_{OUT}(\theta_1)$ is the output of kinetic shape system.

Normal multiplication is the reverse operation. That is, the "ground" or the platform on which the kinetic shape rolls over applies a force at the ground contact point. This reverse force causes at kinetic shape axle to push away and perpendicular to the ground. The Normal multiplication of a first degree kinetic shape system is defined by Equation 4.95

$$F_{OUT}(\theta_1) = F_{IN1}(\theta_1)\frac{F_{IN1}(\theta_1)}{F_1(\theta_1)} \tag{4.95}$$
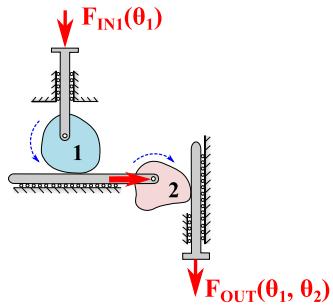
4.3.2.2 Multiple Division and Multiplication

This kinetic shape system arrangement consist of two or more kinetic shapes in series (Figure 4.24). As an input force, $F_{IN1}(\theta_1)$, is applied to the first kinetic shape it applies its reaction force to the second kinetic shape, and so on. In this case, at each step the force is divided by a number greater than one. Equation 4.96 predicts the kinetic shape interaction for force division.
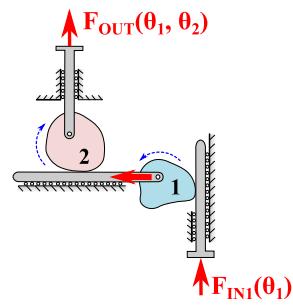
$$F_{OUT}(\theta_1, \theta_2, ...\theta_n) = F_{IN1}(\theta_1)\frac{F_1(\theta_1)}{F_{IN1}(\theta_1)}\frac{F_2(\theta_2)}{F_1(\theta_1)} \cdots \frac{F_n(\theta_n)}{F_{n-1}(\theta_{n-1})} \tag{4.96}$$

Here, 1, 2, ...*n* are the kinetic shapes in counting order where n is also the kinetic shape system degree, and θ_n is the orientation of the *n*th kinetic shape.

Multiple Division

$F_{IN1}(\theta_1)$

1
2

$F_{OUT}(\theta_1, \theta_2)$
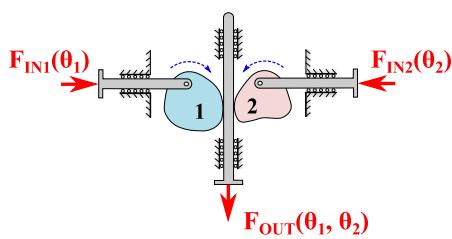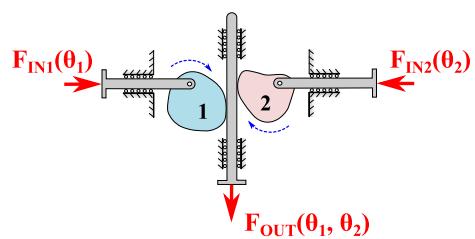
Multiple Multiplication

$F_{OUT}(\theta_1, \theta_2)$

2
1

$F_{IN1}(\theta_1)$

Addition

$F_{IN1}(\theta_1)$ $F_{IN2}(\theta_2)$

1   **2**

$F_{OUT}(\theta_1, \theta_2)$

Subtraction

$F_{IN1}(\theta_1)$ $F_{IN2}(\theta_2)$

1   **2**

$F_{OUT}(\theta_1, \theta_2)$
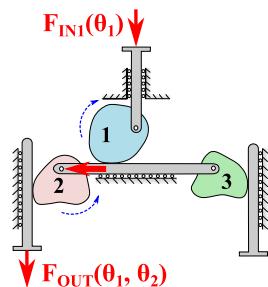
Conditional Statement

If $F_1(\theta_1) > 0$ *THEN B*

$F_{IN1}(\theta_1)$

1
2   **3**

$F_{OUT}(\theta_1, \theta_2)$

If $F_1(\theta_1) < 0$ *THEN C*

$F_{IN1}(\theta_A)$

1
2   **3**

$F_{OUT}(\theta_1, \theta_3)$
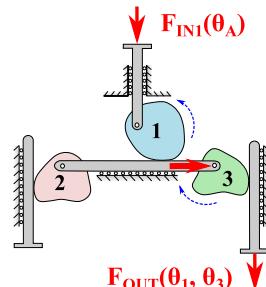
Figure 4.24: Kinetic shape system operations. My discovered force mathematics and kinetic conditional statements can be achieved by manipulating the interactions between kinetic shapes.

In contrast, the platform on which the kinetic shape is pressed on is pulled or pushed underneath the kinetic shape. The kinetic shape will react and push perpendicular to the moved platform through the shape axle. This is the opposite mechanism to division, in this case this multiplies the force applied to the platform below the kinetic shape. Equation 4.97 describes the kinetic interaction for force multiplication of two or more kinetic shapes.

$$F_{OUT}(\theta_1, \theta_2, ... \theta_n) = F_{IN1}(\theta_1) \frac{F_{IN1}(\theta_1)}{F_1(\theta_1)} \frac{F_1(\theta_1)}{F_2(\theta_2)} \cdots \frac{F_{n-1}(\theta_{n-1})}{F_n(\theta_n)} \quad (4.97)$$

Note that for a practical multiplication process, a sufficiently large friction force is needed for this force transfer. In the following section, I will discuss more detail and offer suggestions on how to enhance this friction between the kinetic shape and ground.

4.3.2.3 Addition and Subtraction

Defined forces can be added by aligning the shape ground reaction forces of multiple shapes to push onto a shared platform. Redefinition or reorientation of the kinetic shapes can equal the subtraction of radial ground reaction forces. While the schematics for addition and subtraction in Figure 4.24 show a second kinetic systems (two kinetic shapes), addition and subtraction of forces can be achieved with only one kinetic shape. For example, one kinetic shapes may push on one side of the platform, while a force is applied to the opposite side of the platform. Addition of forces is described by Equation 4.98, while subtraction is defined by Equation 4.99.

$$F_{OUT}(\theta_1, \theta_2, ...\theta_n) = F_{IN1}(\theta_1)\frac{F_1(\theta_1)}{F_{IN1}(\theta_1)} + F_{IN2}(\theta_2)\frac{F_2(\theta_2)}{F_{IN2}(\theta_2)} + \cdots + F_{INn}(\theta_n)\frac{F_n(\theta_n)}{F_{INn}(\theta_n)} \quad (4.98)$$

$$F_{OUT}(\theta_1, \theta_2, ...\theta_n) = F_{IN1}(\theta_1)\frac{F_1(\theta_1)}{F_{IN1}(\theta_1)} - F_{IN2}(\theta_2)\frac{F_2(\theta_2)}{F_{IN2}(\theta_2)} - \cdots - F_{INn}(\theta_n)\frac{F_n(\theta_n)}{F_{INn}(\theta_n)} \quad (4.99)$$

Note that when subtracting, a negative force means that the resultant force will act in the negative direction of a specified force direction convention.

4.3.2.4 Conditional Statements

Kinetic shape systems can be used to make decisions that depend on mechanical force data. For example, as a mechanical device component applies a force onto a kinetic shape system, it may be desirable to output two different types of force profiles depending on the orientation of the mechanical device component which applied the initial force. In essence, a kinetic shape system can be arranged as a kinetic conditional statement to decide between two options depending on the reaction force profile of the conditional kinetic shape. Equation 4.100 shows this conditional

statement of Figure 4.24.

$$IF \;\; F_1(\theta_1) > 0 \;\; THEN$$

$$F_{OUT}(\theta_1, \theta_2) = F_{IN1}(\theta_1) \frac{F_1(\theta_1)}{F_{IN1}(\theta_1)} \frac{F_2(\theta_2)}{F_1(\theta_1)}$$

(4.100)

$$IF \;\; F_1(\theta_1) < 0 \;\; THEN$$

$$F_{OUT}(\theta_1, \theta_3) = F_{IN1}(\theta_1) \frac{F_1(\theta_1)}{F_{IN1}(\theta_1)} \frac{F_3(\theta_3)}{F_1(\theta_1)}$$

The outcome of this conditional statement depends on the force reaction function, $F_1(\theta_1)$, and orientation angle, θ_1, of the first kinetic shape. As $F_1(\theta_1)$ becomes negative, kinetic shape 2 is engaged and when $F_1(\theta_1)$ becomes positive, kinetic shape 3 is engaged. If $F_1(\theta_1)$ is zero, neither decision happens and the system produces a zero output force.

4.3.2.5   Other System Operations

Other combinations of kinetic shape system operations are possible. Figure 4.25 shows an example of a more complex sixth degree kinetic shape system. This system includes the previously discussed division, addition, subtraction, and a conditional statement. This example kinetic shape system also describes percent force transfer between steps, inclusion of spring components, and a torque input. Notice that depending on the orientation of the conditional kinetic shape 5, it will either engages kinetic shape 6 or do nothing. Using my formulation of kinetic shape systems, this example can be described by Equation 4.101

$$IF \;\; F_5(\theta_5) > 0 \;\; THEN$$

$$F_{OUT} = (F_{IN\;1} + F_k)[\frac{F_1}{(F_{IN\;1} + F_k)} \frac{0.9\,F_2}{F_1} \cdots$$

$$\cdots + F_{IN\;3} \frac{F_3}{F_{IN\;3}} - (10/0.1) \frac{F_4}{(10/0.1)}]0.8\, \frac{F_5}{F_{IN\;5}} \frac{0.8\,F_6}{(F_5 + F_{IN\;6})}$$

(4.101)

$$IF \;\; F_5(\theta_5) < 0 \;\; THEN \; F_{OUT} = 0$$
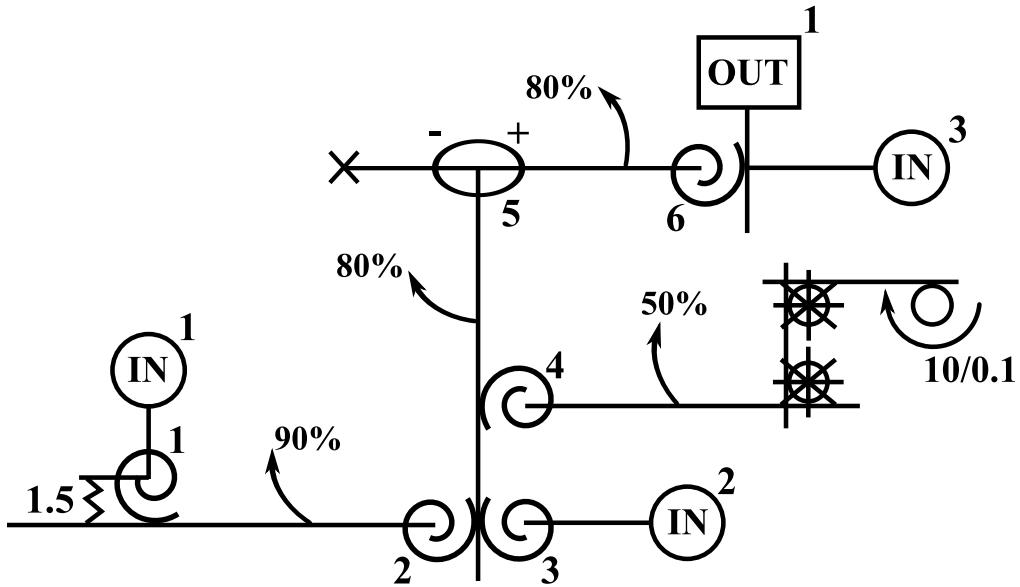
Figure 4.25: Kinetic shape system example with kinetic shape system notation

Notice that for brevity I did not include dependencies (i. e. (θ_1, θ_2...)). The a spring attached to the kinetic shape and ground in the kinetic shape system can be defined by Equation 4.102. A additional force onto the kinetic shape axle, such an elastic spring, will either add or subtract form the force exerted by that kinetic shape. The direction is determined by what system operation is performed.

$$F_{OUT}(\theta_1) = (F_{IN1}(\theta_1) + F_k(\theta_1)) \frac{F_1(\theta_1)}{F_{IN}(\theta_1) + F_k(\theta_1)} \tag{4.102}$$

The force of the spring acting on a kinetic shape in the system is defined by Equation 4.103

$$F_k(\theta_1) = k \left[R(\theta_1) sin[\psi(\theta_1)] + (x_{pre} - x_0) \right] \tag{4.103}$$

Here, k is the stiffness constant of the spring, x_0 is the unstretchable/nominal string length, and x_{pre} is the pre-streched distance (pre-tension).

    A complete list of operations and descriptions that I was able to think of are listed in Appendix C.

4.3.3 Kinetic Shape System Losses

Depending on the quality of a physical kinetic shape system, kinetic losses due to striction, friction, or misalignment may occur. These kinetic losses in the kinetic shape system I am accounting for by including a force transfer coefficient, represented by the variable D_f. The *force transfer coefficient, D_f*, is the percentage of the force saved, or successfully transfered, during transfer due to imperfections in the physical design. The force transfer coefficient has a range from zero to one, where zero indicates no force transfer and one indicates no force losses.

To apply the force transfer coefficient to a kinetic shape system force transfer step, the coefficient is simply multiplied for each step. For example, if one was to add a force decay coefficient to each step in a chain of multiplication operations, Equation 4.97 is turned into Equation 4.104.

$$F_{OUT}(\theta_1, \theta_2, ...\theta_n) = F_{IN1}(\theta_1)D_{f1}\frac{F_{IN1}(\theta_1)}{F_1(\theta_1)}D_{f2}\frac{F_1(\theta_1)}{F_2(\theta_2)} \cdots D_{fn}\frac{F_{n-1}(\theta_{n-1})}{F_n(\theta_n)} \tag{4.104}$$

If a system has one force input and one force output, it is also possible to specify the cumulative force decay coefficient for the entire kinetic shape system from input to output. I will choose to represent this cumulative force transfer coefficient as $\overline{D_f}$. For multiplication and division operation the cumulative force decay coefficient multiplies at each step, while in addition and subtraction it does not.

4.3.4 Kinetic Shape System Example

In this example, I will examine a kinetic shape system with two divisions of forces by two kinetic shapes that are independently defined (kinetic shape definition method 2). That is, the second kinetic shape is not defined by the first kinetic shape's output force profile, but independently defined by some other applied force function. The first kinetic shape is defined by the force functions in Equations 4.105 and 4.108, while the resulting shape is defined in Equation 4.110 and shown in Figure 4.26.

$$F_{IN\,1}(\theta_1) = 100 \tag{4.105}$$
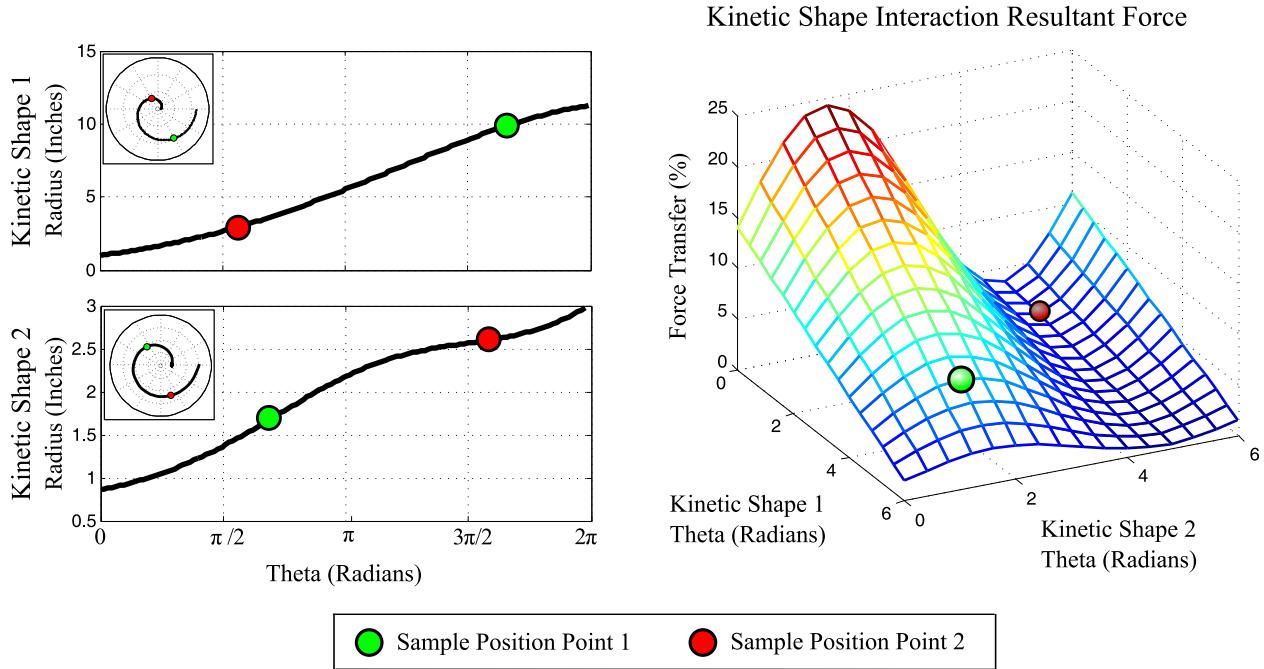
Figure 4.26: As a force is applied to kinetic shape 1, it presses its radial ground reaction force onto kinetic shape 2 to produce a resultant force transfer

$$F_1(\theta_1) = -10\theta_1 + 75 \tag{4.106}$$

$$R(\theta_1) = 1.0 \ \exp\left[\frac{3\theta_1}{4} - \frac{\theta_1^2}{20}\right]_{\theta_1=0}^{\theta_1=2\pi} \tag{4.107}$$

The second kinetic shape is defined by the force functions in Equations 4.108 and 4.109, while the resulting shape is defined in Equation 4.110 and shown in Figure 4.26.

$$F_{IN\ 2}(\theta_2) = 800 \tag{4.108}$$

$$F_2(\theta_2) = 15\sin(\theta_2) + 20 \tag{4.109}$$

$$R(\theta_2) = 1.0 \ \exp\left[\frac{\theta_2}{40} - \frac{3\cos(\theta_2)}{160}\right]_{\theta_2=0}^{\theta_2=2\pi} \tag{4.110}$$

Because these two shapes are in series, the forces will divide twice. This division is described in the previous Equation 4.96 which in this example is shown in Equation 4.111 and 4.112.

$$F_{OUT}(\theta_1, \theta_2) = F_{IN1}(\theta_1)\frac{F_1(\theta_1)}{F_{IN1}(\theta_1)}\frac{F_2(\theta_2)}{F_{IN2}(\theta_2)} \tag{4.111}$$

$$F_{OUT}(\theta_1, \theta_2) = -(10\theta_1 - 75)\left[\frac{3sin(\theta_2)}{160} + \frac{1}{80}\right] \qquad (4.112)$$

This force output $F_{OUT}(\theta_1, \theta_2)$ is shown in the three dimensional plot in Figure 4.26. This plot shows a percent force transfer, that is, given 100% input force, this kinetic shape system reacts with a cumulative output % force transfered. Figure 4.26 also shows two sample kinetic shape orientations, θ_1 and θ_2.

4.4   Notes for Practical Kinetic Shape Application

As previously mentioned, my kinetic shape equations are able to exactly produce a shape that will exert kinetic properties. In this section, I will review how kinetic shapes can be used and what things need to be considered when integrating a kinetic shape into practical designs.
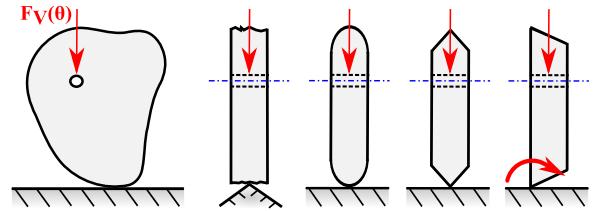
The most critical application consideration for the kinetic shape is the contact surface between the shape and a level plane/ground. Theoretically the plane/ground onto which the shape is pressed on is infinitely rigid and perfectly flat and the kinetic shape is also infinitely rigid and makes contact with the ground perfectly along the shape definition, and the friction between ground and the kinetic shape is assumed to be infinitely high. However, in practice these conditions are often times never the case and I am going to outline some work-around techniques which may help enhance the theoretically predicated values obtained by my kinetic shape equations.

Note for clarity I am only describing these practical techniques for the 2D kinetic shape, however these practicalities outlined in this section are also applicable for 3D kinetic shapes but may carry additional practical design problems.
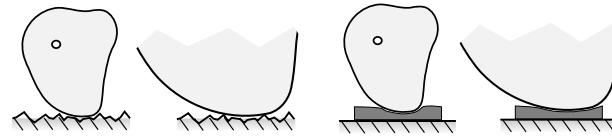
4.4.1   Ground-Shape Contact

The contact between the kinetic shape and the flat surface onto which it is pressed should be as close to a point as possible. For the two dimensional kinetic shape, this point can also be the orthogonal line between the kinetic shape faces. If the 2D kinetic shape is cut from a flat material with finite thickness, the cut could be made with an angle (or curvature) to force the

A angled and rounded edge may create a point contact.

$F_V(\theta)$

Increasing shape scale may reduce surface imperfection and deformation effects.

Possible practical solutions to increase surface friction grip.

Sand Paper   Rubber   Fine Gearing
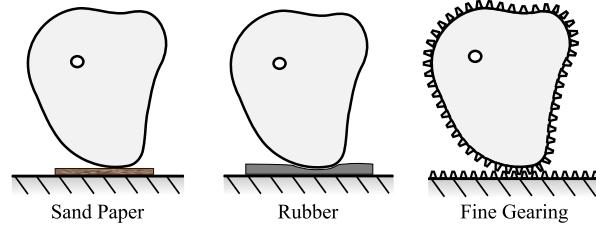
Figure 4.27: Practical 2D kinetic shape application. Practical suggestion on how to create a point contact between the two dimensional kinetic shape and flat ground surface. Note that when creating a point contact or increasing friction it is possible to alter the kinetic shape or the ground onto which it is placed.

kinetic shape to roll on a edge instead of a surface, which may be irregular depending on the cut. Such edge modification can be seen in Figure 4.27. Note that edge modification may not be necessary, however may improve results. If however the angled edge is cut sideways, it may cause an unwanted moment at the shape axle.

The ground contact point may be improved by scaling the kinetic shape up. A small kinetic shape may be more affected by contact point imperfections such as ground contact deformation or imperfections in surfaces. To clarify, this shape alteration can be viewed in Figure 4.27.

4.4.2   Ground-Shape Contact Friction

For the kinetic shape equation to work the friction between the shape and the flat surface has to be as high as possible. After some experimentation and implementation of the kinetic shape, I have found that there are potentially three different ways of increasing friction (Figure 4.27). This can be achieved by layering the flat surface (or the kinetic shape rolling surface) with sand paper,

124

rubber, or even gearing the kinetic shape, in a sense creating a rack-and-pinion. If one is to use a rubber surface, it should be noted that the ground-shape contact point may be blunted yielding inacurate results. As I've previously mentioned, this may be alleviated to some degree using a larger shape. If one is to use a geared kinetic shape, it is important that the gear teeth are relatively small compared to the kinetic shape. A rough approximation would be using gear teeth which are under 5% of smallest shape radius. Relatively large gear teeth create large angled edges which can affect the force redirection of the kinetic shape.

4.4.3 Force Application

Naturally, the application of the applied vertical force at the shape axle, F_v, can be done by pushing or pulling. It is only important that this force is applied orthogonal to the flat rolling surface. Depending on the application of the kinetic shape one means of force application may be better then the other.

If one is to push onto a kinetic shape that is in static equilibrium, the force applicator experiences a bending moment as shown in Figure 4.28(a). This bending moment is directly proportional to the radial ground reaction force. In the two dimensional kinetic shape this bending moment, M, can be defined by Equation 4.113 and 4.114.

$$M = F_v(\theta)[R(\theta)\cos(\varphi(\theta))] = F_r(\theta)[R(\theta)\sin(\varphi(\theta))]. \tag{4.113}$$

$$\psi(\theta) = \tan^{-1}\left(\frac{F_v(\theta)}{F_r(\theta)}\right). \tag{4.114}$$

Pulling on the shape axle may be more beneficial in design situations if one can pull perpendicular to the flat surface. In some situations this may be easier since one could hang a weight from the shape axle. Naturally due to gravitational forces, the weight will produce a perfectly orthogonal force to the flat surface *if* the flat surface is perfectly horizontal. This method can be seen in Figure 4.28(b). However, note that if the shape is rolling in this setup, depending on the size of the weight, the hanging weight may sway and produce a force that is not constant.
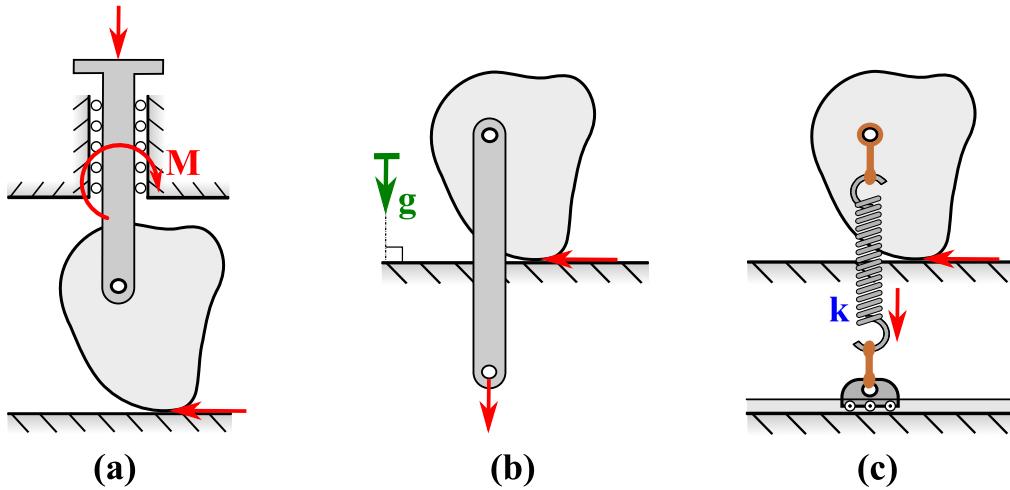
Figure 4.28: Vertical force application. Via (a) pushing, (b) hanging a weight, (c) or a spring

A swaying weight during shape rolling could be compensated for by defining the applied force, F_v in terms of the swinging weight dynamics.

A third possibility of applying a force to the kinetic shape axle is by a spring/rubber band/elastic member pulling the shape toward the ground (Figure 4.28(c)). This setup applies a variable force to the kinetic shape axle. As the shape changes orientation, so does the distance from the shape axle to the ground contact point and in turn the force applied to the shape changes. The force applied to the shape axle in this setup can be described as Equation 4.115.

$$F_v(\theta) = k \left[R(\theta) sin[\psi(\theta)] + (x_{pre} - x_0) \right] \tag{4.115}$$

Here, k is defined as the stiffness of the spring, x_0 is the nominal/free/unstreched spring length, and x_{pre} is the distance the spring is already stretched from its nominal/free length (pre-tension). Note that the force application has to come from below the kinetic shape. If the the spring does not move and pulls directly below the shape axle, proper geometric force decomposition needs to be applied. This misalignment will result in a force pulling the shape along the ground plane, adding or subtracting from horizontal ground reaction force, F_r.

4.4.4 Kinetic Shape Radius Change with Time

One thing that I thought of as I was developing the kinetic shape is that a *kinetic shape radial function can be dependent with time*, i.e. $R(\theta,t)$ for the 2D kinetic shape. This means that it is possible to implement the kinetic shape such that it physically changes its shape to produce other radial force functions over time. This dynamic morphing property opens up many more possibilities for the kinetic shape application.

This dynamic shape change could be implemented with internal spokes that are actuated with some lead screw and a electric motor or electric servos. One could also change the shape by using Bowden cables like used in bicycle brakes and gear shifter. However, for a changing kinetic shape it to be rigid enough to transfer the applied force while also flexible enough to change its shape. If the rim material is too loose, one may consider a larger shape to offset the deformation of the rim.

4.5 Kinetic Shape Applications and Innovations

Here I will describe my inventions, ideas, and projects that involved the application of my kinetic shape concept. These innovations include the kinetic crutches, which uses a kinetic shape as a crutch tip to control crutch walking dynamics, the kinetic board, which uses the kinetic shape for human locomotion, and a kinetic shape included in a novel musical string instrument.

4.5.1 Kinetic Board and Kinetic Transport

After discovering the kinetic shape concept, one of the novel applications I invented was the kinetic board and the kinetic transport. The kinetic board and the kinetic transport both utilize the dynamic kinetic shape concept outlined in Section 4.2.1 and involve two or more kinetic shapes that alter movement. In essence the kinetic board/transport is a device that a person or a machine uses to move linearly over a flat surface in a continuous motion. This is achieved by pressing two or more kinetic shapes onto a flat surface, one kinetic shape at a time. In addition, each kinetic shape has two small rollers at the shape perimeter and at two points of eventual ground contact
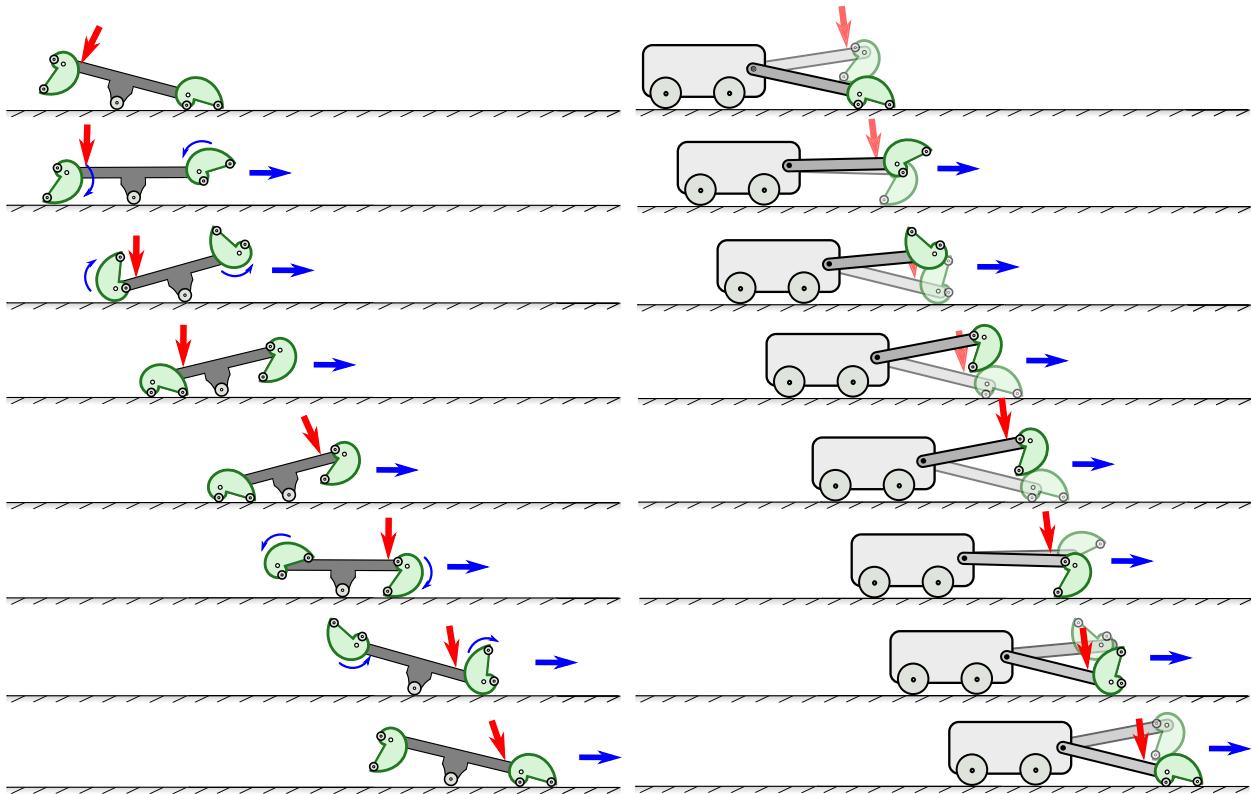
Figure 4.29: Kinetic board/transport concept. The motion of a kinetic board (left) and a kinetic transport (right)

as the shape rolls over. In other words, as a kinetic shape rolls around and over itself, instead of colliding with the ground, the kinetic shape's rollers hit and roll along the ground. This concept can be seen in Figure 4.29.

On the left side of Figure 4.29 is the kinetic board, which is a see-saw that has a roller in the middle and a two kinetic shapes on either side of the pivoting platform. Pivoting to either side will engage a kinetic shape and pushes the entire board forward. On the right side of Figure 4.29 is the kinetic transport concept. This concept is similar to the kinetic board, but with both kinetic shapes facing and rolling into one direction. In this type of setup, the user or machine would "pump press" the two pedals holding the kinetic shapes onto a flat surface allowing the kinetic shapes to push the entire device forward. Again, as with the kinetic board, as the kinetic shapes roll over, two rollers contact the ground and continue the linear motion.
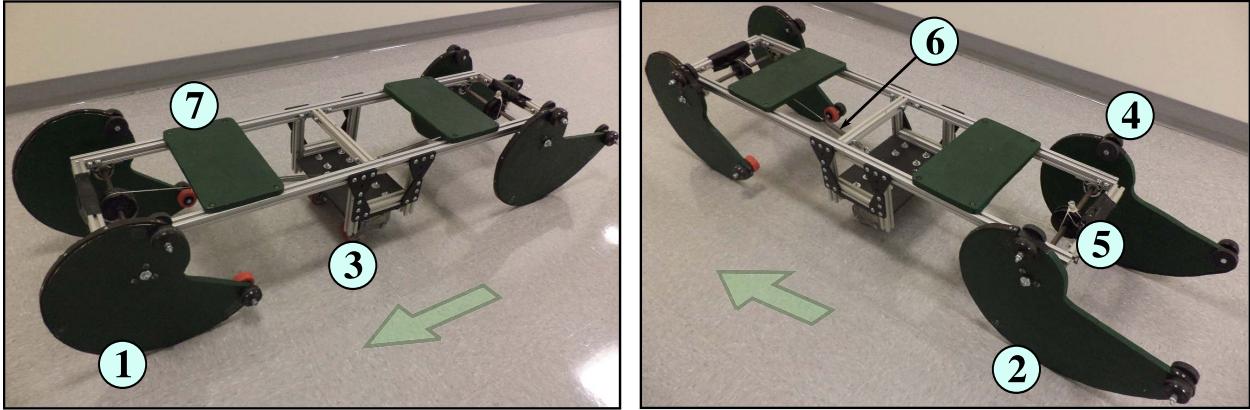
Figure 4.30: The kinetic board. (1) Front kinetic shape wheel (2) Rear kinetic shape wheel (3) Pivot (middle) roller (4) Kinetic shape roller (5) Reset pulley with stopper (6) Reset Extension Spring (7) Stepping surface

To prove the concept of this invention and validate it with my dynamic kinetic shape equations, I chose to design, construct, and analyze the dynamics of a kinetic board.

4.5.1.1   Kinetic Board Design

My complete design of the kinetic board can be seen in Figure 4.30 while more detailed drawing can be viewed in Appendix D. The entire kinetic board is framed and held together with rigid 1in by 1in (2.65cm by 2.65cm) 80/20® aluminum extrusion pieces. Aluminum extrusion framing offered an easy and adjustable solution to forming a frame structure for the kinetic board. Two heavy duty caster wheels with rubber rollers were used for the middle pivot. For smoother operation for pivoting from front to back, the caster wheels were spring loaded (shock absorbing) and were specified for loads up to 400lb (180kg) each (R.T. Laird, inc® 203803). The caster wheels were attached to the frame so that the axle center of the wheels was in line with the mid point in the length direction (Appendix D).

The entire framing structure including the caster wheels was approximately 12in (30.7cm) wide, 48in (123cm) long, and 12in (30.7cm) high (from ground). The middle pivot caster wheels were able to be moved higher or lower at a range of ±1.5in (3.8cm), which altered the angle at which the board could be pivoted. This adjustable height and pivot angle allowed me a degree of freedom in potential troubleshooting during the testing phase. Two 7in by 12in (17.9cm by

30.7cm) stepping platforms made of 0.625in (1.60cm) thick wood were attached on top of the frame and on either side of the middle pivot. These stepping platforms could be moved along the top of the frame, but generally were fixed at 25in (64cm) apart (center to center), which is a slightly greater distance than the average adult male's shoulder width (18 in (46cm)).

The design included two kinetic shapes on either side that needed to be reset at each pivot of the kinetic board. To reset these kinetic shapes to their initial position, a pretensioned extension spring with a stiffness of 2.37 lb/in (4.12 N/cm) was attached to a pulley that was attached to the kinetic shape wheel axle. This reset mechanism was mirrored for each side (front and rear). I made the pulleys by laser cutting three circular polyoxymethylene (a.k.a POM, acetal, Delrin®, etc.) plastic pieces and joining them together using an adhesive (BondiT® B-45TH) to make one whole 3.0in (7.7cm) diameter and 0.875in (2.24cm) thick pulley with two shoulders, where the two outside plastic pieces were 0.25in (0.65cm) thick and the inside piece was 0.375in (0.96cm). A Universal® Laser Systems VLS4.60 60W laser cutter was used to precisely cut the plastic pieces. The pulley was attached to the steel shaft by a $0.1875in^2$ ($0.48cm^2$) key with a set screw shaft collar on each side of the pulley to prevent it from moving along the steel shaft. A 1/4in (0.64cm) diameter, with 20 threads per inch, and 1.75in (4.48cm) in total length bolt was screwed into the pulley orthogonal to the steel shaft axle. This bolt served as a stopper, hitting the end member of of the aluminum framing which was padded with 1in (2.56cm) quick-recovery natural gum foam covered with duct (or gaffer) tape to dampen the stopping impulse.

The relatively large kinetic shapes on either side of the kinetic board were first paper printed using a 1:1 scale, which divided the kinetic shape outlines into smaller sections that fit onto standard printer paper. These outlines were subsequently cut out and the individual paper section were assembled with adhesive tape. This template was traced onto a 0.625in (0.159cm) thick pine wood material and cut out with a jigsaw. All rough edges were carefully sanded down avoiding irregularities around the shape perimeter. To ensure that the kinetic board could be used on various surfaces with minimal amount of slip and a maximum ground to wheel friction, a strip 0.25in (0.64cm) thick abrasion resistant styrene-butadiene rubber (SBR) (60A durometer) was

firmly screwed (with countersink) to the perimeter the kinetic shape wheel. The kinetic shape wheels were joint to a 0.5in (0.20cm) steel shaft. The kinetic shapes were attached to the steel shaft via a steel bushing which is keyed onto the the steel shaft with a $0.1875in^2$ ($0.48cm^2$) key. Two shaft collars prevent the wheels form slipping off the shaft. The steel shaft rotated smoothly on two base mount ball bearing (per shaft) attached to the bottom of the aluminum framing.

The rollers on the perimeter of the kinetic shapes and which continue the linear momentum generated by the kinetic shapes, where 0.5in (1.28in) rubber caster wheels and 2.0in (5.12cm) in diameter. For a more stable rolling and to eliminate twisting moments onto the kinetic shape wheels, a 3in (7.68cm) shoulder bolt joined two rollers wheels. Each entire wheel with steel bushing and four rubber rollers weighed approximately 3.2lb (1.45kg). The difference in weight between the front kinetic shape and the rear kinetic shape was minimal.

My entire kinetic board design was approximately 17.6in (45cm) wide and had a weight of around 35lb (15kg).

4.5.1.2 Kinetic Shapes for Forward Propulsion

The parameters of the kinetic shapes for the kinetic board were strategically selected. When I initially thought of the kinetic board concept, I quickly constructed a preliminary design prior to this presented design. This preliminary design had two of the same kinetic shapes on either side of the rocking platform. Because the user always stepped into the motion of the board (down and forward) the front kinetic shape had not problem of rolling with this applied motion. However, as the user stepped onto the rear kinetic shape, the stepping force was against the motion of the board (down and back), hence the rear kinetic shape had difficulty rolling forward. This impedance seemed only present at the beginning of the rolling motion, that is, once the equilibrium was unbalanced the rear shape had also no trouble rolling on and propelling the user forward.

With the consideration of this preliminary prototype and study, I figured to describe a kinetic shape which when a constant vertical weight was applied to it, would initially react with a high radial ground reaction force followed by a steady decline in reaction force as the shape rolls

131
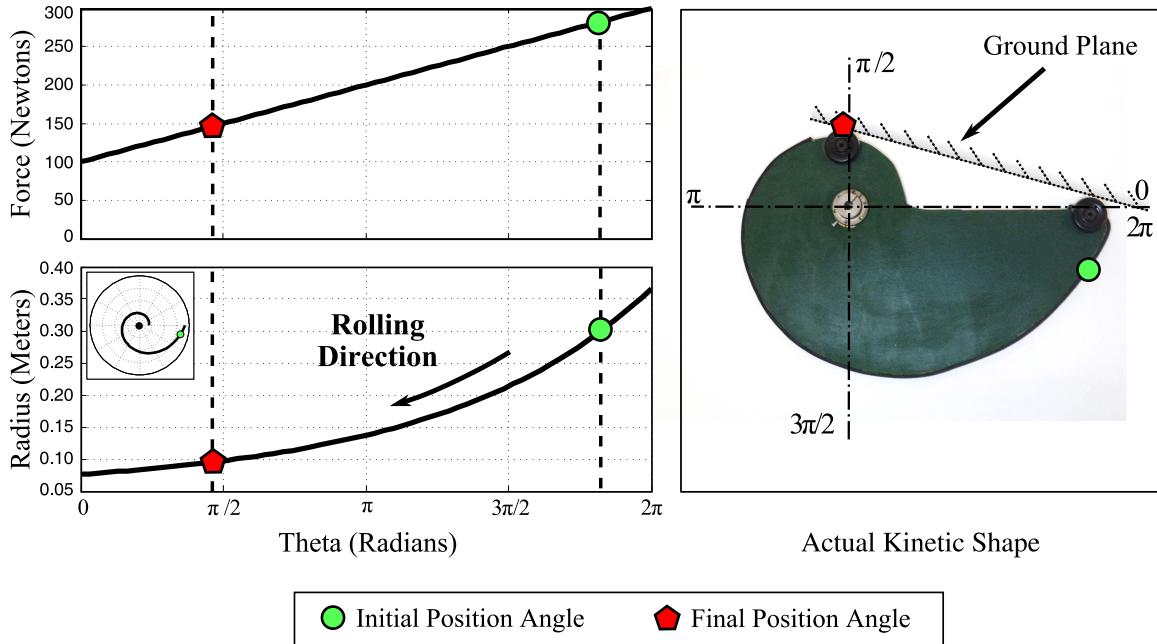
Figure 4.31: The kinetic shape that is the rear wheel of the kinetic board

around. This rear kinetic shape was described using Equation 4.10 in Section 4.1.1. The vertically applied force was chosen to be the average weight of the potential test user of the board which was 180lb (800N) (Equation 4.116). The ground reaction force was described by Equation 4.117 to yield a radial shape function in Equation 4.118. The initial radius, $R(\theta_i = 0)$, for the rear wheel was chosen to be 3.0in (0.077m).

$$F_{v\ rear}(\theta) = 800\ N \tag{4.116}$$

$$F_{r\ rear}(\theta) = \frac{200}{2\pi}\theta + 100\ N \tag{4.117}$$

$$R_{rear}(\theta) = 0.077\ \exp\left[\frac{\frac{\theta^2}{2} + \pi\theta}{8\pi}\right]_{\theta=0}^{\theta=2\pi} \tag{4.118}$$

This kinetic shape for the rear kinetic board wheel can be seen in Figure 4.31.

Since during kinetic board use the front wheel does not encounter a resistive force as the user steps onto the front of the kinetic board, it does not have to exert such a drastic or even changing ground reaction force. On the contrary, the front wheel experiences a slight assistive push forward by the user steps onto the front of the board. Considering this front kinetic wheel shape
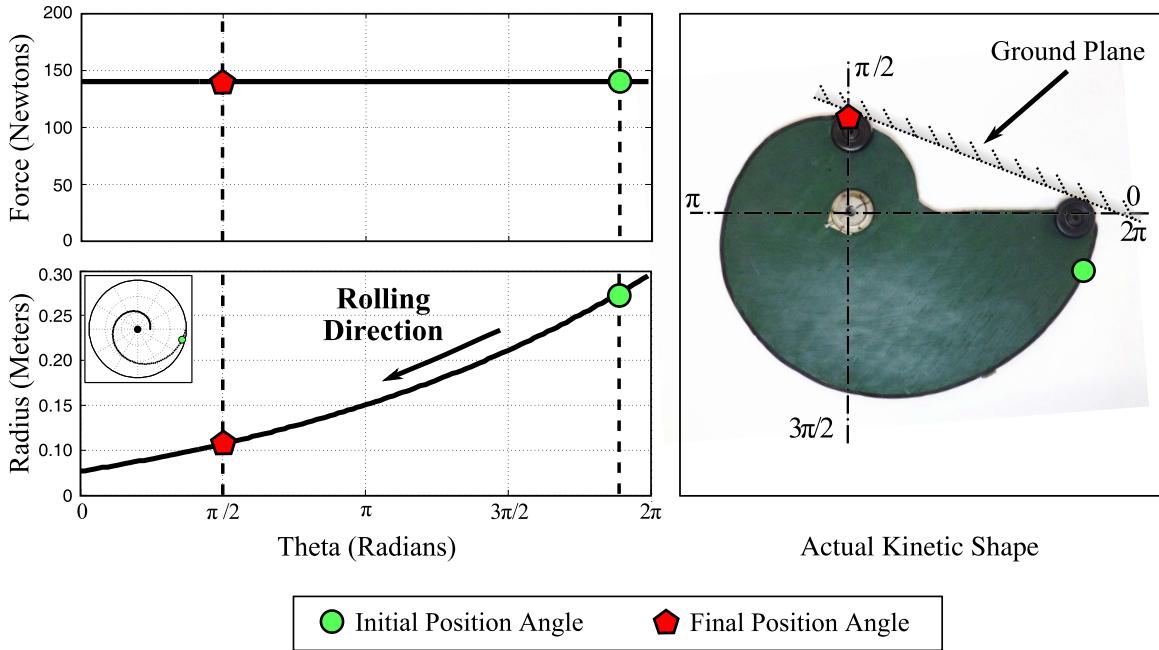
Figure 4.32: The kinetic shape that is the front wheel of the kinetic board

for the front of the kinetic board is defined by forces shown in Equations 4.119 and 4.120, while the radial function of the kinetic shape is defined by Equation 4.121 and shown in Figure 4.32.The initial radius, $R(\theta_i = 0)$, for the front wheel was chosen to be 3.0in (0.077m) as well.

$$F_{v\ rear}(\theta) = 800\ N \tag{4.119}$$

$$F_{r\ rear}(\theta) = 140\ N \tag{4.120}$$

$$R_{rear}(\theta) = 0.077\ \exp\left[\frac{7\theta}{40}\right]_{\theta=0}^{\theta=2\pi} \tag{4.121}$$

Note that both wheels where chosen to have a substantially large overall size. I chose a large kinetic shape size because the larger the size of the shape, the greater the wheel parameter would be, hence the shape will roll further and gain more momentum on just one pivot.

4.5.1.3 Dynamic Kinetic Shape Model for the Kinetic Board

The novelty of the kinetic board and the kinetic transport is that because of my kinetic shape equations, the dynamics of the device can be predicted and accounted for. The dynamic
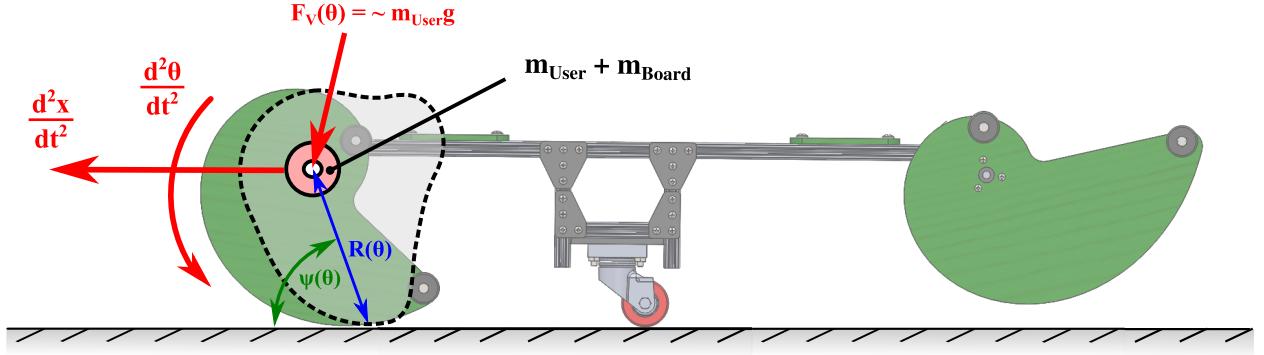
Figure 4.33: The dynamic kinetic shape model as it is fitted to the kinetic board dynamics as a user steps onto the front of the kinetic board

model used to mathematically describe the motion of the kinetic board during use, is described by Equations 4.70, 4.71, and 4.72 in Section 4.2.1.1. In Section 4.2.1.1, a platform is dispensed underneath the kinetic shape as it rolls on top of it. In this case the shape rolls over firm ground, while pulling a mass at shape axle and parrallel to the ground plane. This setup is shown in Figure 4.33. This setup requires an adjustment to the definition of the polar mass moment of inertia *about the ground contact point*. This polar mass moment of inertia about the ground contact is defined by Equation 4.122.

$$J_G(\theta) = J_O(R, \theta) + m_{KS}R(\theta)^2 + (m_{Board} + m_{User})R(\theta)^2 \sin[\psi(\theta)] \qquad (4.122)$$

Here, the first term, $J_O(R, \theta)$, is the polar mass moment of inertia of the kinetic shape around the axle point and is defined by Equation 4.48 Section 4.2.1. The middle term, $m_{KS}R(\theta)^2$, transfers the rotation point form shape axle to ground contact by the parallel axis theorem, where m_{KS} is the total mass of the kinetic shape. The last term, $(m_{Board} + m_{User})R(\theta)^2 \sin[\psi(\theta)]$, is a point mass at kinetic shape axle point moving into the direction parallel to the flat ground, where m_{Board} is the mass of the kinetic board and m_{User} is the mass of the user riding on top of the kinetic board.

To properly match my dynamic kinetic shape model to actual measurements, a system friction model was defined. The friction model was the same model explained in Equation 4.68, seen in Figure 4.13, and found in Section 4.2.1.1. This model joins Stribeck, Coulomb, and viscous

friction forces acting upon the kinetic board's bearing or rolling surfaces. By pulling the kinetic board with a fish (hanging) scale the static and kinetic friction was approximated. The static friction, μ_S, was found to be 0.4, while the kinematics friction, μ_K, was found to be around 0.07. The exponential decay coefficient, C_f, was approximated to be 7.0.

The simulation model was evaluated at 400Hz with a 0.002 radian step size around the kinetic shape definition.

4.5.1.4 Kinematic Testing Setup

To measure the kinematics of the kinetic board a VICON® motion tracker infrared camera system was used. The motion tracker system was equipped with six VICON® Bonita B10 cameras set to record at 100 Herz. This setup is shown in Figure 4.34. Two low resolution video cameras recording movements in the sagital (side) and frontal plane also recorded the kinematics, which were also directly synchronized with the infrared motion capture cameras. A video recording of a test trial can be seen in Figure 4.35. The motion capture system was powered by the VICON® Nexus® software. Reflective infrared markers that were used were 14mm in diameter. These
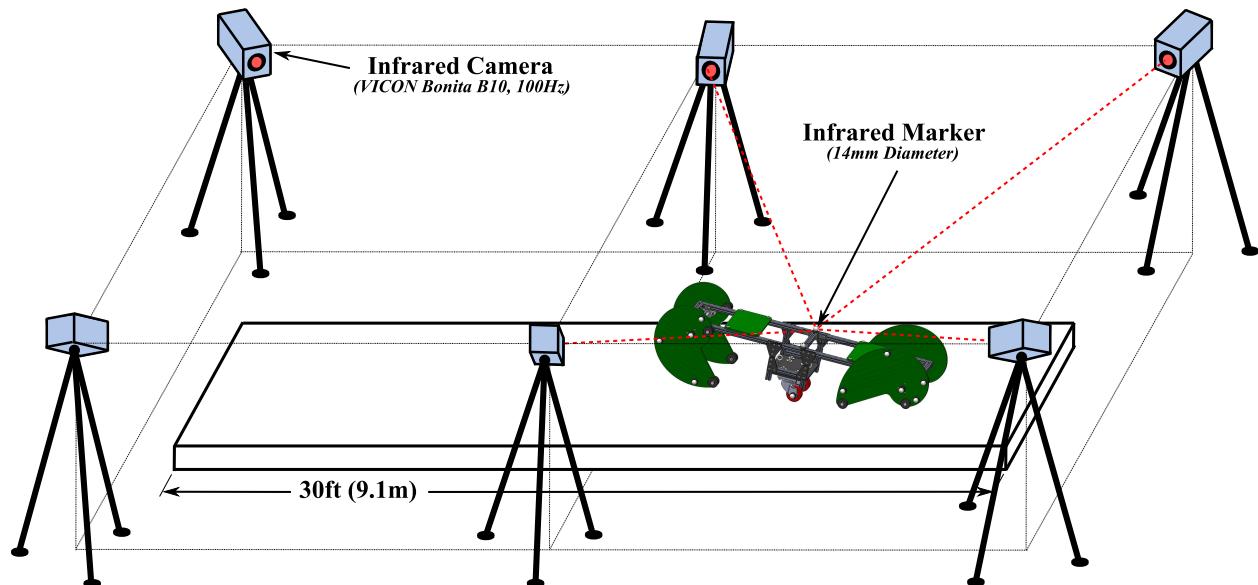
Figure 4.34: Infrared marker motion capture setup for the measurement of the kinetic board kinematics
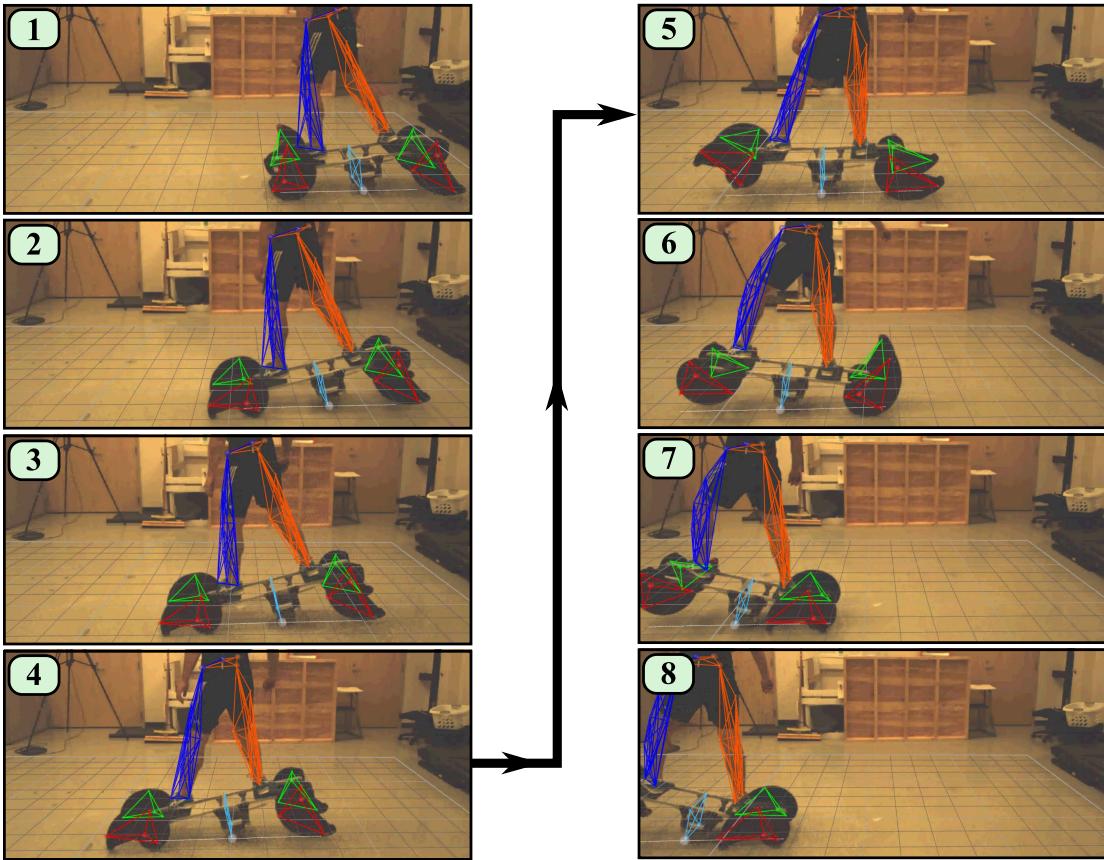
Figure 4.35: Kinematics of a person using the kinetic board during motion capture

markers were placed on the individual riding the kinetic board during testing, onto each kinetic shape wheel and axle, and also placed onto the middle pivot roller of the kinetic board. This middle marker is used to track the board's linear kinematics. The kinematics of the kinetic board was recorded three times with the same individual riding the board, particularly recording the linear overground movement of the moving platform. The individual testing the kinetic board was a 5ft-10in (1m-79cm) tall 23 year old male weighing 180lb (82kg). The recorded infrared position data was numerically differentiated (finite difference formula) for linear velocity which in turn was filtered using a first order butterworth low pass filter with a normalized cutoff frequency of 0.05 (10Herz). The filtered velocity was then again numerically differentiated for linear acceleration. All post processing was completed in Matlab®.

Since the kinetic shape kinematics greatly depend on the forces applied to the shape, it was necessary to measure how much force was applied to the rear and front kinetic shapes as the
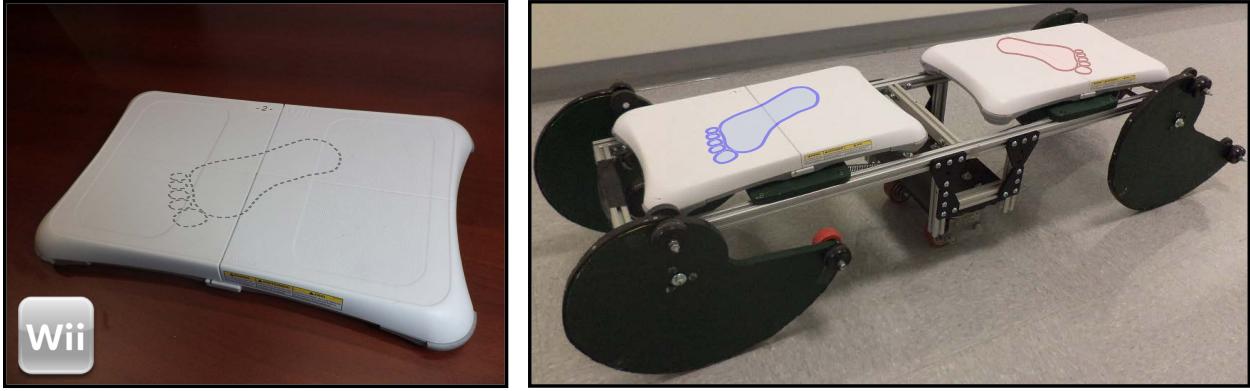
Figure 4.36: The force application by the kinetic board user onto the board was measured using two Nintendo® Wii® boards, one for the front foot and one for the rear

kinetic board pivoted back and forth. It has been proven that a relatively inexpensive *Nintendo® Wii® Balance Board (WBB)* is sufficiently accurate in quantifying center of pressure trajectory, and overall amplitude and velocity during single-leg stance balance tasks [93]. Thus, to approximate how much force is applied to the rear and front kinetic shape as the user presses down onto the shapes, I utilized a WBB by placing one on each side of the kinetic board as shown in Figure 4.36. The force data was *not* taken simultaneously with the kinematic motion capture data. Four trials with the same subject, motions, and traveled distance was recorded with the WBB. It is important to note that the WBB was only able to measure forces that wwas perpendicular to the WBB surface, hence, horizontal pushing forces applied by the user onto the kinetic board were not recorded. The WBB was programed in Python and read the force data at a sampling rate of 36 Hertz with an accuracy of ± 6 N. The measured kinetics from the WBB was applied to the kinetic shape dynamics model to predict the resulting kinematics.

4.5.1.5   Results and Discussion

The kinematic motion capture data shows an expected trend as the kinetic board accelerates during kinetic shape engagement periods, while it decelerates during the cruising periods when the kinetic shape flips over and rolls. It is interesting to see that the acceleration is noticabbly lower when the subject presses down on the front kinetic shape than the rear. Given a equal amount of applied force, this follows the what is expected by the definition of the kintic shapes.
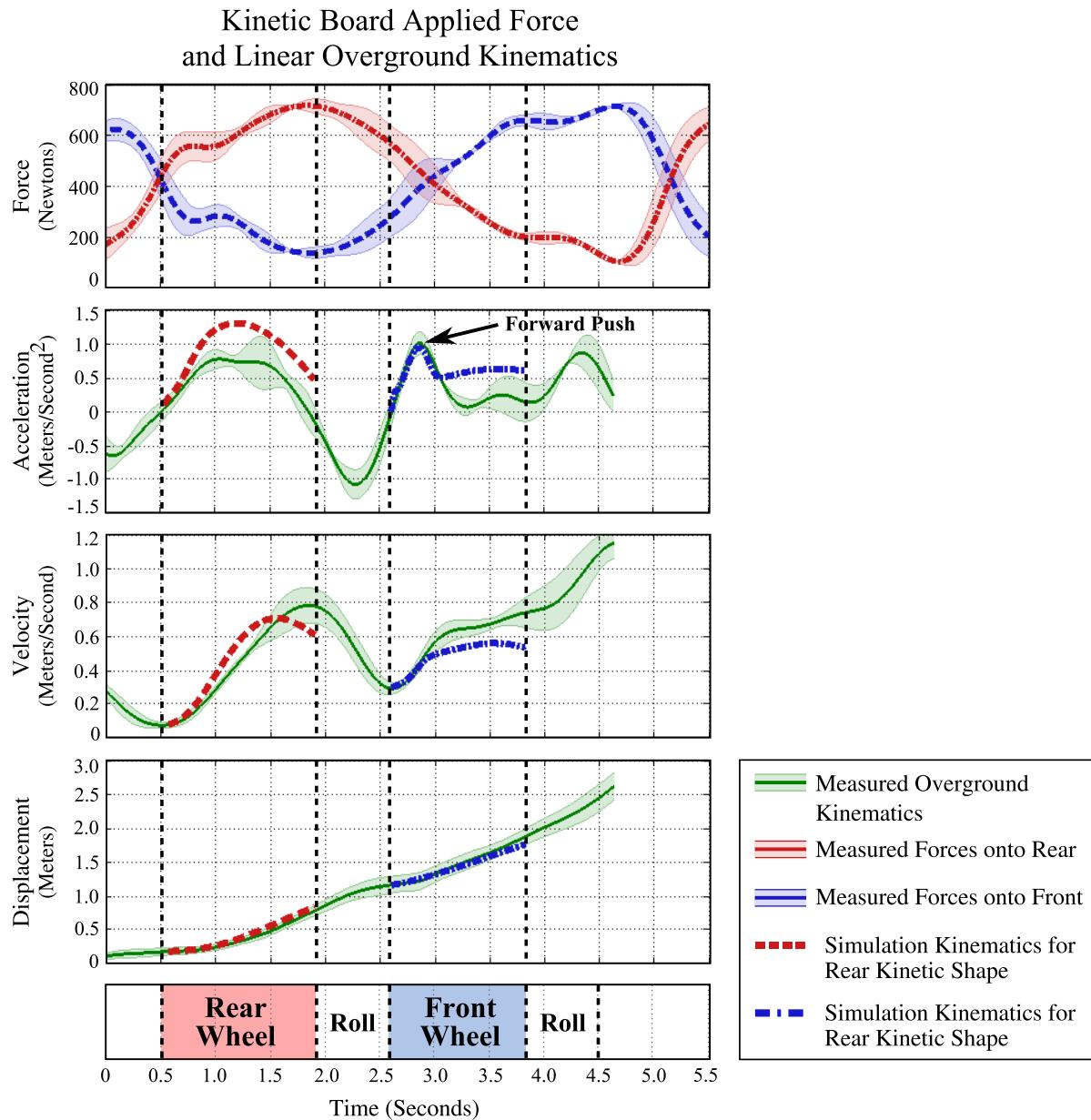
Figure 4.37: Measured and predicted kinetic board dynamics. The measured applied forces were inputted into the dynamic kinetic shape model.

The simulation model of the dynamic kinetic shape showed to be a good predictor of kinetic board movement. A bump in acceleration during the front kinetic shape wheel engagement was due to the subject pressing forward and down onto the kinetic shape. This horizontal force component did no show up in the kinetic measurements, however was noticeable in the kinematic video review.

To acount for this steep hump, the simulated kinetic shape in the front was added a slight 20N of horizontal force pressing parallel to the ground.

My resulting kinetic shape design proved to be tough, reliable, and was used for multiple preliminary experiments. Future analysis include using different kinetic shapes for the rear and front wheels and possibly adding a steering method. This steering method may include a middle swivel point, or using three kinetic shapes instead of four. Further plans also include designing and constructing a kinetic shape transport, discussed at the beginning of this section.

4.5.2   Musical Kinetic Shape String Instrument

In this section I am presenting my novel variable tension string instrument invention which relies on a kinetic shape to actively and discretely alter the tension of a fixed length taut (stretched) string. In this section I will derive a mathematical model that relates the two-dimensional kinetic shape equation to the string's physical and dynamic parameters. With this model I designed, constructed, and programmed an automated instrument that is able to play frequencies/notes within predicted and recognizable frequencies. My prototype instrument invention is also able to play programmed melodies.

It is possible to vary the fundamental natural oscillation frequency of a taut and uniform string by either changing the string's length, linear density, or tension. Most string musical instruments produce different tones by either altering string length (fretting) or playing preset and different string gages and string tensions. Although tension can be used to adjust the frequency of a string, it is typically only used in this way for fine tuning the preset tension needed to generate a specific note frequency.

Here I present a novel string instrument concept that is able to continuously change the fundamental oscillation frequency of a plucked (or bowed) string by altering string tension in a controlled and predicted manner. I manipulated the tension in the string by attaching the string to the axle of a weight-loaded kinetic shape. As previously discussed, a kinetic shape essentially acts as a mechanical force modifier redirecting an applied weight into a predicted ground reaction

Figure 4.38: The musical kinetic shape variable tension string instrument. In the image on the bottom, applied weights to the kinetic shape axle have been removed.

force with respect to the shape's orientation angle. As the weight-loaded kinetic shape changes orientation, the tension of the attached taut string produces a variation of tone on that plucked string. My complete string instrument setup can be seen in Figure 4.38.

A computer controlled stepper motor linearly moves a platform beneath the kinetic shape, re-orientating the shape at various angles. A constant-length guitar string is attached to the axle of the kinetic shape causing variable tension in the taut string as the shape is re-oriented. A thin guitar pick is attached to a computer controlled servo motor, plucking the string while a microphone records and analyzes the emitted sound.
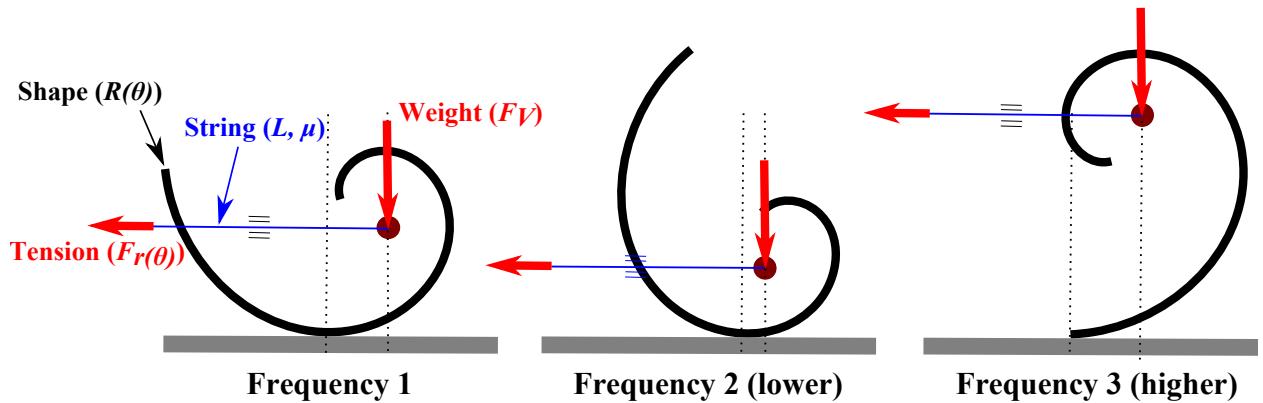
Figure 4.39: The musical kinetic shape concept. Due to the variable radius of curvature of the kinetic shape, repositioning the kinetic shape will cause different tensions in the taunt string and in turn cause the string to vibrate at different frequencies.

4.5.2.1 Kinetic Shape and String Vibration Theory

As previously discussed, the vibration frequency of a taut string can be described with Equation 2.3, Marsenne's law, which relates string length, linear density, and tension.

It is also common to specifically relate a keynote number to a note frequency. Keynote numbers are the conventionally designated numbers to discrete key sound frequencies. For example, the note $A0$, which sounds at a frequency of 27.5 Hz, has a keynote number of 1, while the note $G\#4$ has a frequency of 415.3 Hz and is referred as keynote number 48. The relationship between keynote frequency (f) and keynote number (k) is given in Equation 4.123.

$$f = 2^{\frac{k-49}{12}} * 440 \qquad (4.123)$$

The previously reviewed kinetic shape and string acoustic concepts can be combined to actively change the tension of a constant length string with constant linear density, and in turn produce different vibration frequencies of that string. This is possible if a kinetic shape axle is attached to a string, preventing it from rolling as a weight is applied to the kinetic shape's rotation axle. This setup can be seen in Figure 4.39.

The kinetic shape is actively rotated to specific positions around its perimeter to produce a predicted horizontal force (string tension), $F_r(\theta)$, which in turn produces different vibration

141

frequencies in a plucked taut string (Figure 4.39). *Note that the horizontal force, $F_r(\theta)$, applied by the kinetic shape onto the string is the string tension (T)* in Equation 4.9 in Section 4.1.1.

To correlate the shape form function, $R(\theta)$, string tension, T, and key note number, k, I will first combine Equation 4.9 and Equation 4.123 to obtain a resulting horizontal force function (string tension function) exerted by the kinetic shape with respect to keynote number.

$$F_r(k) = \mu \left[880 \, L \, 2^{\frac{k-49}{12}} \right]^2 \tag{4.124}$$

Here, the key note number, k, is a natural number. Equation 4.124 can also be presented as a continuous function between an initial and final keynote n times around the kinetic shape.

$$F_r(\theta) = \mu \left[880 \, L \, 2^{\frac{\frac{\theta}{2\pi n}(k_f - k_i) + (k_i - 49)}{12}} \right]^2 \tag{4.125}$$

I then plug this tension function and a constant weight, W, as $F_v(\theta)$ into Equation 4.9 to obtain the form of the kinetic shape in Equation 4.126.

$$R(\theta) = exp \left[\int \frac{\mu \left[880 \, L \, 2^{\frac{\frac{\theta}{2\pi n}(k_f - k_i) + (k_i - 49)}{12}} \right]^2}{W} d\theta + C \right] \tag{4.126}$$

After solving the indefinite integral, I obtain Equation 4.127

$$R(\theta) = exp \left[\frac{12\pi n \, 880^2 \, L^2 \, \mu \, 2^{\frac{\theta(k_f - k_i)}{12\pi n} + \frac{k_i - 49}{6}}}{W \ln(2)[k_f - k_i]} + C \right] \tag{4.127}$$

Given an initial shape radius, $R(0) = R_i$, I am able to solve for the integration constant, C,and obtain the final kinetic shape definition.

$$R(\theta) = R_i \, exp \left[\frac{12\pi n \, 880^2 \, L^2 \, \mu \, (2^{\frac{k_i - 49}{6}})(2^{\frac{\theta(k_f - k_i)}{12\pi n}} - 1)}{W \ln(2)[k_f - k_i]} \right] \tag{4.128}$$

Equation 4.128 defines a continuous radius of a kinetic shape from zero to $2\pi n$, where given string parameters (L, μ), initial and final keynote numbers (k_i, k_f), and an applied constant weight (W) at the shape axle, will produce adequate string tension to provide the desired keynote string vibration frequencies. I will name Equation 4.128 the *kinetic shape string equation*. Since keynote angular positions are distributed around the derived kinetic shape. For a kinetic shape of n revolutions $(0 \; to \; 2\pi n)$, discrete keynotes angular positions (θ_k) are found using Equation 4.129, where $k_i < k < k_f$ and k is a natural number.

$$\theta_k = (k - k_i)\frac{2\pi n}{k_f - k_i} \tag{4.129}$$

For example, on a kinetic shape that covers one revolution $(n = 1)$ for initial keynote $k_i = 10$ to final keynote $k_f = 20$, keynote $k = 15$ is found at angular position $\theta_k = \pi$.

4.5.2.2 Kinetic Shape Design and Fabrication

The 2D kinetic shape equation indicates that the total dimensions (size) of a kinetic shape are irrelevant, while only the curvature of the shape contributes to its behavior. However, preliminary tests concluded that in practice, a larger kinetic shape will produce more accurate results than an overall smaller one due to the fact that a smaller kinetic shape will be more affected by fabrication/surface imperfections and misalignment during use. Given all parameters, my kinetic shape string equation Equation 4.128 allows me to design a kinetic shape that produces a specified range of string vibration frequencies with adequate total shape dimensions.

For adequate accuracy, final kinetic shape, and (in turn) instrument dimensions, we selected the parameters presented in Table 4.1. The selection of these parameters was a process of trial and error using Equation 4.128 to determine the necessary range to play certain melodies. For example, in order to achieve the same keynote frequency range, choosing a lighter applied weight, longer string length, or heavier string would yield a larger radius change around the kinetic shape and vice versa. Note that the parameters chosen could be selected to cover different frequency ranges or to yield any overall size kinetic shape.

Table 4.1: Parameters Used to Derive the Instrument's Kinetic Shape.

Shape Initial Radius (R_i)	2.5 in (6.35 cm)
Revolutions (n)	1
Applied Weight (F_V)	82 lbf (365 N)
String Length (L)	18 in (45.7 cm)
String Linear Density (μ)	0.0002159 lbm/in (0.00003856 kg/cm) Guitar String Type: *D'Addario NW034*
Initial Keynote (k_i)	19 *(D#2 / 77.8 Hz)*
Final Keynote (k_f)	31 *(D#3 / 155.6 Hz)*

These chosen parameters are entered into Equation 4.128 to generate the shape shown in Figure 4.40. Note that it is possible to derive a kinetic shape for more than one revolution $(n > 1)$, however, the curved rolling surface in such case would be more difficult to access with a flat and tangent surface. Also, unless specially fabricated, such a resulting kinetic shape could result in a less rigid structure. For ease of fabrication, robustness, and convenience I chose a kinetic shape that spans across one revolution $(n = 1)$. Inserting parameters of Table 4.1 into Equation 4.125, I found that the string tension around the derived kinetic shape spans from $19.5N(k_i = 19)$ to $78.0N(k_f = 31)$.
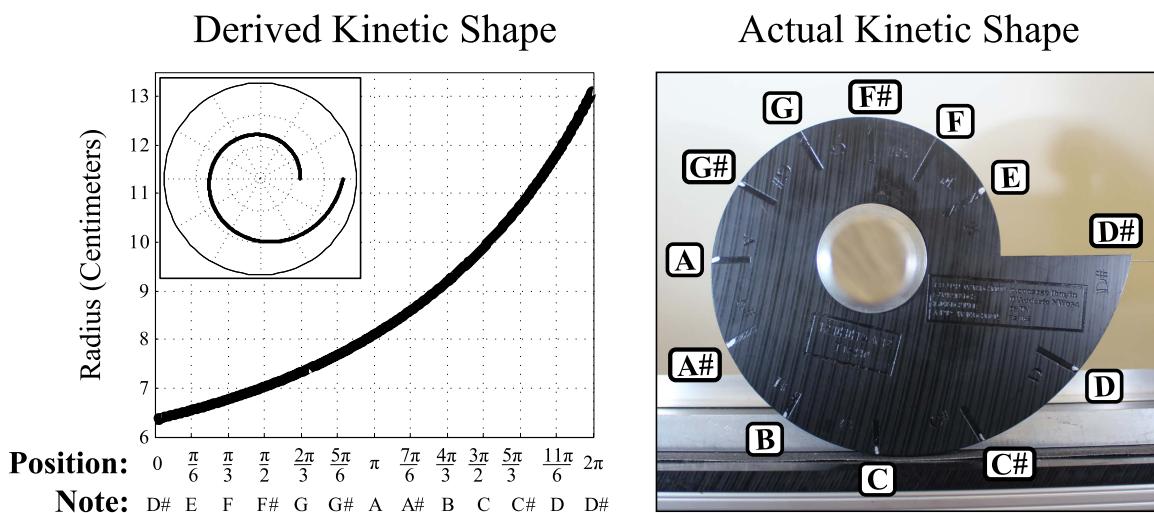
Figure 4.40: Derived kinetic shape to be used on kinetic shape musical instrument

144

The chosen two-dimensional kinetic shape was laser cut from a 0.375" (0.9525 cm) thick sheet of tough Acetal Resin (Delrin®) plastic. The laser cutter used to cut the shape was a 60 Watt Universal Laser System® VLS4.60. After cutting, the rolling surface of the kinetic shape was carefully sanded smooth to reduce any surface imperfections.

4.5.2.3   Kinetic Shape Reorientation

For our instrument, the derived kinetic shape has to be reorientated in a simple and accurate manner onto discretely defined points around the shape perimeter. Instead of repositioning the kinetic shape with respect to ground, a platform beneath the shape is moved, thus rolling the shape into position. To minimize error due to slippage between the kinetic shape rolling surface and the moving platform surface, course sandpaper was firmly screwed onto the moving surface. No soft material such as rubber could be utilized for the contact point between the shape and movable platform since the contact area needs to be as small as possible. To ensure accuracy the movable platform beneath the kinetic shape is actuated with a stepper motor. A schematic of this setup can be seen in Figure 4.41. The stepper motor is firmly mated to a timing belt pulley which moves a tightened kevlar timing belt. The belt loops around an idler pulley to move a platform linearly on a smooth linear bearing.
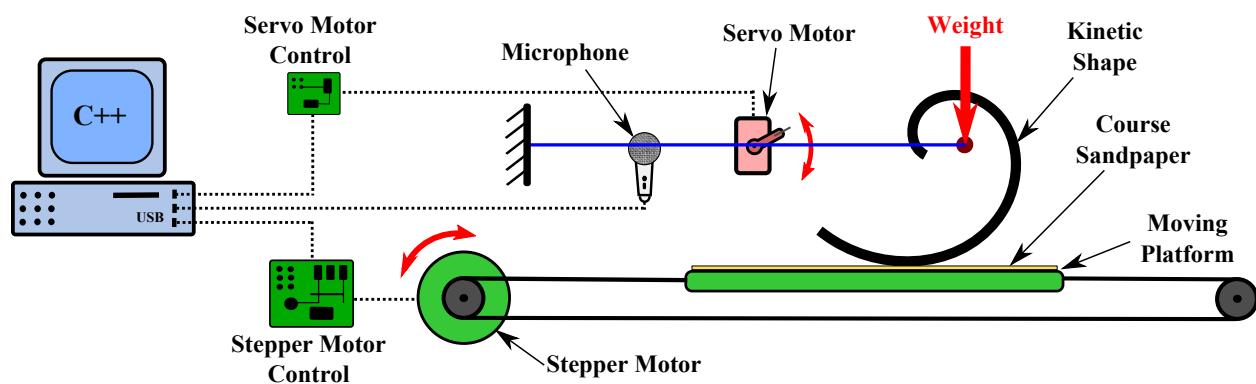
Figure 4.41: The complete schematic of the proposed string music instrument setup

| E2
(82.4 Hertz) | F2
(87.3 Hertz) | F#2
(92.5 Hertz) | G2
(98.0 Hertz) | G#2
(103.8 Hertz) | A2
(110.0 Hertz) |

| A#2
(116.5 Hertz) | B2
(123.5 Hertz) | C2
(130.8 Hertz) | C#2
(138.6 Hertz) | D3
(146.8 Hertz) |
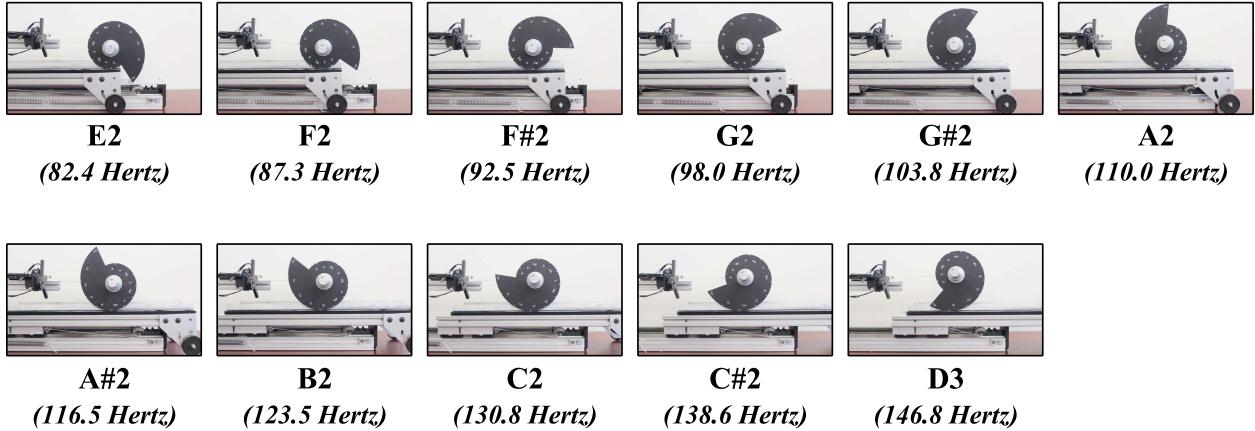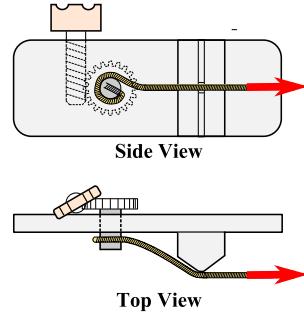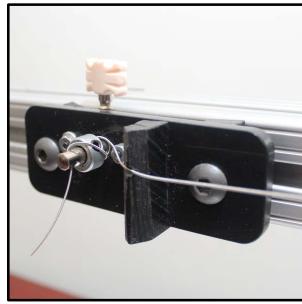
Figure 4.42: The orientation of the kinetic shape determines the string vibration frequency when the string is plucked. In this image, the weight applied to the kinetic shape axle has been removed for clarity.

The stepper motor was sized so that it can overcome the highest system torque, which is where the kinetic shape exerts the highest horizontal ground reaction force onto the movable platform ($\theta = 2\pi$ or $D\#3$). I chose a bipolar hybrid stepper motor with an $1.8°$ resolution (MotionKing® 23HS2430). However, in the final design stages I added an extension spring in-line to the movable surface to provide additional force along with the stepper motor. The stepper motor was controlled by a Phidgets® 1067 board that was interfaced with a C++ program on a personal computer via USB.
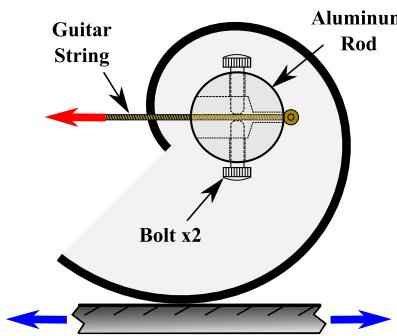
Note that even without an electric motor it is easily possible to reorient the kinetic shape with the described setup by manually sliding the movable platform beneath the kinetic shape.

4.5.2.4 Loading the Kinetic Shape

For the shape to exert proper and predicted string tension, it cannot distribute any portion of the applied weight, W, onto its support structures. Also, it must exert all ground reaction forces in the direction of the string vector. To alleviate this design constraint, two identical kinetic shapes were fabricated and positioned parallel to each other onto a $1.00in$ ($2.54cm$) aluminum rod with a fixed distance between them. Both kinetic shapes are held orthogonal with the rod, while being

(a)

(b)

Figure 4.43: On one end the string is lengthened and shortened by a machine screw (worm gear mechanism), while the other end is fed through and fixed at the center of the aluminum rod

able to spin freely around their axle via smooth ball bearings. The actual setup of the two parallel kinetic shapes can be seen in Figure 4.38.

After the string is attached, weight is applied to the shape axles by placing discrete barbell weights on the outside of the kinetic shapes. For balance, the same amount of barbell weights are carefully placed on both sides. As the kinetic shapes are attached to the aluminum rod via ball bearings, the barbells do not rotate as the kinetic shape is rotated into different positions.

4.5.2.5 Attaching, plucking, and Recording the Vibrating String

Since I was using a steel guitar string, the two ends of the taut string are attached in a very similar fashion as a conventional electric guitar. The string's peg end is attached midway between the two parallel kinetic shapes. This end is pulled through a hole in the center of the aluminum rod, while it is held at rod center by two opposing set bolts as seen in Figure 4.43b. The other

end is attached to a customized machine head (tuner, gear head) set at a fixed distance from the kinetic shape axle. The string passes over an elevated bridge, while it can be changed in length (lengthened or shortened) by the machine head for frequency calibration purposes (Figure 4.43a). Before usage, the kinetic shape was repositioned a number of times, dynamically loading and unloading the string, before the string assumed steady state length and tension.

The string is plucked by an extra light/thin nylon guitar pick ($0.44mm$), attached to a limited rotating servo motor that is held in position by an adjustable bracket. This servo motor (Phidgets$^{\circledR}$ SM-S4505B) is controlled by a Phidgets$^{\circledR}$ 1061 servo controller board that is interfaced with a C++ program on a personal computer via USB. The schematic of this setup is shown in Figure 4.41.

To verify and amplify the oscillation frequency of the string as the kinetic shape is re-oriented, a microphone is placed in close proximity along the string to record emitted sound frequencies. The utilized microphone is the Samson$^{\circledR}$ GoMic$^{\circledR}$ $16bit/44.1kHz$ condenser USB microphone with a frequency range of $20Hz$ to $18kHz$. The frequency range is well within our targeted frequency range from $77.8Hz$ to $155.6Hz$. After the string is plucked, the audio signal is recorded and a C++ program computes the fast Fourier transform (FFT) while extracting the string's fundamental oscillation frequencies in real time.

4.5.2.6   Playing a Melody

The C++ interface program was also able to be programed to reorient the kinetic shape to manually or automatically play keynote frequencies in a linear succession with a specified rhythm by taking into account the time it takes to reposition the shape. In other words, the program allowed the instrument prototype to play simple pre-programmed melodies. This prototype is only able to play linear note sequences, because only one string is plucked at one time. The instrument is also able to play vibratos by simply rocking the kinetic shape back and forth, increasing and decreasing the tension in the taut string.

String Frequency around Kinetic Shape Parimeter
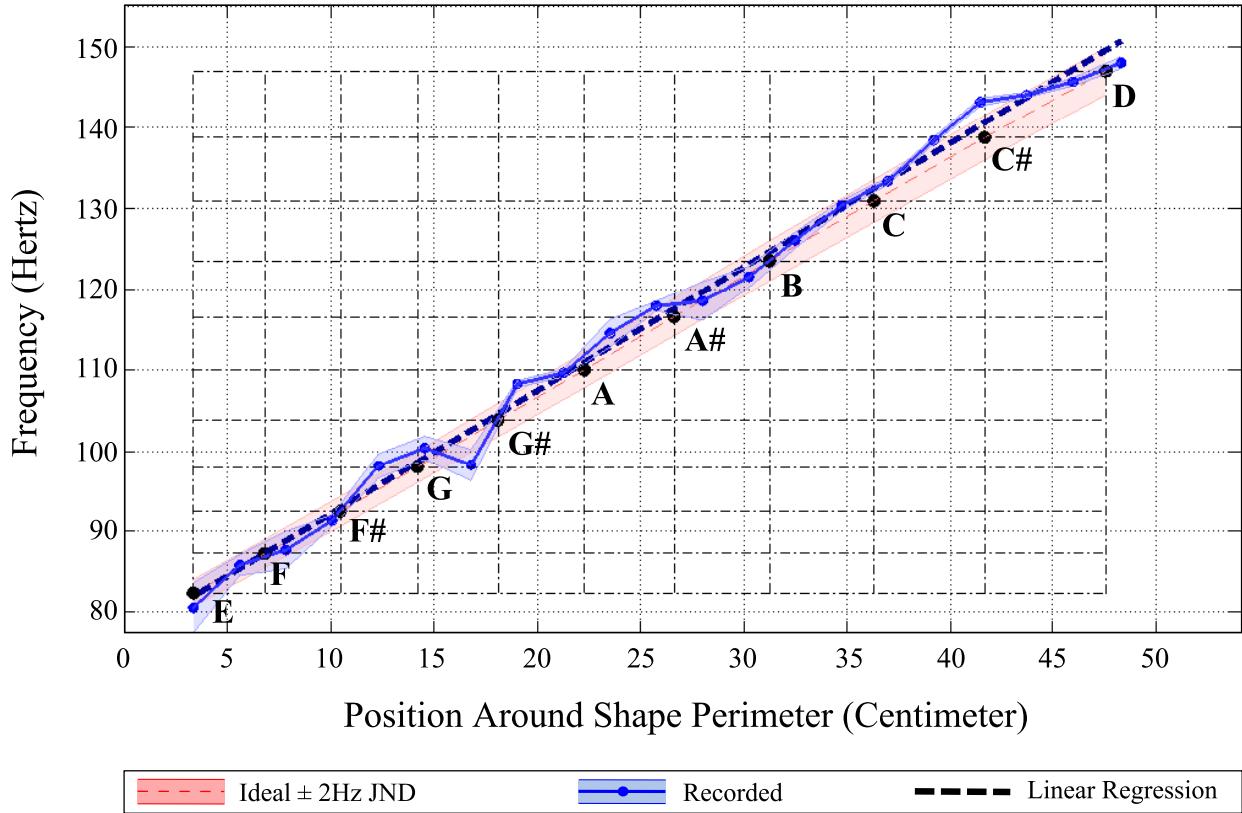
Figure 4.44: Measured and predicted string vibration frequency of the kinetic shape musical instrument. A guitar string was plucked at twenty different positions around the kinetic shape while the string vibration frequency was recorded. The shaded band is the standard deviation of all readings at that particular position.

4.5.2.7 Results and Discussion

Once our musical kinetic shape string prototype instrument was assembled and dynamically loaded, it was calibrated to known frequencies around the kinetic shape by slightly lengthening or shortening the guitar string. After calibration the shape was automatically oriented from $\theta = \pi/6$ ($E2$) to $\theta = 11\pi/6$ ($D3$) at 20 even intervals. $\theta = 0$ ($D\#2$) and $\theta = 2\pi$ ($D\#3$) were not tested due to inaccessibility (see Figure 4.40). At each step the string was plucked ten times with three seconds between plucks, while the dominant string oscillation frequency was recorded at each pluck. After ten plucks the average and standard deviation for one shape orientation was computed and the stepper motor moved the shape into the next orientation. Figure 4.44 shows the recorded frequencies as a function of positions around the kinetic shape's perimeter.

Figure 4.45: Sample songs played by the kinetic shape musical instrument. The musical kinetic shape instrument is programmed to automatically reorient the kinetic shape at even time intervals (beats) to produce two separate melodies.

As a standard we compare our recorded frequencies to expected frequencies with an offset of the human ear's just noticeable difference (JND) for pitch. JND (or differential threshold) of the ear is the smallest detectable difference in pitch that the human ear can detect. Although this JND varies depending upon frequency, sound level, and sound duration, the JND for frequencies below 500 *Hertz* is generally found to be 2 *Hertz* [107].

Despite that the recorded frequencies around the kinetic shape vary slightly from ideal, they are mostly within the JND range. That is, the average human ear could not detect the difference between ideal frequency and the frequency produced by our instrument. The jumps and variations in recorded frequencies can be accounted by imperfections in surface contact between the kinetic shapes and the movable platform and slight misalignment between the two parallel kinetic shapes.

Slight variation persisted due to possible misalignments and slippage of the kinetic shape surface. This type of slippage could possibly be alleviated by coating the movable platform with higher friction material or even gearing the kinetic shape.

Since the constructed prototype instrument is able to play melodies that include available notes $E, F, F\#, G, G\#, A, A\#, B, C, C\#$, and D, I chose two melodies that include these notes to be

played by the musical kinetic shape prototype instrument. The chosen melodies are presented in Figure 4.45. The prototype was unable to play the melodies at full original tempo due to the fact that faster movement of the kinetic shape required more power than the stepper motor could provide. Larger accelerations and decelerations also accounted for slight slippage at the contact surface between the kinetic shape and movable platform. Melodies were played at 55 *bpm*, which is roughly half of the songs' original playing tempo. More complicated and faster melodies and even chords could be produced by having two or more strings with corresponding kinetic shapes parallel to each other reoriented independently and played simultaneously. For example, as one string-shape is being played other string-shapes rotate into position for upcoming notes.

However, although the melodies were played at half tempo, the notes were precisely timed and played at the correct frequency throughout the two melodies. It is interesting to note that after a longer period of usage, the instrument had to be calibrated due to contact surface slippage, but adding a feedback controller would allow the instrument to be continuously calibrated in real time.

My pilot design embodies a string that is being plucked, but it may also be possible to have the same instrument by bowing the string in variable tension. While my kinetic shape string instrument only utilizes one revolution around a kinetic shape, it is possible to design a very similar instrument with a greater range by creating a kinetic shape with more than one revolution, or even a 3D kinetic shape that is attached to two string with two independent tensions. Although this prototype is used to generate music, the same concept can be applied to manufacture strain gages that have adjustable sensitivity. This could be done by placing the kinetic shape into a soil, concrete, or other medium such that the deformed medium applies a force onto the shape which tightens or loosens a vibrating wire such as a vibrating wire strain gage used for macro level deformation detection.

4.5.3 Kinetic Crutches and Canes

An interesting and very practical innovation I come up with is the kinetic crutch. The kinetic crutch uses the kinetic shape as a crutch tip to regulate the dynamics of crutch walking.
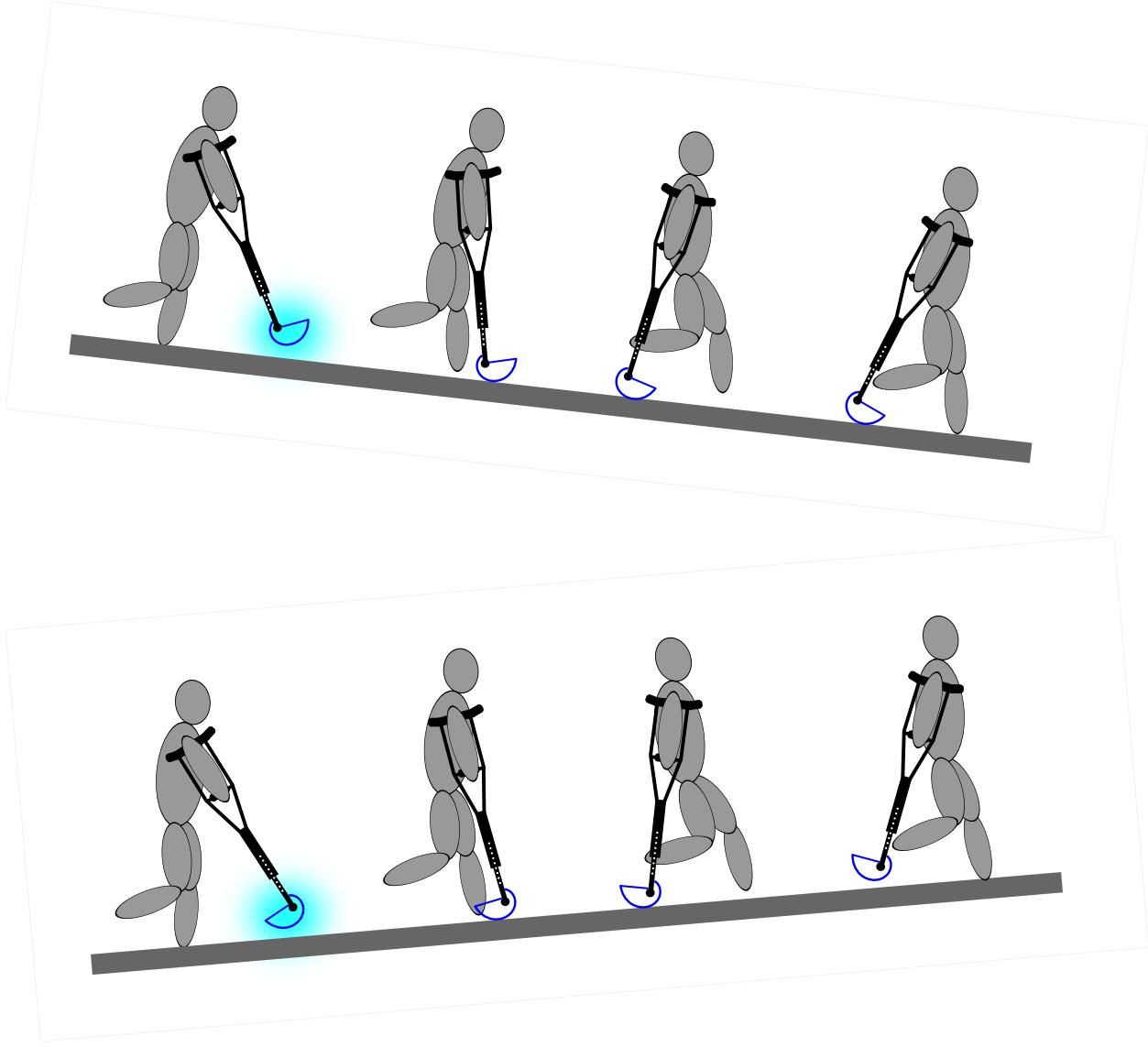
Figure 4.46: The kinetic crutch can assist a user for uphill walking or resist the user when rolling over the crutch tip and walking downhill

The crutch can either assist or resist walking depending on the kinetic shape used as the crutch tip. The concept of the kinetic crutch can be seen in Figure 4.46. If the crutch user propagates on a decline, it may be desirable to impede or slow down down the roll-over motion over the crutch tip in a more controlled fashion. This rolling impedance is created when the kinetic shape tip increases in radius in the direction of walking. However, if the user propagates up an incline, an assistive force helping the user roll over the crutch tip can be produced by a kinetic shape crutch tip which decreases in radius in the direction of walking.
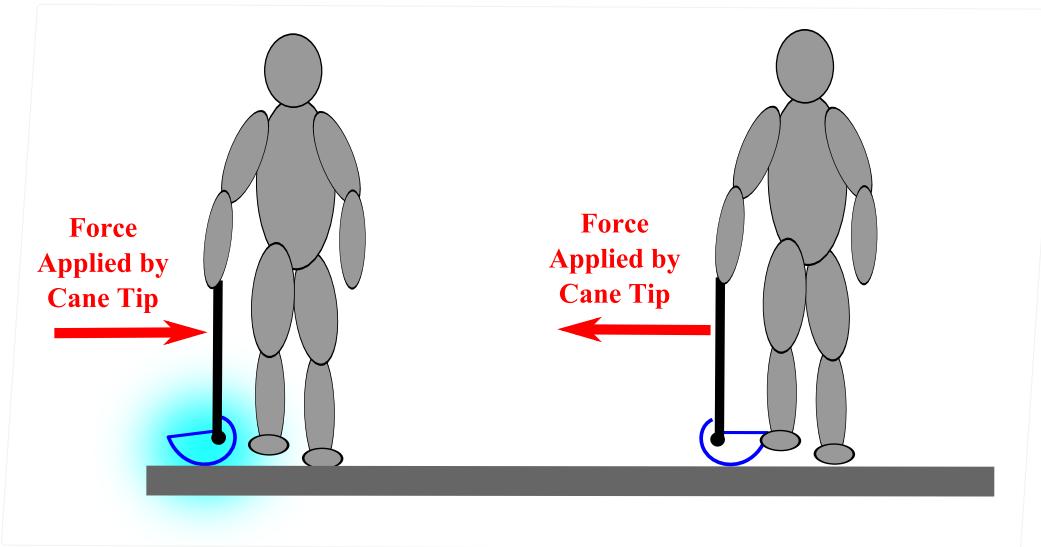
Figure 4.47: The kinetic cane tip can add customized lateral support to a person walking with a cane

As previously discussed, the application and reaction forces of the kinetic shape can be customized, hence the kinetic shape as a crutch tip may be derived such that it takes into account the crutch walking dynamics. For example, as the user plants the crutch tip onto the ground it may be desirable for the crutch to instantly roll, reducing the user's push-off by dorsiflexsion. However, during the terminal phase of the crutch rolling phase one may want to have the kinetic shape passively impede the rolling motion for a more controlled heel strike.

This concept can also be used for a cane tip for side support as shown in Figure 4.47. This cane tip lateral support force can be customized by specifying the kinetic shape used for the cane tip. As an individual using the kinetic cane supports themselves onto the cane, it may react by either reacting towards or away from the individual.

The examination of the effectiveness and efficiency of the kinetic shape crutch and cane is currently pending. However, a qualitative preliminary study of individuals walking with the kinetic crutch showed a positive and predominate consensus on the kinetic crutch's increased efficiency. When individuals compared walking with a regular point-tip crutch to walking with a kinetic crutch, they reported smoother and more efficient dynamics when walking with the kinetic crutch. Further quantitative investigation will compare the kinematics and kinetics of a regular and

Active Radius Change
by Modifying Spoke Length

Motion

Constant Radius
Neutral

Decreasing Radius
Assisting

Incrasing Radius
Resisting
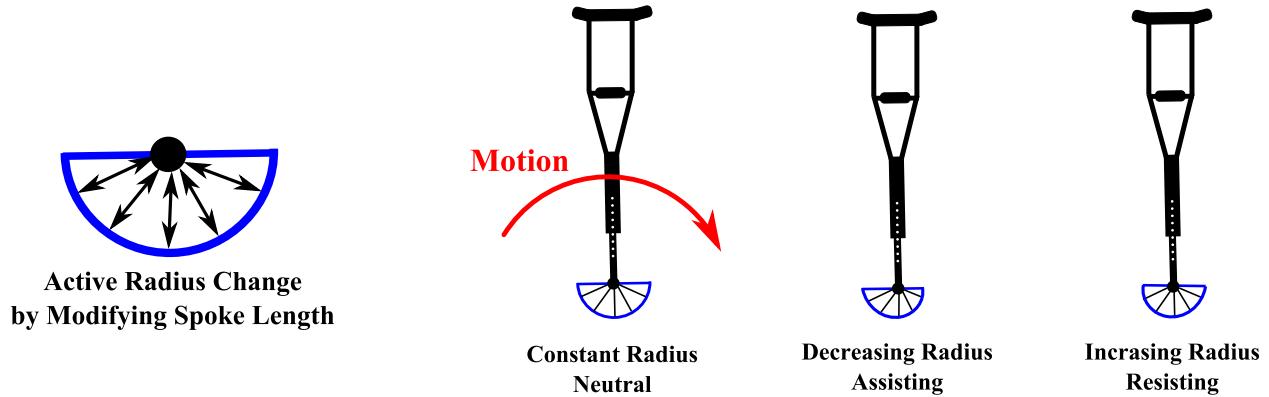
Figure 4.48: The kinetic cane tip can add customized lateral support to a person walking with a cane

kinetic crutch. Among other dynamic parameters, I will analyze the ground reaction forces, handle grip forces, angular positions, and angular velocities throughout the crutch walking cycle.

This kinetic crutch tip concept can be extended by having a kinetic shape with a controllable dimensions. That is, a shape that is able to change its form during the crutch walking as seen in Figure 4.48. This possibility allows the kinetic shape crutch tip to adapt to the walking environment in real time. For instance, as an individual with a kinetic crutch walks over uneven ground, the kinetic shape crutch may change its tip shape from assisting to resisting at every step. This control could also be made as a function of walking kinematics. That is, as the user speeds up their crutch walking, the kinetic shape tip may adapt to a form that impedes the crutch tip roll-over motion slightly more.

154

Chapter 5: Dynamic Synchronization

Human body locomotion is achieved as arms and legs that are similar in mass and mass distribution swing in sync back and forth. However, as these limbs can become dissimilar resulting in an asymmetric kinematics. These asymmetric kinematics may result by limb amputation, wearing a cast for a broken bone, or even carrying an object with one arm.

Kinematic synchronization of dissimilar systems such as human limbs is the matching of motion between two moving systems. The synchronization of any two rotating systems can be as simple as placing a joining spring or damper between the systems or may require sophisticated controllers. In this chapter, I focus on the question of how two *dissimilar* rotating systems can be synchronized *without* coupling the systems. This passive kinematic matching technique that I have developed allows two separate systems to generate the same rotating motion without any system coupling or mediating control law. To validate this method, this synchronization technique is applied to two open-ended rotating kinematic chains: single- and double- link pendulums with different masses and mass distributions. Even though double-link pendulums are nonlinear systems that are sensitive to changes in parameters, my matching technique enables the same generated motion on dissimilar double-link pendulums.

The practical application of such a passive matching technique is the flexibility in mechanical design as one is able to describe the same kinematics with a variety of parameters (i.e., masses and mass distributions). In essence, one can decouple the mass and the first and second moments of inertia so systems with dissimilar masses and mass distributions will have the same kinematics. For example, the motion of a double-link pendulum modeled as two links with one mass per link can only be described by one unique combination of masses and mass locations along the links. However, having two masses per link allows the kinematics to be described with

155

an infinite number of distinct systems that all have the same motion. In fact, the minimum number of masses per rotating link to describe any arbitrary rotational kinematics is two masses, yet many models only include one mass. Using only one mass per link inherently couples the moments of inertia so that any change in the location of the mass necessarily affects both the first and second moments of inertia.

My matching technique can also be used to simplify complicated kinematics problems that yield identical results. For example, the rotation of a fan blade can be represented with two masses distributed as specified using this method instead of finding detailed masses, mass distributions, or moments of inertias of the continuous system. In turn, using this matching technique, it is possible to design a second completely different rotating system that moves identically. Such a method can be useful in the simplification of a kinematic system model, in the manipulation of human or robotic limb movement, and in prosthesis design. The only requirements for my passive kinematic synchronization method are:

1. *The matched rotating system have to have the same numer of degrees of freedom.*

2. *The matched rotating system have to have the same kinematic initial conditions.*

3. *The matched rotating system have to have identical torques applied to the system, that is, applied or non-conservative torques.*

These same requirements are also needed to cause two identical systems to have the same motion.

I will present two examples providing proof and application of this passive matching method by mathematically and experimentally analyzing three dissimilar one-degree-of-freedom systems and also two dissimilar two-degree-of-freedom systems.

5.1 The General Rotating System Model

In this section I will outline the equations used to derive the kinematics of a two-dimensional general rotating system while drawing out a method to synchronize two or more dissimilar rotating systems with the same degrees of freedom, initial conditions, and torque input.

5.1.1 Equations of Motion

I will begin by deriving a general rotating system with *ň degrees of freedom* and *m̌ masses per degree of freedom.* Note that *m* symbolizes each individual mass whereas *m̌* symbolizes the *total number* of masses. This generalized model is shown in Figure 5.1a, and can be described using Lagrangian mechanics where the Lagrangian is defined as the difference of kinetic and

(a)

(b)
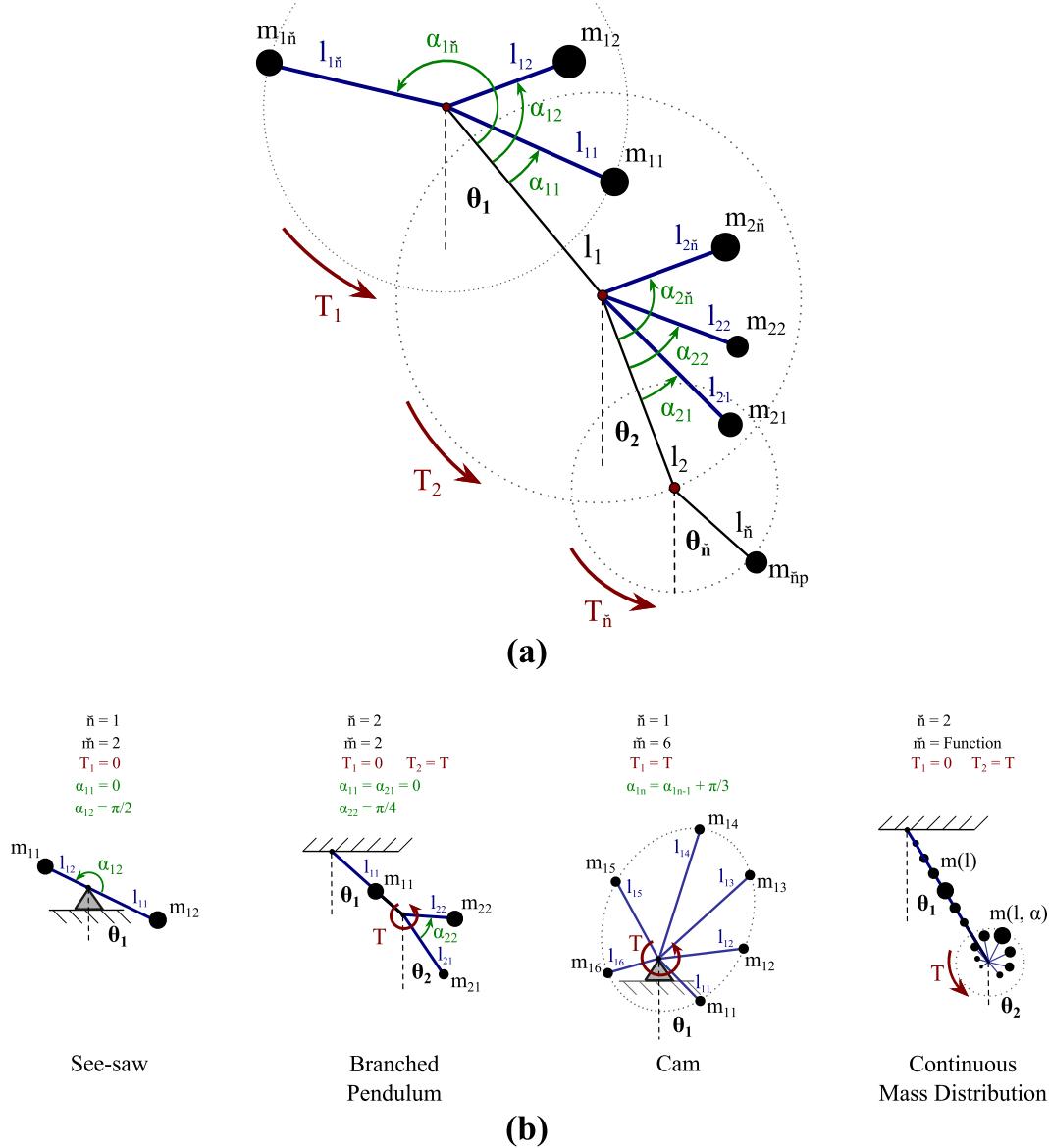
Figure 5.1: The general rotating system model. (a) General Rotating System Model. (b) The general rotating systems model can be adjusted to represent various configurations for rotating systems. These configurations can represent a sea-saw/rotor, double pendulum, cam, or a continuous mass distribution along rotating members.

potential energy.

$$L(\theta, \dot{\theta}, t) = K(\theta, \dot{\theta}, t) - U(\theta, t) \tag{5.1}$$

To find the equation of motion, the Euler-Lagrange expression is applied.

$$\frac{d}{dt}\left(\frac{\partial L(\theta, \dot{\theta}, t)}{\partial \dot{\theta}_{1,2...\check{n}}}\right) = \frac{\partial L(\theta, \dot{\theta}, t)}{\partial \theta_{1,2...\check{n}}} \tag{5.2}$$

Equation (5.2) produces $\check{n}$ equations. After differentiating and collecting coefficients, the equations of motion of this general dynamic system is a set of first order nonlinear ordinary differential equations.

$$[M]\ddot{\Theta} + [N]\dot{\Theta}^2 + [G] = [T] \tag{5.3}$$

Here, the coefficient matrices [M], [N], and [G] are given in following Equations (5.4), (5.7), and (5.8), respectively. [M] is the inertia matrix coefficient dependent, [N] is the velocity matrix coefficient, [G] is the position/gravity coeffecient matrix, and [T] can represent any applied or non-conservative torque applied to the system.

$$[M]_{\text{sym}}^{\check{n},\check{n}} = \begin{bmatrix} M_{1,1} & M_{1,2}\cos(\theta_1 - \theta_2) & \cdots & M_{1,j}\cos(\theta_1 - \theta_j) \\ M_{1,2}\cos(\theta_1 - \theta_2) & M_{2,2} & & \vdots \\ \vdots & & \ddots & M_{i-1,j}\cos(\theta_{i-1} - \theta_j) \\ M_{1,j}\cos(\theta_1 - \theta_j) & \cdots & & M_{i,i} \end{bmatrix} \tag{5.4}$$

Here, each of the coefficients on the diagonal are given by Equation 5.5.

$$M_{i,i} = \sum_{p=1}^{\check{m}} l_{i,p}^2 m_{i,p} + l_i^2 \sum_{q=i+1}^{\check{n}} \sum_{p=1}^{\check{m}} m_{q,p} \tag{5.5}$$

The remaining non-diagonal coefficients in matrix [M] are given by Equation 5.6.

$$M_{i,j} = l_i \left[\sum_{p=1}^{\check{m}} l_{j,p} m_{j,p} + l_j \sum_{q=j+1}^{\check{n}} \sum_{p=1}^{\check{m}} m_{q,p} \right] \tag{5.6}$$

$$[N]^{\check{n},\check{n}} = \begin{bmatrix} 0 & M_{1,2}\sin(\theta_1 - \theta_2) & \cdots & M_{1,j}\sin(\theta_1 - \theta_j) \\ -M_{1,2}\sin(\theta_1 - \theta_2) & 0 & & \vdots \\ \vdots & & \ddots & M_{i-1,j}\sin(\theta_{i-1} - \theta_j) \\ -M_{1,j}\sin(\theta_1 - \theta_j) & \cdots & & 0 \end{bmatrix} \tag{5.7}$$

$$[G]^{\check{n}} = \begin{bmatrix} \sum_{p=1}^{\check{m}} l_{1,p} m_{1,p} sin(\alpha_{1,p} + \theta_1) + (l_1 \sum_{q=2}^{\check{n}} \sum_{p=1}^{\check{m}} m_{q,p})\, sin(\theta_1) \\ \vdots \\ \sum_{p=1}^{\check{m}} l_{i,p} m_{i,p} sin(\alpha_{i,p} + \theta_i) + (l_i \sum_{q=i+1}^{\check{n}} \sum_{p=1}^{\check{m}} m_{q,p})\, sin(\theta_i) \\ \vdots \\ \sum_{p=1}^{\check{m}} l_{\check{n},p} m_{\check{n},p} sin(\theta_{\check{n},p} + \theta_{\check{n}}) \end{bmatrix} g \tag{5.8}$$

These are the coefficient matrices for the equations of motion of a general rotating system model with $\check{n}$ degrees of freedom and $\check{m}$ masses per degree of freedom distributed a distance l from each rotational joint. The [M] matrix is a symmetric matrix, while the [N] matrix is a negatively mirrored matrix with a zero diagonal. Note that the coefficients [Equations (5.5) and (5.6)] are all unique matrix components in the $[N]$ matrix that all appear in the $[M]$ matrix. Also note that the last row of $[G]$ $(i = \check{n})$ is different since there are no masses from links further down the chain. Matrix indexes are i rows and j columns. *Kinematically matched coefficients (KMC)*, discussed in the forthcoming section, are highlighted in *green*. Masses, m, and mass distributions, l are shown in Figure 5.1a.

Equation (5.3) can model any degree of rotating system or rotating system links. Degrees of freedom (links), mass, and mass distribution within each link can be easily modified to create models for such systems as shown in Figure 5.1b. These modified models can, but are not exclusive to, represent rotors, pendulums, cams, or rotating kinematic systems and open kinematic chains.

5.1.2 Kinematically Matched Coefficients

Given the same torque input and initial conditions, two or more arbitrary systems with the same degrees of freedom will exactly match *if* all four coefficient matrices, $[M]$, $[N]$, $[G]$, $[T]$ in Equation (5.3) are matched between two or more systems. *Since only the total values of the coefficients determine the behavior of the systems, the masses and mass distribution do not have to match between them.* This allows for two or more systems with dissimilar mass and mass distribution parameters to behave kinematically identical. For instance, assuming identical torque input (same $[T]$) and initial conditions, a swinging single link pendulum with one mass can be designed to swing identically to another single link pendulum of two or more masses. Note that this concept allows for the first and second moments of inertia to be decoupled and greater design flexibility is obtained.

I will call all the unique terms that appear in the coefficient matrices that have to be matched between matched systems *kinematically matched coefficients (KMC)*. The number of KMCs that have to be matched between kinematically synchronized systems is given in Table 5.1.

Table 5.1: Number of Kinematically Matched Coefficients For Synchronized Uncoupled Motion Between Two or More Systems

DOF ($\check{n}$)	Number of KMCs
1	2
2	5
3	9
$\vdots$	$\vdots$
$\check{n}$	$KMC_{\check{n}-1} + (\check{n}+1)$
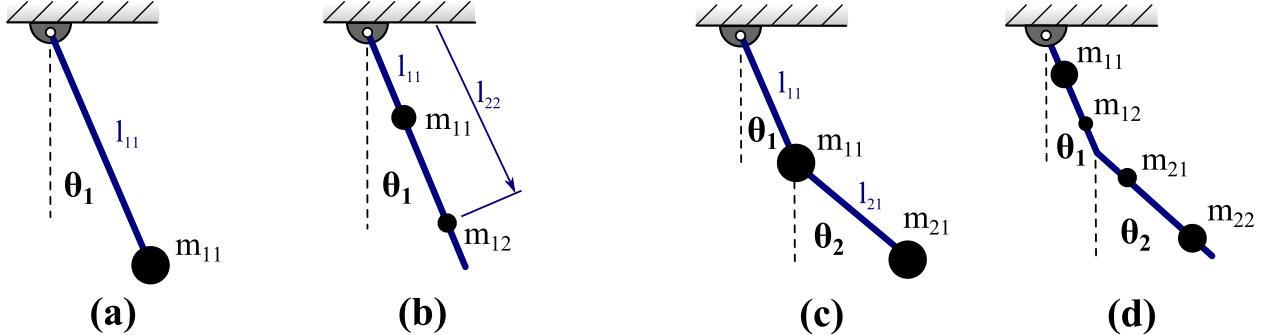
Figure 5.2: Single and double link pendulum used for experimentation. (a) and (b) are the dissimilar single link pendulums used in the first example experiment, while (c) and (d) were used experimentally in the second example.

Equation 5.3 does not include any nonconservative forces (e.g., friction), however if added, it would be included into the $[T]$ coefficient matrix which would similarly need to be matched between systems in order to produce matching kinematics. Coefficient [T] on the right side of Equation 5.3 can include any torque created by actuators, breaks, dampers, or any other source of linear or non-linear torque that is a function of angular position, angular velocity, or angular acceleration. This additional matrix, $[T]$, that can potentially be matched from applied torques has intentionally been excluded since it can represent any type of applied torque which includes anything form simple applied motor torque to complex non-linear friction models.

In the forthcoming sections, I will present two examples of this matching technique for one and two degree-of-freedom systems with experimental validation.

5.2   Example 1: Passive Single Link Pendulum

In Section 5.1, a general method for compound systems was derived which allows two or more dissimilar rotating systems to be kinematically matched. In this section I will utilize this method and experimentally demonstrate its validity. I will start with an experiment by synchronizing the kinematics of three simplified versions of my general model, which are all passive single
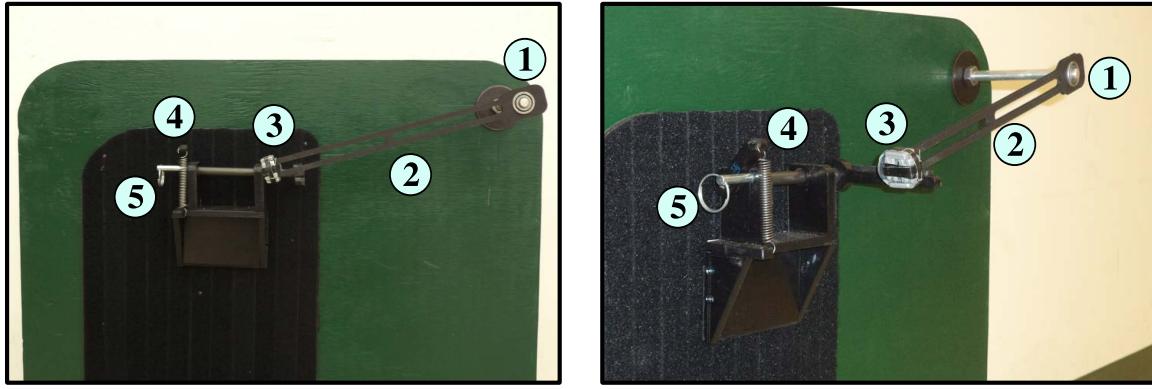
Figure 5.3: Release mechanism used for all pendulum measurements. (1) Ball Bearing (2) Rigid Foam Link (3) Lead Weights (4) Extension Spring (5) Release Pin

link pendulums (shown in Figures 5.2a and 5.2b). One of the experimental pendulums has one mass and the remaining two have two masses per link. Although more masses could be utilized to match the motion of this single link pendulum, two masses are sufficient to describe any number of masses and mass distributions. The parameters of these three dissimilar single link pendulums are shown in Table 5.2. Since a single link pendulum is one degree of freedom, only two KMCs had to be matched between systems ($M_{1,1}$=33,600 g-cm^2 and G_1=1,260 g-cm).

Table 5.2: Single Pendulum (ň=1) System Synchronization Coefficient Equations and Experimental Parameters

	Coefficient Index	System 1 (m̌=1)	System 2 (m̌=2)	System 3 (m̌=2)
KMCs	$M_{1,1}$	$m_{11}l_{11}^2$	$m_{11}l_{11}^2 + m_{12}l_{12}^2$	
	G_1	$m_{11}l_{11}$	$m_{11}l_{11} + m_{12}l_{12}$	
Masses (g)		$m_{11} = 47.3$	$m_{11} = 35.0$ $m_{12} = 21.0$	$m_{11} = 49.0$ $m_{12} = 31.8$
Lengths (cm)		$l_{11} = 26.7$	$l_{11} = 15.0$ $l_{12} = 35.0$	$l_{11} = 5.0$ $l_{12} = 31.9$
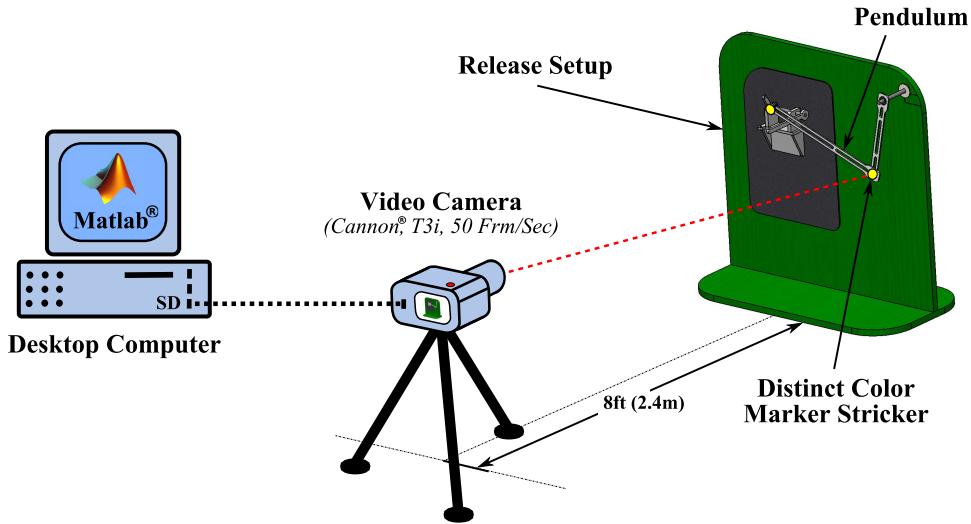
Figure 5.4: Setup used to measure pendulum dynamics

5.2.1 Experiment Description

The three dissimilar single link pendulum systems were constructed from rigid foam board that was light (0.039oz (1.125g) per link) relative to the pendulum masses. Mass and mass distributions were calculated using KMCs. Lead weights were used as pendulum masses and attached to the link at appropriate positions. The mass values listed in Table 5.2 were rounded to whole grams for the experimental pendulums. To ensure precise link dimensions, each pendulum was cut with a 60W laser cutter (Universal® Laser Systems VLS4.60).

The links were attached to a short and rigid 0.375in (0.953cm) aluminum rod using a precision steel ball bearing to reduce friction. To minimize variability due to friction (negative torque), the exact same bearing was used for each system. Each pendulum system was dropped from the same initial position with an adjustable spring loaded release mechanism. This complete setup can be seen in Figure 5.3.

To measure the rotational motion of the pendulums, the pendulums had a distinct color marker sticker attached to the end of the link. The pendulums were video recorded at separate times at 50 frames/second (50 Hertz) with a Canon® T3i with a Canon® EF 50mm f/1.8 II lens. Link angular position was interpreted with Matlab®, which I used to read the video file and identify each link's distinct color sticker while in motion. A fast Fourier transfer (FFT) was applied to

163
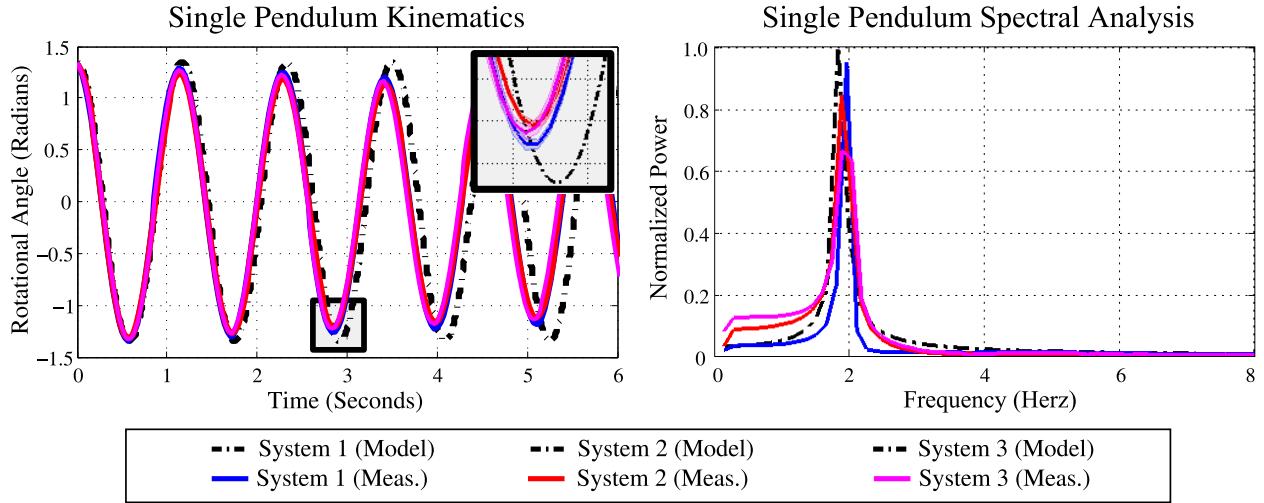
Figure 5.5: Single pendulum (ň=1) model and experimental rotational link position and spectral analysis

convert the link angular position from the time to frequency domain. The complete recording setup is shown in Figure 5.4.

5.2.2 Example 1 Results

Five videos of each of the three pendulums were recorded (15 total). The recorded angular position was averaged and filtered using a low pass 2nd order Butterworth filter at 6 Hz. This angular position data is presented in Figure 5.5 and compared with ideal predicted model behavior. Modeled systems have the same masses and mass distribution as measured systems. As predicted, all three ideal modeled systems have the same temporal kinematics and overlap in Figure 5.5. Spectral analysis shows the same frequency peak between all measured systems, while all three modeled systems peaked 0.06 Hz below the measured system peaks.

While the recorded systems were affected by nonconservative forces, such as air resistance and friction, all three dissimilar pendulums matched kinematically. Their slight difference in amplitude can be explained by the variable mass and mass distribution in the pendulums that leads to variable weight and centripetal forces on the bearing which in turn increases friction. Similarly, the effect of the friction torque is affected by the inertia of the system. Although the kinematics are matched, the kinetics in these dissimilar systems does not match; the different masses will

164

generate different forces. Despite these small effects, all three physically dissimilar pendulums had a frequency of $0.88 \pm 0.04\,\mathrm{Hz}$.

When comparing the collected and model data, the effects of damping become distinct. As a result, the amplitude and period decrease over time for the actual systems as shown in Figure 5.5. As previously explained, the model derivation did not include a damping coefficient, thus its effects on motion was not predicted. However, damping could have been accounted for by including the matrix coefficent $[T]$ shown in Equation 5.3. Despite this difference, the model and all three physically dissimilar pendulums had very similar motion.

5.3   Example 2: Passive Double (Two-Link) Pendulum

I will further investigate my kinematic matching technique by showing how to synchronize two dissimilar two degree-of-freedom systems (passive double pendulums). The double pendulum model is depicted in Figure 5.2c and 5.2d and KMCs are shown in Table 5.3.

Traditionally the double pendulum is modeled in Figure 5.2c, however this model is impractical from a design perspective considering that the pivot point between the upper and lower link is exactly where the mass is placed and the link is massless. Hence, for my comparison, I will add design flexibility and utilize two masses per link.

5.3.1   Experiment Description

Two double pendulums were created using the same fabrication technique and material as the single pendulum experiment in Section 5.2. An additional small ball bearing was placed at the pivot point between the upper and lower link with a 0.25in (6.25mm) wooden pin. Both small bearing and wooden pin had a combined weight less than 0.07oz (2g).

The links were attached to the same aluminum rod, ball bearing, and were released with the same release mechanism shown in Figure 5.3, while the complete recording setup is shown in Figure 5.4. Specific distinct colored stickers were placed on the end of each link to track their angular positions. The double pendulum nonlinear kinematics were recorded at rate of 50

Table 5.3: Double Pendulum (ň=2) Synchronization Coefficient Equations and Experimental Parameters

	Coefficient Index	System 1 (m̌=2)	System 2 (m̌=2)
KMCs	$M_{1,1}$	$l_{11}^2 m_{11} + l_{12}^2 m_{12} + l_1^2 (m_{21} + m_{22})$	
	$M_{1,2}$	$l_1 (l_{21} m_{21} + l_{22} m_{22})$	
	$M_{2,2}$	$l_{21}^2 m_{21} + l_{22}^2 m_{22}$	
	G_1	$l_{11} m_{11} + l_{12} m_{12} + l_1 (m_{21} + m_{22})$	
	G_2	$l_{21} m_{21} + l_{22} m_{22}$	
Masses (g)		$m_{11} = 35.0$	$m_{11} = 52.6$
		$m_{12} = 35.0$	$m_{12} = 29.1$
		$m_{21} = 14.0$	$m_{21} = 23.0$
		$m_{22} = 35.0$	$m_{22} = 28.0$
Lengths (cm)		$l_1 = 20.0$	$l_1 = 20.0$
		$l_{11} = 7.0$	$l_{11} = 5.0$
		$l_{12} = 14.0$	$l_{12} = 15.0$
		$l_{21} = 10.0$	$l_{21} = 12.4$
		$l_{22} = 30.0$	$l_{22} = 32.4$

frames/second (50 Hertz) with a Canon® T3i with a Canon® EF 50mm f/1.8 II lens. The angular position was again converted to the frequency domain using a fast Fourier transfer (FFT).

5.3.2   Example 2 Results

As before, each pendulum's angular kinematics were recorded five times (10 total), averaged, and filtered with a 2nd order Butterworth filter at 6 Hz. The results of these angular positions are illustrated in Figure 5.6 and compared with the ideal predicted systems.

The motion for both link 1 (upper link) and link 2 (lower link) was in agreement with model conditions through around 4 seconds, but were in good agreement between experimental measurements throughout the whole trial, which was 12 seconds. This movement of the two dissimilar systems can be seen in Figure 5.7 and in the accompanying video. All collected data deviates less for link 1 than link 2, which can be explained by the non-linear movement of the lower link and also because of more variability due to friction in the additional middle pivot. In
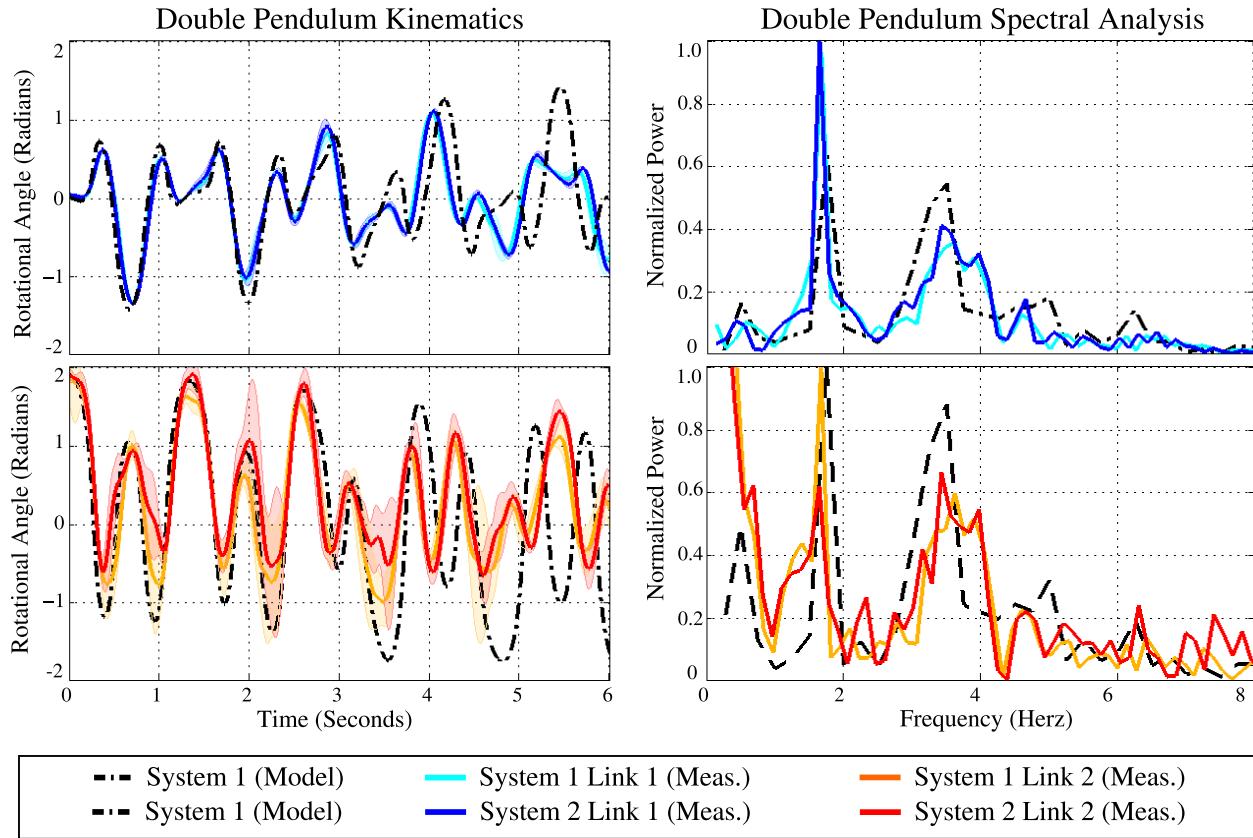
Figure 5.6: Double pendulum (ň=2) model and experimental rotational link position and spectral analysis
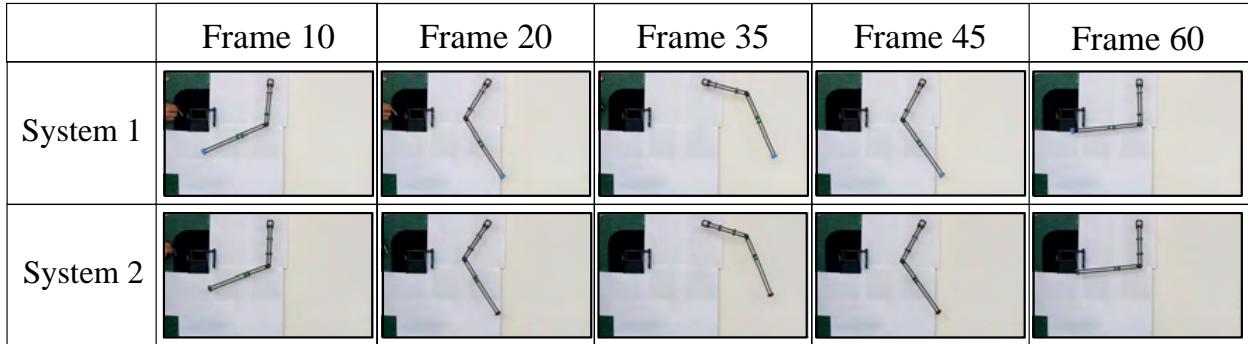
Figure 5.7: Two dissimilar double pendulums (ň=2) move in synchronization as they are released with identical initial conditions

summary, I have demonstrated two dissimilar non-linear systems that have the same motion by kinematically matching the two systems.

5.4 Practical Application

The preceding sections presented the derivation and validation of the kinematic synchronization technique. In this section I will discuss how to apply this matching technique in practice, after which I am going to discuss some possible applications of this passive synchronization method.

5.4.1 Application Steps

In practice, to apply this kinematic matching technique one would first model the rotating systems to be matched in the form shown in Figure 5.1. That is, the rotating systems have to be modeled with lumped masses distributed on the rotating member. For example, if modeling a swinging human arm, one could model it as a swinging pendulum, representing mass distribution (muscle, bone, tissue, etc.) as lumped mass parameters distributed at specified locations along the swinging limb. These limb parameters can be measured or found in limb parameter research literature. If one is to model and match two helicopter blades, the blades would be represented as swinging systems with lumped mass parameters. Again, note that these two systems to be matched have to have equal degrees of freedom (joints), initial conditions (initial angle, angular velocity, etc.), and applied torque (motor, friction, etc.).

Masses and mass distribution may also be approximated by finding the mass moment of inertia of the swinging member. This moment of inertia may be represented as one single mass rotating at some radius from the rotation joint. For instance, in a single degree of freedom system, this approximation is described by Equation 5.9.

$$J_1 = m_{11} l_{11}^2 \tag{5.9}$$

Here the J_1 is the polar mass moment of inertia of the rotating link, m_{11} is the approximated mass a perpendicular distance, l_{11}, from the rotation joint. Returning to the previously mentioned example of a swinging arm, one could calculate or look up/reference a polar mass moment of inertia of the

rotating/swinging arm. After that a mass, m_{11} and a distance, l_{11} from the rotation joint (shoulder socket) are found that produces the value of the polar mass moment of inertia, J_1. This swinging arm would be the exact same model as my first example in Section 5.2, which could be matched to another swinging link with a dissimilar swinging single degree of freedom system.

Next, one would match KMCs between both systems. KMCs are highlighted in Equation 5.3. For example, a two degree of freedom system, the values of 5 KMCs have to be matched between systems. To match these values, masses can be added, subtracted, or even moved along the rotating member. For my swinging arm example, two rotating/swinging human arms may be matched by adding weight, subtracting weight, or even moving weight up or down the arm.

5.4.2 Kinematic System Simplification Technique

I have shown that given the same degrees of freedom and torque input, two dissimilar rotating systems can be motion matched. A minimum of two masses per degree of freedom are required to mimic the motion of a matching system. In essence, this kinematic matching technique can be used to simplify a complicated rotating system. For example, a rotating fan blade, gear, or cam of arbitrary shape can be modeled as one link with two masses, while an open ended chain with any number of links can be modeled as two masses per link. This can greatly simplify computation resulting in the same kinematics.

5.4.3 Gait Pattern Passive Manipulation

In humans [53, 71, 76], animals [50], and some insects [137], the limbs can be modeled as swinging pendulums that swing in accordance to their masses and mass distribution. It is possible to manipulate limb movements by simply changing mass and mass distributions such as adding mass to a specific location of the limb. For example, a gait asymmetry (walking limp) can be created in an individual by attaching an extra weight to one leg [76], while in contrast a symmetric gait can be restored from an asymmetric walking pattern by adding weight to a specific location [54]. With my generalized kinematic matching technique, it is possible match two

169

swinging limbs, such as human legs, so they move symmetrically, but out $180°$ out of phase. While walking kinematics are the most obvious application, other parts of the body can be synchronized such as swinging arms during walking or moving fingers while playing an instrument or typing on a keyboard. This technique can also be used for the kinematic behavior prediction of swinging robotic limbs [50, 56].

5.4.4 Prosthetics

Wearing a prosthesis that does not have the exact size and weight of the missing limb can create gait asymmetries [86]. Prosthetics research commonly tries to mimic the lost limb in regards to size, weight, and length; however this design constraint can often times seem unrealistic and over-constraining. Using a numerical passive dynamic walker model, Sushko et. al [195] showed that this design constraint can be alleviated by changing left and right limb mass and mass distribution parameters to obtain symmetric gait with asymmetric limb parameters. As previously stated the presented kinematic matching technique can analytically match two limbs with symmetric limb mass and mass distribution parameters. That is, it is possible to apply this technique to match the healthy limb with the other limb with a prosthetic by adding masses to one or both limbs, yielding a symmetric gait.

5.5 Kinematic Synchronization with Collision Events

As this generalized kinematic synchronization technique works well with freely dissimilar and rotating systems, it breaks down as the systems independently and simultaneously encounter an inelastic collision or other external impulses. Because the two systems are inherently dissimilar in mass and mass distribution, a sudden impact will effect the matched systems differently.

Figure 5.8 shows two kinematically synchronized single-link pendulums as they swing before and after a sudden impact applied at the same instant. As seen, the two systems move identically before the collision, however since the two systems are different, they react with different
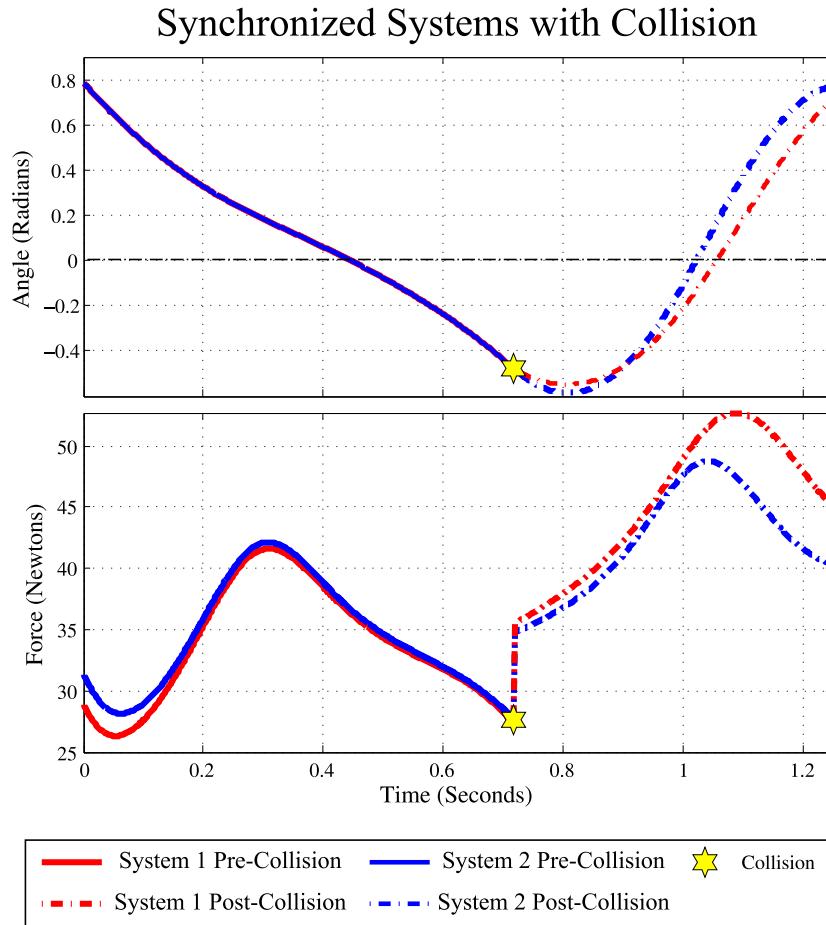
Figure 5.8: Two dissimilar and synchronized single pendulums before and after an external inelastic collision

forces at the pivot point. After the collision, the two rotating systems kinematically differ, while the kinetic differ even more than before the collision.

Hence, the kinematic passive synchronization technique for dissimilar rotating and open-ended systems which I have devloped in this chapter, becomes invalid if confronted with a applied force impulse. However, as I have derived the generalized kinematics synchronization equations, it would also be possible to perform a similar task with the conservation of angular momentum equations, yielding so-called kinetically matching coefficients that could be used in conjunction with the presented kinematically matching coefficients for total dynamic synchronization of rotating systems.

Chapter 6: Passive Dynamic Walking

As previously described in the Background Section 2.3, a passive dynamic walker (PDW) is an entirely mechanical device that is able to exhibit a steady and stable gait down an inclined slope purely due to gravitational forces and no other energy input. The energy gained by its progression down a slope due to gravity is lost during two inelastic collision events such as knee strick (knee lock) or heel strike, hence it is completly passive.

An attractive aspect of a PDW to the field of gait analysis is that it allows us to separate the purely mechanical attributes of walking from the cognitive controls of the human body. This characteristic is advantageous when it is desired only to study the physical parameters of human gait. A dynamically stable passive model is more realistic of the natural human gait dynamics and can predict the motions from altered dynamics. It is precisely for this reason I am presenting an advanced PDW model.

In this chapter, I will derive the kinematics and kinetics of a asymmetric point foot and variable curved foot two dimensional PDW model able to steadily walk down a ramp, while also being able to walk down a tied- or split-belt treadmill. That is, my derived PDW model is able to be manipulated to simulate and approximate the dynamics of various gait asymmetries, such as hemiplegia, limb length discrepancy, or limb mass discrepancy. This model is also able to simulate various roll-over shapes (ROS) that are not constant radius. Asymmetric non-constant feet have never been simulated nor studies using PDWs, while very few studies exist that have addressed this subject. With these options my model offers to be an excellent tool in the kinematic and kinetic approximation and analysis of pathological gait patterns and the Gait Enhancing Mobile Shoe (GEMS).

6.1 PDW Model Derivation

In the forgoing sections I will derive the computational model for the point-foot and variable curve-foot, 2-link (compass gait) and 3-link PDWs. It is important to understand that the 3-link PDW consists of a 3-link phase prior to knee lock (knee strike), and a 2-link phase after knee lock. During this transition the PDW switches its dynamics from a inverted triple link pendulum (3-link) to a inverted double link pendulum (2-link). The 2-link PDW model is included in the 3-link PDW model. This is true for the point-foot model and the variable curve-foot model.

It is important for me to mention that I will be explaining my derivation of the PDW in vast detail that can be interpreted by person's outside and unfamiliar with PDWs. My detailed elaboration of the derivation of my PDW computational model stems from the fact that currently and throughout the development of this model, I am not and was not aware of a clear and practical PDW model description.

Derivation schematics for all point-foot and curve-foot models can be found in Appendix E.

6.1.1 PDW Algorithm Operational Process

The computational algorithm for my PDW model is shown in Figure 6.1. The model alternates between the left stance phase and the right stance phase. The masses and mass distribution relative to ground contact can be different between the left and right stance phase. As the PDW model parameters and initial conditions are defined, my PDW program starts computing the left stance phase kinematics. The kinematics are in turn used to compute the PDW ground reaction forces (kinetics). The program loops the kinematics until a collision event occurs. This collision event may be a knee strike, in which case the program goes into 2-link PDW dynamics, or the collision event may be a heel strike, in which case the program switches from the left-stance phase to the right stance phase. This operational order is repeated for the right stance side, while the entire process is repeated until a total amount of steps is reached or the PDW becomes unstable.
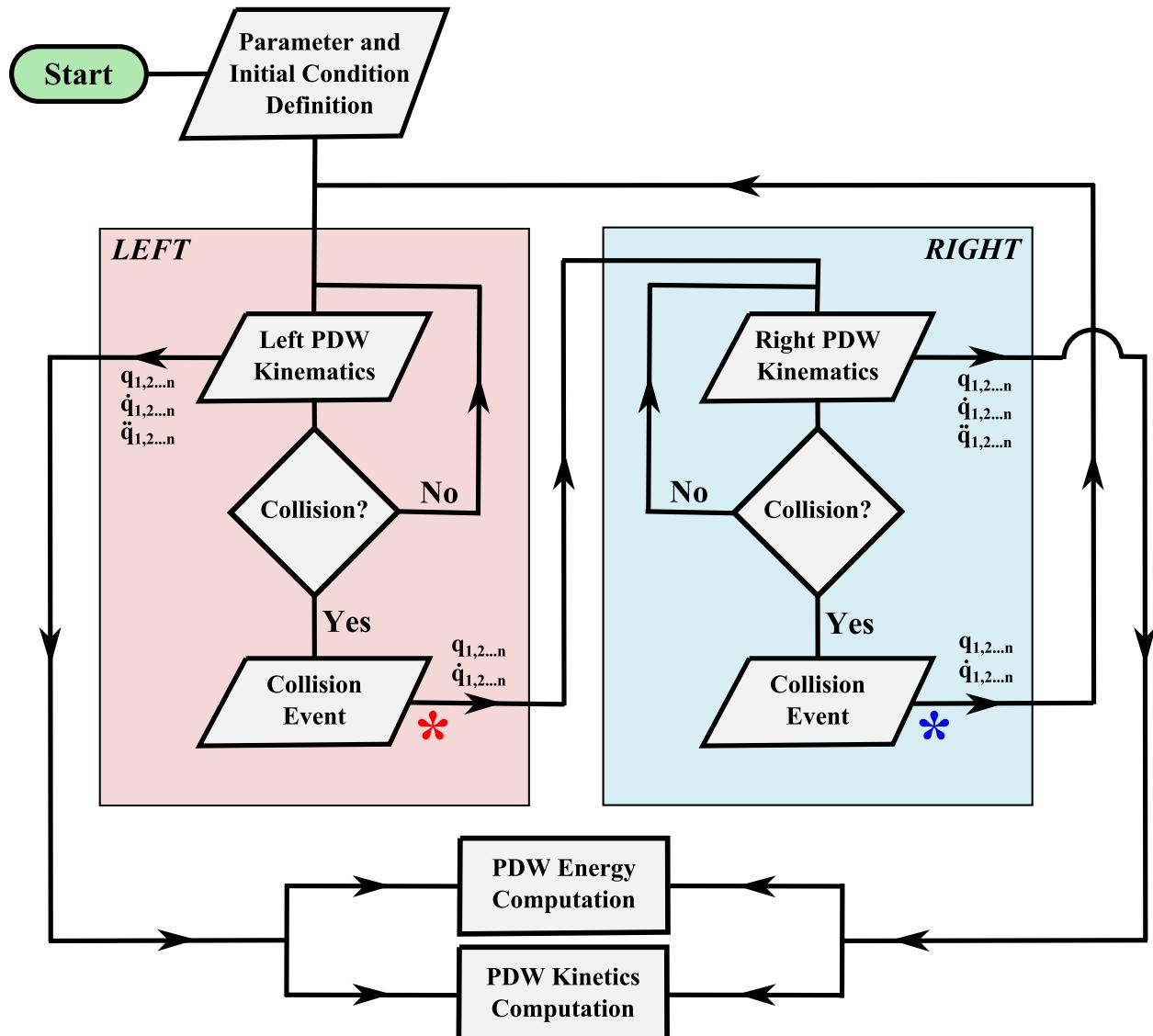
Figure 6.1: Passive dynamic walker operational process for an asymmetric walker

Stability for the PDW is judged by the number of steps it takes. A PDW with a fully stable gait completes a total of fifty strides without falling onto the ramp. In other words, a PDW configuration was measured a success if it was able to walk fifty strides (left + right step).
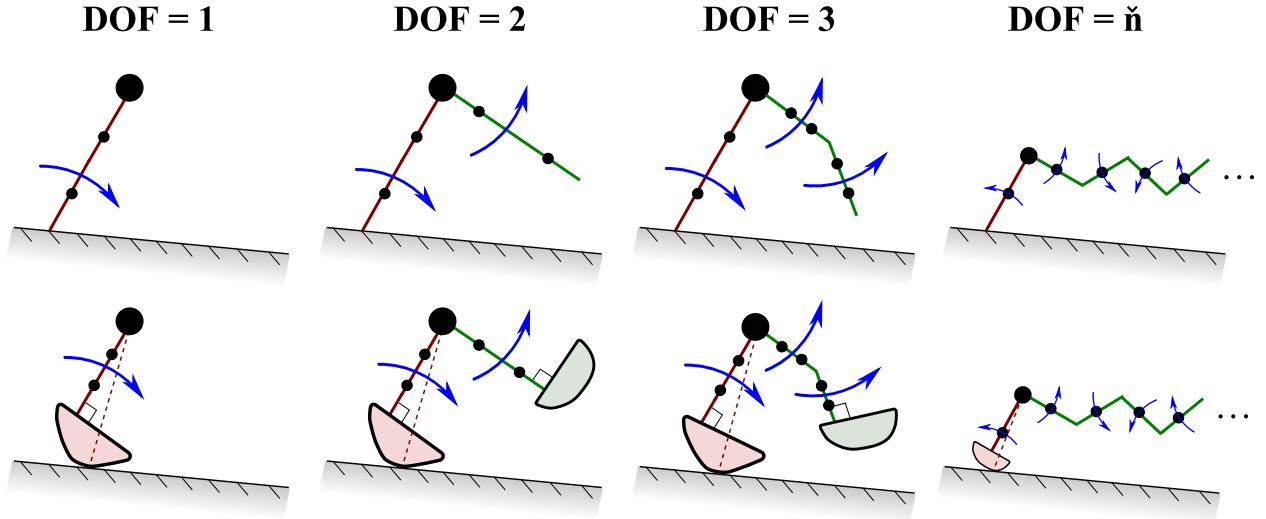
Figure 6.2: Passive dynamic walker models with various degrees of freedom

6.1.2 General Walker Kinematics

The formulation techniques presented here for the generalized $\check{n}$-link PDW models are the exact same as for my derivation for the generalized passive synchronization model in Section 5. However, because there exists no clear and comprehensive explanation of PDW model derivation, in this section I will specifically and in detail explain the steps needed to derive a two dimensional general PDW model kinematics. My derivation method can be applied to find the kinetmatics of a PDW of any number of degrees of freedom, however I will more so stress the derivation of a three or two link PDW. Examples of the models derived with this method can be seen in Figure 6.2.

Presented here are the general kinematics equations, the specific models differ in their definition of kinetic and potential energies of the system, which I will separately define in the assigned and specific model sections which will follow subsequent to this analysis. These derivations of PDW kinetic and potential energies can be seen the subsequent Section 6.1.3 while additional PDW derivations are provided in Appendix E

I will begin deriving the kinematics of the n-link PDW model by defining the general equation for the Lagrangian. The Lagrangian for a rotating system such as the PDW is defined as

the difference between the kinetic and potential energy, or Equation 6.1.

$$L(q,\dot{q},t) = K(\dot{q},t) - U(q,t) \tag{6.1}$$

Here, q is the angular position, $\dot{q}$ is the angular velocity, and t is the time. $K(\dot{q},t)$ is the kinetic energy of the system dependent on the angular velocity of the walker legs over time, while $U(q,t)$ is the potential energy dependent on the angular position of the walker over time. This is the equation for the general Lagrangian.

The dynamic equation of motion for the system (PDW) can be obtained by applying the Euler-Lagrange equation differential equation resulting in the Euler-Lagrange derivative for $\check{n}$ degrees of freedom (Equation 6.2).

$$\frac{\mathrm{d}}{\mathrm{d}t}\left(\frac{\partial L}{\partial \dot{q}_{1,2...\check{n}}}\right) = \frac{\partial L}{\partial q_{1,2...\check{n}}} + T \tag{6.2}$$

In this equation, $q_{1,2...\check{n}}$ are the generalized coordinates and $\dot{q}_{1,2...\check{n}}$ are the generalized velocities. The term T is included as a applied torque to the rotational system later used for PDW joint damping or other miscellaneous applied joint torques. For clarity this equation can be defined by a less common form, again in terms of kinetic and potential energies in Equation 6.3

$$\frac{\mathrm{d}}{\mathrm{d}t}\left(\frac{\partial K}{\partial \dot{q}_{1,2...\check{n}}}\right) - \frac{\partial K}{\partial q_{1,2...\check{n}}} + \frac{\partial U}{\partial q_{1,2...\check{n}}} = T \tag{6.3}$$

Hereinafter, Equation 6.3 is solved by inserting the kinetic energy, $K(q,\dot{q},t)$, and potential energy, $U(q,t)$, of the PDW configuration (2-link, 3-link, ... $\check{n}$-link). The number of equations generated by Equation 6.3 is dependent of the number of degrees of freedom, $\check{n}$, of the PDW. That is, a 2-link (inverted double pendulum) PDW will have two degrees of freedom, or $\check{n} = 2$, while a 3-link (inverted triple link pendulum) PDW will have three degrees of freedom, or $\check{n} = 3$. A walker may be modeled with more degrees of freedom by including additional joints such as a ankle join or if a torso is added, a joint controlling the torso angle. However, for my PDW application purposes,

it is sufficient to have a maximum of three joints: the pivot around ground contact by the entire walker, the pivot around the hip by the swinging leg, and the pivot about the swinging knee. As defined by Equation 6.3, the PDW may experience non-conservative torque losses, T. These non-conservative force losses are dependent on position, q or rotational velocity, $\dot{q}$, for the purpose of simulating joint stiffness experienced with injury, hemiplegia, or even a normal (healthy) amount of joint stiffness and joint damping.

The obstacle of defining the kinematics with the Larangian method lies in the identification of the exact values of kinetic energy, $K(q,\dot{q},t)$, and potential energy, $U(q,t)$, of the entire system that is the PDW. Theses kinetic and potential energies depend on the masses and mass distribution of the walker system.

The specific identification of the kinetic and potential energy values for each mass on the walker (Figure 6.9) are too long and specific for me to include in this chapter, however I am presenting a clear method for defining the kinetic energy, $K(q,\dot{q},t)$, and potential energy, $U(q,t)$, in the subsequent Section 6.1.3. *To assist in the derivation of the 2-link point-foot model, derivation schematics are found in Appendix E.2, while the derivation schematics for the 3-link point-foot model is located in Appendix E.3.*

Once the kinetic and potential energies are found and the Euler-Lagrange derivative is solved, one is left with $\check{n}$ number of equation containing a tangled and scrambled terms that are coefficients of $\ddot{q}_{\check{n}}$, $\dot{q}^2_{\check{n}}$, and the gravity term g, which have to be rearranged into their coefficients. Rearranging these equations will yield a system of equation of motion for the rotational system, Equation 6.4.

$$[M]_{\check{n},\check{n}}\,[\ddot{q}_{1,2,...\check{n}}]_{\check{n},1} \;+\; [N]_{\check{n},\check{n}}\,[\dot{q}^2_{1,2,...\check{n}}]_{\check{n},1} \;+\; [G]_{\check{n},1}\,g \;=\; [T]_{\check{n},1} \tag{6.4}$$

Here, the matrix [M] is a $\check{n}$ by $\check{n}$ square and symmetric matrix that contains all the coefficients of matrix $[\ddot{q}_{1,2,...\check{n}}]$, which is a $\check{n}$ by 1 vector and contains all angular acceleration variables, $\ddot{q}_{1,2,...\check{n}}$. The [N] matrix is a $\check{n}$ by $\check{n}$ negatively mirrored square matrix with a zero diagonal. The [N] contains

all the coefficients of matrix $[\dot{q}^2_{1,2,...\check{n}}]$, which is a $\check{n}$ by 1 vector and contains all squared angular velocity terms, $\ddot{q}^2_{1,2,...\check{n}}$. The [G] matrix is a $\check{n}$ by 1 vector that contains all coefficients with the gravity term, g. The matrix [T] is a $\check{n}$ by 1 vector that contains the values for negative or positive torque applied to any of the joints of the PDW, which may be dependent on rotational position, velocity, acceleration, or held zero.

The equation of motion, Equation 6.4 and in turn Equation 6.71 and 6.72, have to be rearranged such that the angular acceleration variable is on one side of the equation while the remainder of the equation is on the other. Reordering Equation 6.4 for the angular acceleration of each PDW link yields Equation 6.5. This angular acceleration can is integrated to find the remaining components of kinematics, angular velocity, $\dot{q}$, and angular position, $\dot{q}$.

$$[\ddot{q}_{1,2,...\check{n}}] \;=\; [M]^{-1} \; (-[N]\,[\dot{q}^2_{1,2,...\check{n}}] \;-\; [G]\,g \;+\; [T]) \tag{6.5}$$

6.1.2.1 Numerical Evaluation

Equation 6.5 can be used/evaluated numerically by numerical integration. There are several ways to integrate the angular acceleration of Equation 6.5, which include midpoint (rectangle) rule, trapezoidal rule, or Simpson's rule. The adaptive numerical algorithms for each method can readily be found in common numerical method texts such as [103].

However, for my computational PDW model I have chosen to apply the basic Euler method that will approximate the the angular velocity, $\dot{q}$, then again to approximate the angular position, q, for each the PDW link. As the time step for my model was taken to be $\Delta t = 0.0001s$, this numerical approximation was adequate for the purpose of approximating the PDW kinematics. Euler numerical integration of the angular acceleration, $\ddot{q}$, to obtain angular velocity, $\dot{q}$, is shown in Equation 6.6

$$[\dot{q}(t)_{1,2,...\check{n}}]_{\check{n},1} \;=\; [\dot{q}(t-\Delta t)_{1,2,...\check{n}}]_{\check{n},1} \;+\; [\ddot{q}(t)_{1,2,...\check{n}}]_{\check{n},1}\Delta t \tag{6.6}$$

Here, $[\ddot{q}(t)_{1,2,...\check{n}}]$ is defined by Equation 6.5, t is the current time value of the current iteration, while $t - \Delta t$ is the time value of the preceding iteration. Euler numerical integration of the angular

velocity, $\ddot{q}$, to obtain angular position, $\dot{q}$, of each PDW link is defined by Equation 6.7

$$[q(t)_{1,2,...\check{n}}]_{\check{n},1} = [q(t-\Delta t)_{1,2,...\check{n}}]_{\check{n},1} + [\dot{q}(t)_{1,2,...\check{n}}]_{\check{n},1}\Delta t \tag{6.7}$$

Note that this method requires a given initial velocity, $[\dot{q}](0) = [\dot{q}]_i$, and initial position, $[q(0)] = [q]_i$.

For example, for a 3-link PDW (inverted triple pendulum) the initial two time steps shown in Equation 6.6 would be represented by Equation 6.8 and 6.9. Here, I'm showing the time step to be $\Delta t = 0.0001s$

$$\begin{bmatrix} \dot{q}(0.0001)_1 \\ \dot{q}(0.0001)_2 \\ \dot{q}(0.0001)_3 \end{bmatrix} = \begin{bmatrix} \dot{q}(0)_1 \\ \dot{q}(0)_2 \\ \dot{q}(0)_3 \end{bmatrix} + \begin{bmatrix} \ddot{q}(0.0001)_1 \\ \ddot{q}(0.0001)_2 \\ \ddot{q}(0.0001)_3 \end{bmatrix} \Delta t \tag{6.8}$$

$$\begin{bmatrix} \dot{q}(0.0002)_1 \\ \dot{q}(0.0002)_2 \\ \dot{q}(0.0002)_3 \end{bmatrix} = \begin{bmatrix} \dot{q}(0.0001)_1 \\ \dot{q}(0.0001)_2 \\ \dot{q}(0.0001)_3 \end{bmatrix} + \begin{bmatrix} \ddot{q}(0.0002)_1 \\ \ddot{q}(0.0002)_2 \\ \ddot{q}(0.0002)_3 \end{bmatrix} \Delta t \tag{6.9}$$

6.1.3 PDW Potential and Kinetic Energy

To compute the PDW kinematics potential and kinetic energies of the dynamic system are inserted into Equation 6.3. Potential energy for PDW is the energy of the all the masses raised a relative height from ground contact point. This relative potential energy is the weight times the height, which is measured from the ground contact point. The cumulative potential energy of a PDW system is given by Equation 6.10.

$$U(q,t) = \sum_{i=1}^{\check{n}} \sum_{i=1}^{\check{m}} m_{i,j} \, g \, h_{i,j} \tag{6.10}$$

Here, $\check{n}$ is the total number of links with $\check{m}$ number of masses per link. $m_{i,j}$ is mass number j on PDW link/limb number i. PDW link number i is at an angular position q_i. The mass height, $h_{\check{n},\check{m}}$, is defined by Equation 6.11.

$$h_{\check{n},\check{m}} = \sum_{i=1}^{\check{n}} \left[r_{i-1} \cos(q_{i-1}) \right] + r_{\check{n},\check{m}} \cos(q_{\check{n}}) \tag{6.11}$$

The height of a mass is the sum of the height of all previous link lengths plus the height of the mass relative to the last joint. For example, the potential energy of the simplified system in Figure 6.4 is defined by Equation 6.12.

$$U(q,t)_{Ex} = m_1 \ g \ r_1 \cos(-q_1) + m_2 \ g \left[r_1 \cos(-q_1) + r_2 \cos(q_2) \right] \tag{6.12}$$

Note that the potential energy is measured form the ground contact point, therefore as the PDW switches stance legs, this point moves to the subsequent ground contact point.

The kinetic energy is the work done by the PDW model as it is in motion. The kinetic energy is proportional to the velocity of all the masses in the system and is defined by Equation 6.13.

$$K(\dot{q},t) = \frac{1}{2} \sum_{i=1}^{\check{n}} \sum_{i=1}^{\check{m}} m_{i,j} \ v_{i,j}^2 \tag{6.13}$$

The velocity of each mass particle, $v_{\check{n},\check{m}}$, is defined by the subsequent equation, Equation 6.14.

$$v_{\check{n},\check{m}} = \sum_{i=1}^{\check{n}} \left[r_{i-1} \dot{q}_{i-1} \right] + r_{\check{n},\check{m}} \dot{q}_{\check{n}} \tag{6.14}$$

The velocity of an arbitrary mass in on the rotating PDW system is relative to the ground contact and the sum of all previous link velocities. If we again take Figure 6.4 as an example, the total kinetic energy of the PDW system for this simple system is given by Equation 6.15.

$$K(\dot{q},t)_{Ex} = \frac{1}{2} \left[m_1 \ r_1 \dot{q}_1^2 + m_2 \left[r_1 \dot{q}_1^2 + r_2 \dot{q}_2^2 \right] \right] \tag{6.15}$$

A good check if the passive dynamic walker model does not have any mistakes, is to verify if the sum of the potential and kinetic energies is constant (Equation 6.16).

$$K(\dot{q},t) \ + \ U(q,t) \ = \ E(\dot{q},q,t) \ = \ \mathit{Constant} \tag{6.16}$$

Note that in a numerical PDW model the total energy may not be fully constant but slightly fluctuate. These fluctuations depend on simulation temporal resolution, spacial resolution, or computational round-off error. These slight fluctuations may especially be pronounced over a collision event computation.

6.1.3.1   Walking Collision/Transition Event

In this section, I will outline the the equations for the collision events during PDW walking. The purpose of defining collision event equations is to predict the angular velocities after the PDW encounters a external or internal collision.

One of the collision events is the moment when the swinging knee locks (knee strike), transforming two swinging links into one swinging links. In other words, the knee strike collision event converts the PDW from the 3-link phase to a 2-link phase. The other collision event during PDW walking is the instant when the heel hits the ground (heel strike). If the PDW is modeled to be a exclusively 2-link (compass gait) PDW model, the heel strike does not change the degrees of freedom, $\check{n}$, of the PDW system, in this case the PDW system remains at $\check{n} = 2$ degrees of freedom. However, if the PDW model is to be a 3-link model, alternating between a 3-link and 2-link phase, the heel strike converts the PDW system from a 3-link system ($\check{n} = 3$) to a 2-link system ($\check{n} = 2$).

I will be modeling the collision events as inelastic and instantaneous. The angular momentum of the rotational system rotating about unchanging reference point, is defined by Equation 6.17

$$H_O = \vec{r} \ \times \ m\vec{v} \tag{6.17}$$

Here, $\vec{r}$ is the distance vector from the rotation point to the rotating mass particle, m, while $\vec{v}$ is the linear velocity of the mass particle. '$\times$' is the cross product between the directional vectors $\vec{r}$ and $m\vec{v}$. It is also possible to define the linear velocity, $\vec{v}$, with angular velocity, $\dot{q}$, of the mass about the rotation reference point. This is definition is shown in Equation 6.18.

$$\vec{v} = \vec{r\dot{q}}$$ (6.18)

As stated before, the angular momentum of the PDW system is conserved during collision/transition events. The Equation 6.19 defines this conservation of angular momentum principle as it is applied to each mass in the system.

$$H_O = \sum_{i-1}^{\check{n}} (\vec{r}_i \times m_i \vec{v}_i)$$ (6.19)

This cumulative system value of H_O is the same before and after the collision. Hence, Equation 6.17, 6.18, and 6.19 can be summarized for a system of rotating particles, such as the PDW with its lumped masses. The system of particles for the conservation of momentum of a rotational system before and after a collision is defined in Equation 6.20.

$$H_O = \left[\sum_{i=1}^{n} (\vec{r}_i \times m\vec{v}_i) \right]^{-} = \left[\sum_{i-1}^{n} (\vec{r}_i \times m_i \vec{v}_i) \right]^{+} = Constant$$ (6.20)

In this equation and hereinafter, the subscript "$-$" denotes pre-collision terms, while the subscript "$+$" denotes all post-collision terms. The rotation of a system is about constant reference point, hence the definition of the angular momentum before and after the collision are defined from this predetermined origin point.

Note that in practice, Equation 6.20 is solved by defining each vector in terms of the cartesian components of vector space, $[\hat{i}, \hat{j}, \hat{k}]$, before crossing the vectors. An example on how to define the angular momentum in vector format can be viewed in the subsequent section.

As Equation 6.20 is applied to all masses for the *entire* PDW system and about the foot-ground contact *before and after to the collision event*. This is shown in Figure 6.3 as the conserved system number one. Application of the conservation of angular momentum principle for the entire system produces only one equation, however, after the collision the angular velocities of all rotating links, $\dot{q}_{1,2,...\check{n}}^{+}$, are unknown. In fact, the number of unknown angular velocities for the post-collision system is equal to the number of degrees of freedom of the system that is obtained after the collision.

That is, a 2-link system ($\check{n} = 2$) transitioning into 3-link phase ($\check{n} = 3$) via a heel strike, will have three unknown angular velocities: $\dot{q}_1^+$, $\dot{q}_2^+$, and $\dot{q}_3^+$. Likewise, a 3-link system ($\check{n} = 3$) transitioning into 2-link phase ($\check{n} = 2$) via a knee strike, will have two unknown angular velocities: $\dot{q}_1^+$ and $\dot{q}_2^+$.

To obtain additional equations with which one can solve for all post-collision unknown angular velocities, more conserved systems must be defined. As shown in Figure 6.3, for a two degree of freedom PDW system (2-link) the first conserved system is the entire PDW with the reference point at ground contact, while the second conserved system is the entire swinging leg of the PDW, with the reference point at the hip joint. Further, in a three degree of freedom PDW, an additional conserved system encompasses the swinging shank, with the reference point at the knee swinging knee location. If the PDW has more degrees of freedom, a conserved system is simply added to for each additional link, and within the previous conserved systems.

When the systems of conservation of angular momentum of before and after the collision event are set up, again, one is left with $\check{n}$ equations, corresponding to the highest degree of freedom between the system before the collision and after the collision. The critical part of this procedure lies in in organizing and grouping all matching coefficients of the angular velocity terms. Similar to the method used to collect all coefficients of the dynamics matricides in the previous Section 6.1.2, here the coefficients of the pre-collision and post-collision velocities ave to be collected. By collecting all pre-collision(-) coefficients and post-collision(+) coefficients,
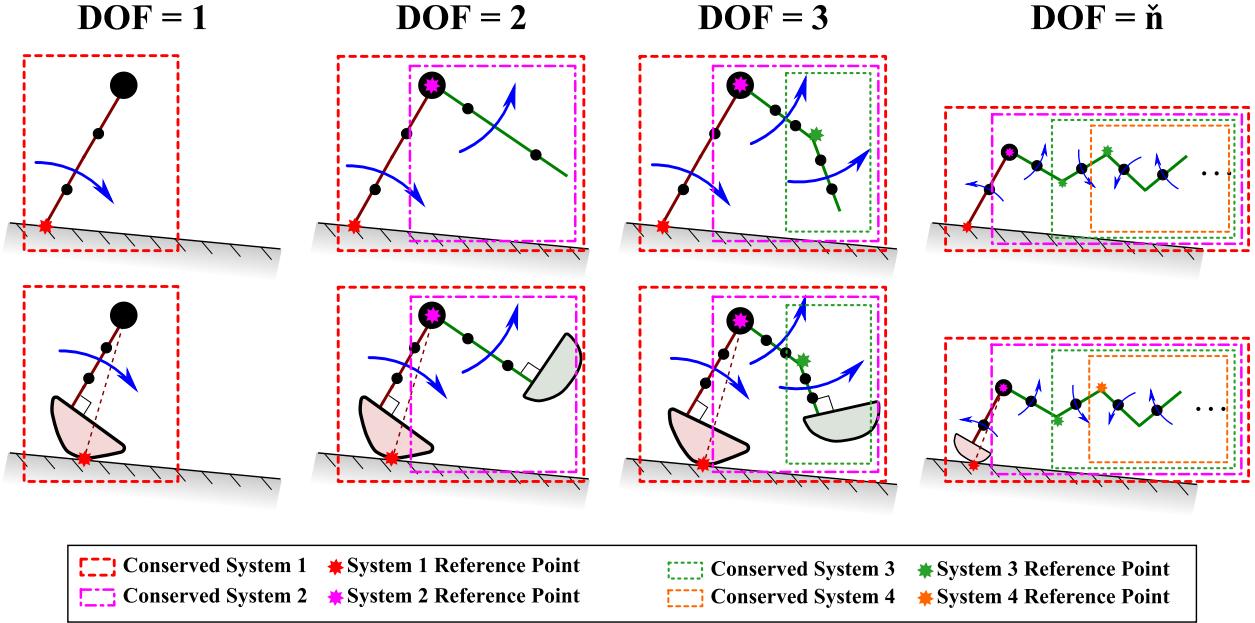
Figure 6.3: Passive dynamic walker conserved systems and conserved system reference points

Equation 6.21 is defined.

$$[Q]_{\check{n},\check{n}}^{-} \; [\dot{q}_{1,2,...\check{n}}]_{\check{n},1}^{-} \;\; = \;\; [Q]_{\check{n},\check{n}}^{+} \; [\dot{q}_{1,2,...\check{n}}]_{\check{n},1}^{+} \tag{6.21}$$

Here, the vector $[\dot{q}_{1,2,...\check{n}}]_{\check{n},1}^{+}$ is an array of all the angular velocities after the collision event. The matrix $[Q]_{\check{n},\check{n}}^{+}$ represents all the coefficients to the angular velocity vector after the collision event. Similarly, $[\dot{q}_{1,2,...\check{n}}]_{\check{n},1}^{-}$ is a vector containing all the angular velocities of all links before the collision, while $[Q]_{\check{n},\check{n}}^{-}$ are the coefficients to the angular velocity vector. However, we are interested in solving for the angular velocities after the the collision, which can be found by Equation 6.22.

$$[\dot{q}_{1,2,...\check{n}}]_{\check{n},1}^{+} \;\; = \;\; \left[[Q]_{\check{n},\check{n}}^{+}\right]^{-1} \; [Q]_{\check{n},\check{n}}^{-} \; [\dot{q}_{1,2,...\check{n}}]_{\check{n},1}^{-} \tag{6.22}$$

6.1.3.2 Example of Computing the Angular Momentum

In this example I am assuming a simplified system shown in Figure 6.4, a 2-link model, and derive part of the heel strike collision/transition. I demonstrate the derivation technique, I will only derive the pre-collision equations for the entire PDW system as the first conserved system.

184

To fully describe the heel strike, one would define the angular momentum for the entire PDW after the collision, and the pre- and post- collision angular momentum for the swinging leg conserved system.

As previously stated, in order to solve for the angular momentum for before and after the collision event, a vector notation ($[\widehat{i}, \widehat{j}, \widehat{k}]$) can be used. In this example, I will first define the angular momentum of the first rotating mass, m_1, rotating with a angular velocity, $-\dot{q}_1$, in a plane a distance, $\overrightarrow{r_1}$, from the rotational reference point, O. Here the the vector that defines the distance between the rotation reference point, O, and the the first mass can be defined in Cartesian component vector space as Equation 6.23.

$$\overrightarrow{r}_{O1} = [\, r_1 \sin(-q_1)\widehat{i}, \; r_1 \cos(-q_1)\,\widehat{j}, \; 0\,\widehat{k}\,] \tag{6.23}$$

The linear velocities of m_1 prior to heel strike is given by Equation 6.23.

$$\overrightarrow{v}_{O1}^- = [\, -r_1 \dot{q}_1^- \cos(-q_1)\,\widehat{i}, \; -r_1 \dot{q}_1^- \sin(-q_1)\,\widehat{j}, \; 0\,\widehat{k}\,] \tag{6.24}$$

Thus angular momentum for mass particle, m_1, prior to heel strike is found by Equation 6.17 and so equals Equation 6.25.

$$H_{O\,m1}^- = [\, 0\,\widehat{i}, \; 0\,\widehat{j}, \; m_1 \dot{q}_1^- r_1^2 [\cos(2q_1)]\,\widehat{k}\,] \tag{6.25}$$

Further the second mass in the rotating chain in the example shown in Figure 6.4, must also be referenced from the system's reference point O. That is, the rotational distance and velocity vector of the second mass must be relative to system reference point O. This is relative principle is defined in Equation 6.26 and 6.27 for the rotation distance and velocity vector, respectively.

$$\overrightarrow{r}_{O2} = \overrightarrow{r}_{O1} + \overrightarrow{r}_{12} \tag{6.26}$$
$$\overrightarrow{v}_{O2}^- = \overrightarrow{v}_{O1}^- + \overrightarrow{v}_{12}^- \tag{6.27}$$

185
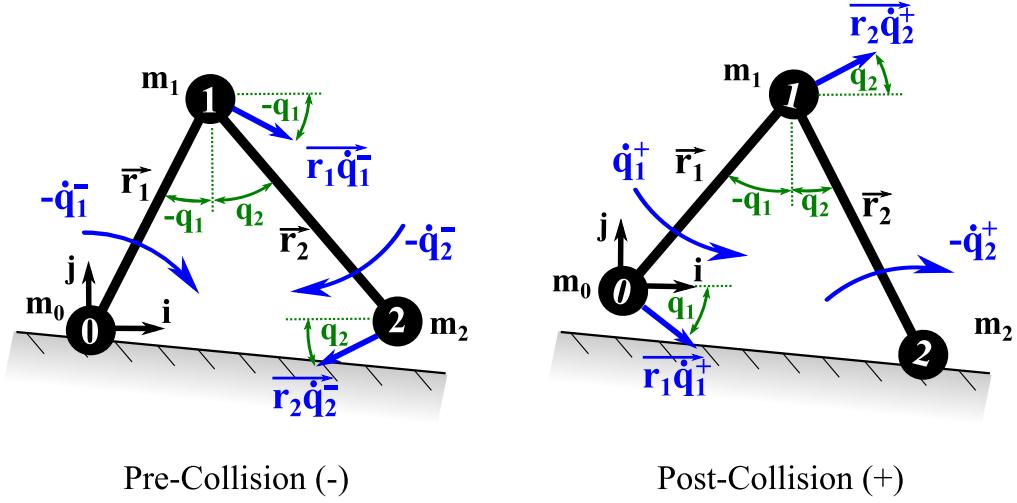
Figure 6.4: A simplified passive dynamic walker model used in the presented example

Therefore, the rotation distance and velocity vector for the second mass is defined by Equations 6.28 and 6.29, respectively.

$$\overrightarrow{r}_{O1}^- = [\, r_1 \sin(-q_1) + r_2 \sin(q_2)\, \widehat{i}, \ r_1 \cos(-q_1) + r_2 \cos(q_2)\, \widehat{j}, \ 0\, \widehat{k}\,] \tag{6.28}$$

$$\overrightarrow{v}_{O1}^- = [\, -r_1 \dot{q}_1^- \cos(-q_1) - r_2 \dot{q}_2^- \cos(q_2)\, \widehat{i}, \ -\sin(-q_1) r_1 \dot{q}_1^- - r_2 \dot{q}_2^- \sin(q_2)\, \widehat{j}, \ 0\, \widehat{k}\,] \tag{6.29}$$

This yields an angular momentum for the second mass, m_2, before the heel strike collision as Equation 6.30.

$$H_{O\,m2}^- = [\, 0\, \widehat{i}, \ 0\, \widehat{j}, m_2 [\dot{q}_1^- r_1^2 \cos(2q_1)...$$
$$... + \dot{q}_2^- r_2^2 \cos(2q_2) + \dot{q}_1^- r_1 r_2 \cos(q_1 - q_2) + \dot{q}_2^- r_1 r_2 \cos(q_1 - q_2)]\, \widehat{k}\,] \tag{6.30}$$

Adding the angular momenta for both masses on the PDW, the total angular momentum for the whole PDW about reference point O before the heel strike is defined by Equation 6.31.

$$H_O^- = H_{O\,m1}^- + H_{O\,m2}^- \tag{6.31}$$

Collecting angular acceleration terms, the first row of the $[Q]^-$ matrix is derived. In this example, these terms are defined by Equations 6.32 and 6.33.

$$Q_{11}^- = m_1 r_1^2 \cos(2q_1) + m_2 r_1^2 \cos(2q_1) + m_2 r_1 r_2 \cos(q_1 - q_2) \qquad (6.32)$$

$$Q_{12}^- = m_2 r_2 [r_2 \cos(2q_2) + r_1 \cos(q_1 - q_2)] \qquad (6.33)$$

These coefficient terms are part of the pre-collision coefficient matrix, $[Q]^-$, that in turn is par of Equation 6.21. To put the derived terms into perspective, Equation 6.21 for a compass gait walker which transitions from 2-link to 2-link is defined as Equation 6.34.

$$\begin{bmatrix} \dot{q}_1^+ \\ \dot{q}_2^+ \end{bmatrix} = \begin{bmatrix} Q11^+ & Q12^+ \\ Q21^+ & Q22^+ \end{bmatrix}^{-1} \begin{bmatrix} Q11^- & Q12^- \\ Q21^- & Q22^- \end{bmatrix} \begin{bmatrix} \dot{q}_1^- \\ \dot{q}_2^- \end{bmatrix} \qquad (6.34)$$

The highlighted terms are the terms I have derived in this example. In the subsequent steps, one would repeat the same steps three more times. Once more for the post-collision angular momentum, and twice for the pre- and post- collision momentum of the swinging leg. It is important to note that, the instant before and the instant after a collision event, the dimensional parameters of the rotating system do not change. The only thing that does change is the direction or signs of the velocities. Further, the reference point remains the same the instants prior and after the collision.

6.1.3.3   Ground Contact Detection

During a PDW numerical simulation it is important to find the point and time when the PDW's foot hits the ramp. This is the point when the PDW's heel hits the ramp, while pivoting into a subsequent step. As the PDW is in 2-link (no knee or straightened knee), the PDW computer simulation has two criteria for a heel strike. The first criteria is that the swinging PDW link has a negative angular velocity, moving towards the ramp line. This first criteria is outlined in Equation 6.35.

$$\dot{q}_{swing} \leq 0 \qquad (6.35)$$

The second criteria is that the lowest part of the swinging leg (i.e. heel) vertical position passes the ramp platform. This can be seen in Figure 6.5 for a point foot model and a variable curve-foot
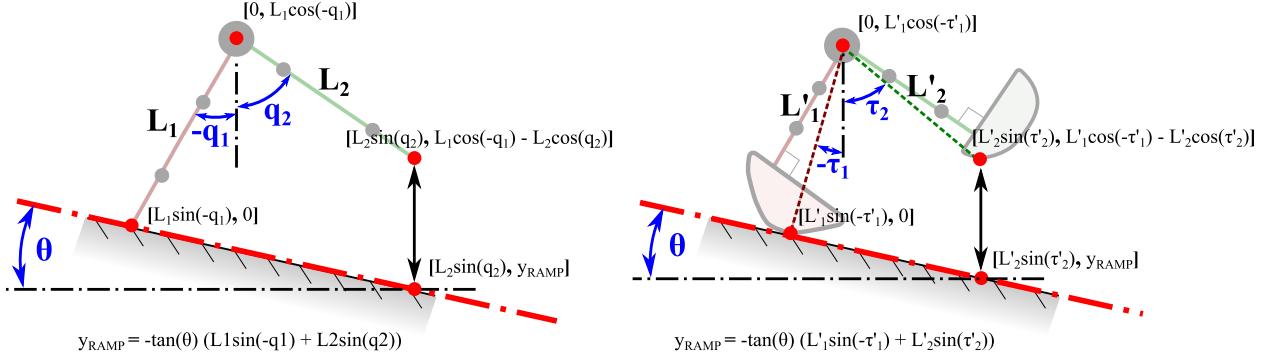
Figure 6.5: Passive dynamic walker conserved systems and conserved system reference points

model. This second criteria is outlined in Equation 6.36 for a point-foot model and Equation 6.37

for a variable curve-foot model.

$$L_1 \cos(-q_1) - L_2 \sin(q_2) \leq -\tan(\theta)(L_1 \sin(-q_1) - L_2 \sin(q_2)] \tag{6.36}$$

$$L_1 \cos(-\tau_1) - L_2 \sin(\tau_2) \leq -\tan(\theta)(L_1 \sin(-\tau_1) - L_2 \sin(\tau_2)] \tag{6.37}$$

Notice that in the variable foot model, this lowest point is somewhere on the perimeter of the

curved foot and is dependent on the configuration of the PDW. Because of this geometrical offset,

the configuration angles at which the collision occurs will be different than the point-foot model.

6.1.4   Ground Reaction Kinetics

The ground reaction forces of the PDW model is the sum static forces (R_S) of the particle masses distributed along the PDW links and the dynamic forces (R_D) caused by the radial (centriptal) and tangential accelerations acting on the masses (Equation 6.38 and Equation 6.39).

$$R_x = R_{xS} + R_{xD} \tag{6.38}$$

$$R_y = R_{yS} + R_{yD} \tag{6.39}$$

Here, R_x is the ground reaction force along (parallel) to the ramp, while R_y is the ground reaction

force perpendicular to the ramp. This can be seen in Figure 6.6 for a point-foot and curved-foot

ground contact. For the mass particle rotating about a ramp contact, the static ground reaction
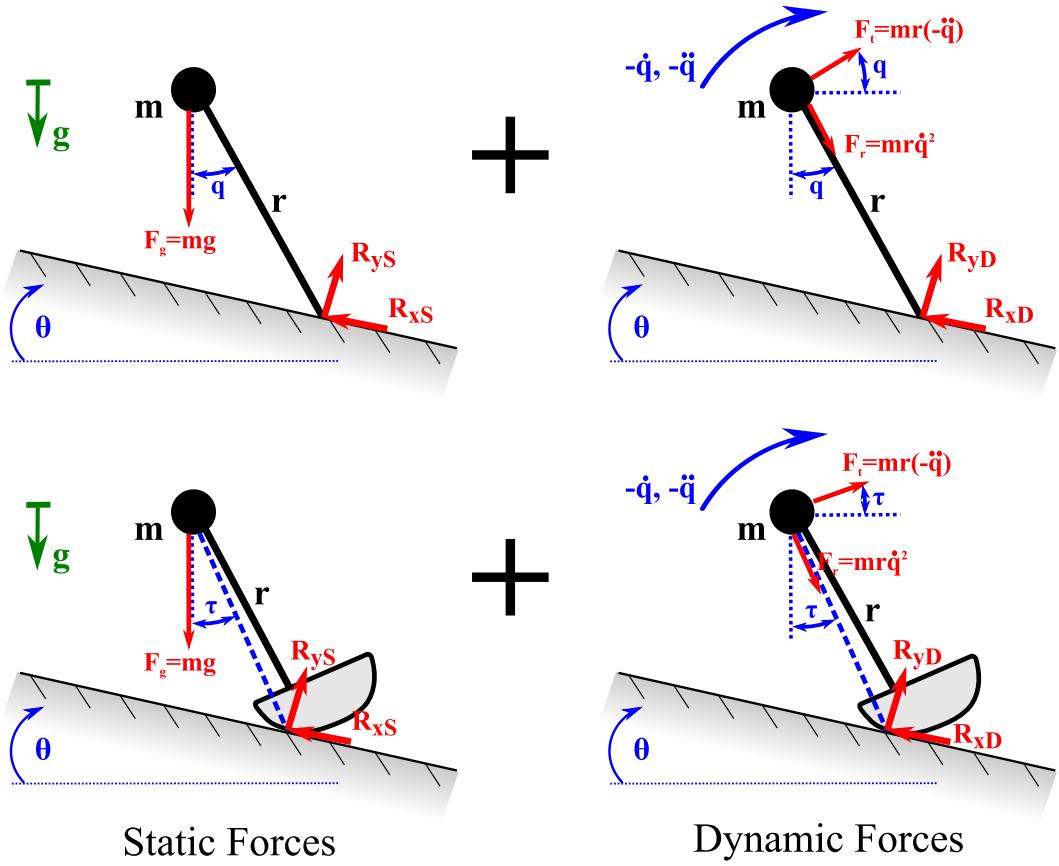
Figure 6.6: The PDW ground reaction forces are a sum of the static and dynamic forces acting on each mass particle in the PDW

forces generated by gravity in the direction along the ramp are defined by Equation 6.40, while the ground reaction forces perpendicular to the ramp are defined by Equation 6.41.

$$R_{xS} = mg\sin(\theta) \tag{6.40}$$

$$R_{yS} = mg\cos(\theta) \tag{6.41}$$

Here, θ is the ramp angle. Hence, cumulative ground reaction force solely due to gravitational forces acting on the PDW masses is defined by Equation 6.42 along the ramp and Equation 6.43 perpendicular to the ramp.

$$R_{xS\ TOT} = \sum_{i=1}^{\check{n}} \sum_{i=1}^{\check{m}} m_{i,j} g\ \sin(\theta) \tag{6.42}$$

$$R_{yS\ TOT} = \sum_{i=1}^{\check{n}} \sum_{i=1}^{\check{m}} m_{i,j} g\ \cos(\theta) \tag{6.43}$$

189

In these equations, $m_{i,j}$ is particle mass number j on PDW link number i.

From Newton's 2nd law of motion, it is known that an accelerating mass will produce a force. Therefore, the dynamic ground reaction forces are proportional to the acceleration of the mass in motion. The acceleration of the moving mass can be divided into its radial and tangential component. That is, the total linear acceleration of the rotating mass has a component pointing towards the rotating center one component that is points in the instantaneous direction of motion. For the rotating particle such as the one shown in Figure 6.6, the radial (centripetal) force, a_r, is given by Equation 6.44, while the tangential force is given by Equation 6.45.

$$F_r = ma_r \tag{6.44}$$

$$F_t = ma_t \tag{6.45}$$

The radial and and tangential acceleration is in turn defined by Equation 6.46 and Equation 6.47, respectively.

$$a_r = mr\ddot{q} \tag{6.46}$$

$$a_t = mr\dot{q}^2 \tag{6.47}$$

Here, $\ddot{q}$ and $\dot{q}$ are the angular acceleration and velocity of the the rotating link, while r is the distance from the rotation origin to the rotating mass, m.

However, we are interested in the ground reaction forces along and perpendicular to the ramp ground at ground contact. The radial and tangential force can be decomposed into the direction parallel and perpendicular to the ramp. This decomposition defines the dynamic ground reaction forces for one mass rotating over ground and down declined slope in Equation 6.48 for along the ramp and Equation 6.49 for normal to the ramp.

$$R_{xD} = m[a_r \sin(q - \theta) + a_t \cos(q - \theta)] \tag{6.48}$$

$$R_{yD} = m\left[a_r \cos(q - \theta) + a_t \sin(q - \theta)\right] \tag{6.49}$$

The cumulative ground reaction force solely due to dynamics forces acting on all PDW masses is not as straight forward as in the static force case. Since we are interested in the ground reaction forces as the PDW pivots over ground, the acceleration for each mass is relative to the ground contact point. For example, a mass located on the swinging leg of a 2-link PDW will rotate about the hip joint, while the entire swinging leg rotates about the ground contact point. Therefore, the radial and tangential acceleration of a mass located on link $\check{n}$ relative to ground contact, O, is defined by Equation 6.50 and Equation 6.51. This relative procedure is similar to the outlined in the previous Section 6.1.3.2.

$$a_{r\ O\check{n}} \ = \ a_{r\ O1} \ + \ a_{r\ 12} \ + \ ... \ + \ a_{r\ n-1\check{n}} \tag{6.50}$$

$$a_{t\ O\check{n}} \ = \ a_{t\ O1} \ + \ a_{t\ 12} \ + \ ... \ + \ a_{t\ n-1\check{n}} \tag{6.51}$$

Finally, I am defining the cumulative ground reaction force caused by dynamic forces as the PDW moves. Equation 6.52 defines the ground reaction forces parallel to the ramp, while Equation 6.53 represents the ground reaction forces normal to the ramp.

$$R_{xD\ TOT} = \sum_{i=1}^{\check{n}} \sum_{i=1}^{\check{m}} m_{i,j} \left[a_{r\ Oij} \sin(q_i - \theta) \ + \ a_{t\ Oij} \cos(q_i - \theta) \right] \tag{6.52}$$

$$R_{yD\ TOT} = \sum_{i=1}^{\check{n}} \sum_{i=1}^{\check{m}} m_{i,j} \left[a_{r\ Oij} \cos(q_i - \theta) \ + \ a_{t\ Oij} \sin(q_i - \theta) \right] \tag{6.53}$$
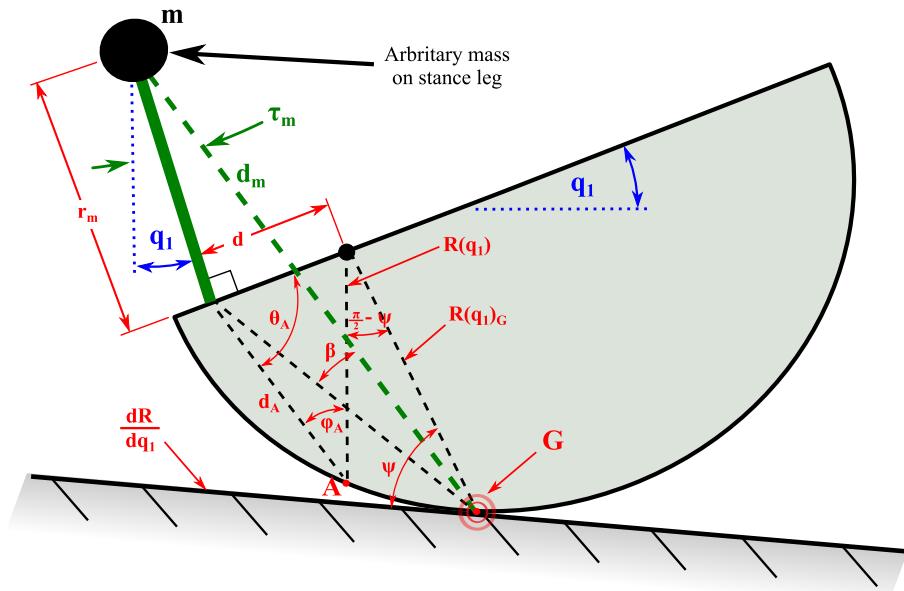
6.1.5 Modeling a Variable Curve-Foot

The PDW model that I have developed can walk on a variable curve foot shape. In this section I will derive the geometric parameters needed to define the Lagrangian (Equation 6.3) for the PDW dynamics and collision event equations in Section 6.1.3.1.

The PDW foot shape is defined by a variable (or constant) radius function. This variable radial foot function can be defined by Equation 6.54

$$R(q_1, \ \dot{q}_1, \ \ddot{q}_1)_{foot} = R_i + Bq_1 + C\sin(q_1) + D\dot{q}_1 + \ \cdots \tag{6.54}$$

Stance Leg Angular Position: $+ q_1$

Stance Leg Angular Position: $- q_1$
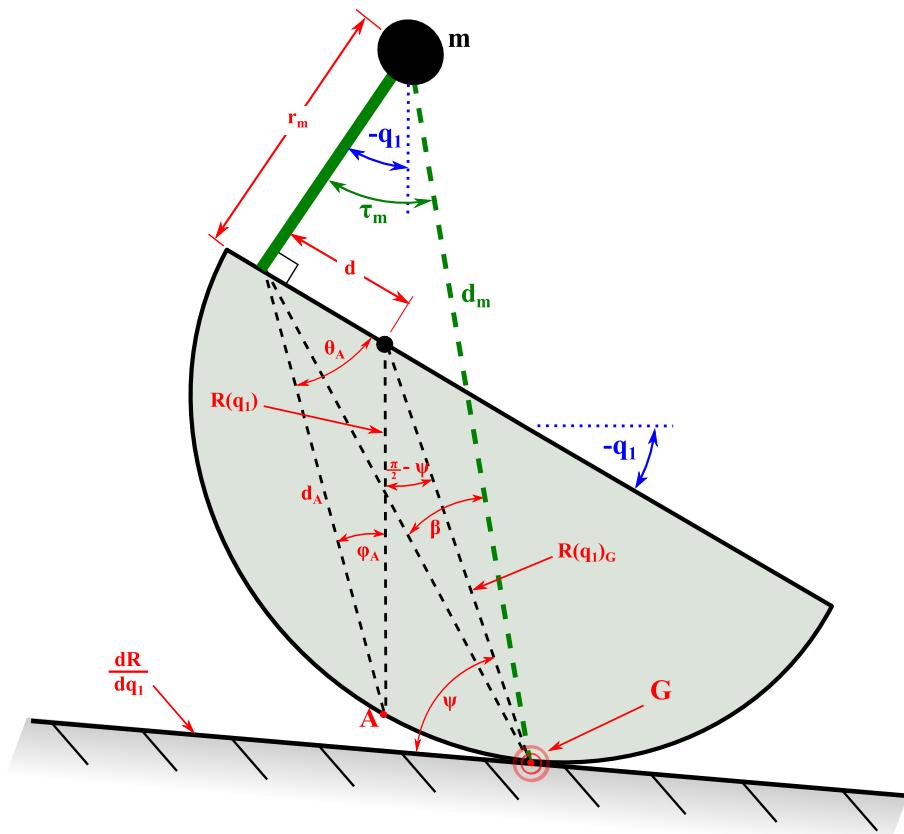
Figure 6.7: Geometric parameters of a variable curved/radius PDW foot as it relates to a stance mass

The radial function that defines the foot shape must be positive, continuous, and defined over and interval from $-\frac{pi}{2}$ to $\frac{pi}{2}$. In other words the radial foot curve must be bounded by Equation 6.55 and Equation 6.56.

$$R_{foot} \geq 0 \tag{6.55}$$

$$\left\{ R_{foot} \in \mathbb{R} \mid -\frac{\pi}{2} \leq q_1 \leq \frac{\pi}{2} \right\} \tag{6.56}$$

Notice that the radius of passive dynamic walker's curve foot, R_{foot}, can be dependent on the any PDW variable such as the stance leg angular velocity, $\dot{q}$, or angular acceleration, $\ddot{q}$. For example, a steadily increasing or decreasing foot radius is defined by Equation 6.57.

$$R(q_1)_{foot} = R_i + C q_1 \tag{6.57}$$

Here, R_i is the initial foot radius while C is a constant constituting the increase in foot shape radius. The origin of the foot curve is where the shank is connected to the curved food, while $R(q)$ is projected vertically as shown in Figure 6.7. Note that as the stance foot angle is perfectly vertical ($q_1 = 0$), the foot radius function is defined as $R(0)$ which lies directly under the shank attachment. The shank may also be attached to the curved foot at an offset distance, d. This offset distance, d, is seen in Figure 6.7.

The polar tangential angle that is the angle between a polar curve radius vector, $R(q)$, and a vector that is a tangent to the curve, dR_{foot}/dq_1, is defined by Equation 6.58

$$\psi = \tan^{-1} \left[\frac{R_{foot}}{dR_{foot}/dq_1} \right] \tag{6.58}$$

Here, the tangent vector to the foot curve is the ground. This definition of the polar tangential angle allows us to define the the point on the curved foot that is in contact with the ground. The modified angle at which the foot is in contact with the ground is defined by Equation 6.59, while the radius point that is in contact with the ground is defined by Equation 6.60. This modified radial point is

defined from our example foot radius function in Equation 6.57.

$$q_{1G} = q_1 + \theta + (\frac{pi}{2} - \psi)$$ (6.59)

$$R_{footG} = A + Bq_{1G}$$ (6.60)

The ramp angle is denoted by θ. By analyzing the curved foot geometric parameters in Figure 6.7, geometric variables d_A, ϕ_A, and θ_A are defined in following Equation 6.61, Equation 6.62, and Equation 6.63.

$$d_A = \sqrt{d^2 + R_{footG}^2 - 2dR_{footG}\cos(\psi - q_1 - \theta)}$$ (6.61)

$$\phi_A = \sin^{-1}\left[\frac{d\sin(\psi - q_1 - \theta)}{d_A}\right]$$ (6.62)

$$\theta_A = pi - \phi_A - \psi + q_1 + \theta$$ (6.63)

Given these geometric parameters, the distance from a mass, m, on along the stance leg to the ground contact point, G is defined by Equation 6.64.

$$d_m = \sqrt{r_m^2 + d_A^2 + 2r_m d_A sin(\theta_A)}$$ (6.64)

Here, r_m is the distance from the point the PDW shank is attached to the foot to the mass along the stance leg. The angle from the vertical to the vector defined by d_m is defined by Equation 6.65.

$$\tau_m = \phi_A - \beta_m - \theta$$ (6.65)

Here, the angle β_m is defined by Equation 6.66.

$$\beta_m = \sin^{-1}\left[\frac{r_m\cos(\theta_A)}{d_m}\right]$$ (6.66)

6.1.6 Imposing a Moving Ground Contact

It is possible to impose a moving ground onto one or both of the PDW legs. This may represent a tied- or split-belt treadmill or an arbitrary perturbation to the stance foot. This perturbation to the foot is applied to the walker by adjust the position of the walker as it is computing the kinematics. The addition of positive or negative foot velocity is given either by Equation 6.67 or Equation 6.68

$$q = q + \Delta q_{Pertrub} \tag{6.67}$$

$$\dot{q} = \dot{q} + \Delta\dot{q}_{Pertrub} \tag{6.68}$$

Here $\Delta q_{Pertrub}$ is the angle added to the current stance leg angle, while $\Delta\dot{q}_{Pertrub}$ is the angular velocity added to the current stance leg angular velocity. In other words, $\Delta q_{Pertrub}$ and $\Delta\dot{q}_{Pertrub}$ are the perturbation angle or velocity caused by the ground onto the foot and are defined by Equations 6.69 and Equations 6.70, respectively.

$$\Delta q_{Pertrub} = \sin^{-1}\left[\frac{\overrightarrow{v}_{PertrubVel}\Delta t \cos(\theta)}{r_{Stance}}\right] \tag{6.69}$$

$$\Delta\dot{q}_{Pertrub} = \sin^{-1}\left[\frac{\overrightarrow{v}_{PertrubVel}\cos(\theta)}{r_{Stance}}\right] \tag{6.70}$$

Here, the $\overrightarrow{v}_{PertrubVel}$ is the desired foot perturbation velocity, Δt is the computational time step, θ is the ramp angle, and r_{Stance} is the distance from ground contact to the hip joint.

6.2 Point-Foot Model

The general point-foot PDW model, shown on the bottom of Figure 6.8, is a standard model commonly used to define a two or three link PDW with point ground contact. That is, the rigid leg link pivots over the ground and does not roll, but acts strictly as a pivot. In this section, I will analyze a 3-link asymmetric PDW able to walk on a tied-belt treadmill, split-belt treadmill, or even on my gait enhancing mobile shoe outlined in Chapter 3. Further, I will validate this model to actual normal human kinematic and kinetic parameters.

As shown in Figure 6.9, my passive dynamic walker model consists of nine masses, that is, on each leg there are two shank masses and two thigh masses with an additional hip mass as shown in Figure 6.9. I've chosen two masses per link because in this configuration the first and second moment of inertia can be decoupled and a dissimilar mass and mass distribution can result in the same polar mass moment of inertia.

The two PDW sides are differentiated between the left and right side. This allows the mass and mass distribution to be distributed asymmetrically, allowing for the analysis of pathological gait of the PDW.

For the two degree of freedom (2-link) PDW phase (inverted double pendulum) shown in the top of Figure 6.8, Equation 6.4 becomes Equation 6.71.

$$
\begin{bmatrix} M_{11} & M_{12} \\ M_{12} & M_{22} \end{bmatrix} \begin{bmatrix} \ddot{q}_1 \\ \ddot{q}_2 \end{bmatrix} + \begin{bmatrix} 0 & N_{12} \\ -N_{12} & 0 \end{bmatrix} \begin{bmatrix} \dot{q}_1^2 \\ \dot{q}_2^2 \end{bmatrix} + \begin{bmatrix} G_1 \\ G_2 \end{bmatrix} g = \begin{bmatrix} T_1 \\ T_2 \end{bmatrix} \tag{6.71}
$$
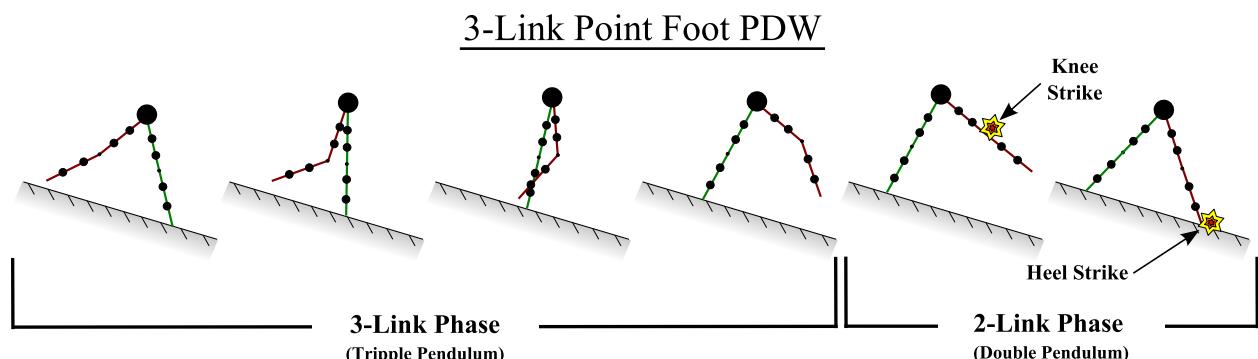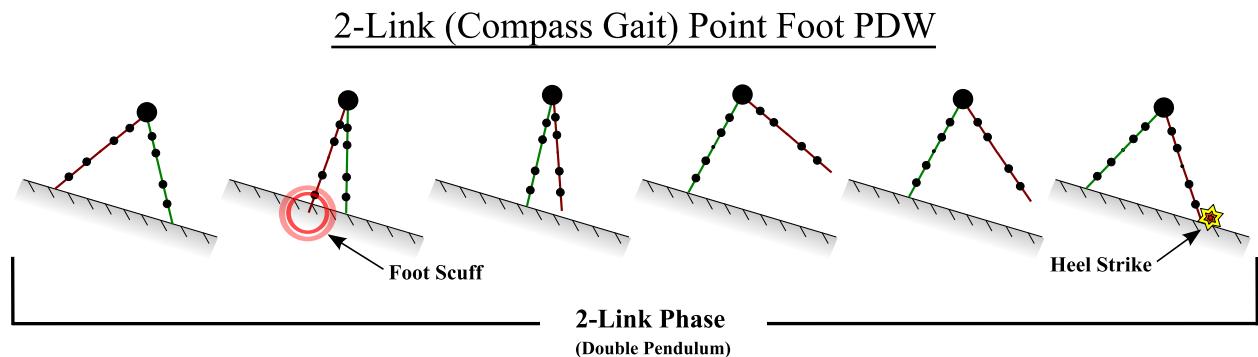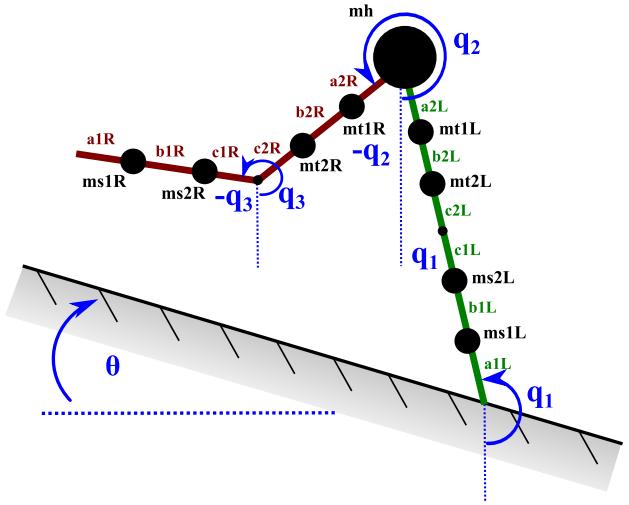
Figure 6.8: Phases of the two and three link point-foot PDW
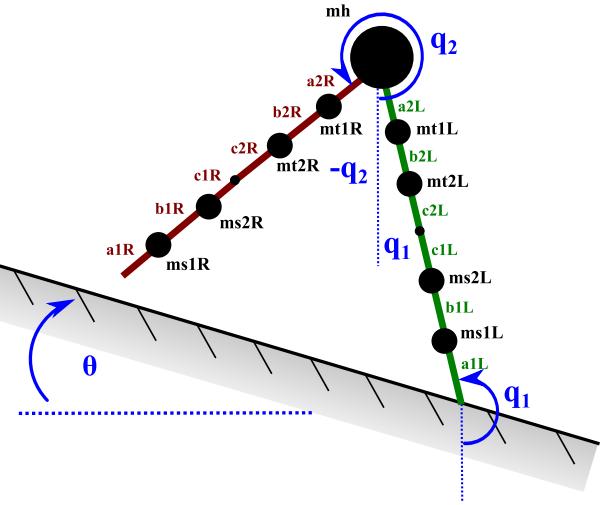
Figure 6.9: PDW point-foot model used during three-link and two-link phase

Here, T_1 and T_2 may be non-conservative torques applied to walker pivot points (ground and hip). Equation 6.71 is used to define the dynamics of a 2-Link (compass gait) PDW with point feet. This equation also defines the 2-link phase of the 3-link PDW as shown in Figure 6.8. For a three degree of freedom (3-link) PDW (inverted triple pendulum) shown in the first phase of the bottom of Figure 6.8, Equation 6.4 becomes Equation 6.72.

$$
\begin{bmatrix} M_{11} & M_{12} & M_{13} \\ M_{12} & M_{22} & M_{23} \\ M_{13} & M_{23} & M_{33} \end{bmatrix} \begin{bmatrix} \ddot{q}_1 \\ \ddot{q}_2 \\ \ddot{q}_3 \end{bmatrix} + \begin{bmatrix} 0 & N_{12} & N_{13} \\ -N_{12} & 0 & N_{23} \\ -N_{13} & -N_{23} & 0 \end{bmatrix} \begin{bmatrix} \dot{q}_1^2 \\ \dot{q}_2^2 \\ \dot{q}_3^2 \end{bmatrix} + \begin{bmatrix} G_1 \\ G_2 \\ G_3 \end{bmatrix} g = \begin{bmatrix} T_1 \\ T_2 \\ T_3 \end{bmatrix} \tag{6.72}
$$

Note that the equation of motion in Equation 6.72 is used for the 3-link phase (before knee strike) for the kneed PDW model, while the remaining 2-link phase is defined by Equation 6.71.

The collision/transition event equation for the knee strike for this model is generally defined by Equation 6.22 and becomes Equation 6.73.

$$
\begin{bmatrix} \dot{q}_1^+ \\ \dot{q}_2^+ \end{bmatrix} = \begin{bmatrix} Q_{11}^+ & Q_{12}^+ \\ Q_{21}^+ & Q_{22}^+ \end{bmatrix}^{-1} \begin{bmatrix} Q_{11}^- & Q_{12}^- & Q_{13}^- \\ Q_{21}^- & Q_{22}^- & Q_{23}^- \end{bmatrix} \begin{bmatrix} \dot{q}_1^- \\ \dot{q}_2^- \\ \dot{q}_3^- \end{bmatrix} \tag{6.73}
$$

The collision/transition event equation for the heel strike, as the model transitions from a two-link PDW to a three-link PDW is defined by Equation 6.74.

$$
\begin{bmatrix} \dot{q}_1^+ \\ \dot{q}_2^+ \\ \dot{q}_3^+ \end{bmatrix} = \begin{bmatrix} Q_{11}^- & Q_{12}^- \\ Q_{21}^- & Q_{22}^- \end{bmatrix}^{-1} \begin{bmatrix} Q_{11}^+ & Q_{12}^+ \\ Q_{21}^+ & Q_{22}^+ \end{bmatrix} \begin{bmatrix} q_1^- \\ q_2^- \end{bmatrix} \tag{6.74}
$$

However, notice that the resulting vector has a size of 3 by 1. In this case, the third link's angular velocity, $\dot{q}_3^+$, will be the same value as the second link's angular velocity. This is expressed in Equation 6.75
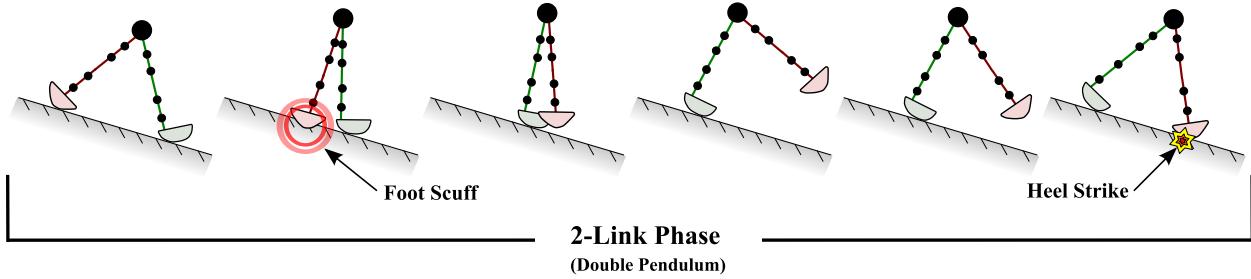
$$
\dot{q}_3^+ = \dot{q}_2^+ \tag{6.75}
$$

6.3   Variable Curve-Foot Model

The curved foot model offers the possibility in modifying the roll-over shape of the PDW as it progresses down a decline. This model as it is defined is novel in its abilities to vary the curved foot to any continuous shape or size. This model is able to change the foot radius, while also offering the possibility of changing the foot curvature. As the point-foot model, my curved foot model is able to differentiate between the left and right PDW side, enabling asymmetric gait analysis.

The variable curve-foot model is defined with nine masses, that is, each leg has two shank masses and two thigh masses with on additional hip mass. The masses can be increases and moved along PDW limbs symmetrically or asymmetrically. This curve foot model with all its masses and notation is displayed in Figure 6.11. The derivation of this model is described in the previous sections with the aid of Appendix E. The dynamics matrices are similar to the ones described in Section 6.2, however due to more complicated parameter definitions an additional damping matrix, $[N]$, and that is multiplied my the angular velocity vector, $[\dot{q}_{1,2,...\check{n}}]$.

2-Link (Compass Gait) Variable Curve Foot PDW

Foot Scuff

Heel Strike

2-Link Phase
(Double Pendulum)

3-Link Variable Curve Foot PDW

Knee
Strike

Heel Strike

3-Link Phase
(Tripple Pendulum)

2-Link Phase
(Double Pendulum)
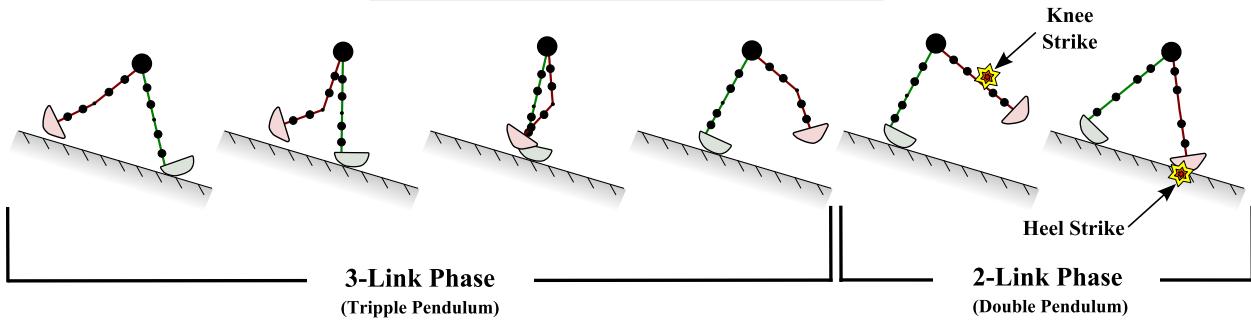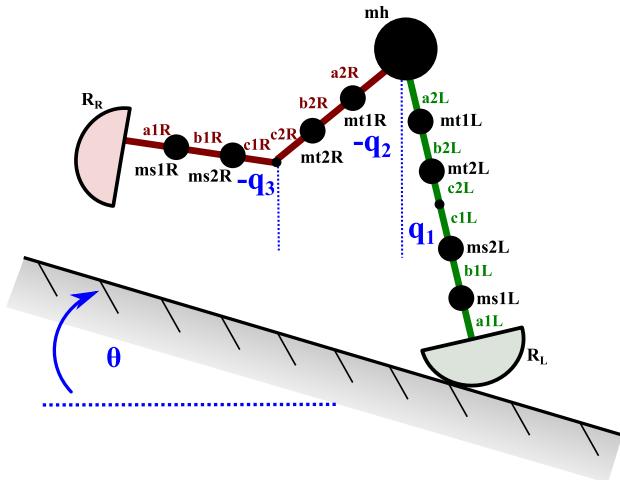
Figure 6.10: Phases of the two and three link variable curve foot PDW

Three-Link Curve-Foot Model

Two-Link Curve-Foot Model
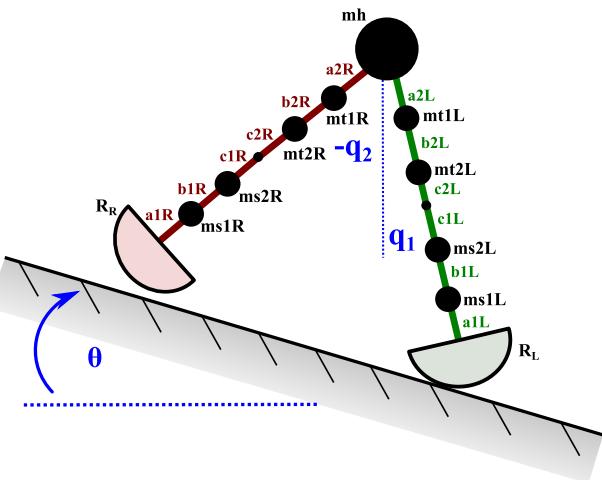
Figure 6.11: PDW curve-foot model used during three-link and two-link phase

6.4 Validation for Human Gait Approximation

In this section I will compare the kinematics, kinetics, and asymmetric behavior of a passive dynamic walker (PDW) to human gait. A useful characteristic of PDWs is that a PDW model

focuses on the passive dynamics of gait, excluding the cognitive controls of subject testing, so the purely dynamic aspects of gait can be analyzed. Here, I will directly compare PDW and human gaits.

For a rational comparison, the PDW model parameters are extracted from an anthropomorphic model [42] and proportionally sized such that the masses and mass distributions are scaled down from an average adult person (Figure 6.12). I will define upper body to include the head, neck, and trunk without the arms. While this walking model has limitations, such as the lack of dorsiflexion (ankle movement in the sagittal plane), joint stiffness, and joint damping, it can give further insight into gait rehabilitation methods by modeling kinematic and kinetic gait characteristics.

First, I will focus on explaining my PDW computer model specifically for this study. Then I will compare and contrast kinematic and kinetic data of a normal, undisturbed, steady state, and symmetric PDW gait to a recorded normal human gait. Finally, we compare the gait of an asymmetric PDW to human gait with a weight attached to one shank.
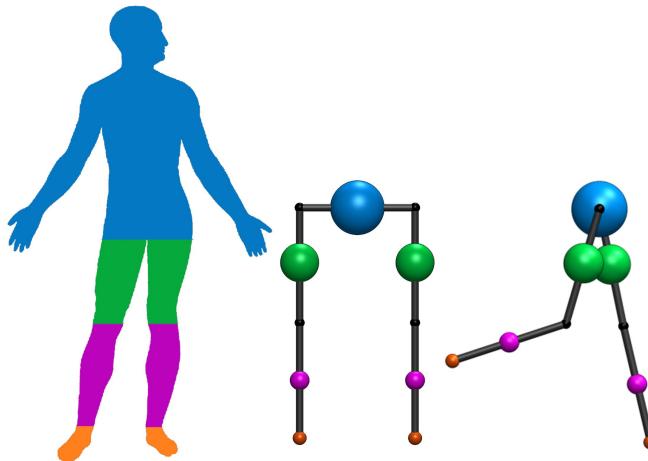
Figure 6.12: PDW model used in this study based on an anthropomorphic model

6.4.1   PDW Model Description

This model however does not account for dorsiflexion, joint stiffness, and joint damping. This model also does not exhibit a double support phase during walking. However, despite these limitations, the model captures certain aspects of gait. We are also able to easily change model parameters such as limb length, masses, and mass distribution, all of which affect the PDW gait stability and symmetry, some of which are difficult to change in humans.

6.4.1.1   Seven Mass Model

While in the previous section I defined a nine mass PDW model with a hip mass, two thigh masses on each leg, and two shank masses on each leg. Due to the nature of this research here, I only employed seven of the nine masses, setting two thigh masses to zero and moving the lower shank mass down to represent a foot mass. As shown in Figure 6.12, the seven mass model relates directly to the trunk, thigh, shank, and foot masses.

6.4.1.2   Model Scaling

The objective is to validate and present insight into using a PDW for human gait analysis. Therefore, it is important to closely match and properly scale the PDW model to an actual individual. For correct scaling, I reference available anthropomorphic data [42], which outlines average masses and mass distributions for a human upper body, thigh, shank, and foot. According to Perry et al. [153], the upper body travels as a unit during normal gait and only moves up and down; hence the upper body, which includes the head, neck, and trunk, is represented in my PDW model as only one hip mass. Arms are excluded here, but are typically only included in physical PDWs to prevent twisting.

This PDW model is one meter in height (ground to hip) while the hip height for the tested individuals is also approximately one meter. In conjunction with the anthropomorphic data, this yielded a scaled down mass distribution between the tested individuals and PDW model, scaling the thigh, shank, and foot masses accordingly. Table 6.1 shows the masses and mass distribution

Table 6.1: Human and PDW Model Parameters Used for Model Validation and Experimental Comparison.

	Anthropomorphic Model Mass for Person (kg)		Anthropomorphic Model Mass for PDW model (kg)		Anthropomorphic Model Segment COM Distance From Hip (m)	
	Human	% Total	Human	% Total	Human	Model
Upper Body	52.90	58.32 %	4.00	57.31 %	0.00	0.00
Thigh	24.40	26.90 %	1.90	27.22 %	0.22	0.22
Knee	0.00	0.00 %	0.00	0.00 %	0.50	0.49
Shank	9.23	10.18 %	0.60	8.60 %	0.72	0.72
Foot	2.91	3.21 %	0.22	3.15 %	0.98	1.00
Full Body	90.7	100.00 %	6.98	100.00 %	–	–

of actual subject measurements for normal walking and corresponding PDW model values. All center of mass distributions for the human and the PDW adhere to the anthropomorphic model.

6.4.1.3 Model Criteria

For the model comparison and experiment, steady state measurements were taken of a stable walking model for normal walking. My stability criteria was defined as fifty steps without the PDW tumbling or with foot drag. To ensure steady state, the PDW model results were taken during stride number thirty-five and thirty-eight, at which point all trials reached asymptotic stability. During each trial the position and velocity of the PDW heel and hip mass were recorded. All PDW data is in the sagittal plane. The PDW ramp angle was $3.2°$ for all trials because it was found to be the most stable decline value.

6.4.2 Human Experiment Data

All seven participants read and signed a consent form approved by the University of South Florida's IRB prior to participating in the three experiment types below.

For comparison, human walking kinetics were recorded from one healthy subject (male, age 32, 1.83 m, 71 kg) walking over a force plate seven times. Horizontal and vertical ground reaction forces were recorded during the stance phase during steady state walking. This data was
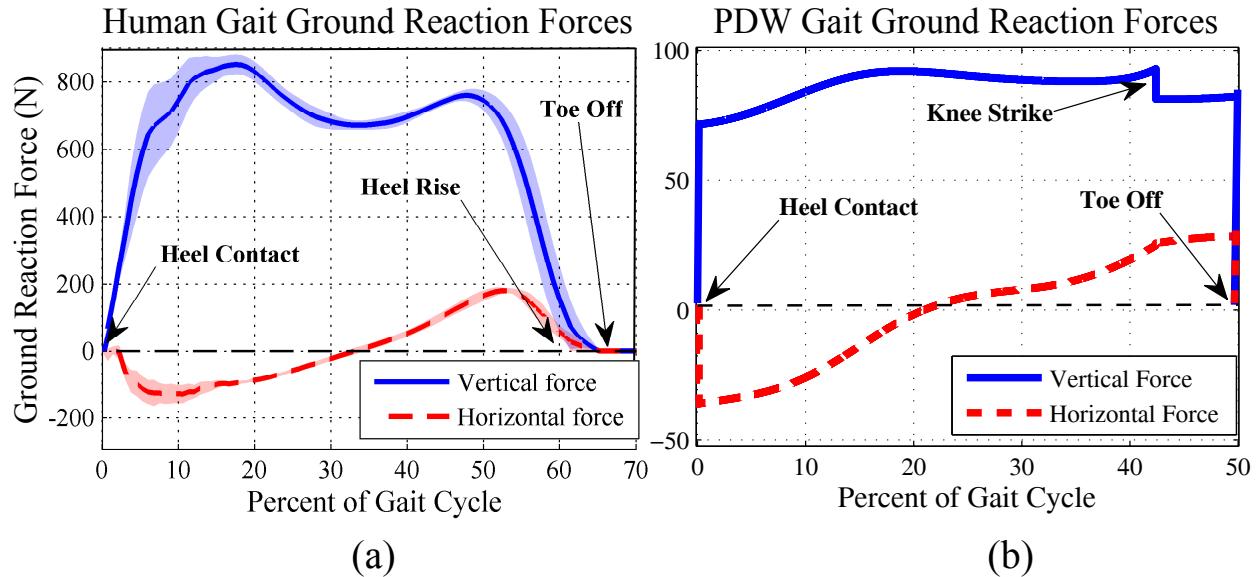
Figure 6.13: Kinetics comparison between human and point foot PDW model. Comparison of kinetics of (a) a human and (b) the modeled PDW gait during stance phase. Shading represents one standard deviation in the human data; there was no variation in the PDW model.

recorded using a AMTI model OR6-5 biomechanics platform. Figure 6.13a presents this recorded kinetics data.

Human walking kinematics were recorded from one healthy subject (male, age 26, 1.86 m, 90.7 kg) by a 3D VICON motion capture system infrared camera at 120Hz in the sagittal plane, capturing strides three and four out of five total. The recorded individual had markers placed on their knees, left and right ilium of the hip bone, and on the lowest point on the back of the subject's sneaker of both feet. Figure 6.14a presents this recorded kinematics data.

Five participants (age 22 ± 1.9, 1.74 ± 0.06m, 88 ± 13kg) were asked to walk with and without a mass attached to their shank. First, each participant walked normally with a blindfold and no mass attached. By blindfolding the participant, visual feedback was removed. They walked 9.1m where the deviation from the straight forward path was measured every 2.3 m by laying markers down as they crossed each discrete distance, shown in Figure 6.15a.

Next, the participants walked wearing a blindfold twice more in the same fashion; however this time with a 4.54kg mass firmly strapped to the middle of their right shank. To trace the participants' walking trajectories, the deviation from the straight forward path was measured
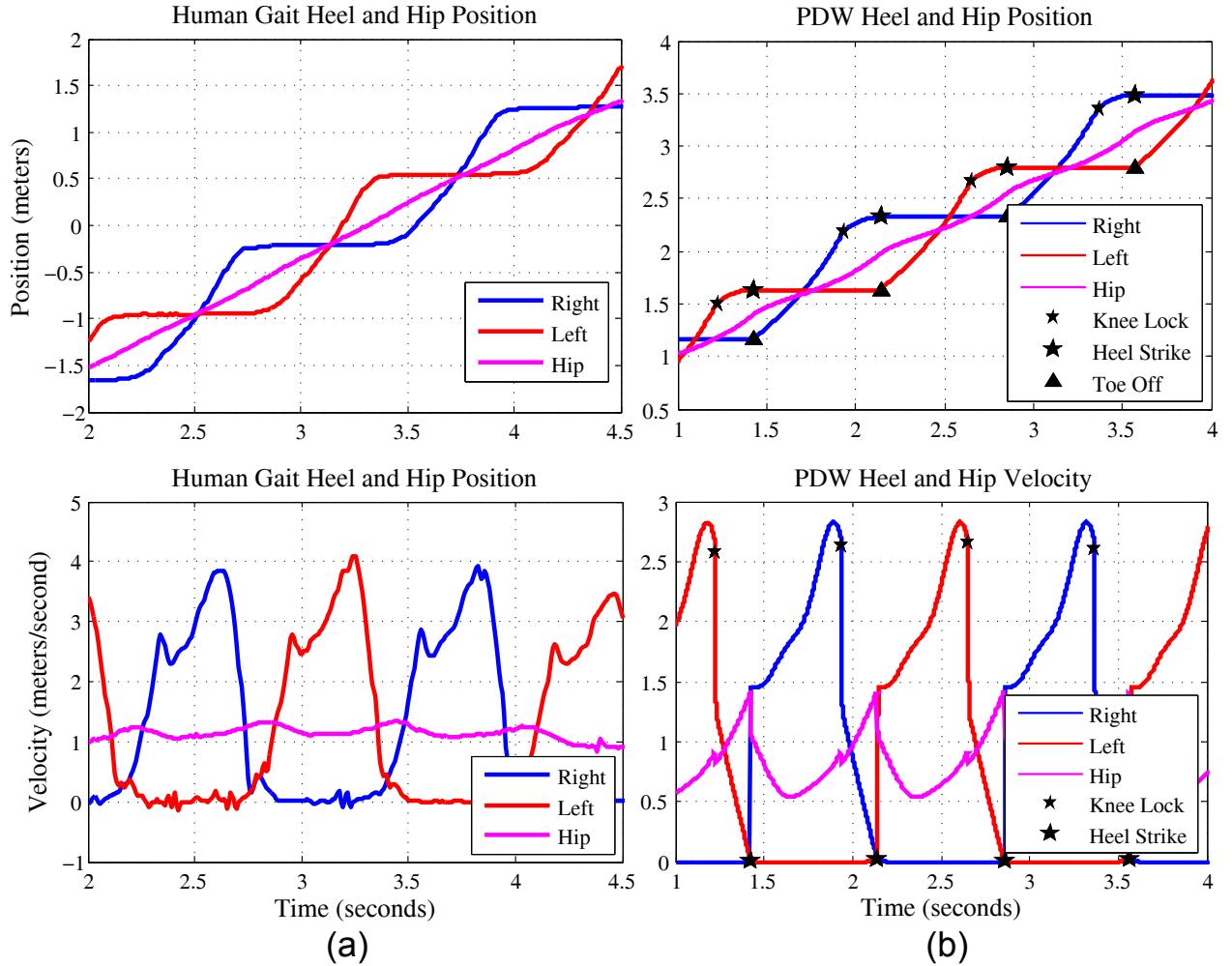
Figure 6.14: Kinematic comparison of human and PDW model walking. (a) Human and (b) PDW walking. While similar in general kinematics, differences arise due to the lack of double support and dorsiflexion in the PDW model.

discretely. After each trial, the weight was removed from the participant's leg in order to minimize gait adaptation. To further prevent adaptation, the blindfolded participant was told that each trial may use a different weight.

6.4.3 Results and Discussion

Considering the limitations of the PDW model, the gait kinetics of the PDW and human are very comparable. As shown in Figure 6.13, the vertical forces peak and valley during the midstance phase at similar instances, but the magnitudes are different. The exaggerated shape of the
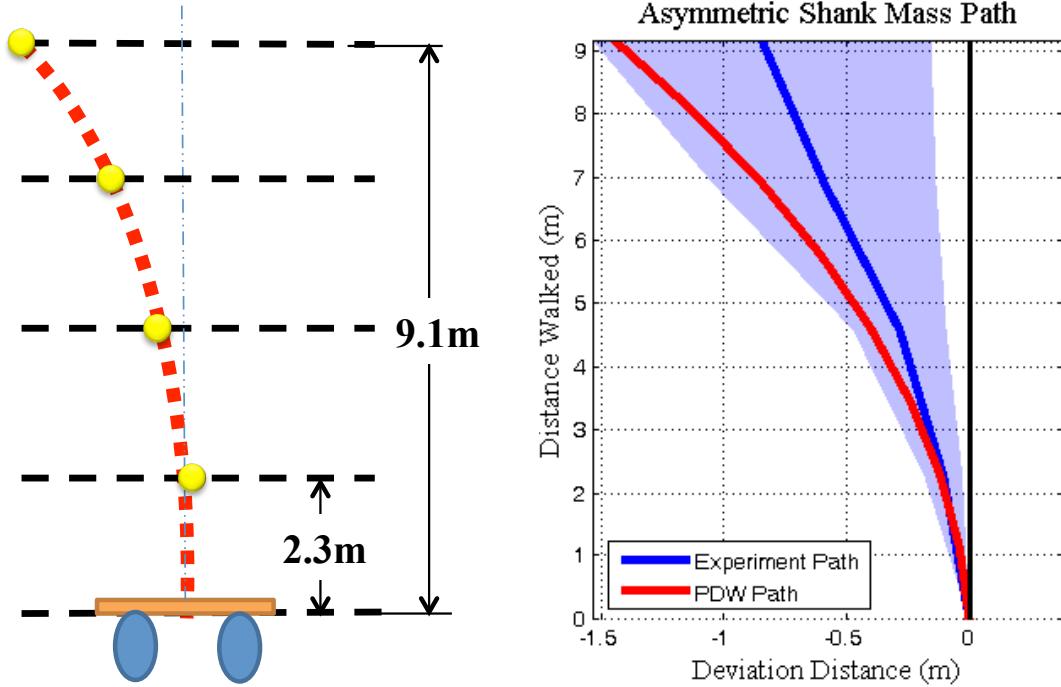
Figure 6.15: Asymmetric walking trajectory deviation comparison between human and PDW model. (Left) blindfolded the subject is asked to walk forward while deviation from initial trajectory path was recorded at discrete distances. (Right) Mean experimental trajectory compared to PDW Model.

human is likely caused by the model's lack of dorsiflexion. The smooth initial and final change in the human walking is not present in the PDW model.

The PDW model and human horizontal reaction forces switch from resisting to assisting forward progression at the same time during stance. However, the maximum forces are slightly different. The PDW model's horizontal reaction forces have a maximum backward force of 48% of the walker mass at heel contact and a maximum forward force of 37% of the walker mass at toe off. The human data shows smaller forces: maximum backward force is 23% of the body mass at 8% of the gait cycle and the forward force is 26% of the body mass at 53% of the gait cycle.

It is apparent that the lack of double support and muscle energy storage/release in the PDW model creates differences. As the PDW engages heel contact and toe off, ground reaction forces instantaneously change, while human walking gradually transitions. This abrupt change in the PDW is due to the absence of dorsiflexion of the opposite foot and double support phase, both of which smooth out the switching in human walking. Also, the collision events are modeled as an

inelastic collision, so the knee strike becomes apparent as a drop in vertical forces and a leveling of horizontal ground reaction forces. This is not evident in normal walking kinetics due to joint stiffness and joint damping.

As observed in Figure 6.14, both human and PDW model kinematics have rhythmic, repetitive, and symmetric motions; however the foot velocity of the scaled down model is 83% of the human. This difference in velocity magnitude is due to the PDW's passive nature in that it has no muscle action to propel it forward and only relies on gravity.

While fluctuations of the hip's velocity profile happen during the same instances in the human and model gait cycles, the model's hip velocity profile is more exaggerated: 40% variation for the model and 10% for the human. This higher fluctuation is explained by the PDW movement down a ramp and the participant's dorsiflexion, which softens the gait. Unlike horizontal walking, the PDW hip drops the extra distance down the ramp prior to heel strike. Also, during the gait cycle in human walking the ankle flexes (dorsiflexion) right before toe off (storing elastic energy) and recoils during toe off (dissipating energy); this movement creates a smoother transition between stance and swing phase.

During stance phase, as the foot approaches knee strike, the human data has a slight dip in velocity while the model velocity at the same instant has a minor bump with a steady increase until knee strike. The velocity dip in human walking is caused by dorsiflexion of the ankle in humans when the tibialis anterior (frontal shank) muscles contract, while the posterior shank muscle group stretches, again storing and releasing energy for a smoother transition [153].

Table 6.2: PDW Model Versus Human Average Walking

	PDW Model	Measured	McIntosh et. al.[133]
Gait Cycle Time (s)	1.42 ± 0.01	1.24 ± 0.1	1.0 ± 0.1
Stride Length (m)	1.17 ± 0.001	1.46 ± 0.02	1.41 ± 0.08
Walking Velocity (m/s)	0.82 ± 0.24	0.98 ± 0.37	1.57 ± 0.12

Both human and model temporal and spacial characteristics such as gait cycle duration, stride length, and walking velocity are in good comparison. Table 6.2 shows these characteristics, including data found in the literature (McIntosh et. al) [133] taken from eleven subjects.

This analysis examines walking patterns with asymmetric mass loading. Increasing the right shank mass yielded an increased right step length naturally causing the individuals to veer to the left (Figure 6.15). Participants veered to the left $9.3 \pm 3.8\%$ with a shank mass that was $5.26 \pm 0.8\%$ body mass.

In order to compare a two dimensional step asymmetry of the PDW walker, the deviation per stride was calculated using the mean participant hip width of 0.381 m and Equation 6.76.

$$\frac{\text{Deviation}}{\text{Stride}} = \text{Stride Length} * \frac{\text{Step Asymmetry}}{\text{Hip Width}}, \tag{6.76}$$

The PDW was shown to be unstable with a properly scaled shank mass asymmetry matching the experiment. However, if the asymmetry mass is scaled down additionally by a factor of twenty (0.26% total walker mass), the walker trajectory is within the bounds of experimental data. This deviation is compared to experimental data in Figure 6.15. Because the vestibular system in humans likely measures the trajectory change and the sensorimotor system compensates slightly to prevent drastic deviation from initial path, the PDW model is assumed to always deviate more due to its purely dynamic nature. Although the scale factor is off, the direction is still in agreement. Thus, the model can be used to predict general trends, but is unlikely to predict magnitudes.

6.5 PDW Walking with Tied-belt Treadmill, Split-belt Treadmill, and the GEMS

This section I will focus on the passive dynamics of gait separate from the cognitive influences associated with walking. I will aim to determine how the passive dynamics affect the gait so rehabilitation methods can be evaluated prior to testing on humans. I will compare the passive dynamics to humans walking in four environments: (1) over ground, (2) on a tied-belt treadmill, (3) on a split-belt treadmill, and (4) on the Gait Enhancing Mobile Shoe (GEMS).

As mentioned before an important characteristic of PDWs is that the focus is on the dynamic effects of a gait, excluding the cognitive aspects. For a rational comparison, the PDW model parameters used for this analysis are extracted from an anthropomorphic human model and proportionally sized such that the masses and mass distribution are relatively sized down from an individual (Figure 6.12). While my walking model has limitations, it does give further insight into gait and gait rehabilitation.

First, I will focus on explaining our PDW computer model structure and parameters. Next, I will compare a normal, undisturbed, steady state, and symmetric PDW gait to a recorded normal human gait. I will then explain and discuss our results of the PDW model in the four walking conditions.

The PDW model used in this experiment will be the same point-foot model used in the previous section, Section 6.4.

6.5.1 Experimental Setup

In addition to normal walking, our seven mass model enables testing on three additional setups: tied-belt treadmill, split-belt treadmill, and onto a motion that resembles a GEMS. For clear interpretation and comparison of normal and PDW model gait behavior, we show the position and velocity versus time data for each environment for each heel. All participants read and signed a University of South Florida IRB approved consent form prior to participating.

6.5.1.1 Normal Walking

- *Human*: Measurements for humans walking normally were taken by a 3D VICON motion capture system infrared camera at 120 Hz at the University of South Florida. Measurements were taken in the sagittal plane, capturing strides three and four out of five total. The recorded individual had markers placed on the left and right ilium of the hip bone and on the lowest point on the back of the subject's sneaker of both feet. The subject was age 26, male, 1.85 m in height, with a weight of 90.7 kg.

208

- *Model*: Normal walking model used the anthropomorphically scaled PDW model is described in the previous section.

6.5.1.2 Tied-belt Treadmill Walking

- *Human*: Human measurements for tied-belt walking were taken at Moss Rehabilitation Research Institute using CODAmotion infrared motion system at 100 Hz in the sagittal plane. Tied-belt and split-belt data were both recorded on a 1.49 kW (2 hp) WoodWay split-belt treadmill. The subject for tied-belt and split-belt treadmill was age 30, male, 1.81 m in height, with a weight of 81.6 kg. The tied-belt treadmill was run at a constant 0.48 ± 0.02 m/s. To match walking data, a speed equivalent to the recorded negative belt speed was added; thus, their walking speed is comparable to walking over ground at the same speed as the treadmill.

- *Model*: The PDW model was modified so that the ramp it is walking on constantly moves at a set velocity. Each time a leg is in stance phase, a steady backward velocity is applied, displacing the foot backwards like a treadmill. One of the feet is always in contact with the ground and that foot experiences a constant backward velocity. The velocity magnitude for the tied belt treadmill was the mean of the treadmill speed used in weight-supported treadmill training for rehabilitation scaled down to match the model.

6.5.1.3 Split-belt Treadmill Walking

- *Human*: Split-belt walking measurements were taken in the same location, setup, and fashion that the tied-belt measurements were taken. The slower belt on the split-belt treadmill was run at a constant 0.48 ± 0.02 m/s, while the faster belt was run at 1.45 ± 0.03 m/s. Again, as with the tied-belt treadmill data, we standardized the collected split-belt data by adding an equivalent amount of belt speed to the recorded negative belt speed.

- *Model*: The model is able to simulate a PDW walking on a split-belt treadmill by treating each tread independently. As only one tread has a greater relative velocity than the other, we set one tread to zero and move the opposite tread at a constant velocity during the stance phase. The velocity magnitude for the split-belt treadmill was determined using a split-belt treadmill adaptation study for post-stroke patients. The velocity is the mean walking speed of the hemiplegic affected individuals.

6.5.1.4 GEMS Walking

- *Human*: This study was performed in the same location and fashion as normal walking, but while wearing the GEMS.

- *Model*: Like a split-belt treadmill, the GEMS pushes one foot backward relative to the opposite foot (faster belt). As per its design, the shoe pushes the user's foot back only a limited distance before smoothly bottoming out and coming to a halt so the user can toe off. We proportionally scaled down the mass of the GEMS, but because the size of the PDW model is closely matched to our test subject, the dimensional aspects such as height remain constant. To model the GEMS, its mass, velocity, and travel distance were scaled to the size of the PDW at 7%. The actual GEMS weight of 1.65 kg was scaled down to 7% of actual to 0.12 kg and added to the right foot mass of the PDW. GEMS velocity was scaled from 0.35 m/s to 0.025 m/s and the GEMS fixed travel distance from 0.15 m to 0.01 m.

6.5.2 Results and Discussion

These results compare the differences between the PDW model (passive) and a human walking (active), thus we do not expect results to align perfectly. We aim to understand the effect that the passive dynamics have on the gait pattern separate from the cognitive influences. This understanding can help us to validate the use of a PDW model for gait pattern prediction. The temporal and spatial values for human and PDW model are summarized in Table II.
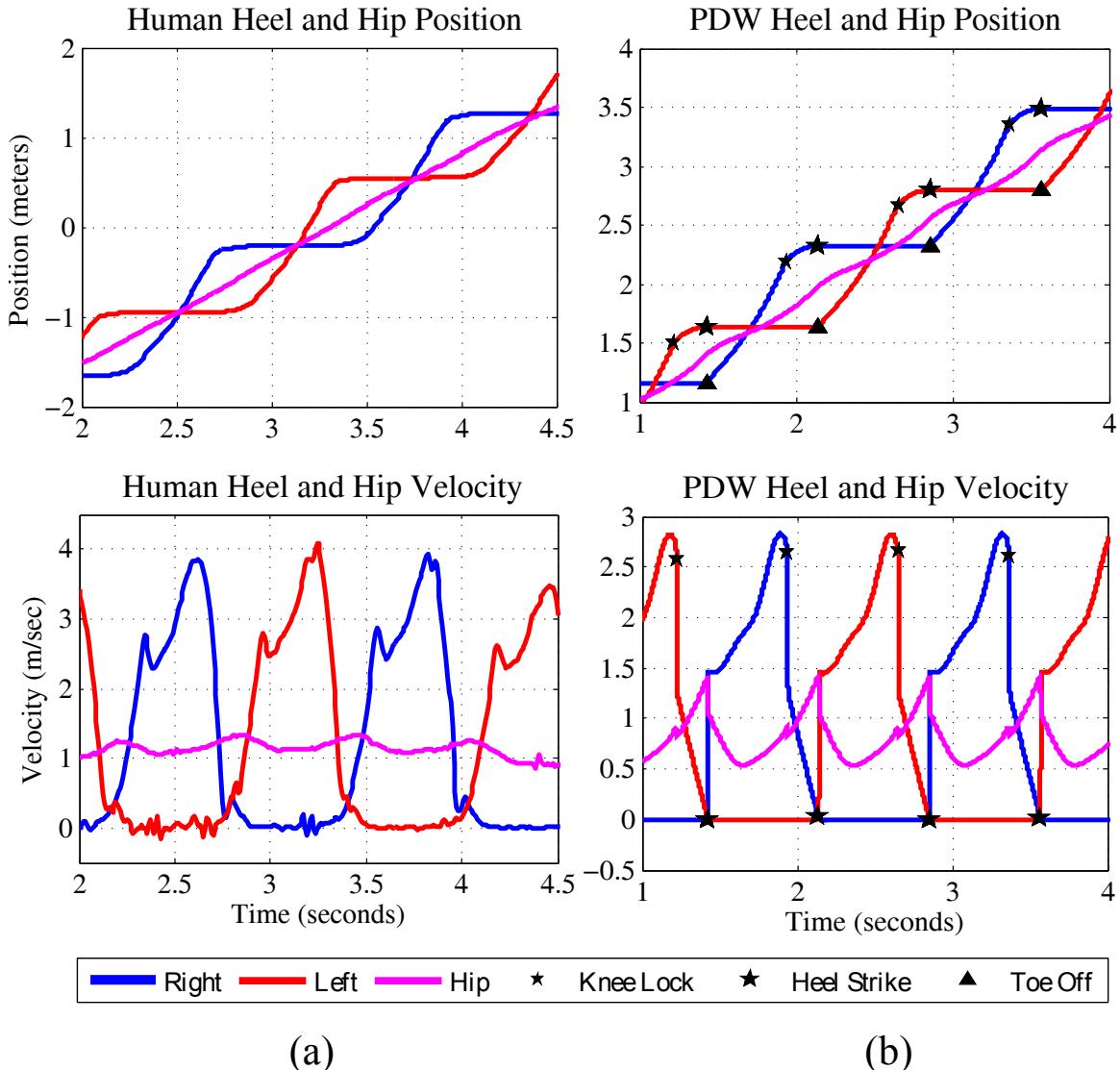
Figure 6.16: Kinetically comparison between human and point foot PDW model. Normal human walking data as captured by a motion system (a) compared to steady state PDW walking down a decline (b)

6.5.2.1 Normal Walking and Tied-belt Walking

Normal human walking kinematics has a rhythmic, repetitive, and symmetric motion. As observed in Figure 6.16, both human and model results follow this description and are very comparable, however velocity of the model is 83% of the human. The PDW model is completely passive and does not rely on any energy input such as human walking controls, hence the slower PDW walking velocity down the ramp. Normal walking in the model and human were both

symmetric in swing time and step length. Both temporal and spatial aspects of walking in PDW and human walking were within 13% and 21%, respectively.

There is a variation in the model's velocity profile during three-link phase. As the foot approaches knee strike, the human data has a slight decrease in velocity while the model velocity at the same instance in the gait cycle has a minor increase with a steady increase until knee strike. This difference can be explained by the kinematics of the opposite leg and the nature of the PDW model. At that instant the human data velocity decrease is caused by stance leg dorsiflexion of the ankle when the tibialis anterior (frontal shank) muscles contract, while the posterior shank muscle group stretches, dissipating and storing kinetic energy and creating potential muscle energy for toe-off (energy conservation). This generates an elastic recoil, preparing the limb for swing phase. As our PDW model does not have ankles, this "push-off" phenomenon does not occur.

While wavering of the hip's velocity profile happens during the same instances in the gait cycle as the model, the model's hip velocity profile is more exaggerated, with velocity fluctuation of 40% for the model and 10% for a human. This higher fluctuation is explained by the PDW movement down a ramp and dorsiflexion. Unlike horizontal walking, the PDW hip drops the extra distance down the ramp subsequent to knee strike and prior to heel strike. Also, during the gait cycle in human walking, the ankle flexes just before toe off and recoils during toe off. This movement creates a smoother transition between stance and swing phase.

It is interesting to note that hip velocity fluctuation in human walking on the tied-belt treadmill is more pronounced than when walking over ground; walking on the treadmill more closely resembles the hip velocity of the PDW in both normal and tied-belt walking.

In order to further investigate the similarities between human walking and PDW walking, we compared walking on an incline. The ramp angle of the PDW was decreased from $3.0°$ to $3.4°$ at $0.1°$ intervals and compared to A.S.McIntosh et. al.'s [133] human trial data which measured duration, stride length, and walking speed of walking on a $0°$ to $10°$ decline. The PDW model gait cycle duration, stride length, and walking speed trends matched that of human data. As walking
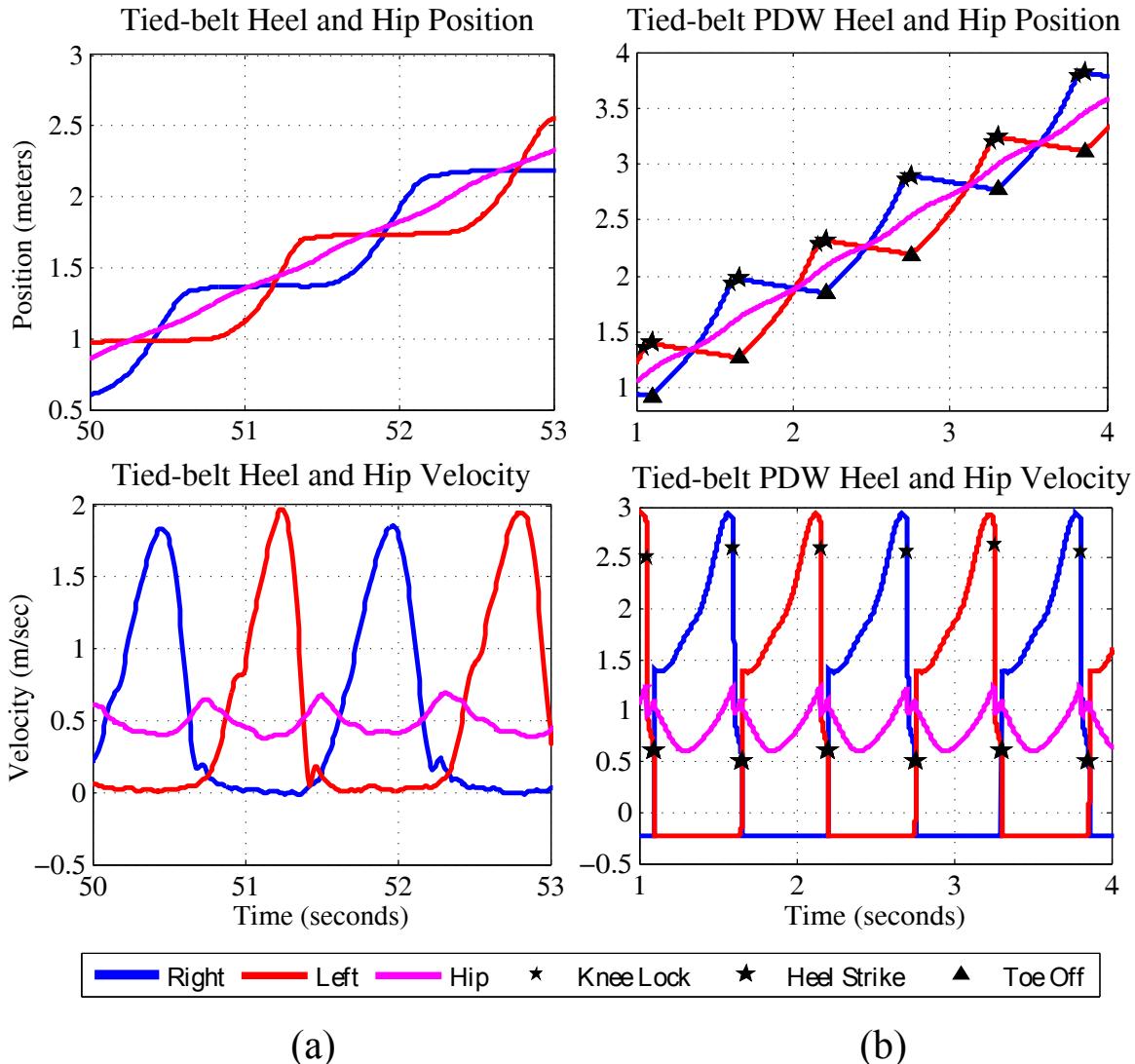
Figure 6.17: Kinematic comparison between human and PDW model during tied-belt treadmill walking. Kinematics of tied-belt walking for (a) human and (b) PDW model.

surface slope decreased, both human and model stride length and walking speed increased, while both human and model gait cycle time decreased.

Due to PDW walker instability, tied-belt velocity could not be fully simulated at a properly scaled model velocity of 0.48 m/s. Instead walker tied-belt velocity was iterated to find a maximum possible speed of 0.23 m/s (52% less). For consistency and comparison, human tied-belt data was normalized to a non-zero hip velocity. Figure 6.17 shows both human and modeled tied-belt walking.
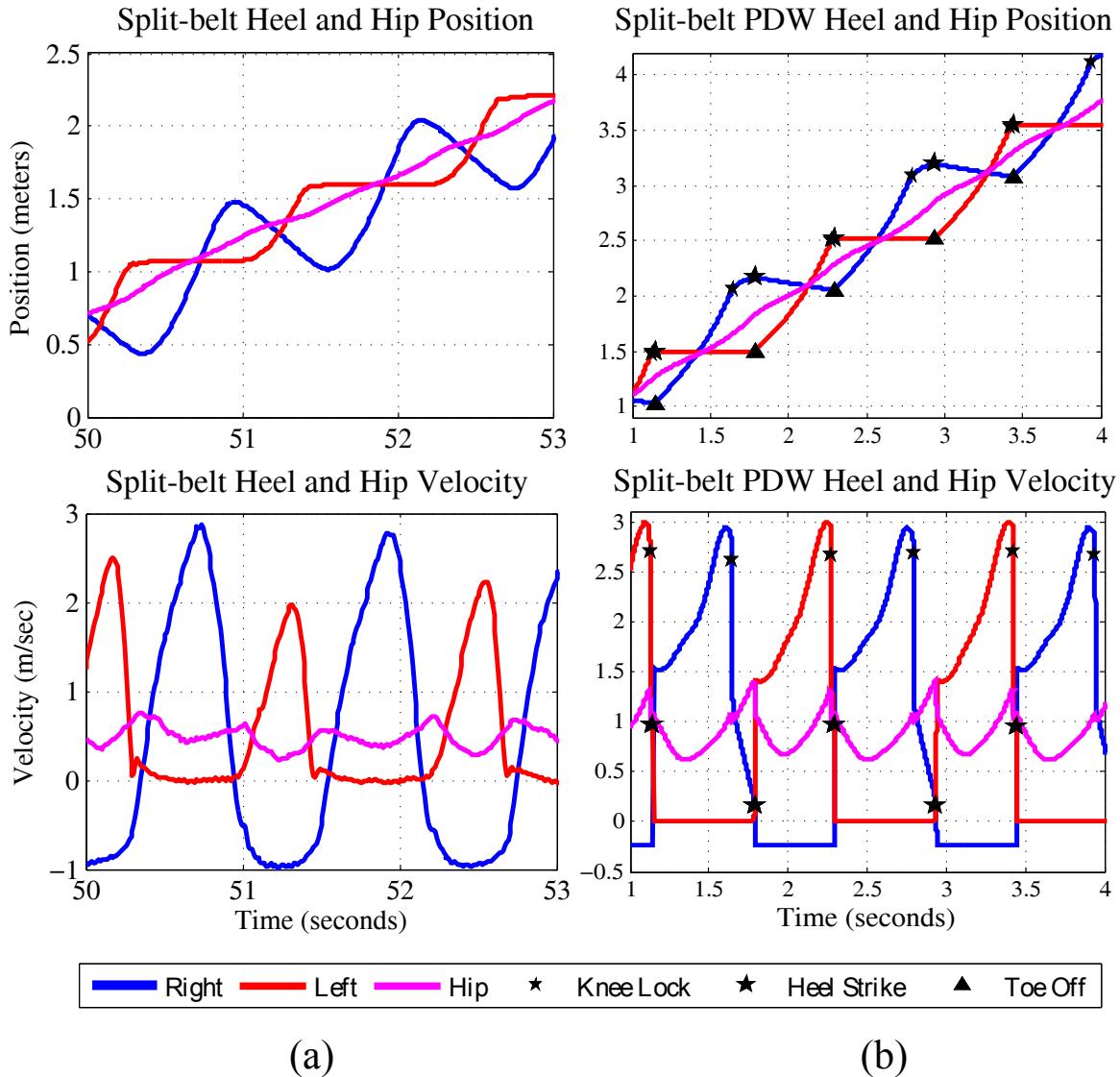
Figure 6.18: Kinematic comparison between human and PDW model during split-belt treadmill walking. Kinematics of split-belt walking for (a) human and (b) PDW model.

While human and model walking parameters are comparable, spatial and temporal walking characteristics between tied-belt human and model walking show a greater difference with gait cycle time, step length, and maximum foot velocity difference of 35%, 58%, and 41%, respectively. Although this difference seems significant, one must consider that the belt speed was run at nearly half the speed due to walker instability.

6.5.2.2 Split-belt Walking and GEMS Walking

As shown in Figure 6.18, the PDW model could not simulate a scaled down split-belt treadmill velocity of 0.78 m/s due to instability. Using appropriate anthropomorphic data, the PDW tied-belt and split-belt speed was iterated to find a maximum split-belt speed of 0.25 m/s (75% less). However, asymmetric trends persisted in the temporal domain. With respect to temporal parameters, the model's asymmetry followed the same trend with a right swing phase and left swing phase.

When wearing the GEMS, position and velocity profiles for the human and the model data yielded asymmetric tendencies as expected. As seen in Figure 6.19, human and modeled profiles are very comparable in shape. As the GEMS pushes the right foot backward, the left foot compensates by attaining a 25% greater peak velocity during swing phase. This difference in velocities is only 13% in the simulated data. Also during the right foot swing phase with the GEMS, both human and simulated velocity profiles take a slight dip prior to knee strike and do not summit as sharply as the opposite foot velocity without the GEMS. This dip is largely due to the extra weight of the shoe.

While the test subject substantially compensated for the backward GEMS movement by a faster forward step of the opposite leg and in turn a faster hip progression, the model's hip does not portray this. The simulated model hip movement shows the same trend subsequent to GEMS movement, and it kept a constant maxima and minima.

Swing duration trends agree between human and model. Both show a greater swing time on the GEMS foot in comparison to the opposite foot, 25% and 28% increase respectively. However, the step length difference trend between human and model varied. Although the individual's right step length was 32% lower than the left, PDW model right step length was 29% higher than the left.

215
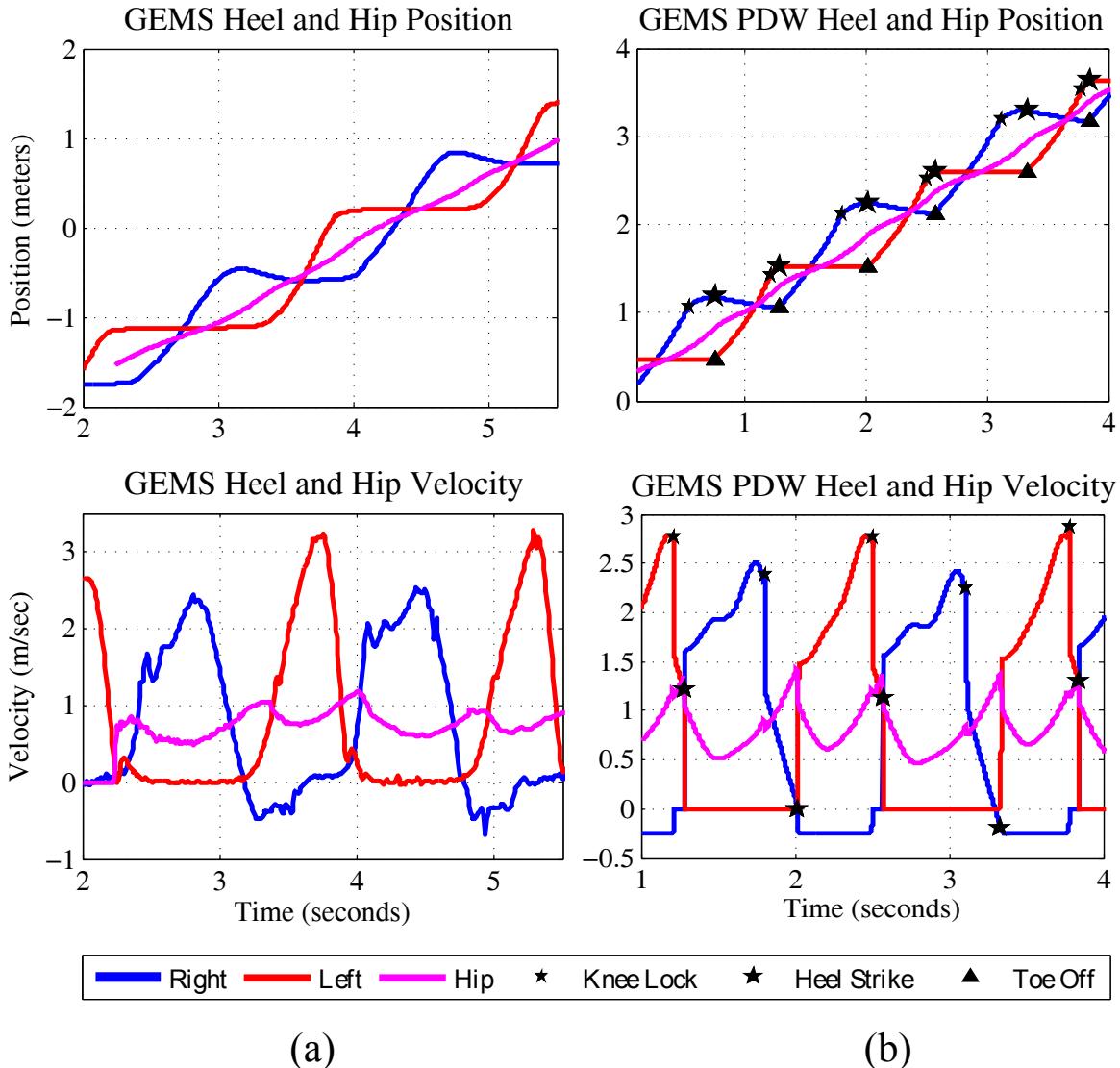
Figure 6.19: Kinematic comparison between human and PDW model during Gait Enhancing Mobile Shoe walking. Measured (a) and PDW modeled (b) walking kinematics with the Gait Enhancing Mobile Shoe (GEMS)

6.6 Effects of Foot Roll-Over Radius and Curvature

In this section, I will be using the variable curve-foot model to analyze the effects of changing the radius of a PDW roll-over shape. That is, I will be increasing the increasing the foot radius of a compass gait PDW model.

6.6.1   Experimental Setup

The compass gait variable curve-foot model was set up such such that it iterated through increasing foot roll-over shape radius. The PDW was set up to have a hip mass of 2kg, thigh mases of 1kg each, and shank masses of 0.05kg each. Masses were distributed evenly along the legs at an interval of 0.33m. The PDW was perfectly symmetric and does not have a offset distance at the shank-foot point, the shank is attached to the foot curve origin.

In order to change the foot radius, which is held constant, the initial foot roll-over-shape radius was increased form 0.1m to to 0.45m at an interval of 0.05m, where the PDW total leg length was specified at 1.0m. The radius change was only applied such that the radius would increase towards the front of the walker. Curving the foot shape such that it decreased towards the front of the walker would make the PDW become unstable and topple forward. In this part of the experiment the PDW walked down a decline of $2°$.

In the second part of the study, the PDW foot curvature was changed from 0m/rad (constant radius) to 0.20m/rad. In this part, in order to better identify trends independent of ramp angle, the PDW walked down a combination of three ramp angles: $3.72°$, $2.86°$, and $2.01°$.

Only stable PDW combinations were recorded. As mentioned before, the PDW was deemed stable if it walked fifty steps or more.

6.6.2   Results and Discussion

As seen in Figure 6.20, as the foot roll-over shape radius increased, the vertical ground reaction force decreased, while the horizontal force along the ramp approached a constant value. The trend of these results perfectly simulates a rolling foot in human walking study by Adamcyk et al. [1, 2], which shows the same settling ground reaction forces with human walking as the foot roll-over radius is increased.

It is also observed that the as the foot radius is further increased the ground reaction forces settle to a constant value. This constant force profile is the same as a round wheel rolling down a ramp. So, as the PDW's foot radii roll increase to where the foot radius equals the PDW's leg
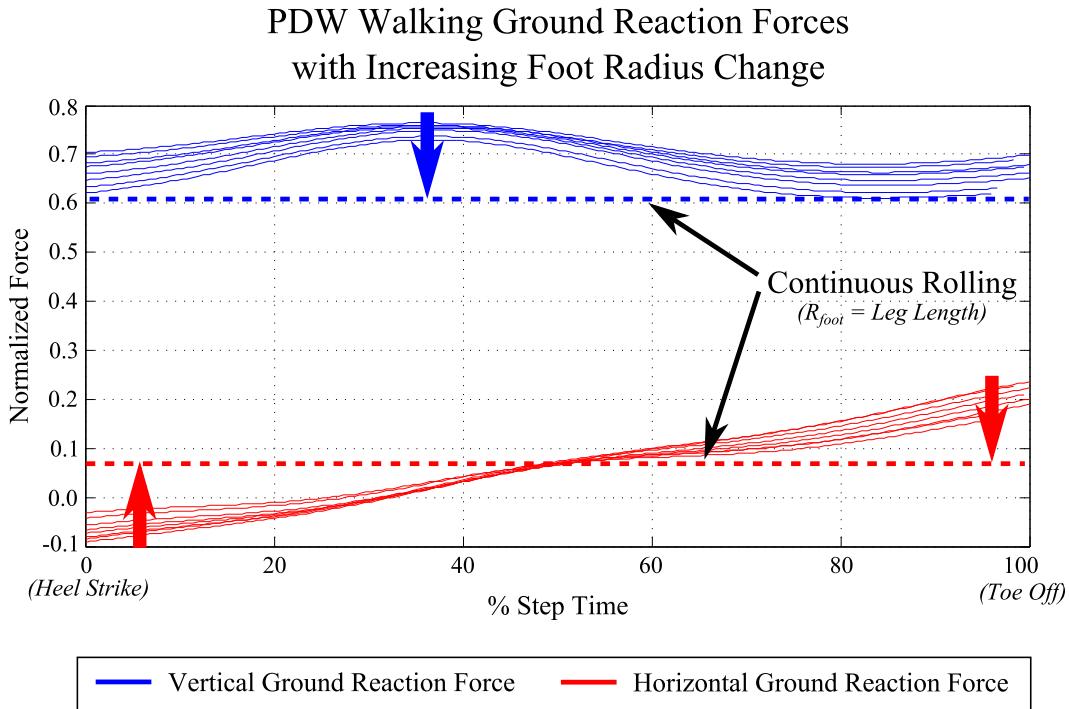
Figure 6.20: PDW model walking ground reaction forces for increased foot radius. As the foot radii increase, the ground reaction forces settle to a constant value. In essence, when the foot radius equals the leg length, the entire PDW becomes a circle and continuously rolls down the ramp.

length, discrete steps disappear and the PDW progresses down the decline with a continuous rolling motion

As the curvature of the foot was increased the PDW used more energy to progress down the ramp. That is, the energy per distance traveled became greater as the foot roll-over shape radius increased towards the front of the walker. This trend can be seen in Figure 6.21 is interesting in that it clearly shows a trend in energy expenditure with foot curvature. Although the walker became unstable with a negative curvature, I hypothesize that the same energy expenditure trend is mirrored as a roll-over shape decreases in radius. In other words, less energy is spend walking with feet that decrease radius towards the front.

Looking at the ground reaction forces in Figure 6.22, it can be seen that as the foot curvature towards the front increases, the the vertical ground reaction force increases, while the horizontal
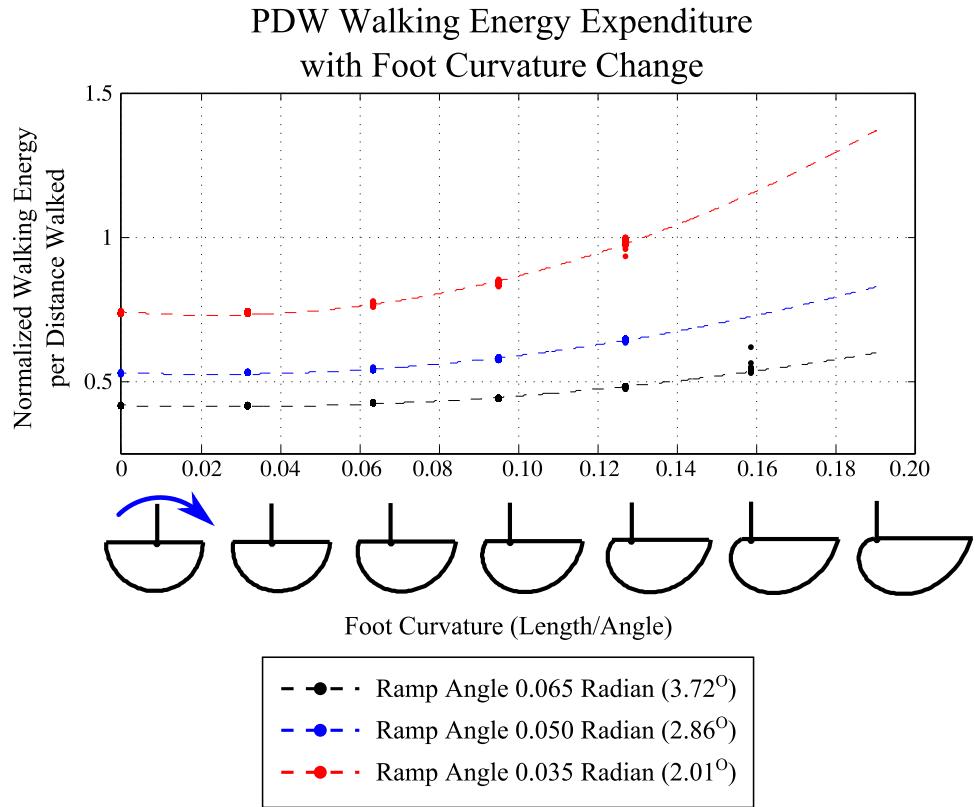
Figure 6.21: PDW model energy expenditure for increased foot curvature. As the foot curvature increases, the PDW uses more energy to walk

ground reaction force along the ramp decreases. Intuitively this simulation result hold true in that, as one rolls onto a greater radius, more pressure is applied to the foot.

By my kinetic shape concept discussed in the previous chapter, it is known that a decreasing radius produces a rolling ground reaction force. Given that the PDW walks (or rolls) down an incline, gravitational forces produce a constant force along and down the incline, this is seen in previous Figure 6.20. This constant rolling force acting down the ramp caused by gravity is impeded by the rolling force caused by the decreasing foot radius. The difference in these two is the resulting horizontal force along the ramp and seen in Figure 6.22.

Again, due to instability to the PDW a negatively curved foot was not tested, however, I am hypothesizing that the simulation results presented in Figure 6.22 are mirrored about the zero foot curvature axis.
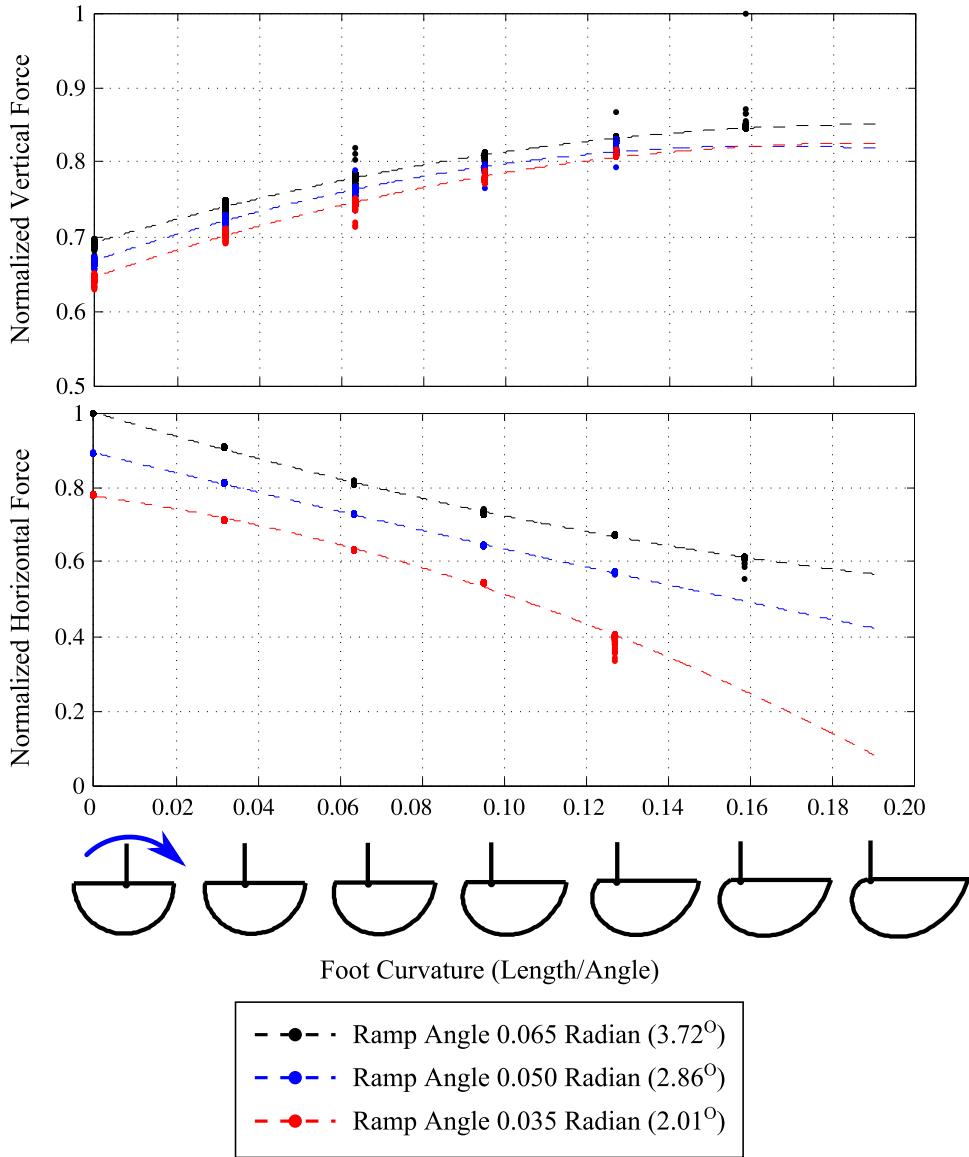
Figure 6.22: PDW model ground reaction forces for increased foot curvature. As the foot curvature increases, the PDW exerts more vertical and less horizontal force during locomotion

6.7 Uncanny Gait in Biped Walking

This section aims to determine the depths to which the uncanny valley relates to the perception of pathological and normal human gait using my PDW models. Altering gait biomechanics is generally done in the fields of prosthetics and rehabilitation, however the perception of the gait is often neglected. Although a certain gait can be functional, it may not be considered as normal by

observers. On the other hand, an abnormally perceived gait may be more practical or necessary in some situations, such as limping after an injury. This research will help to find the balance between the form and function of gait. In this section, gait patterns are created using my PDW model that allows gait patterns to be systematically changed without the confounding influence from human sensorimotor feedback during walking. This standardized method allows the perception of specific changes in gait to be studied. The PDW model was used to produce walking patterns that showed a degree of abnormality in gait cadence, knee height, leg step length, and swing time created by changing the foot roll-over-shape, knee damping, knee location, and leg masses. Different gait patterns were shown to participants who rated them according to abnormality or human-likeness.

6.7.1 The PDW and The Uncanny Valley

A healthy human body with a human-like shape and movements is perceived as normal, healthy, and familiar. Also, an exaggerated caricature animation of a human body and its movements can be accepted as normal and familiar as we expect the caricature to be un-human-like. However, human-like objects, models, robots, or dolls often are designed to mimic normal human body parts, motions, or gestures that almost look normal, but cause a repulsion or abhorrence. This psychological reaction to the almost human-like is known as the uncanny valley and is recognized in the fields of cinematography, biomedical technology, and neurological conditions [49, 96, 138]. The uncanny valley can sometimes be described as the perception of something that is familiar, yet incongruous, creating a repulsive effect. As shown in Figure 6.23 and further discussed in the previous background chapter, the uncanny valley is the decent of the plot between human likeness (horizontal axis) and our familiarity (vertical axis) [138]. Although the notion of the uncanny valley is widely known, the depths and edges of it are still fuzzy and open for study.

As we approach the uncanny valley from the left (low human likeness), we encounter it with lifeless objects, models, and movements such as industrial robots, stuffed puppets, or humanoid robots. The left side of the valley is characterized by motions and attributes that we know not to be human. However, approaching the uncanny valley from the right (high human likeness),

221
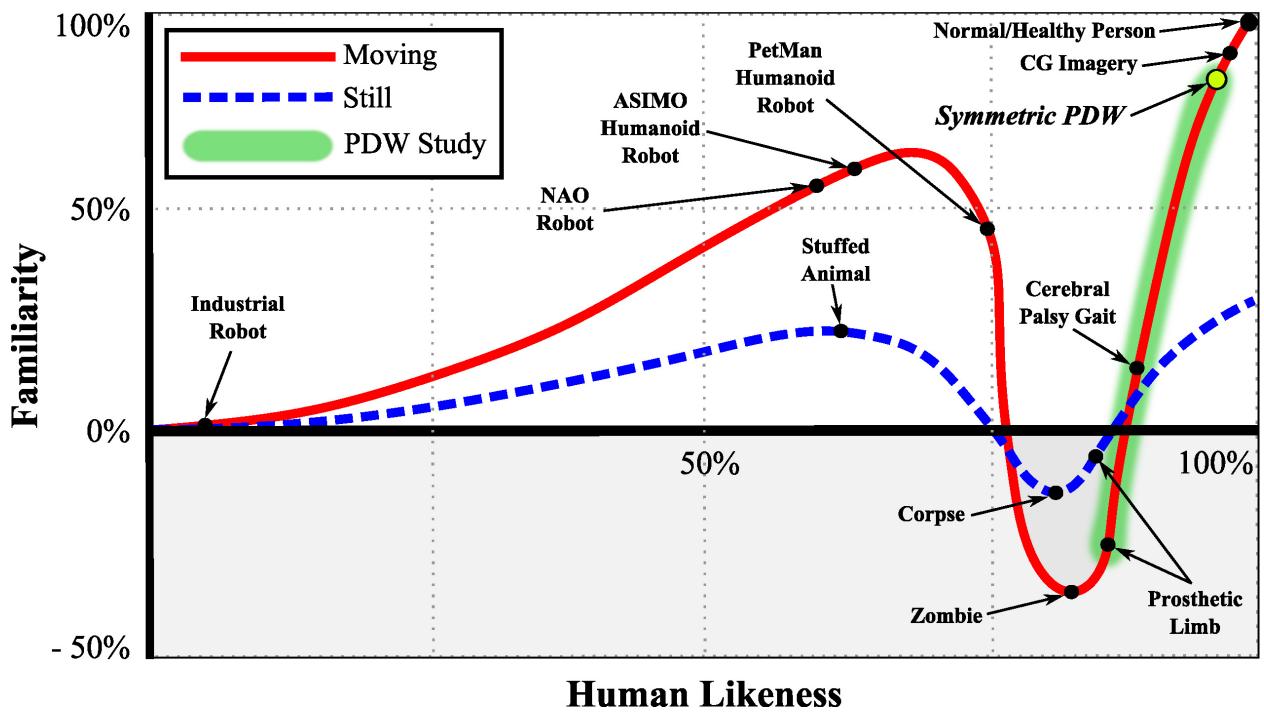
Figure 6.23: The uncanny valley of still and moving objects. As human likeness increases, so does the observer's familiarity up until a sudden decrease in familiarity into the uncanny valley where familiarity becomes abnormal, perceived with an uneasy or eerie feeling.

that is, coming from the perception of a normal and healthy person, we encounter it with lively computer generated and/or realistic features and motions. This side of the valley is populated by things that are very human-like, however may show some traits that are perceived as not exactly normal. In this chapter I will focus on the edge of the right side of the uncanny valley. Specifically, I will examine the perception of human walking and the limits to which gait will continue to be perceived as normal in the presence of slight abnormalities.

Previous studies have aimed to cross the uncanny valley [44, 202], but this proposed research is coming from the opposite direction and examining what changes cause a human-like gait to begin to appear uncanny. My hypothesis is that gait can appear human-like even when it deviates from perfect temporal and spatial symmetry. These results could guide physical therapists in their treatments and would benefit individuals with disabilities that affect gait by determining

the gait patterns that minimize the perception that their gait is impaired. Appearance is a major concern for individuals with a disability [19, 20].

My goal in this chapter is to characterize the decent into the uncanny valley from the right hand side with various walking models, comparing normal healthy gait to variations in gait. Since there are many gait patterns that can provoke uncanny feelings in an observer, I am using simulated gait models to maintain consistency and precision of the measured gait parameters to allow for a controlled experiment on the perception of specific gait changes. Using my PDW computational model, I am specifically looking at what uncanny effects arise from deviations in gait speed, knee location, spatial and temporal symmetry, foot roll-over shapes, and knee damping.

subsectionUncanny Valley and Pathological Gait Humans are keenly aware of walking motions that are close, but not exactly the same as a human makes. To other human observers, a normal healthy gait does not draw any attention and is usually dismissed as ordinary. However, as normal and healthy walking becomes unhealthy or impaired, it starts to raise attention and sometimes uneasy feelings, hence falling into the uncanny valley of gait mechanics. At an extreme end, this uncanny feeling can be provoked when observing the gait of extremely walking-impaired individuals suffering from neurological movement disorders such as athetoid cerebral palsy or dystonia, resulting in involuntary muscle contractions, repetitive movements, or abnormal postures. However, even smaller alterations from normal healthy gait may be easily recognizable and viewed as abnormal or unfamiliar. Pathological human gait, such as a slightly limping leg or sprained ankle, can be viewed as human-like and normal, yet the impairment will be quickly identified.

In healthy humans, the two sides of the body are mostly symmetric with regards to mass and strength; thus, it makes biomechanical sense to have both knees at the same location [195]. However, when wearing a transfemoral prosthesis, the mass and strength of the two legs are no longer equal and the biomechanical reasons to keep the same prosthetic knee location no longer exist. Moving the knee location adds a degree of freedom in the prosthesis design process that allows the gait dynamics to be adjusted to a desired gait pattern. However, changing the knee

location depends on the answer to an essential question: what amount of knee location asymmetry can be considered normal or human-like?

Note that I am only concerned with the bio-mechanical movements of leg limbs and how these movements are perceived in this study. We are not investigating the effects of limb thickness or texture perception, such as wearing a Flex-Foot Cheetah prosthetic blade foot [60].

6.7.2 Uncanny Valley and Artificial Gait

Toyota's ASIMO [176] and Aldebaran Robotics's NAO [5] robots are statically stable robots that are able to simulate a slow and careful walking pattern while always keeping their center of gravity above their support base. Humans can walk this way, but rarely do. Such statically stable robotic gait is only partially perceived as human-like and can come off as unfamiliar, "robotic", and sometimes uncanny. While more elegant and proficient in its gait, Boston Dynamics's PetMan [155] is an anthropomorphically correct biped able to mimic gait very similar to humans. PetMan is able to skillfully navigate across obstacles such as stairs and withstand moderate perturbations during gait. Nonetheless, its more realistic motions invoke an uncanny perception of its movements. These humanoid robots are perceived to be on the left side of the uncanny valley and so are of little direct interest to my study and hypothesis about the right edge of the valley.

On the other hand, dynamically stable walking robots such as a passive dynamic walker (PDW), exhibit a more fluent and human-like gait. A PDW is a biped walking robot that walks down a decline with gravitational energy as its only source of power and with no active feedback [132]. PDW gait is shown to be kinematically and kinetically similar to human gait [71, 76]. While PDWs can be used to recreate and analyze normal and pathological human walking patterns, they can also be utilized to study the effects on gait caused by manipulating swinging limb parameters such as leg lengths, leg masses, joint stiffness, or ROS [87]. Because of the PDWs elegant gait movements, it is perceived as human-like and on the right side of the uncanny valley as shown in Figure 6.23.

224

6.7.3 Experimental Setup

6.7.3.1 Passive Dynamic Walking Gait

In this study, I am using a PDW computational model because the PDW model is repeatable, precise, and can be systematically altered in order to derive model deviations that descend lower towards the uncanny valley. This allows the controlled variation of desired parameters (i.e., step length, limb mass, joint stiffness, ROS etc.) without the inconsistency of human sensorimotor control under the same walking conditions.

The PDW model I am utilizing in this study is a two dimensional nine-mass multi-pendulum system with constant-radius-shaped feet. That is, it represents an anthropomorphically correct walking human from the waist down and viewed from a two dimensional sagital plane. PDW masses are represented as one hip mass and two masses per each thigh and shank. The PDW model also rolls over a constant radius roll-over shape just as a walking human would (Figure 2.8c). Although, the PDW can walk down a greater decline, our model walks down a slope of $3.5°$ for all gait variations presented in this study. We specified the PDW model height, thigh length, and shank length, mass and mass distribution according to widely surveyed anthropomorphic body segment data [42]. The roll-over shape for normal walking was taken to be one-third leg length. All PDW deviations presented in this study were stable for at least fifty steps.

6.7.3.2 Passive Dynamic Walking Animation Videos

Because this study predominantly focuses on normal and abnormal human walking motions, I carefully depicted the PDW model close to the aesthetics of a person walking and viewed form the side. This helps to increase participant's familiarity and human likeness of the presented walking models. Although the PDW walks down a decline, it was rotated to look as if it is walking on level ground. The animation was closely depicted to mimic human muscles, joints, and knees by considering waist, mid-thigh, and max calf circumference as outlined by the Unitied States Department of Health and Human Services Health Statistics Report [130]. This aesthetic transformation of my PDW model can be seen in Figure 6.24. To ensure depicting stable and
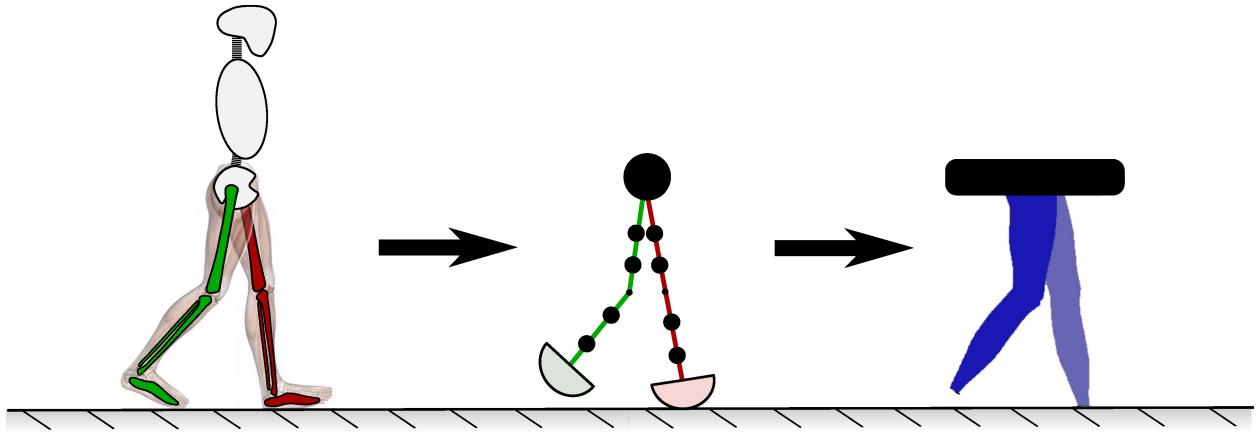
Figure 6.24: The evolution of the PDW model used for gait perception experiment. The human lower limb model presented to participants was modeled with a PDW to move naturally while being carefully depicted to look like normal human limbs.

consistent gait, the PDW model animation recording was performed between strides (left and right step) forty and forty-three.

Various walking parameters were computationally and systematically varied to deliberately deviate from familiar and human-like gait to explore the uncanny valley. With my PDW computational model I was able to simulate many parameters with any parameter resolution, however that would yield many videos to be judged by participants, which would result in a prolonged experiment. The different parameter categories that were chosen to be altered and presented to participants are shown in Table 6.7.3.2. All PDW leg variations were applied to the leg closest to the observer (i.e. darker, right). Note that Equation 6.77 is used to define percent asymmetry between two parameters.

$$Asymmetry\ (\%) = \left(\frac{abs(Left - Right)}{(Left + Right)/2} \right) \tag{6.77}$$

- *Normal Gait*: The walking pattern that was presented as normal and healthy to participants had no asymmetries between left and right sides. This normal gait walking cadence was matched to that of a healthy adult walking cadence at 110 steps/minute. The participants were shown this video of a normal gait prior to viewing and judging all other videos.

226

Table 6.3: Five PDW Parameter Categories were Studied. The 23 Listed Here Plus Normal were Presented.

Gait Speed	Knee Height Asymmetry	Spatial and Temporal Asymmetry	ROS Asymmetry	Knee Damping with Mass Asymmetry
- 50%	+ 83%	5% (LSTA)	29%	0%
- 25%	+ 57%	13% (LSTA)	66%	40%
+ 25%	+ 22%	5% (TSLA)	100%	100%
+ 50%	- 26%	13% (TSLA)		118%
	- 40%	5% (LATA)		
	- 61%	13% (LATA)		

L = Step Length,   T = Swing Time,   S = Symmetry,   A = Asymmetry

- *Category 1: Gait Speed*:   Gait speed/cadence may affect the observer's perception of the gait, so four different videos of the normal gait at four different speeds (two slower and two faster) were included in the study.

- *Category 2: Knee Height*:   As reviewed previously in the background section, in prosthetics, knee location (height) may be altered in order to gain spatial, temporal, kinetic symmetry or comfort while walking. This portion aims to determine how much deviation from normal symmetry is noticeable. As listed in Table 6.7.3.2, I present three videos where the walking model has a knee asymmetry with one knee raised and three videos that show the walking model with knee asymmetry by lowering one knee. All models in this category have symmetric step lengths and swing times. Because the knee is displaced very close to the hip, the video with +83% knee height shows no knee, as seen in Figure 6.26, but is present in the other videos. Knee heights are not evenly distributed from symmetric knee position because equal changes above and below the knee could not yield a stable PDW walk.

- *Category 3: Spatial and Temporal Asymmetry*:   In this video set, my intent is to examine if spatial and temporal asymmetries such as caused by limping, partial leg paralysis (hemiplegia), or a leg prosthesis will be noticeable or viewed as abnormal or uncanny. In two videos, step length is held symmetric while swing time asymmetry is created (LSTA), in two videos

swing time is held symmetric while step length asymmetry is created (TSLA), and in another two videos equal amounts of step length and swing time asymmetries were created (LATA).

- *Category 4: ROS Asymmetry*: Walking impairment and some prosthetics can cause asymmetries in foot ROS. We included three different walking patterns with asymmetric ROS foot curves. At no ROS asymmetry, both roll-over shapes are 0.333 meters (1.09 feet) in radius, whereas at 100% ROS asymmetry the left ROS is 0.333 meters (1.09 feet) while the right ROS is 0.111 meters (0.36 feet).

- *Category 5: Knee Damping with Asymmetric Shank Mass*:   We included four videos of walking patterns with a damped right knee that simulates a stroke gait. To compensate, four different PDW shank masses were tested. The intent was to examine if a damped (i.e., impaired, injured, damaged) knee is recognizable or abnormal. If asymmetry with a damped knee is recognizable, is it possible to remove the uncanny effect by altering the impaired gait? We attempt to alter the damped gait by imposing a shank mass asymmetry. The kinematic
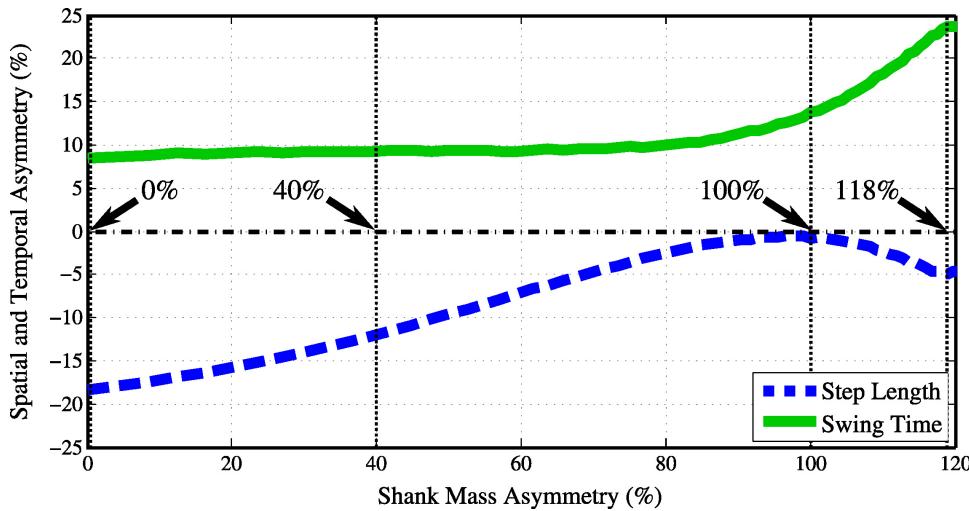
Figure 6.25: Spatial and temporal gait asymmetry with knee damping and asymmetric shank mass loading. As the right knee was damped with 0.275 Newton-radians the shank asymmetry was increased form 0% to 120%. The step length and swing time asymmetries are on opposite legs.
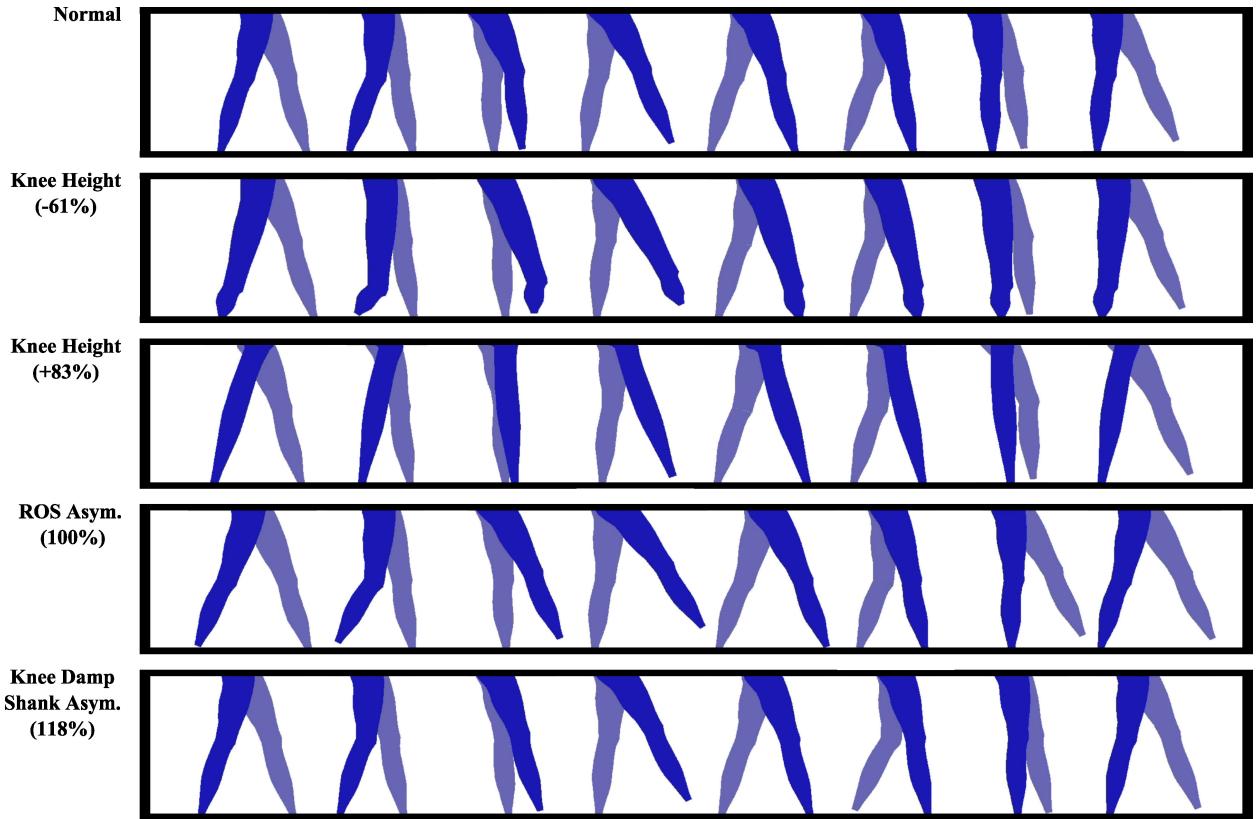
Figure 6.26: Sample video frames of the presented videos shown to participants. All videos are included in the supplemental material.

effects on spatial and temporal gait asymmetry can be viewed in Figure 6.25. Four videos were recorded at 0%, 40%, 100%, and 118% shank mass asymmetry. The knee damping was chosen to be 0.275 Newton-radians, which was the highest knee damping value through which the PDW model with large asymmetric shank mass was stable .

6.7.3.3 Experimental Setup and Protocol

Twenty individuals, 14 males and 6 females, aged 24.6 ± 4.7, participated in this study. No participants reported to have visual impairments of any type. No participants were familiar with the presented walking model. All participants reviewed and agreed to an approved minimal risk Institutional Review Board (IRB) consent form prior to participation.

Initially participants were instructed to observe and examine the normal gait for as long as they chose. They were told that this is a normal walking pattern. After that, participants were shown 24 videos in a different random order for each subject; the 24 videos consisted of the normal walking pattern and the 23 videos of altered gait patterns described in Table 6.7.3.2.

While watching each walking video, participants completed two answer sections for that video. The first was a subjective open-ended question asking *"What (if anything) do you think is wrong/odd/impaired/unhuman-like/weird with this walk"*. The second section asked the participants to discreetly compare the current video with the previously observed normal walking gait on a symmetric seven point Likert scale [120], asking *"How much resemblance does this walk have with a normal walk"*. That is, participants were asked to judge the presented videos with the following options: *"Very normal"*, *"Normal"*,*"Somewhat Normal"*,*"Neutral/Not Sure"*,*"Somewhat Abnormal"*,*"Abnormal"*, and *"Very Abnormal"*.

If participants rated two videos with equivalent scores within a category, participants further evaluated these two walking videos against each other. In this second part, the two walking videos were shown simultanously to the participants asking *"Between the two walking models, which one is more normal/unimpaired/human-like?"*. The video selected as more human-like gains 0.5 Likert points, while the less human-like video loses 0.5 Likert points. This is done to differentiate between videos and impose a rank among the data.

The PDW model depicted in each video repeatedly walked across a 50 centimeters (20 inches) wide computer monitor sitting approximatively 60 centimeters (24 inches) and eye-level in front of the participant. During the second part of the experiment, two videos repeatedly played on two separate computer monitors. All of the videos shown to the participants is included as supplemental material.

6.7.3.4 Statistical Analysis and Evaluation

As described before, participants rated walking videos on a symmetric seven point Likert scale. Because independent participants evaluate the walking videos and provided ranked qualita-

tive responses that hold true throughout the Likert scale range, I will assume continuous linearity between Likert scale points and treat the acquired data as ordinal interval-level. A Chi-square goodness-of-fit test revealed that the comprehensive data does not follow a normal distribution ($\chi^2 = 145$). Data within each category with normal gait included was also found not to follow a normal distribution. Thus, for each category of videos, I will use a Kruskal-Wallis one-way analysis of variance non-parametric test to compare Likert scale ratings for videos within each category.

Videos that have their mean, median, and entire 95% confidence interval of participant perception above the score of 4 (neutral) are evaluated as being perceived as having minimal gait abnormalities. Videos that have their 95% confidence interval intersecting with the neutral line at the score of 4 are evaluated as being perceived as having moderate gait abnormalities. Finally, videos that have their mean, median, and entire 95% confidence interval of participant perception below the score of 4 (neutral) are evaluated as being perceived as having highly recognizable gait abnormalities.

A Tukey's honest significant difference multiple comparison (post hoc) test with an alpha of 0.05 is used to test for statistically significant differences of perception between videos when the Kruskal-Wallis test showed statistical significance.

6.7.4 Results and Discussion

The results of each category are shown in Figure 6.27. Based on participant's ratings and comments, I approximated each video's location on the uncanny valley, which can be seen in Figure 6.28. Each of the categories are reported separately below.

- *Category 1: Gait Speed*: There was a statistically significant difference between the perceived human-likeness of different gait speeds ($\chi^2(4, 95) = 42$, p <0.0001). Post hoc analysis showed that participants were able to spot that there was something abnormal and altered between the normal walking pattern and all altered walking videos in this category. However, participants were not able to statistically significantly distinguish the abnormality among
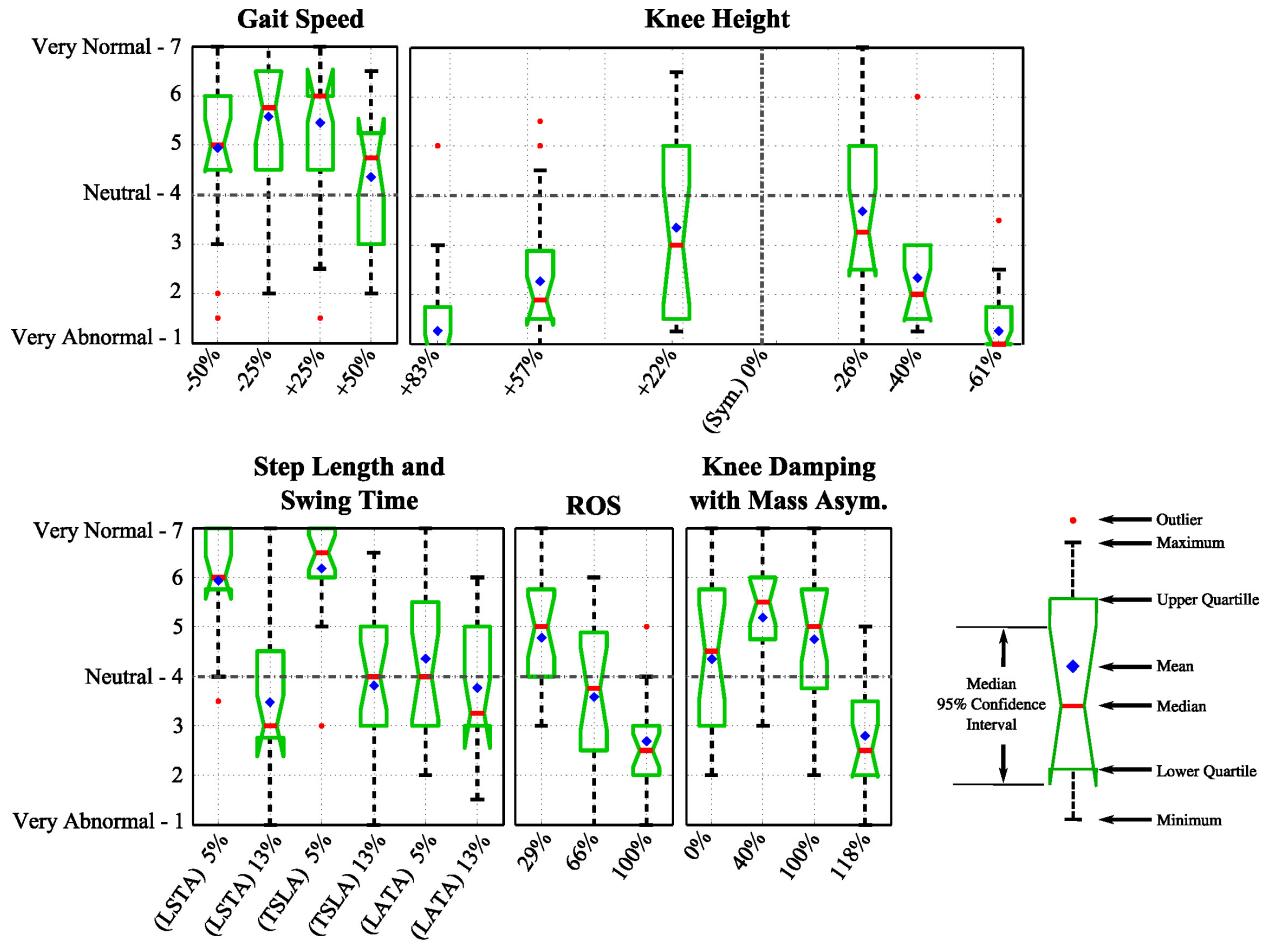
Figure 6.27: Extended box and whiskers notch plots show participant's responses to videos in each category

these altered gaits within this category. Based on my classification of the perception ratings, -50%, -25%, and +25% gait speed changes were perceived as minimally abnormal, whereas a gait cadence increase of +50% was perceived as moderately abnormal. Participants commented that an increase of +50% in gait speed seemed "in a hurry", "unnaturally fast", or "stiff".

It is interesting to note that a normal walking pattern with a gait cadence increase may be perceived as slightly more abnormal compared to a gait cadence decreased the same amount. This may indicate that when seeing someone walking hastily, although perceived as normal, it can be interpreted as out of the ordinary and draws attention. This is not necessarily the
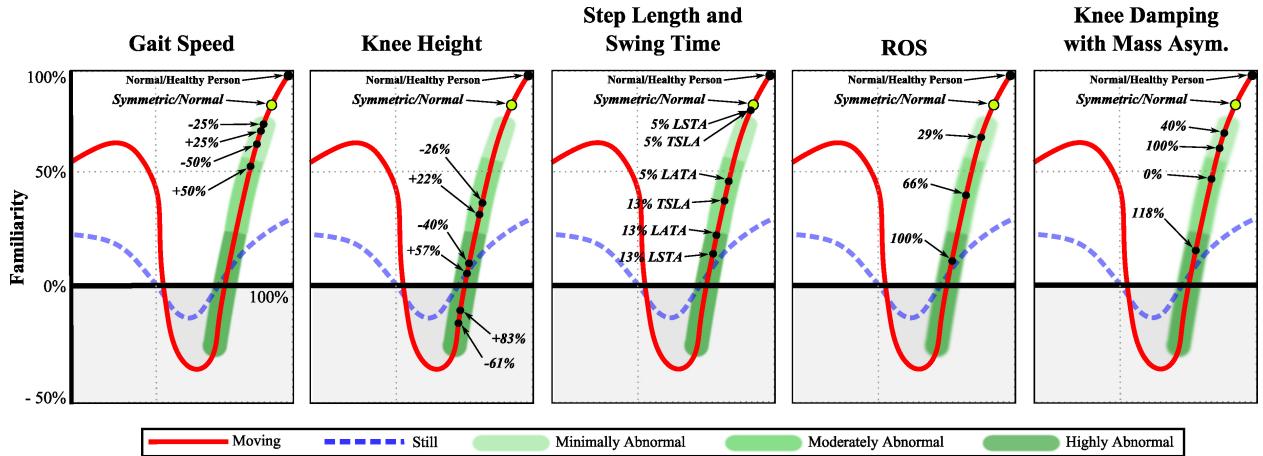
Figure 6.28: Approximate positions in the uncanny valley of the perception of all walking videos

case with the decrease in cadence of the same magnitude, which may imply that more calm, collected, or calculated walking movements are recognized as more typical or normal.

- *Category 2: Knee Height*: Participants perceived all videos in this category as statistically significantly different compared to the normal gait (χ^2(6, 133) = 81, p <0.0001). Participants evaluated knee heights of +83%, +57%, −40%, and +60% as noticeably and highly abnormal, odd, impaired, or unhuman-like. Knee heights of +22% and −26% were only perceived as moderately abnormal, which indicates that some knee height asymmetry with spatial and temporal gait symmetry could be dismissed as somewhat normal by observers. Participants were slightly more consistent in rating a low knee height as abnormal compared to higher knee locations (confidence interval range). The lowest knee height setting was often described by participants as "odd" and "horse-like", while the highest knee height as "crutch leg", "no knee", or "peg-leg".

A clear inverse "V" pattern shows the increase of participant's abnormal perception with knee height alteration, with a focal area between +10% and −20% knee height change. These results imply that given step length and step time symmetry, some knee height asymmetry can be unrecognizable or perceived as normal. Also, a lowered knee location in one leg may seem less normal and less unhuman-like than a lifted knee location at the same

233

distance from symmetric knee height. Although the experiment did not examine clothing, wearing loose-fitting clothes would help to hide the effect of a prosthetic with a knee location in a different location.

- *Category 3: Spatial and Temporal Asymmetry*: Both step length (L) and swing time (T) left-right asymmetries produced statistically significant differences compared to normal gait when there was a 13% asymmetry ($\chi^2(6, 133) = 81$, p $<$0.0001). The gait became moderately abnormal at 13% step length asymmetry (TSLA), while being perceived as highly abnormal at 13% swing time asymmetry (LSTA). A post-hoc test showed that a 5% asymmetry in length or time was not statistically significantly different compared to the normal gait, that is, participants saw small independent changes in swing time and step length as normal. The trend shows that an asymmetric change in swing time is perceived as more abnormal than the same magnitude change in step length, although this difference is not statistically significantly different. An asymmetry magnitude of 5% in both step length and swing time (LATA) showed statistically significantly more abnormal perception than just changing one or the other (LSTA or TSLA alone) by the same amount and was closer to a individual change of 13% in either step length or swing time. A simultaneous deviation of 13% (LATA) for both gait parameters caused a more abnormal perception of the gait, which classifies it as moderately abnormal. Participants reported step length asymmetry to be "stiff" and swing time asymmetry was often described as "limping".

Separately, 5% LSTA and 5% TSLA do not produce a perception of abnormality, however 5% in both measures simultaneously produces a moderate perception of abnormality. It may be concluded that compounding these asymmetries may cause greater perceptions in abnormality, however this is not the case for 13% LATA. The 13% LATA was rated similar to the 13% TSLA and 13% LSTA was rated more abnormal than 13% LATA. A further study using more combinations of these gait measures would help to understand the perceptual interactions more fully.

234

- *Category 4: ROS Asymmetry*:   Post hoc analysis showed participants perceived all videos in this category with a statistically significant difference compared to the normal gait (χ^2(3, 76) = 57, p <0.0001). Walking videos with 29%, 66%, and 100% ROS asymmetry were perceived as minimally, moderately, and highly abnormal, respectively. Participants reported high gait asymmetry to have longer step length and commented that "something is not right", however no participant specifically reported a ROS asymmetry.

  Although more ROS asymmetries would clarify the trent, it can be concluded that with all factors symmetric, a ROS asymmetry below around 35% can pass as minimally abnormal by observers. The trend implies that a ROS asymmetry below 15% may not be distinguishable from a normal and healthy gait.

- *Category 5: Knee Damping with Asymmetric Shank Mass*: Participants perceived all videos in this category with a statistically significant difference compared to the normal gait (χ^2(4, 95) = 61, p <0.0001). Post hoc analysis showed that 40% and 100% shank mass asymmetries were perceived statistically significantly different compared to 118% shank mass asymmetry. 40% and 100% shank mass asymmetries were perceived as minimally abnormal, 0% as moderately abnormal, and 118% as highly abnormal. The highest shank mass asymmetry with damping was described by participants as "limping" and "stiff in one leg", while the lowest shank mass asymmetry (0%) with one knee damped were mostly just described as "stiff in one leg".

  These results imply that if a person suffering from an impairment that causing stiffness in a knee, that person will be seen as moderately abnormal. However, creating an accompanying asymmetry from a different effect, adding a mass in this case, can potentially alleviate the perception of abnormality. This result agrees with the conclusions drawn from category 3 since, looking at Figure 6.25, it can be concluded that the swing time asymmetry has a greater effect on participant perception than step length asymmetry. Normalizing the perception of

joint damping can potentially be achieved by altering other gait paremeters such as having a foot roll-over shape or knee height asymmetry.

Chapter 7: Conclusions

The act of human walking is naturally elegant, however it is highly complex, involving sophisticated dynamics and convoluted cognitive control. In this dissertation, I presented methods, ideas, and models that may be able to offer elegant views or solutions in the realm of gait rehabilitation. Specifically, this work presented topics that support the advancement of passive gait rehabilitation in which the mode of rehabilitation occurs with no or little energy input.

In part of this research on passive gait rehabilitation, I successfully designed, constructed, and tested two iterations of the Gait Enhancing Mobile Shoe (GEMS) for gait rehabilitation, which is able to mimic a split-belt treadmill in that it provided a smooth, consistent, and passive backward motion. I examined strategies that can be used by individuals to alter their gait symmetry by wearing the GEMS either on one or two sides. When a backward moving GEMS was worn on one foot, it successfully produced a spatial asymmetry in healthy individuals, which shows evidence in the effectiveness of using the GEMS for patients suffering from hemiplegia. Wearing two GEMS, one pushing a foot forward and one pushing a foot backward was found to have no significant spatial aftereffects, however this application of the GEMS was able to alter double support (temporal) symmetry. Both GEMS experiments show proof that a new coordination was learned and stored following a period of walking with the GEMS, however further investigation of the effectiveness of the GEMS is needed.

The GEMS design is portable, low-cost, and passive, allowing it to be used at home or in smaller clinical settings, thus enabling training over longer periods than what is currently available. The GEMS is designed such that it can be worn during over-ground walking, thus maximizing improvement in real-world gait. Indeed, the preliminary data shows that control subjects were able to adapt temporal coordination to the GEMS and these changes in coordination

persisted even when tested during normal walking over ground. Note that I do not know why spatial coordination was unaffected by the GEMS, although it has been suggested that these two aspects of gait are controlled by separate neural substrates. This could be investigated in future studies. Nonetheless, the results suggest that the GEMS could be an effective rehabilitation tool to improve over-ground temporal gait symmetry post-stroke. I feel that this would be important for rehabilitation since temporal asymmetries commonly result from hemiparesis post-stroke and are correlated with reduced gait speed, which is a marker of impaired functional walking ability. Investigating whether GEMS training improves abnormal coordination and functional mobility post-stroke is one of the future goals.

As inspired by the optimization of the GEMS wheel, I further developed an analytic definition of two- and three-dimensional irregularly-shaped objects such as a human foot roll-over shape that can be modified for passive gait rehabilitation. This formulation defines the static and dynamic behavior of the kinetic shape, which was used to successfully construct and verify a novel musical instrument, locomotion device, and more efficient crutches. Kinetic shapes could have a great impact on prosthetics by defining a clear foot roll-over shape that can yield healthy or symmetric dynamic gait. Because this kinetic shape concept is novel in its nature, the research presented in this dissertation represents the fundamental derivation and various applications that still are left to be studied in greater detail.

Foot roll-over shapes were also analyzed with my variable curved-foot passive dynamic walker (PDW) model, which is able to be defined with any foot shape radius function. This derived model is advantageous in that is can simulate foot-roll over shapes. This model was successfully derived and utilized by examining the effects of foot roll-over shape radius and foot shape curvature increase. It has been successfully shown that the increase in foot roll over radius will reduce ground reaction forces, while increasing foot curvature may increase or decrease the energy expenditure of walking.

The PDW model was also successfully used to study the effects of pathological gait on gait perception. This study showed that as knee height asymmetry is deviated, the uncanny perception

of it does not linearly increase. However, results suggest that there is a threshold of a finite amount of knee asymmetry that is unnoticeable by observers, however a more definite definition of this threshold is yet to be explored. Temporal asymmetries in walking were shown to be more noticeable than spatial asymmetries, however a gait with both temporal and spatial asymmetry was perceived as most noticeable. Roll over shape asymmetries were noticed with asymmetry increase, while gait speed deviations from normal gait was only observed as mildly abnormal. This work presents the derivation and preliminary results of a point foot and variable radius foot PDW model. An extensive usage of this PDW model for gait studies is currently pending.

To model and match the kinematics of swinging human limbs such as arms or legs, a general equations of motion were derived for passive two-dimensional masses per degree of freedom open ended rotating systems. In order to match the same rotating kinematics, only two masses per degree of freedom are necessary. The motion analysis of three matched one-degree-of-freedom unactuated single link pendulums with dissimilar masses and mass distribution showed that these dissimilar systems were kinematically identical, although unmodeled nonconservative forces created slight deviations between ideal model predictions and actual measurements. While non-linear in motion, the same results were shown in the motion analysis of two two-degree-of-freedom unactuated double link pendulums with synchronous motion lasting for about 4 seconds before nonconservative forces caused deviation. Measured kinematics of the two dissimilar experimental double pendulums matched for more than 12 seconds.

It is possible to alter the mass distribution of a rotating system by moving masses along system links in order to kinematically match it to another system. It is also possible to add or remove masses at key locations along a rotating link. These methods could be utilized to synchronize the kinematics of two swinging legs while walking. However, although dissimilar kinematically synchronized systems move identically, the kinetics can vary. This was be seen in our first example between three dissimilar single link pendulums. While system kinematics matched, pendulum bearing reaction forces varied, yielding dissimilar damping forces. Unless mass and mass distribution parameters are exactly matched, the internal forces throughout the system will not

match. Further work includes the synchronization of rotating systems that experience an external

force or a collision event.

List of References

[1] Peter G. Adamczyk, Steven H. Collins, and Arthur D. Kuo. The advantages of a rolling foot in human walking. *The J. of Experimental Biology*, 209:3953–3963, 2006.

[2] Peter G. Adamczyk and Arthur D. Kuo. Mechanical and energetic consequences of rolling foot shape in human walking. *The Journal of Experimental Biology*, 216:2722–2731, 2013.

[3] Bruce C. Albright and Whitney M. Woodhull-Smith. Rocker bottom soles alter the postural response to backward translation during stance. *Gait and Posture*, 30:45–49, 2009.

[4] Kang An and Qijun Chen. A passive dynamic walking model based on knee-bend behaviour: Stability and adaptability for walking down steep slopes. *INTERNATIONAL JOURNAL OF ADVANCED ROBOTIC SYSTEMS*, 10, 2013.

[5] M. Anderson, O.C. Jenkins, and S. Osentoski. Recasting robotics challenges as experiments [competitions]. *Robotics Automation Magazine, IEEE*, 18(2):10–11, June 2011.

[6] Archimedes. *On Spirals*. 225 B.C.

[7] Fumihiko Asano. Stability analysis of underactuated compass gait based on linearization of motion. *Multibody System Dynamics*, pages 1–19, 2014.

[8] Fumihiko Asano and Zhi-Wei Luo. Pseudo virtual passive dynamic walking and effect of upper body as counterweight. In *Intelligent Robots and Systems, 2008. IROS 2008. IEEE/RSJ International Conference on*, pages 2934–2939. IEEE, 2008.

[9] Fumihiko Asano and Zhi-Wei Luo. On efficiency and optimality of asymmetric dynamic bipedal gait. In *Robotics and Automation, 2009. ICRA'09. IEEE International Conference on*, pages 1972–1977. IEEE, 2009.

[10] H Barbeau and M Visintin. Optimal outcomes obtained with body-weight support combined with treadmill training in stroke subjects. *Archives of Physical Medicine and Rehabilitation*, 84:1458–1465, Oct 2003.

[11] T Beardsworth and T Buckner. The ability to recognize oneself from a video recording of ones movements without seeing ones body. *Bulletin of the Psychonomic Society*, 18(1):19–22, 1981.

[12] Horst Peter Becker, Dieter Rosenbaum, Tohorsten Kriese, Heinz Gerngro, and Lutz Claes. Gait aymmetry following succesful surgical treatment of ankle fracture in young adults. *Clinical Orthopaedics and Related Research*, 311, 1995.

[13] Belda-Lois, Mena del Homo, Bermeio-Bosch, Moreno, JL Pons, D Farina, M Losa, M Molinari, F Tamburella, A Ramos, A Caria, T Solis-Escalante, C Brunner, and M Rea. Rehabilitation of gait after stroke: a review towards a top-down approach. *Journal of NeuroEngineering and Rehabilitation*, 8, Dec 2011.

[14] Anil Bhave, Dror Paley, and John Herzenberg. Improvement in gait parameters after lenghening for the treatment of limb-lengh discrepancy. *Journal of Bone & Joint Surgery*, 81:529–534, 1999.

[15] John Bloom and Lee Whitt. The geometry of rolling curves. *The American Mathematical Monthly*, 88(6):420–426, Jun-Jul 1981.

[16] U Bogataj, N Gros, M Kljaji, and M Malezic. The rehabilitation of gait in patients with hemiplegia: A comparison between conventional therapy and multichannel functinal electrical stimulation therapy. *Physical Therapy*, 75:490–502, 1995.

[17] U Bogataj, N Gros, M Malezic, B Kelih, M Kljaji, and R Acimovi. Restoration of gait during two to three weeks of therapy with multichannel electrical stimulation. *Physical Therapy*, 69:319–27, May 1989.

[18] R Bogey and G Hornby. Gait training strategies utilized in poststroke rehabilitation: Are we really making a difference? *Topics in Stroke Rehabilitation*, 14(6):1–8, Dec 2007.

[19] Richard W Bohannon, A Williams Andrews, and Melissa B Smith. Rehabilitation goals of patients with hemiplegia. *International Journal of Rehabilitation Research*, 11(2):181–184, 1988.

[20] Richard w Bohannon, melissa g morton, and joan b wikholm. Importance of four variables of walking to patients with stroke. *International Journal of Rehabilitation Research*, 14(3):246–250, 1991.

[21] M Brandstater, H de Bruin, C Gowland, and BM Clark. Hemiplegic gait: analysis of temporal variables. *Archives of Physical Medicine and Rehabilitation*, 64:583–7, Dec 1983.

[22] Adolfo M Bronstein, Karen L Bunday, and Raymond Reynolds. What the "broken escalator" phenomenon teaches us about balance. *Ann N Y Acad Sci*, 1164:82–88, May 2009.

[23] David Brown, Jacqueline J. Wertsch, Gerald F. Harris, John Klein, and Dennis Janisse. Effect of rocker soles on plantar pressures. *Arch Phys Med Rehabil*, 85:81–86, 2004.

[24] David R. Budney and Donald G. Bellow. On the swing mechancis of a matched set of golf clubs. *Research Quarterly for Exercise and Sport*, 53(3):185–192, 1982.

[25] K. L. Bunday, R. F. Reynolds, D. Kaski, M. Rao, S. Salman, and A. M. Bronstein. The effect of trial number on the emergence of the 'broken escalator' locomotor aftereffect. *Exp Brain Res*, 174(2):270–278, Sep 2006.

[26] Karen Louise Bunday and Adolfo M Bronstein. Locomotor adaptation and aftereffects in patients with reduced somatosensory input due to peripheral neuropathy. *J Neurophysiol*, Sep 2009.

[27] Matthew Bunnett, Michael F. Schatz, Heidi Rockwood, and Kurt Wiesenfeld. Huygens's clocks. *Proceedings: Mathematical, Physical and Engineering Sciences*, 458(2019):563–579, March 2002.

[28] Fan Y. Chen. *Mechanics and design of cam mechanisms*. New York : Pergamon Press, 18 edition, 1982.

[29] Vanessa F. Hsu Chen. Passive Dynamic Walking with Knees: A Point Foot Model. Master's thesis, Massachusetts Institute of Technology, 2005.

[30] Julia T Choi and Amy J Bastian. Adaptation reveals independent control networks for human walking. *Nat Neurosci*, 10(8):1055–1062, Aug 2007.

[31] Julia T Choi, Eileen P G Vining, Darcy S Reisman, and Amy J Bastian. Walking flexibility after hemispherectomy: split-belt treadmill adaptation and feedback control. *Brain*, 132(Pt 3):722–733, Mar 2009.

[32] M. J. Coleman, M. Garcia, A. L. Ruina, J. S. Camp, and A. Chatterjee. Stability and chaos in passive-dynamic locomotion. In *IUTAM Symposium on New Applications of Nonlinear and Chaotic Dynamics in Mechanics Solid Mechanics and its Applications*, volume 63, pages 407–416, 1999.

[33] G Colombo. The lokomat: A driven ambulatory orthosis. *Medical Orthopedic Tehcnology*, 6:178–181, 2000.

[34] Carolin Curtze, At L. Hof, Helco G. van Keeken, Jan P.K. Halbertsma, Klaas Postema, and Bert Otten. Comparative roll-over analysis of prosthetic feet. *Journal of Biomechanics*, 42(11):1746 – 1753, 2009.

[35] James E Cutting and Lynn T Kozlowski. Recognizing friends by their walk: Gait perception without familiarity cues. *Bulletin of the psychonomic society*, 9(5):353–356, 1977.

[36] James E Cutting, Dennis R Proffitt, and Lynn T Kozlowski. A biomechanical invariant for gait perception. *Journal of Experimental Psychology: Human Perception and Performance*, 4(3):357, 1978.

[37] Allison de Groot, Ryan Decker, and Kyle B. Reed. Gait enhancing mobile shoe (GEMS) for rehabilitation. In *Proc. Joint Eurohaptics Conf. and Symp. on Haptic Interfaces for Virtual Environment and Teleoperator Systems*, pages 190–195, March 2009.

[38] W. Diehl, K. SchÃijle, and T. Kaiser. Use of an assistive movement training apparatus in the rehabilitation of geriatric patients. *NeuroGeriatrie*, 5(1):3–12, 2008.

[39] V. Dietz, W. Zijlstra, and J. Duysens. Human neuronal interlimb coordination during split-belt locomotion. *Experimental Brain Research*, 101:513–520, 1994.

[40] Rui Dilao. Antiphase and in-phase synchronization of nonlinear oscillators: The huygenss clocks system. *Chaos*, 19, June 2009.

[41] ME Dohring and J Janis. Automatic synchronization of functional electrical stimulation and robotic assisted treadmill training. *Neural Systems and Rehabilitation Engineering, IEEE Transactions on*, 16(3):310–313, 2008.

[42] R. Drillis, R. Contini, and M. Bluestein. *Body segment parameters: a survey of measurement techniques*. National Academy of Sciences, 1964.

[43] Cyril Duclos, Sylvie Nadeau, Nicholas Bourgeois, Laurent Bouyer, and Carol L. Richards. Effects of walking with loads above the ankle on gait parameters of persons with hemiparesis after stroke. *Clinical Biomechanics*, 29(3):265–271, 2014.

[44] Scott G. Eberle. *Play: A Polyphony of Research Theories, and Issues*, volume 12, chapter Pinpointing Play at the Edge of the Uncanny Valley, pages 133–162. University Press of America, 2012.

[45] James L. Everett. Dynamical matched set of golf clubs. US Patent. 4,415,156, Oct.17, October 1972.

[46] Giorgio Figliolini, Pierluigi Rea, and Jorge Angeles. The pure-rolling cam-equivalent of the geneva mechanism. *Mechanism and Machine Theory*, 41:1320–1335, 2006.

[47] JM. Finley, M.A. Statton, and A.J. Bastian. A novel optic flow pattern speeds split-belt locomotor adaptation. *Journal of Neurophysiology*, 111(5):969–976, 2014.

[48] Alexander L. Frandkov and Boris Andrievsky. Synchronization and phase relations in the motion of two-pendulum system. *International Journal of Non-Linear Mechanics*, 42:895–901, March 2007.

[49] Sigmund Freud. *The Uncanny (J. Strachey, Trans.). The standard edition of complete psychological works of Sigmund Freud*, volume 17. 1919.

[50] Toshio Fukuda, Yasuhisa Hasegawa, Kosuke Sekiyama, and Tadayoshi Aoyama. *Multi-Locomotion Robotic Systems*, volume 81. Springer, 2012.

[51] M. Garcia, A. Chatterjee, A. Ruina, and M. Coleman. The simplest walking model: Stability, complexity, and scaling. *Journal of Biomechanical Engineering*, 120(2):281ÃŘ288, 1998.

[52] Deanna H Gates, Benjamin J Darter, Jonathan B Dingwell, and Jason M Wilken. Comparison of walking overground and in a computer assisted rehabilitation environment (caren) in individuals with and without transtibial amputation. *Journal of NeuroEngineering and Rehabilitation*, 9(81):81–90, 2012.

[53] Hartmut Geyer, Andre Seyfarth, and Reinhard Blickhan. Compliant leg behavior explains basic dynamics of walking and running. *Proceedings of the Royal Scociety*, (273):2861–2867, August 2006.

[54] Cynthia Gibson-Horn. Balance-based torso-weighting in a patient with ataxia and multiple sclerosis: A case report. *Journal of Neurologic Physical Therapy*, 32(3):139–146, 2008.

[55] JE Gilchrist, JE Campbell, CB Donnelly, JT Peeler, and JM Delaney. Spiral plate method for bacterial determination. *American Society for Microbiology*, 25(2):244–252, Feb 1973.

[56] Tobias Gluck, Andreas Eder, and Andreas Kugi. Swing-up control of a triple pendulum on a cart with experimental validation. *Automatica*, 49:801–808, 2013.

[57] A Goel, Loudon J, Nazare A, Rondinelli R, and Hassanein K. Joint moments in minor limb length discrepancy: a pilot study. *Journal of Orthopedics*, 26(12):852–856, 1997.

[58] Ambarish Goswami, Benoit Thuilot, and Bernard Espiau. Compass-Like Biped Robot Part I : Stability and Bifurcation of Passive Gaits. Rapport de recherche RR-2996, INRIA, 1996.

[59] Ambarish Goswami, Benoit Thuilot, and Bernard Espiau. A Study of the Passive Gait of a Compass-Like Biped Robot. *The International Journal of Robotics Research*, 17(12):1282–1301, 1998.

[60] Alena M. Grabowski, Craig P. McGowan, William McDermott, Matthew Beale, Rodger Kram, and Hugh Herr. Running-specific prostheses limit ground-force during sprinting. *Biology letters*, 6:201–204, 2010.

[61] R. Gregg, Y. Dhaher, A. Degani, and K. Lynch. On the mechanics of functional asymmetry in bipedal walking. *IEEE Transactions on Biomedical Engineering*, 59(5):1310–1318, 2012.

[62] Robert D. Gregg, Amir Degani, Yasin Dhahe, and Kevin M. Lynch. The basic mechanics of bipedal walking lead to asymmetric behavior. In *Proc. IEEE Int. Conf. Rehabilitation Robotics*, pages 816–821, 2011.

[63] P Gregory, L Edwards, K Faurot, S.W. Williams, and AC. Felix. Patient preferences for stroke rehabilitation. *Topics in Stroke Rehabilitation*, 17(5):394–400, 2010.

[64] Wenhao Guo, Tianshu Wang, and Qi Wang. A pssive dynamic walking model with coulomb friction at the hip joint. *Robotica*, 31:1221–1227, 2013.

[65] Jeffrey Haddad, Richard van Emmerik, Saunders Whittlesey, and Joseph Hamill. Adaptations in interlimb and intralimb coordination to asasymmetric loading in human walking. *Gait and Posture*, 23(4):429–434, 2006.

[66] Leon Hall and Stan Wagon. Roads and wheels. *Mathematics Magazine*, 65(5):283–301, Dec 1992.

[67] Ismet Handžić. Design and testing of a motion controlled gait enhancing mobile shoe (gems) for rehabilitation. Master's thesis, University of South Florida, 2011.

[68] Ismet Handžić, E. Barno, E. V. Vasudevan, and K. B. Reed. Design and pilot study of a gait enhancing mobile shoe. *J. of Behavioral Robotics*, 2(4):193–201, 2011.

[69] Ismet Handžić, Haris Muratagić, and Kyle B. Reed. Passive kinematic synchronization of uncoupled rotating systems. *Physica D: NonLinear Phenomena*, page (Under Review), 2014.

[70] Ismet Handžić and Kyle B. Reed. Motion controlled gait enhancing mobile shoe for rehabilitation. In *Proc. IEEE Int. Conf. Rehabilitation Robotics*, pages 583–588, 2011.

[71] Ismet Handžić and Kyle B. Reed. Validation of a passive dynamic walker model for human gait analysis. In *Proc. IEEE Eng. Med. Biol. Soc.*, pages 6945–6948, 2013.

[72] Ismet Handžić and Kyle B. Reed. The 'chopstick' illusion: A simply demonstrated tactile illusion. In *2014 World Haptics Symposium*, 2014.

[73] Ismet Handžić and Kyle B. Reed. Kinetic shapes: Analysis, verification, and application. *ASME Journal of Mechanical Design*, 137:(under review), 2014.

[74] Ismet Handžić and Kyle B. Reed. The musical kinetic shape: A variable tension string instrument. *Applied Acoustics*, 85:143–149, 2014.

[75] Ismet Handžić and Kyle B. Reed. Uncanny gait in biped walking. *Frontiers in Psychology*, page (Under Review), 2014.

[76] Ismet Handžić and Kyle B. Reed. Comparison of the passive dynamics of walking on ground, tied-belt and split-belt treadmills, and via the gait enhancing mobile shoe (GEMS). In *Proc. IEEE Int. Conf. Rehabilitation Robotics*, June 2013.

[77] Ismet Handžić, E. Vasudevan, and K. B. Reed. Developing a gait enhancing mobile shoe to alter over-ground walking coordination. In *IEEE In. Conf. Robotic Automation (ICRA)*, pages 4142–4129, May 2012.

[78] A. Hansen, D. Childress, and E. Knox. Prosthetic foot roll-over shapes with implications for alignment of trans-tibial prostheses. *Prosthetics and Orthotics International*, 24(3):205–215, 2000.

[79] Andrew Hansen and Charles Wang. Effective rocker shapes used by able-bodied persons for walking and fore-aft swaying: Implications for design of ankle-foot prostheses. *Gait and Posture*, 32:181–184, 2010.

[80] Andrew H. Hansen and Charles C. Wang. Effect of rocker shoe radius on oxygen consumption rate in young able-bodied persons. *Journal of Biomechanics*, 44:1021–1024, 2011.

[81] Yuji Harata, Koji Iwano, Fumihiko Asano, and Takashi Ikeda. Efficiency analysis of two-period asymmetric gaits. *International Journal of Dynamics and Control*, pages 1–10, 2013.

[82] Elizabeth C. Hardin, Antonie J. van den Bogert, and Joseph Hamill. Kinematic adaptations during running: effects of footwear, surface, and duration. *Medicine and science in sports and exercise*, 36(5):838–844, 2004.

[83] Jr Harold A. Conklin. Design and tone in the mechanoacoustic piano. part iii. piano strings and scale design. *Acoustical Society of America*, 100(3):1286–1298, 1996.

[84] Ivor Hawkes. Vibratory wire strain gage (patent US4277973A), 1981.

[85] Eiji Hayashi. Automated piano: Techniques for accurate expression of piano playing. In Jorge Solis and Kia Ng, editors, *Musical Robots and Interactive Multimodal Systems*, chapter 9, pages 143–163. Springer, 2011.

[86] Maryam Hekmatfard, Farzam Farahmand, and Ismail Ebrahimi. Effects of prosthetic mass distribution on the spatiotemporal characteristics and knee kinematics of transfemoral amputee locomotion. *Gait*, 37:78–81, 2013.

[87] Craig Honeycutt, John Sushko, and Kyle B. Reed. Asymmetric passive dynamic walker. In *Proc. IEEE Int. Conf. Rehabilitation Robotics*, pages 852–857, June 2011.

[88] Vincent Huang and John Krakauer. Robotic neurorehabilitation: a computational motor learning perspective. *Journal of NeuroEngineering and Rehabilitation*, 6(1):5, 2009.

[89] Yan Huang, Baojun Chen, Qining Wang, and Long Wang. Adding segmented feet to passive dynamic walkers. In *International Conference on Advanced INtelligent Mechatronics*, pages 652–657, Montreal, Canada, 2010. IEEE/ASME.

[90] Critchley Octavius Hunt and Kellet William. Vibrating strain gauges (patent US3052116A), 1962.

[91] J. Hunt. A vertical sonometer. *American Journal of Physics*, 58:93, 1990.

[92] Ken Hunt and Simon Broughton. *"Everything Is Left Behind" in the Rough Guide to World Music*. Rough Guides, London, 2000.

[93] Arnold Huurnink, Duncan P. Fransz, Idsart Kingma, and Jaap H. van DieÃńn. Comparison of a laboratory grade force platform with a nintendo wii balance board on measurement of postural control in single-leg stance balance tasks. *Journal of Biomechanics*, 46(7):1392–1395, 2013.

[94] Yoshito Ikemata, Akihito Sano, Kiyoshi Yasuhara, and Hideo Fujimoto. Dynamic effects of arc feet on the leg motion of passive walker. In *Robotics and Automation, 2009. ICRA'09. IEEE International Conference on*, pages 2755–2760. IEEE, 2009.

[95] RD Jardine. "Climbing Aids". US Patent 4,184,657, Jan. 22, 1980.

[96] Ernest Jentsch. Zur psychologie des unheimliche. *Psychiatrisch-Neuroligische Wochenshrift*, 8(22):195–198, August 1906.

[97] D Jette, N Latham, R Smout, J Gassaway, M Slavin, and S Horn. Physical therapy interventions for patients with stroke in inpatient rehabilitation facilities. *Physical Th*, 85:238–248, 2005.

[98] Theodore P. Jorgensen. Matched set of golf clubs. US Patent. 4,415,156, Nov.15, November 1983.

[99] A Kamps and K Schule. Cyclic movement training of the lower limb in stroke rehabilitation. *Neurol Rehabil*, 11:1–12, 2005.

[100] I. Kato. Devlopment of WABOT 1. *Biomechanism 2*, pages 173–214, 1973.

[101] I. Kato. WABOT-2: Autonomous robot with dexterous finger arm. *Proc. IEEE Robotics Automation*, 5(2), 1987.

[102] KR Kaufman, Miller LS, and Sutherland DM. Gait asymmetry in patients with limb-length inequality. *Jounral of Pediatric Orthopaedics*, 16:144–150, 1996.

[103] A Kaw and E Kalu. Numerical methods with applications: Abridged. *Lulu. com*, 2011.

[104] Ayub Khan and Priyamvada Tripathi. Synchronization, anti-synchronization and hybrid-synchronization of a double pendulum under the effect of external forces. *International Journal Of Computational Engineering Research*, 3(1):166–176, 2013.

[105] Seok Hun Kim and Kyle B. Reed. Robot-assisted balance training for gait modification. In *Proc. IEEE Int. Conf. Rehabilitation Robotics*, 2013.

[106] SH Kim, S. Banala, E Brackbill, S Agrawal, V Krishnamoorthy, and J Scholz. Robot-assisted modifications of gait in healthy individuals. *Experimental Brain*, 202(4):809–824, 2010.

[107] B. Kollmeier, T. Brand, and B. Meyer. *Perception of Speech and Sound*. Springer handbook of speech processing. Springer, 2008.

[108] Derek Koop and Christine Q Wu. Passive dynamic biped walkingâĂŤpart i: Development and validation of an advanced model. *Journal of Computational and Nonlinear Dynamics*, 8(4):041007, 2013.

[109] Lynn T Kozlowski and James E Cutting. Recognizing the sex of a walker from a dynamic point-light display. *Perception & Psychophysics*, 21(6):575–580, 1977.

[110] J. Krakauer, M. Ghilardi, and G. Ghez. Independent learning of internal models for kinematic and dynamic control of reaching. *Nature Neuroscience*, 2:1026–1031, 1999.

[111] Arthur D. Kuo. A simple model of bipedal walking predicts the preferred-step length relationship. *ASME Journal of Biomechanical Engineering*, 123:264–269, 2001.

[112] Arthur D Kuo and J Maxwell Donelan. Dynamic principles of gait and their clinical implications. *Physical therapy*, 90(2):157–174, 2010.

[113] Authur D. Kuo. The six determinants of gait and the inverted pendulum analogy: A dynamic walking perspective. *Human Movement Science*, 26:617–656, July 2007.

[114] Maxine Kwan and Mont Hubbard. Optimal foot shape for a passive dynamic biped. *Journal of theoretical biology*, 248(2):331–339, 2007.

[115] T. Lam, M. Anderschitz, and V. Dietz. Contribution of feedback and feedforward strategies to locomotor adaptations. *J. Neurophysiol*, 95:766–773, 2006.

[116] Tania Lam, Claire Wolstenholme, and Jaynie F. Yang. How do infants adapt to loading of the limb during the swing phase of stepping? *Journal of Neurophysiology*, 89(4):1920–1928, 2003.

[117] SC Landry, BM Nigg, and KE Tecante. Standing in an unstable shoe increases postural sway and muscle activity of selected smaller extrinsic foot muscles. *Gait and Posture*, 32:215–9, Jun 2010.

[118] M. Laupheimer, S. Hartel, and S. Schmidt. Forced exercise effects of motomed training on parkinson's- typical motor dysfunctions. *Neurology and Rehabilitation*, 17:239–246, 2011.

[119] L Legg and P Langhorne. Rehabilitation therapy services for stroke patients living at home: systematic review of randomised trials. *The Lancet*, 363:352 – 356,, 2004.

[120] Rensis Likert. A technique for the measurement of attitudes. *Archives of psychology*, 1932.

[121] Xiangze Lin, Haibo Du, and Shihua Li. Parameter influence on passive dynamic walking of a robot with flat feet. *Kybernetika*, 49(5):792–808, 2013.

[122] Jau-Shin Lou and James R. Bloedel. A new conditioning paradigm: Conditioned limb movements in locomoting decerebrate ferrets. *Neuroscience Letters*, 84(2):185 – 190, 1988.

[123] Noel Lythgoa, Cameron Wilsonb, and Mary Galeaa. Basic gait and symmetry measures for primary school-aged children and young adults whilst walking barefoot and with shoes. *Gait and Posture*, 30:502–506, 2009.

[124] P. Mahmoodi, R.S. Ransing, and M.I.Friswell. Modelling the effect of âĂŸheel to toe roll-over contact on the walking dynamics of passive biped robots. *Applied Mathematical Modelling*, 37:7352–7373, 2013.

[125] Ian R. Manchester and Jack Umenberger. Real-time planning with primitives for dynamic walking over uneven terrain. *CoRR*, abs/1310.7062, 2013.

[126] T.A. Martin, J. G.Keating, H.P. Goodkin, A.J. Bastian, and W.T.Tharch. Throwing while loolook through prisms: i. focal olivocerebellar lesions impair adaptation. *Brain*, 119(4):1183–1198, 1996.

[127] Fabio Martinez, Christian Clifuentes, and Eduardo Romero. Simulation of normal and pathological gaits using a fusion knowledge strategy. *Journal of NeuroEngineering and Rehabilitation*, 10(73), 2013.

[128] Tomoyuki Matsuo, Masashi Hashimoto, Maki Koyanagi, and Ken Hashizume. Asymmetric load-carrying in young and eldery women: Relationship with lower limb coordination. *Gait and Posture*, 28:517–520, 2008.

[129] S. J. Mattes, P. E. M., and T. D. Royer. Walking symmetry and energy cost in persons with unilateral transtibial amputations: Matching prosthetic and intact limb inertial properties. *Archives of Physical Medicine and Rehabilitation*, 81(5):561 – 568, 2000.

[130] Margaret McDowell, Cheryl Fryar, Cynthia Ogden, and Katherine Flegal. Anthropometric reference data for children and adults: United states, 2003âĂŞ2006, 2008.

[131] Tad McGeer. Powered flight, child's play, silly wheels and walking machines. In *Robotics and Automation, 1989. Proceedings., 1989 IEEE International Conference on*, pages 1592–1597. IEEE, 1989.

[132] Tad McGeer. Passive Dynamic Walking. *Int. J. of Robotics Research*, 9(2):62–82, 1990.

[133] Andrew Stuart McIntosh, Karen T Beatty, Leanne N Dwan, and Deborah R Vickers. Gait dynamics on an inclined walkway. *Journal of biomechanics*, 39(13):2491–2502, 2006.

[134] Jasmine C. Menant, Julie R. Steele, Hylton B. Menz, Bridget J. Munro, and Stephen R. Lord. Effects of walking surfaces and footwear on temporo-spatial gait parameters in young and older people. *Gait and Posture*, 29:392–397, 2009.

[135] Alma S Merians, David Jack, Rares Boian, Marilyn Tremaine, Grigore C Burdea, Sergei V Adamovich, Michael Recce, and Howard Poizner. Virtual Reality-Augmented Rehabilitation for Patients Following Stroke. *Physical Therapy*, 82(9):898–915, 2002.

[136] Marin Mersenne. *Harmonice Universelle*. 1636.

[137] Jean-Michel Mongeau, Brian McRae, Ardian Jusufi, Paul Birkmeyer, Aaron M. Hoover, Ronald Fearing, and Robert J. Full. Rapid inversion: Running animals and robots swing like a pendulum under ledges. *Plos One*, 7, June 2012.

[138] Masahiro Mori. The uncanny valley. *Energy*, 7(4):33–35, 1970.

[139] S. Morton and A. Bastian. Cerebellar Contributions to Locomotor Adaptations during Splitbelt Treadmill Walking. *J. Neurosci.*, 26(36):9107–9116, 2006.

[140] AM Moseley, A Stark, ID Cameron, and A Pollock. Treadmill training and body weight support for walking after stroke. *Cochrane Database of Systematic Reviews*, 19, 2005.

[141] K.A. Myers, J.T. Long, J.P. Klein, J. J. Wertsch, D. Janisse, and G.F. Harris. Biomechanical implications of the negative heel rocker sole shoe: Gait kinematics and kinetics. *Gait and Posture*, 24:323–330, 2006.

[142] Sujit Nair and Naomi Ehrich Leonard. Stable synchronization of mechanical system networks. *Journal of Control Optimization*, 47(2):661–683, 2008.

[143] Isaac Newton, Florian CAJORI, Russell Tracy CRAWFORD, and Andrew MOTTE. *Sir Isaac Newton's Mathematical Principles of Natural Philosophy and His System of the World. Translated... by Andrew Motte in 1729. The Translations Revised and Supplied with an Historical and Explanatory Appendix by Florian Cajori.[Edited by RT Crawford. With a Portrait.].* University of California Press, 1934.

[144] Benno Nigg, Sabrina Hintzen, and Reed Ferber. Effect of an unstable shoe construction on lower extremity gait characteristics. *Clinical Biomechanics*, 21:82–88, 2006.

[145] Lee Nolan, Andrzej Wit, Krzysztof Dudziñski, Adrian Lees, Mark Lake, and Michał Wychowañski. Adjustments in gait symmetry with walking speed in trans-femoral and trans-tibial amputees. *Gait & posture*, 17(2):142–151, 2003.

[146] Jun-Ho Oh, David Hanson, Won-Sup Kim, Li Young Han, Jung-Yup Kim, and Ill-Woo Park. Design of android type humanoid robot albert HUBO. In *International Conference on Inteligent Robots and Systems*, 2006.

[147] Grigory V. Osipov, JÃijrgen Kurths, and Changsong Zhou. *Synchronization in Oscillatory Networks*. Springer, 2007.

[148] Erika Ottaviano, Domenico Mundo, Guido A. Danieli, and Marco Ceccarelli. Numerical and experimental analysis of non-circular gears and cam-follower systems as function generators. *Mechanism and Machine Theory*, 43:996–1008, 2008.

[149] Krishnaji Parvataneni, Leone Ploeg, Sandra J. Olney, and Brenda Brouwer. Kinematic, kinetic and metabolic parameters of treadmill versus overground walking in healthy older adults. *Clinical Biomechanics*, 24:95–100, 2009.

[150] Mitesh Patel, Diego Kaski, and Adolfo M. Bronstein. Attention modulates adaptive motor learning in the 'broken escalator' paradigm. *Experimental brain research*, pages 1–9, 2014.

[151] Kara Patterson, Iwona Parafianowicz, Cynthia Danells, and William Mcllroy. Gait asymmetry in community-ambulating stroke survivors. *Archivies of Physical Medicine and Rehabilitation*, 89(2):304–310, 2008.

[152] Kara K. Patterson, William H. Gage, Dina Brooks, Sandra E. Black, and William E. McIlroy. Evaluation of gait symmetry after stroke: A comparison of current methods and recommendations for standardization. *Gait & Posture*, 31(2):241 – 246, 2010.

[153] J Perry. *Gait Analysis: Normal and pathological function*, volume 50. Thorofare, 2 edition, 2010.

[154] Stephen P. Radzevich. *Dudley's Handbook of Practical Gear Design and Manufacture*. CRC Press, 2012.

[155] M. Raibert. Dynamic legged robots for rough terrain. In *Humanoid Robots (Humanoids), 2010 10th IEEE-RAS International Conference on*, pages 1–1, Dec 2010.

[156] Kyle B. Reed, Ismet Handžić, and Samuel McAmis. *Home-based Rehabilitation: Enabling Frequent and Effective Training*, volume 2 of *Neuro-robotics: From brain machine interfaces to rehabilitation robotics, Trends in Augmentation of Human Performance*. Springer, 2014. ISBN: 978-9-4017-8931-8.

[157] D Reisman, H McLean, J Keller, K Danks, and A Bastian. Repeated split-belt treadmill training improves poststroke step length asymmetry. *Neurorehabilitation*, 27, Feb 2013.

[158] D. Reisman, R. Wityk, and A. Bastian. Split-belt treadmill walking adaptation in post-stroke hemiparesis. *J. Neurologic Physical Therapy*, 29:196, 2005.

[159] D. Reisman, R. Wityk, K. Silver, and A. Bastian. Locomotor adaptation on a split-belt treadmill can improve walking symmetry post-stroke. *Brain*, 130(7):1861–1872, 2007.

[160] Darcy S Reisman, Heather McLean, and Amy J Bastian. Split-belt treadmill training post-stroke: a case study. *Journal of Neurologic Physical Therapy*, 34(4):202, 2010.

[161] Darcy S Reisman, Robert Wityk, Kenneth Silver, and Amy J Bastian. Split-belt treadmill adaptation transfers to overground walking in persons poststroke. *Neurorehabil Neural Repair*, 23(7):735–744, Sep 2009.

[162] A.J.S. Renard, B.G. Schutte, N. Verdonschot, and A. Van Kampen. The ilizarov external fixator: What remains of the wire pretension after dynamic loading? *Clinical Biomechanics*, 20:1126–1130, 2005.

[163] R. F. Reynolds and A. M. Bronstein. The broken escalator phenomenon. aftereffect of walking onto a moving platform. *Exp Brain Res*, 151(3):301–308, Aug 2003.

[164] R. Riener, L. Lunenburger, S. Jezernik, M. Anderschitz, G. Colombo, and V. Dietz. Patient-cooperative strategies for robot-aided treadmill training: first experimental results. *Neural Systems and Rehabilitation Engineering, IEEE Transactions on*, 13(3):380–394, 2005.

[165] J. Rietman, K. Postema, and J. Geertzen. Gait analysis in prosthetics: Opinions, ideas and conclusions. *Prosthetics and Orthotics International*, 61(1):50–57, 2002.

[166] Patrick O. Riley, Gabriele Paolini, Ugo Della Croce, Kate W. Paylo, and Casey Kerrigan. A kinematic and kinetic comparison of overground and treadmill walking in healthy subjects. *Gait and Posture*, 26:17–24, 2007.

[167] MA Roa, CA Villegas, and RE Ramírez. Extensive modeling of a 3 dof passive dynamic walker. In *Climbing and Walking Robots*, pages 349–356. Springer, 2006.

[168] Gianna Rodriguez and Alexander Aruin. The effect of shoe wedges and lifts on symmetry of stance and weight bearing in hemiparetic individuals. *Archives physical medicine & rehabilitation*, 83(4):478–482, 2002.

[169] Thomas D. Rossing, editor. *The Science of String Instruments*. Springer, New York, 2010.

[170] Kazi Rushdi, Derek Koop, and Christine Q Wu. Experimental studies on passive dynamic bipedal walking. *Robotics and Autonomous Systems*, 2013.

[171] Valentina La Russa, Bjorn Skallerud, Jomar Klaksvik, and Olav A. Foss. Wire tension versus wire frequency: An experimental ilizarov frame study. *Journal of Biomechanics*, 43:2327–2331, 2010.

[172] Tony Ryan, Pam Enderby, and Alan S Rigby. A randomized controlled trial to evaluate intensity of community-based rehabilitation provision following stroke or hip fracture in old age. *Clinical Rehabilitation*, 20(2):123–131, 2006.

[173] Heydar Sadeghi, Paul Allard, Prancois Prince, and Hubert Labelle. Symmetry and limb dominance in able-bodied gait: A review. *Gait and Posture*, 12:34–45, 2000.

[174] Heydar Sadeghi, Paul Allarda, and Morris Duhaimeb. Functional gait asymmetry in able-bodied subjects. *Human Movement Science*, 16:243–258, 1997.

[175] Ali Tehrani Safa and Mahyar Naraghi. The role of walking surface in enhancing the stability of the simplest passive dynamic biped. *Robotica*, pages 1–13, 2014.

[176] Yoshiaki Sakagami, Ryujin Watanabe, Chiaki Aoyama, Shinichi Matsunaga, Nobuo Higaki, and Kikuo Fujimura. The intilligent ASIMO: System overover and integration. In *Intl. Conference on Intelligent Robots and Systems*, pages 2478–2483. IEEE, 2002.

[177] Hirotsuga Sakata and Masayuki Okunda. Fluid compressing device having coaxial spiral members. US patent 5,603,614, Sep. 30, 1994.

[178] Reza Shadmehr and Ferdinando A. Mussa-lvaldi. Adaptive representation of dynamics during learning of a motor task. *J. Neurosci.*, 14(5):3208–3224, 1994.

[179] Koji Shibuya. Violin playing robot and kansei. In Jorge Solis and Kia Ng, editors, *Musical Robots and Interactive Multimodal Systems*, chapter 11, pages 179–193. Springer, 2011.

[180] Joseph Edward Shigley. *Shigley's Mechanical Engineering Design*, volume 8. McGraw-Hill, 2008.

[181] Camila Rocha Simon, Deborah Oliveira Fonseca da Silveira, and Amanda Andrade. Effects of adding load on the gait of children with cerebral palsy: report of three cases. *Physiotherapy and Research*, 21(1), 2014.

[182] L.H. Sloot, M.M. van der Krogt, and J. Harlaar. Effects of adding a virtual reality environment to different modes of treadmill walking. *Gait and Posture*, 39(3):939–945, 2014.

[183] L.H. Sloot, M.M. van der Krogt, and J. Harlaar. Energy exchange between subject and belt during treadmill walking. *Journal of Biomechanics*, 6:1510–1513, 2014.

[184] Tarek M. Sobh, Bei Wang, and Kurt W. Coble. Experimental robot musicians. *Journal of Intelligent and Robotic Systems*, 38:197–212, 2003.

[185] N.e. Spear. *Handbook of Learning and cognitive processes*. Lawrence Erlbaum Associates, Hillsdale, NJ, 1976.

[186] Manoj Srinivasan and Andy Ruina. Computer optimization of a minimal biped model discovrs walking and running. *Nature*, 439:72–75, 2006.

[187] S. Srinivasan, E.R. Westervelt, and A. H. Hansen. A low-dimensional sagital-plane forward-dynamic model for asymmetric gati and its applicaiton to study the gait of transtibial prothesis users. *ASME Journal of Biomechanical Engineering*, 131, 2009.

[188] C. Stackley, P.B. Disler, L. Turner-Stokes, T. D. Wade, N. Brittle, and T. Hoppitt. Rehabilitation interventions for foot drop in neuromuscular disease. *Cochrane Database Syst Rev*, 3(3), 2009.

[189] U. Stanic, R. Acimovi-Janezic, N. Gros, A. Trnkoczy, T. Bajd, and M. Kljaji? Multichannel electrical stimulation for correction of hemiplegic gait. methodology and preliminary results. *Scandinavian journal of rehabilitation medicine*, 10:75–92, 1978.

[190] Ted J Stevenson and S Jayne Garland. Standing balance during internally produced perturbations in subjects with hemiplegia: validation of the balance scale. *Archives of physical medicine and rehabilitation*, 77(7):656–662, 1996.

[191] Thomas Stoggl, Anita Haudum, Jurgen Birklbauer, Markus Murrer, and Erich Muller. Short and long term adaptation of variability during walking using unstable (mbt) shoes. *Clinical Biomechanics*, 25:816–822, 2010.

[192] Yuuta Sugiyama and Shinichi Hirai. Crawling and jumping by a deformable robot. *International Journal of Robotics Research*, 25(5-6):603–620, Jun 2006.

[193] Hong Sun and George T.-C. Chiu. Motion synchronization for dual-cylinder electrohydraulic lift systems. *Transactions on Mechatronics*, 7(2):171–181, June 2002.

[194] Huijing Sun and Hongjun Cao. Chaos control and synchronization of a modified chaotic system. *Chaos Solitions & Fractals*, 37:1442–1455, October 2006.

[195] John Sushko, Craig Honeycutt, and Kyle B. Reed. Prosthesis design based on an asymmetric passive dynamic walker. In *Proc. IEEE Conf. Biorob*, pages 1116–1121, June 2012.

[196] Takashi Takuma and Koh Hosoda. Controlling walking behavior of passive dynamic walker utilizing passive joint compliance. In *Intelligent Robots and Systems, 2007. IROS 2007. IEEE/RSJ International Conference on*, pages 2975–2980. IEEE, 2007.

[197] K.S. Tang and D. Kaski. The effect of gait approach velocity on the broken escalator phenomenon. *Experimental brain research*, 226(3):335–346, 2013.

[198] Russ Tedrake, Teresa W. Zhang, Minkg fai Fong, and H. Sebastian Seung. Actuating a simple 3d passive dynamic walker. In *International Conference on Robotics & Automation*, New Orleans, LA, April 2004. IEEE.

[199] LF Teixeira-Salmela, S Nadeau amd I Mcbride, and SJ Olney. Effects of muscle strengthening and physical conditioning training on temporal kinematic and kinetic variables in gait stroke survivors. *Journal of Rehabilitation Medicine*, 33:53–60, 2001.

[200] LF Teixeira-Salmela, SJOlney, SN, and B Brouwer. Muscle strengthening and physical conditioning to reduce impairment and disability in chronic stroke survivors. *Archives of Physical Medicine and Rehabilitation*, 80(10):1211 – 1218, 1999.

[201] L. Tesio and V. Rota. Gait analysis on split-belt force treadmills: validation of an instrument. *Amer J. Phys Med Rehabil*, 87:515–526, 2008.

[202] A. Tinwell and M. Grimshaw. Bridging the uncanny: an impossible traverse? In *Proceedings of the 13th international MindTrek conference: Everyday life in the ubiquitous era*, pages 66–73, 2009.

[203] Sarah Tyson and Gill Turner. Discharge and follow-up for people with stroke: what happens and why. *Clinical Rehabilitation*, 14(4):381–392, 2000.

[204] James Richard Usherwood. Why not walk faster? *Biology Letters*, (1):338–341, 2005.

[205] Erin V. L. Vasudevan and Amy J. Bastian. Split-Belt Treadmill Adaptation Shows Different Functional Networks for Fast and Slow Human Walking. *J Neurophysiol*, 103(1):183–191, 2010.

[206] JC Wall and GI Turnbull. Gait asymmetries in residual hemiplegia. *Archives of Physical Medicine and Rehabilitation*, 67:550–3, Aug 1986.

[207] Jaclyn R. Watt, Jason R. Franz, Keith Jackson, Jay Dicharry, Patrick O. Riley, and D. Casey Kerrigan. A three-dimensional kinematic and kinetic comparison of overground and treadmill walking in healthy elderly subjects. *Clinical Biomechanics*, 25:444–449, 2010.

[208] M. Whittle. *Gait Analysis*. Elsevier Health Sciences, 5 edition, 2012.

[209] T. Williems, E. Witvrouw, K. Delbaere, and D. De Clercq. Relationship between gait biomechanics and inversion sprains: a prospective study of risk factors. *Gait and Posture*, 21(4):379–387, 2005.

[210] Martijn Wisse and Arend L Schwab. First steps in passive dynamic walking. In *Climbing and Walking Robots*, pages 745–756. Springer, 2005.

[211] Martijn Wisse and Richard Q Van der Linde. *Delft pneumatic bipeds*, volume 34. Springer, 2007.

[212] Martijn Wisse and Jan Van Frankenhuyzen. Design and construction of mike; a 2-d autonomous biped based on passive dynamic walking. In *Adaptive motion of animals and machines*, pages 143–154. Springer, 2006.

[213] Justin Wong, Rosyln Boyd, Nigel Keenan, Richard Baker, Paulo Selber, and Graham Kerr. Gait pattern after fracture of the femoral shaft in children, manged by external fixation or early hip spica cast. *Journal of Pediatric orthopaedics*, 24(5):463–471, 2004.

[214] Q. Wu and J. Chen. Effects of ramp angle and mass distribution on passive dynamic gait - an experimental study. *International Journal of Humanoid Robotics*, 7(1), 2010.

[215] Q. Wu and N. Sabet. An experimental study of passive dynamic walking. *Robotica*, 22(3):251–262, 2004.

[216] Robert C. Yates. *A Handbook on Curves and Their Properties*. J.W. Edwards, US Military Acadamy, 1947.

[217] Galit Yogev, Meir Plotnik, Chava Peretz, Nir Giladi, and Jeffrey M. Hausdorff. Gait asymmetry in patients with parkinson's disease and elderly fallers: when does the bilateral coordination of gait require attention? *Experimental Brain Research*, 177(3):336–346, 2007.

[218] Li Peng Yuan, Li Ming Yuan, and Hong Ying Lu. Optimal energy-effective gait for biped robot. *Applied Mechanics and Materials*, 347:839–843, 2013.

[219] Peijie Zhang, Yantao Tian, and Zhenze Liu. Gait analysis of the passive dynamic walker with knees. In *Intelligent Robotics and Applications*, pages 992–1002. Springer, 2008.

[220] Peijie Zhang, Yantao Tian, Zhenze Liu, Shufan Yang, and Rong Tian. Further research and comparison of gaits for compass-like biped and kneed passive dynamic walker. *Intelligent Robotics and Applications*, 5314:1216–1226, 2008.

[221] Enlai Zheng, Fang Jia, Hongwei Sha, and Suhao Wang. Non-circular belt transmission design of mechanical press. *Mechanism and Machine Theory*, 57:126–138, 2012.

Appendices

Appendix A: Gait Enhancing Mobile Shoe Drawings

In this appendix section, I am presenting more detailed computer aided drafting (CAD) drawings and other appropriate schematics for my second and third Gait Enhancing Mobile Shoe (GEMS) design. CAD drawings were produced in SolidWorks®.

A.1 GEMS Prototype Two
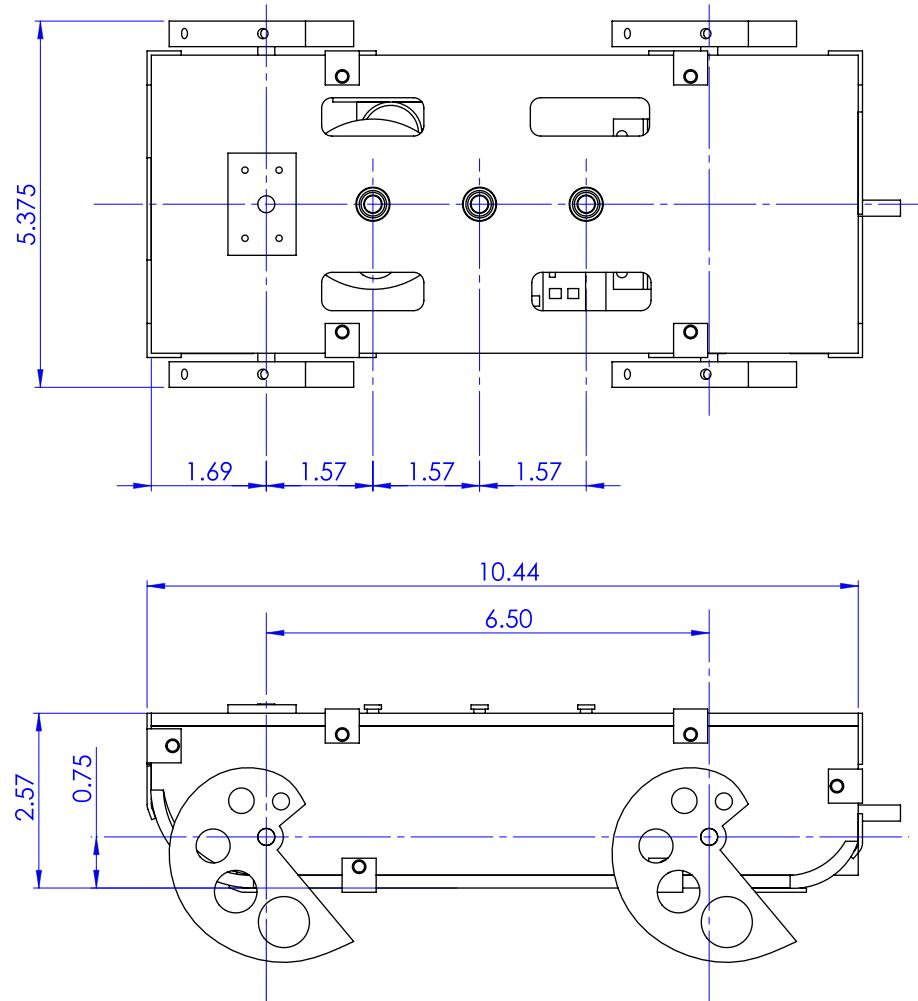
Figure A.1: GEMS prototype two general dimensions. All dimensions are in inches.
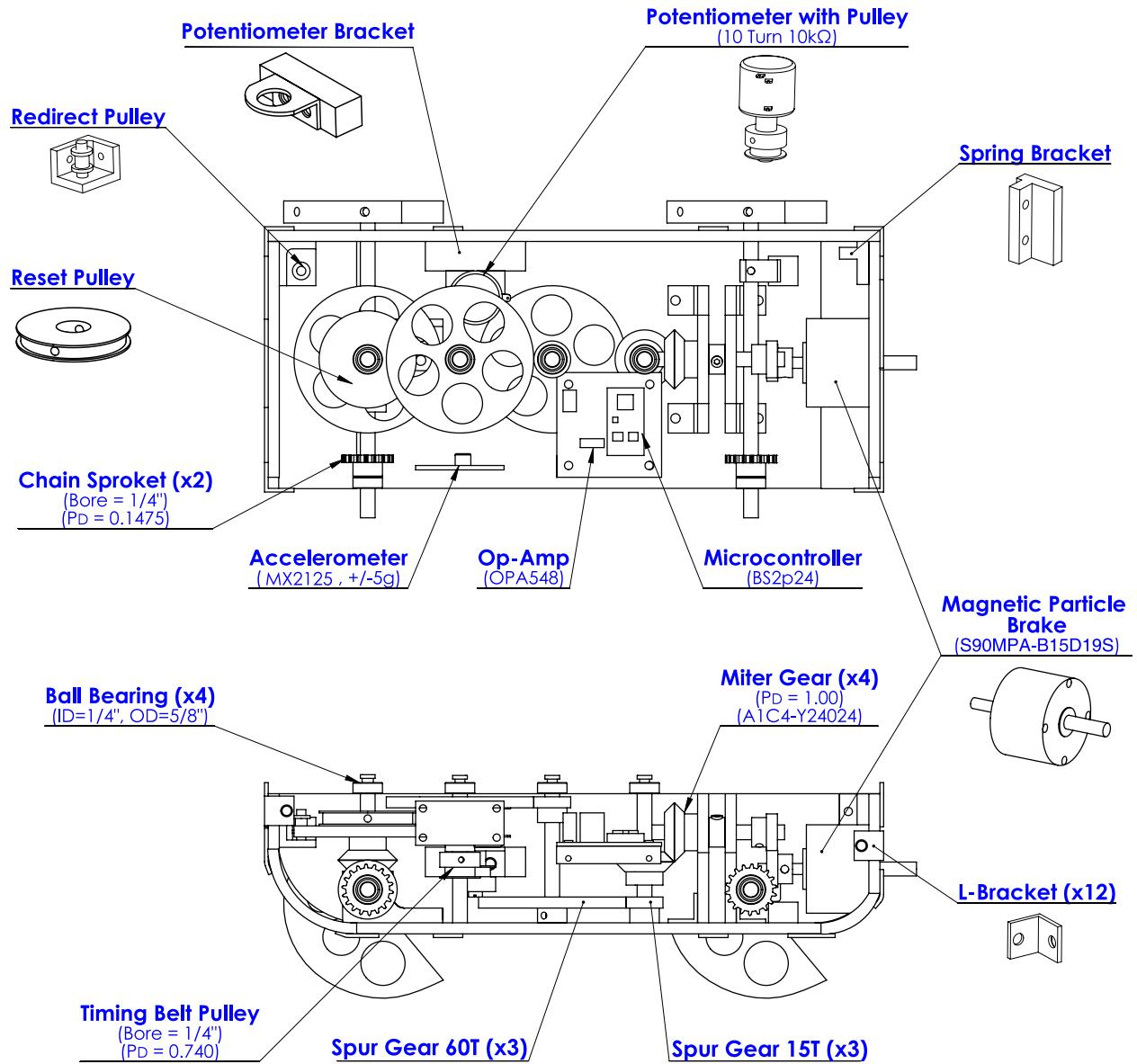
Figure A.2: GEMS prototype 2 parts anatomy. Top and side cover are not shown.
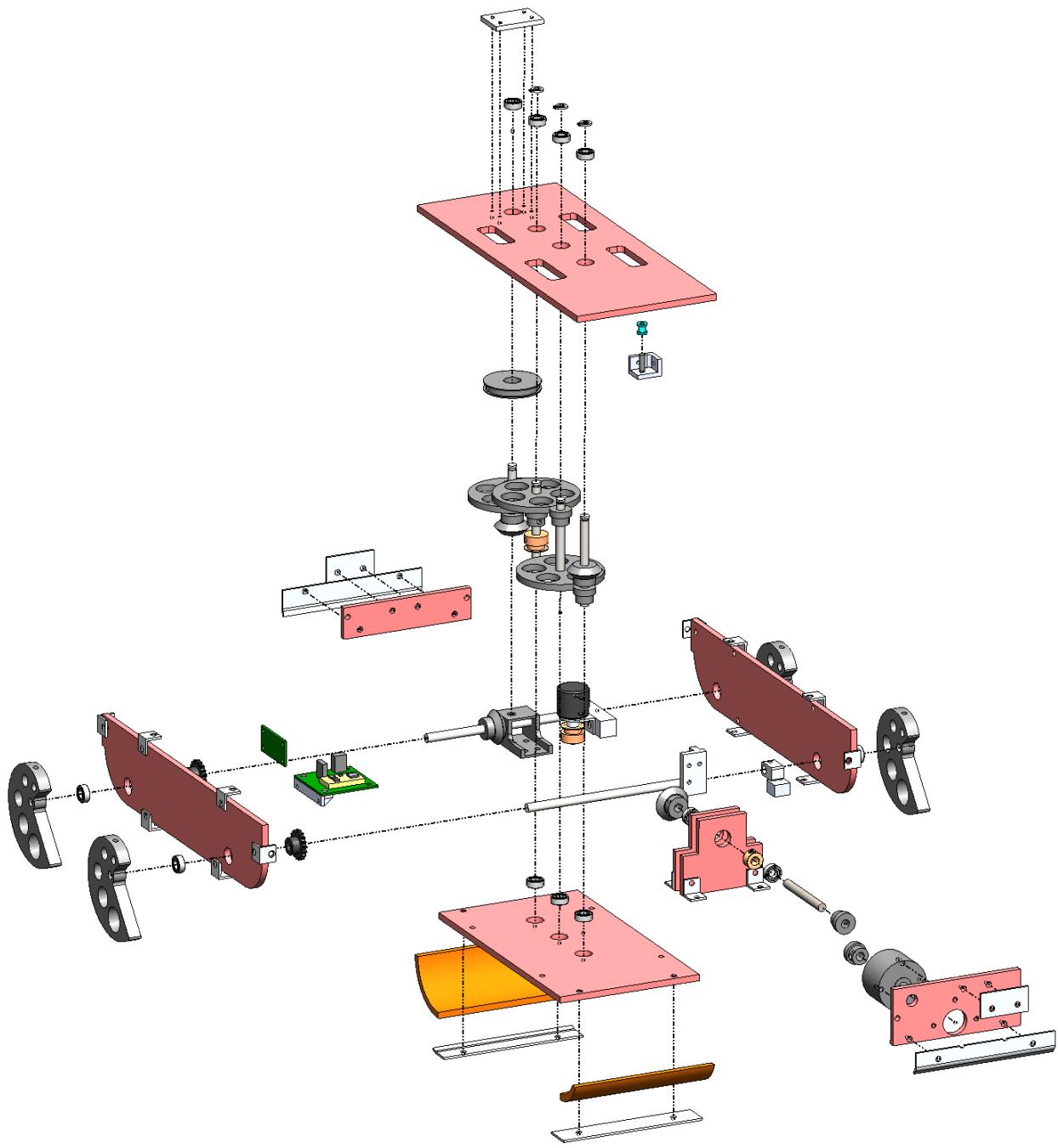
Figure A.3: GEMS prototype 2 exploded view
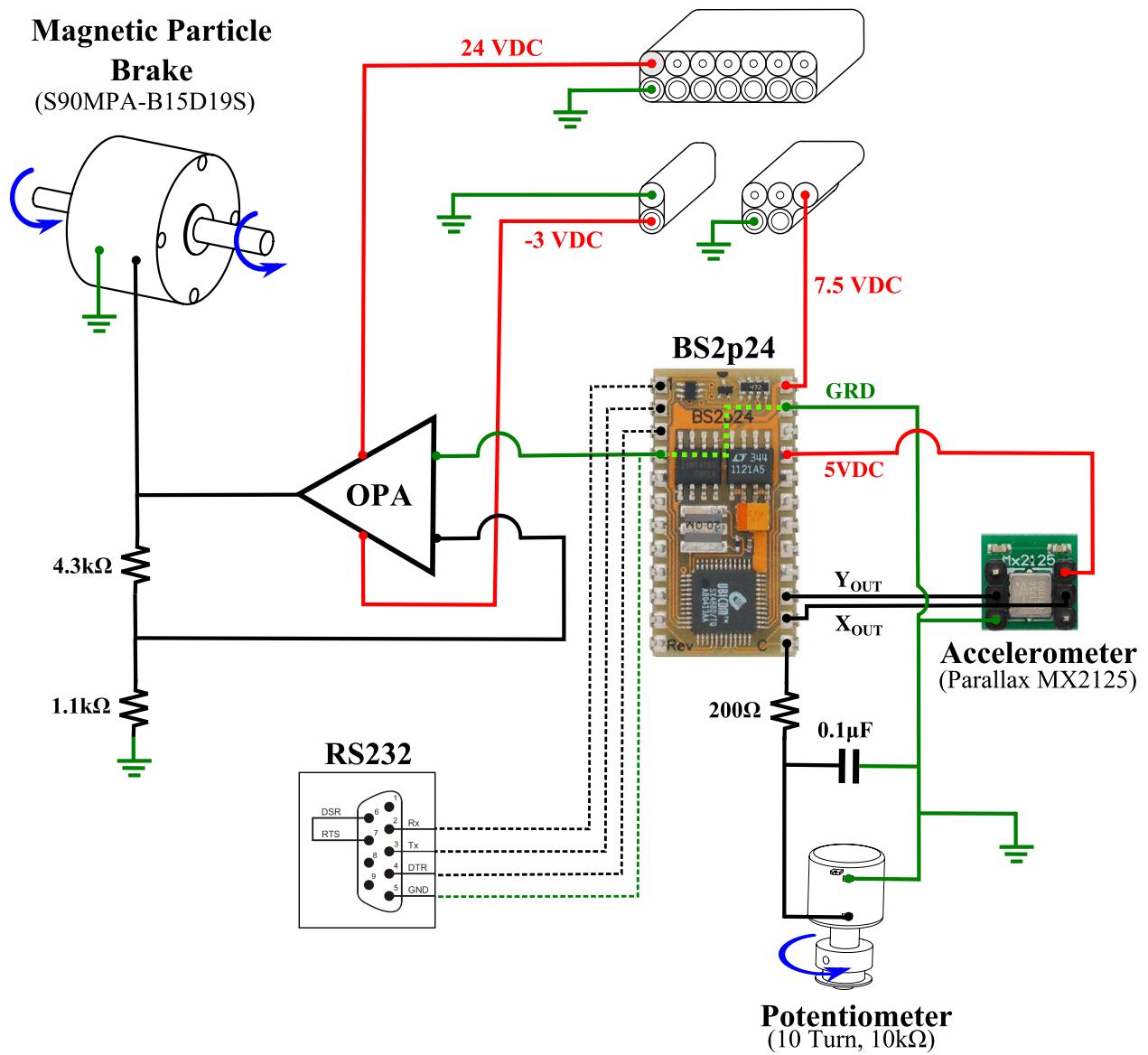
Figure A.4: GEMS prototype 2 control circuit that controls the movement of the GEMS through the a magnetic particle brake

A.2   GEMS Prototype Three
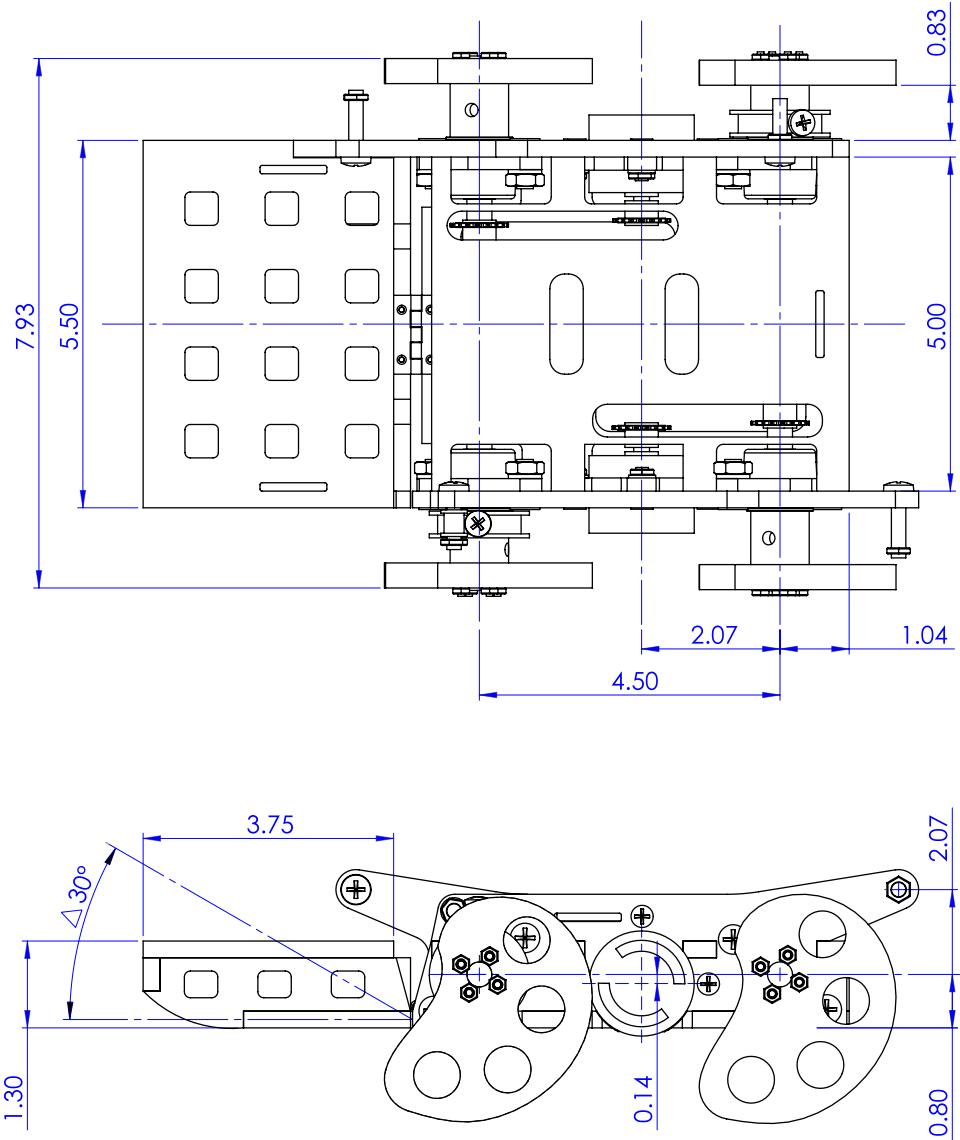
Figure A.5: GEMS prototype three general dimensions. All dimensions are in inches.

Wheel Hub (x2)
(0.80" Long)

Reset Pulley (x2)

Chain Sprocket (x4)
(p=0.25, 11 Tooth)

Hindge

Bronze Bearing (x4)
(3/8 Shaft, Flange Mount)

Redirect Pulley

Wheel Hub (x2)
(0.375" Long)

Uni-Directional
Damper (x2)
(RT-F2-R-203 - Right)
(RT-F2-L-203 - Left)
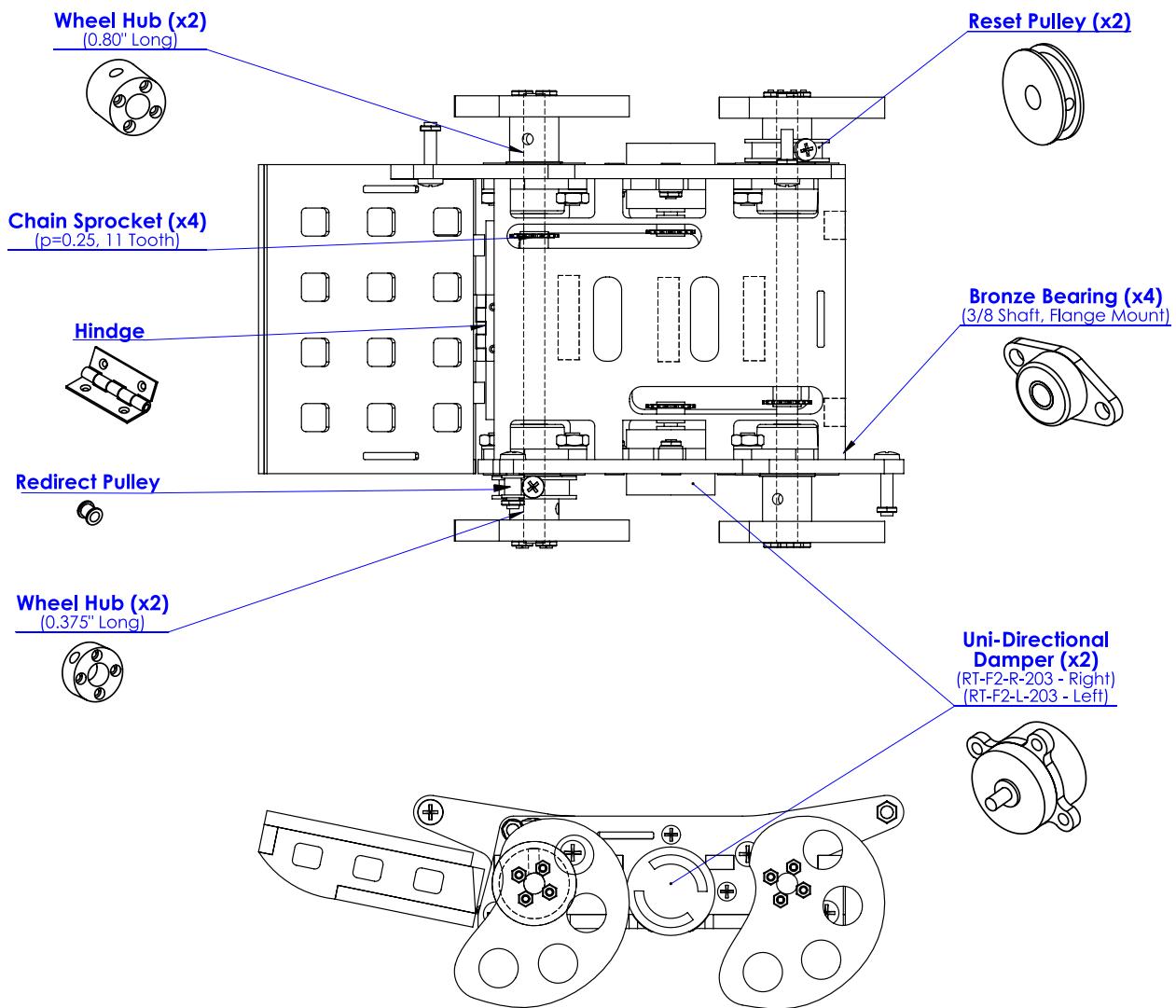
Figure A.6: GEMS prototype 3 parts anatomy
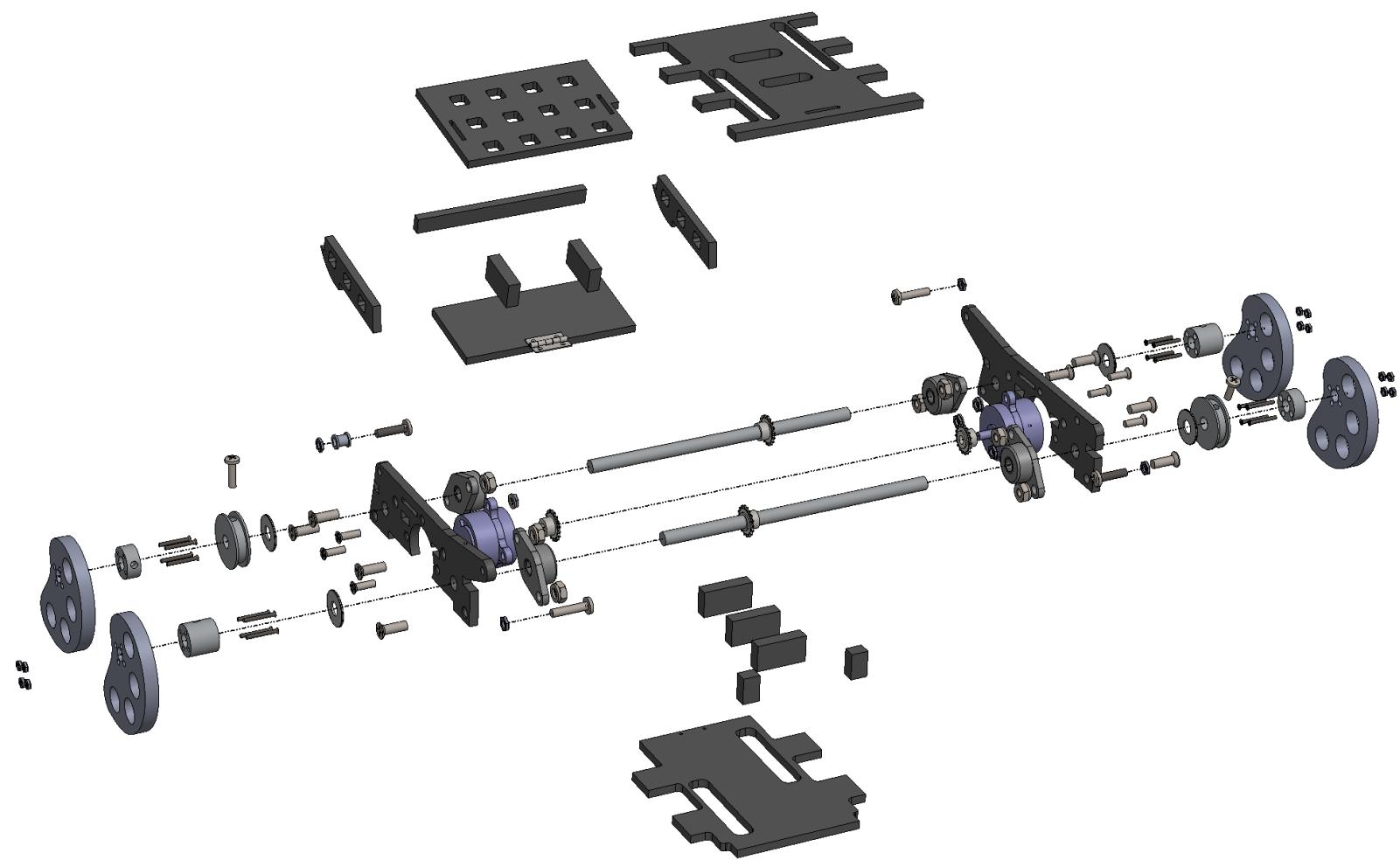
Figure A.7: GEMS prototype 3 exploded view

Appendix B: Kinetic Shape Matlab® Code

Presented here is my Matlab® code that generates my two- and three- dimensional kinetic shapes with specified parameters. While the presented code for the 2D kinetic shape produces the shape and computes its kinematics, the 3D kinetic shape code only derives the shape. This code was tested and is fully functional in Matlab® version R2014a (and prior). It can be copied and pasted with convenience.

Note that this code can also be run (with some minor syntax modification) on Matlab® equivalent open-source multi-paradigm numerical computing environments such as GNU Octave, Freemat, or Scilab.

B.1   Two Dimensional Kinetic Shape Matlab® Code

```matlab
clc         %Clear the command window
close all   %Close all open figures/matlab windows
clear all   %Clear all data in matlab workspace

syms theta1  %Define Angle theta symbolic variable
syms LinVel1 %Define Linear velocity symbolic variable


%===============================================================================
%                                 INPUT
%===============================================================================
%Angle Range Around Kinetic Shape                 %Unit Radians
Resolution  = 0.01;     %Discrete Devisions
Begin       = 0;        %Starting Angle
End         = 2*pi;     %Ending Angle
theta = [Begin : Resolution : End]';

%Initial Shape Definition Radius
Ri = 2.75*0.0254;                                 %Unit Length

%Radial Input Force
%    Note:  Has to be as a function of "theta1"
Fr_Input = 5*cos(theta1) + 8;                     %Unit Force

%Applied Vertical Input Force (Applied Weight)
%    Note:  Has to be as a function of "theta1"
Fv_Input = 25;                                    %Unit Force

%Intitial Angular Position and Angular Velocity (For Kinematics)
Initial_AngPos = 6.0;                             %Unit Radians
```

```matlab
Initial_AngVel = 0;                                    %Unit Radians/Second


%Kinetic Shape Material (For Kinematics)
Density   = 632.68;                                    %Unit Mass/Length^3
Thickness = 0.0159;                                    %Unit Length


%Axle Mass or Dispensed Platform Mass (For Kinematics)
%  Note:  Enter '0' if none present
Mass2 = 5.5;                                           %Unit Mass


%Total Simulation Time and Time Resolution (For Kinematics)
TotalTime = 0.850;                                     %Unit Seconds
dt        = 0.0025;                                    %Unit Seconds


%After the Kinetic Shape is derieved, it is possible
%to apply another vertical applied force onto the shape
%and observe how it move. (For Kinematics)
%('theta1' as Variable)
%    Note:  Fv_Input_App = Fv_Input to keep original applied force
Fv_Input_App = 14.5*4.45;                              %Unit Force


%Linear Rolling/Dispenser friction Coefficient Model (For Kinematics)
%  This is the resistance of linear motion
%  between ground and axle
%('LinVel1' as Variable)
Mu_k = 0.145;                        %Kinetic Friction Coef   - Unitless
Mu_s = 0.450;                        %Static Friction Coef    - Unitless
C    = 8.0;                          %Friction Decay Constant - Unitless
Mu_L_fric = sign(LinVel1)*(Mu_k + (Mu_s - Mu_k)*exp(-abs(LinVel1)*C))...
            + Mu_k*LinVel1;                            %Unitless


%Over-ground rolling option
%Set Ground = 1 for when shape rolls over ground contact
%Set Ground = 0 for when shape rolls around its origin
Ground = 0;
%=================================================================================
%=================================================================================


fprintf('\n=============================================\n')
fprintf('Initial Orientation Angle: %4.2f Radians\n',        Initial_AngPos)
fprintf('                           %4.2f Degrees\n',        ...
   Initial_AngPos*(180/pi))
fprintf('Initial Angular Velocity:  %4.2f Radians/Seconds\n', Initial_AngVel)
fprintf('                           %4.2f Degrees/Seconds\n', ...
   Initial_AngPos*(180/pi))
fprintf('=============================================\n')


%Check if shape is contionous all around
%Output-print if continous or not
Shape_Cont = eval(int(Fr_Input, theta1, 0, 2*pi));
if Shape_Cont < 40
   fprintf('    ** Kinetic Shape is Continuous all Around. **\n')
else
```

```matlab
    fprintf('     ** Kinetic Shape is NOT Continuous. **\n')
end
fprintf('===============================================\n')

%Output-print Kinetic Shape Definition Forces
fprintf('Given/Desired Radial Force Input:\n')
Fr_Input
fprintf('===============================================\n')
fprintf('Applied Vertical Force Input:\n')
Fv_Input
fprintf('===============================================\n\n')




%==============================================================================
%                Applying Two-Dimensional Kinetic Shape Equation
%==============================================================================
Rad = zeros(length(theta), 1);       %Creating Blank Vector
Rad(1) = Ri;                         %Initial Kinetic Shape Radius

Fr     = zeros(length(theta),1);     %Creating Blank Vectors
Fv     = zeros(length(theta),1);
Fv_app = zeros(length(theta),1);

F_Input = Fr_Input / Fv_Input;       %Devide Radial by Vertical Force
Fi      = int(F_Input, theta1);      %Inegrate Radial Force wrt theta1

ds   = 0;
Area = 0;
J    = 0;
for i = 2:length(theta)
    %Subbing values into integral equation
    F_int_1 = subs(Fi, [theta1],[theta(i)]);
    F_int_2 = subs(Fi, [theta1],[theta(i-1)]);

    %Derive Shape Radius, Rad(theta)
    Rad(i) = exp(  (F_int_1 - F_int_2)  ) * Rad(i-1);

    %Evaluating Specified Functions at Angle Step
    Fr(i)     = subs(Fr_Input,    [theta1],[theta(i)]);%Radial Force
    Fv(i)     = subs(Fv_Input,    [theta1],[theta(i)]);%Vertical Force
    Fv_app(i) = subs(Fv_Input_App,[theta1],[theta(i)]);%Vertical Force (Post)

    %Finding other Parameters
    dtheta = theta(i)-theta(i-1);                      %Step Angle (Radians)
    Area   = Area + (  (Rad(i)*dtheta)/2)*(Rad(i));%Shape Area (Length^2)
    ds     = ds + Rad(i) * dtheta;                     %Shape Arc Length (Length)
    J      = J + ( (Rad(i)^4)/4 ) * dtheta;            %Polar Moment of Inertia
                                                       %        (Length^4)
end
Mass = Area*Density*Thickness;                         %Shape Mass

%==============================================================================
%                             Backward Check/Verification
```

272

```matlab
%==========================================================================
dr_dt_check    = zeros(length(Fr),1);    %Derivative of Shape Vector
Fr_check       = zeros(length(Fr),1);    %Horizontal Force Vector
%Comparing Given and Calculated Horizontal Reaction Force
for i = 2:length(Fr)
    %Derrivative of shape
    dr_dt_check(i) = (Rad(i)-Rad(i-1)) / (theta(i)-theta(i-1));

    %Polar Tangential Angle
    psi_check = atan( Rad(i) / dr_dt_check(i));

    %Horizontal Force From Derived Shape
    Fr_check(i) = Fv(i) * (cos(psi_check) / sin(psi_check));
end


%Command Window Parameter Output
fprintf('Minimum Shape Radius:\t %2.3f\t\t(Length)\n', Ri)
fprintf('Maximum Shape Radius:\t %2.3f\t\t(Length)\n', Rad(end))
fprintf('Shape Arc Length:\t\t %2.3f\t\t(Length)\n', ds)
fprintf('Shape Area:\t\t\t\t %2.3f\t\t(Length^2)\n', Area)
fprintf('Polar Moment of Inertia: %2.3f\t(Length^4)\n', J)
fprintf('Shape Mass:\t\t\t\t %2.3f\t\t(Mass)\n', Mass)
fprintf('=====================================\n\n')



%==========================================================================
%           Mapping Angular Acceleration Around the Kinetic Shape
%==========================================================================
dtheta    = mean( diff(theta) );      %Angle change/step
AngAcc    = zeros(length(theta), 1);  %Blank vector variables
J_ground  = zeros(length(theta), 1);
psi       = zeros(length(theta), 1);

for i = 2:length(Fr)
    %Polar Mass Moment of Inertia for Shape (Mass*Length^2)
    J_mass    = Density * Thickness * J;        %Polar mass moment of inertia

    %Polar Mass Moment of Inertia For Axle or Dispenser (Mass*Length^2)
    J_Lin = Mass2*Rad(i)^2 * sin(psi(i));

    %Apply Parallel Axis Theorem for ground contact rolling
    J_ground(i) = J_mass + J_Lin + Ground*Mass*Rad(i)^2;  %Parallel Axis Thrm

    %Shape Radius Function Derrivative (Length/Radian)
    drdth = (Rad(i)-Rad(i-1)) / (theta(i)-theta(i-1));

    %Polar Tangential Angle (Radian)
    psi(i) = atan2( Rad(i), drdth );

    %Angular Acceleration Value around Perimeter (Radian/Time^2)
    AngAcc(i) = Fv(i) * Rad(i)*cos( psi(i) ) / J_ground(i);
end
```

```matlab
%=================================================================
%                Simulating Kinetics Shape Movement with Time
%=================================================================
%Expanding Vectors
Rad2 = Rad;
for i = 1:4
    Fr       = [Fr, Fr];                Fv        = [Fv, Fv];
    Fv_app   = [Fv_app, Fv_app];        Rad2      = [Rad2; Rad2];
    psi      = [psi; psi];              drdth     = [drdth; drdth];
    J_ground = [J_ground; J_ground];
end
theta2 = [];                            %Expanding and Mirroring theta Vector
for i = 0:4;    theta2 = [theta2; theta+i*2*pi];    end
theta2 = [-theta2(end:-1:2); theta2];


time_index = linspace(1, TotalTime/dt, TotalTime/dt); %Creating Time Vector
time = zeros(length(time_index), 1);                  %Time Index Vector

%Blank vector variables
Mu_Rad_fric  = zeros(length(time_index), 1);    %Rotation Friction Model
Mu_Lin_fric  = zeros(length(time_index), 1);    %Linear Friction Model
AngPos       = zeros(length(time_index), 1);    %Angular Position
AngVel       = zeros(length(time_index), 1);    %Angular Velocity
AngAcc2      = zeros(length(time_index), 1);    %Angular Acceleration
LinAcc       = zeros(length(time_index), 1);    %Linear Position
LinVel       = zeros(length(time_index), 1);    %Linear Velocity
LinPos       = zeros(length(time_index), 1);    %Linear Acceleration

%Initial Conditions (Initial Position, Velocity, Acceleration)
AngPos(1)    = Initial_AngPos;
theta_tri    = delaunayn(theta2);                       %Triangulate 'theta'
AngPos_idx   = dsearchn(theta2, theta_tri, AngPos(1));  %Find initial angle ...
    index

AngVel(1)    = Initial_AngVel;                          %Radians/Second
LinVel(1)    = AngVel(1)*Rad2(AngPos_idx)*sin(psi(1));  %Length/Second

Mu_Lin_fric(1) = -subs(Mu_L_fric, [LinVel1, theta1],...
                 [LinVel(1), theta2(AngPos_idx)]);          %Unitless
F_Lin_fric     = Fv_app(AngPos_idx)*Rad2(AngPos_idx)*sin(psi(AngPos_idx))...
                 *Mu_Lin_fric(1);                           %Force*Length

AngAcc2(1)   = -(  (Fv_app(AngPos_idx)*Rad2(AngPos_idx)*cos(psi(AngPos_idx))...
             - F_Lin_fric) / J_ground(AngPos_idx)  ) ;


for t = time_index(2:end)
    Mu_Lin_fric(t) = -subs(Mu_L_fric, [LinVel1, theta1],...
                     [LinVel(t-1), theta2(AngPos_idx)]);  %Unitless
```

```matlab
    F_Lin_fric      = ...
        Fv_app(AngPos_idx)*Rad2(AngPos_idx)*sin(psi(AngPos_idx))...
                    *Mu_Lin_fric(t);                        %Force*Length

    %=========== Kinetic Shape Angular Kinetmatics ===========
    AngAcc2(t) = ...
        -((Fv_app(AngPos_idx)*Rad2(AngPos_idx)*cos(psi(AngPos_idx))...
                - F_Lin_fric) / J_ground(AngPos_idx));

    if isnan( AngAcc2(t) ) == 1;    %Check if AngAcc2 is a number
        AngAcc2(t) = 0;             %If not, assign zero value
    end

    %Numerical Integration
    AngVel(t) = AngVel(t-1) + AngAcc2(t)*dt;    %Angular Velocity
    AngPos(t) = AngPos(t-1) + AngVel(t) *dt;    %Angular Position


    %============ Kinetic Shape Linear Kinematics =============
    LinAcc(t) = AngAcc2(t)* Rad2(AngPos_idx)*sin(psi(t));
    LinVel(t) = AngVel(t)* Rad2(AngPos_idx)*sin(psi(t));
    LinPos(t) = LinPos(t-1) + LinVel(t) *dt;    %Position(Numerical ...
        Integration)

    AngPos_idx = dsearchn(theta2, theta_tri, AngPos(t)); %Find angle index
    time(t) = time(t-1) + dt;                            %Increment Time Step
end


%==============================================================================
%               Plotting Kinetic Shape, Kinetics, and Kinematics
%==============================================================================
%Initial Angle Index
theta_tri = delaunayn(theta);       %Triangulat 'theta'
AngPos_idx = dsearchn(theta, theta_tri, Initial_AngPos); %Find angle index

figure(1);  %Plotting Wheel Shapes in Polar Coordinates
polar(theta, Rad, '.k')
hold on
h1 = polar(theta(AngPos_idx), Rad(AngPos_idx), 'ob');
set( findobj(h1, 'Type', 'line'), 'MarkerEdgeColor','b',...
    'MarkerFaceColor','b', 'MarkerSize',9);
title('Two Dimensional Kinetic Shape (Polar)','FontSize',15,...
    'FontName','Times New Roman')
xlabel('Theta (Degrees)','FontSize',12, 'FontName','Times New Roman')
ylabel('Radius (Inches)','FontSize',12, 'FontName','Times New Roman')
ylabh = get(gca,'ylabel');
set(ylabh,'Position',get(ylabh,'Position') - [.2 .2 0])
grid on

figure(2);  %Plotting Wheel Shapes in Cartasian Coordinates
hold on
plot(theta, Rad, '-k','Linewidth',2)
plot(theta(AngPos_idx), Rad(AngPos_idx),'ob','MarkerEdgeColor','b',...
```

275

```matlab
        'MarkerFaceColor','b', 'MarkerSize',9);
yLimits = get(gca, 'YTick');
plot([theta(AngPos_idx), theta(AngPos_idx)], ...
     [min(yLimits), max(yLimits)],'--k', 'Linewidth', 2);
title('Two Dimensional Kinetic Shape (Cartesian)','FontSize',15,...
      'FontName','Times New Roman')
xlabel('Theta (Radians)','FontSize',12, 'FontName','Times New Roman')
ylabel('Radius (Inches)','FontSize',12, 'FontName','Times New Roman')
set(gca,'xLim',[0,2*pi]);
set(gca,'XTick',[0:pi/2:2*pi])
grid on


figure(3);  %Plotting Given and Calculated Horizontal Reaction Force
plot(theta, Fr, '--r','Linewidth',6)
hold on
plot(theta, Fv, '--b','Linewidth',6)
plot(theta, Fr_check, '-k','Linewidth',3)
plot([0 2*pi],[0 0],'k--','LineWidth',2)        %Zero Line
yLimits = get(gca, 'YTick');
plot([theta(AngPos_idx), theta(AngPos_idx)], [min(yLimits), max(yLimits)],...
     '--k', 'Linewidth', 2);  %Initial Line
title('Kinetic Shape Applied and Reaction Force','FontSize',15, ...
   'FontName','Times New Roman')
xlabel('Theta (Radians)','FontSize',12, 'FontName','Times New Roman')
ylabel('Force (Newtons)','FontSize',12, 'FontName','Times New Roman')
set(gca,'xLim',[0,2*pi]);
set(gca,'XTick',[0:pi/2:2*pi])
grid on

figure(4)  %Kinetic Shape Angular Acceleration around Perimenter
plot(theta, AngAcc, '-.k', 'linewidth', 4)
hold on
yLimits = get(gca, 'YTick');
plot([theta(AngPos_idx), theta(AngPos_idx)], [min(yLimits), max(yLimits)], ...
   '--k', 'Linewidth', 2);
title({'Kinetic Shape Angular';'Acceleration at all ...
   Points'},'FontSize',15, 'FontName','Times New Roman')
set(gca,'xLim',[0,2*pi]);         set(gca,'XTick',[0:pi/2:2*pi])
xlabel('Theata(Radians)');
ylabel('Angular Acceleration (Rad/s^2)','FontSize',12, 'FontName','Times ...
   New Roman')
grid on

figure(5) %KS Angular Position
plot(time, AngPos, '--g', 'linewidth', 3)
title('Angular Position','FontSize',15, 'FontName','Times New Roman')
xlabel('Time(Seconds)','FontSize',12, 'FontName','Times New Roman')
ylabel('Angle (Radians)','FontSize',12, 'FontName','Times New Roman')

figure(6) %KS Angular Velocity
plot(time, AngVel, '--b', 'linewidth', 3)
title('Angular Velocity','FontSize',15, 'FontName','Times New Roman')
xlabel('Time(Seconds)','FontSize',12, 'FontName','Times New Roman')
```

```matlab
ylabel('Angular Velocity (Radians/Second)','FontSize',12, ...
    'FontName','Times New Roman')

figure(7) %KS Angular Acceleration
plot(time, AngAcc2, '-.k', 'linewidth', 4)
title('Angular Acceleration','FontSize',15, 'FontName','Times New Roman')
xlabel('Time(Seconds)','FontSize',12, 'FontName','Times New Roman')
ylabel('Angular Acceleration (Radians/Second^2)','FontSize',12, ...
    'FontName','Times New Roman')

figure(8) %KS Linear Position
plot(time, LinPos, '--g', 'linewidth', 3)
title({'Linear (Rolling) Position'},'FontSize',15, 'FontName','Times New ...
    Roman')
xlabel('Time(Seconds)','FontSize',12, 'FontName','Times New Roman')
ylabel('Position (Length)','FontSize',12, 'FontName','Times New Roman')

figure(9) %KS Linear Velocity
plot(time, LinVel, '--b', 'linewidth', 3)
title({'Linear (Rolling) Velocity'},'FontSize',15, 'FontName','Times New ...
    Roman')
xlabel('Time(Seconds)','FontSize',12, 'FontName','Times New Roman')
ylabel('Velocity (Length/Second)','FontSize',12, 'FontName','Times New Roman')

figure(10) %KS Linear Acceleration
plot(time, LinAcc, '-.k', 'linewidth', 4)
title({'Linear (Rolling) Acceleleration'},'FontSize',15, 'FontName','Times ...
    New Roman')
xlabel('Time(Seconds)','FontSize',12, 'FontName','Times New Roman')
ylabel('Acceleration (Length/Second^2)','FontSize',12, 'FontName','Times ...
    New Roman')

%=================================================================================
%                          Position and Format Plots
%=================================================================================
%Positions of Plots on Screen
Pos  = zeros(10,4);
Pos(1,:)   = [0      0    440    348]; %KS in polar coordinates
Pos(2,:)   = [467    0    440    347]; %KS in Cartesian coordinates
Pos(3,:)   = [0     459   440    540]; %Applied/Reaction Forces
Pos(4,:)   = [470   459   440    540]; %Angular Acceleration around KS
Pos(5,:)   = [927   730   475    267]; %KS Angular Position
Pos(6,:)   = [927   379   475    258]; %KS Angular Velocity
Pos(7,:)   = [929    12   476    271]; %KS Angular Acceleration
Pos(8,:)   = [1420  730   480    267]; %KS Linear Position
Pos(9,:)   = [1420  377   480    263]; %KS Linear Velocity
Pos(10,:)  = [1421   16   481    268]; %KS Linear Acceleration

for i = [1, 2, 3, 4, 5, 6, 7, 8, 9, 10]
    figure(i)
    set(gca, 'FontSize',10, 'FontName','Times New Roman')
    xlabel('Time(Seconds)')
    set(figure(i),'position', Pos(i,:));
    grid on
```

```
end


%=============================================================================
%                      Export 2D data points to Text File
%=============================================================================
[X,Y] = pol2cart(theta, Rad);
Z = zeros(length(theta),1);
DATA = [X Y Z];
dlmwrite('2D_KS_XY.txt', DATA, 'precision', '%g', 'newline', 'pc');


%=============================================================================
%                      Export Dynamics Data to Text File
%=============================================================================
DATA = [time, AngPos, AngVel, AngAcc2, LinPos, LinVel, LinAcc];
dlmwrite('2D_KS_KIN.txt', DATA, 'precision', '%g', 'newline', 'pc');


fprintf('Done.\n\n')
```

B.2 Three Dimensional Kinetic Shape Matlab® Code

```
clc        %Clear the command window
close all   %Close all open figures/matlab windows
clear all   %Clear all data in matlab workspace


%=============================================================================
%                                  INPUT
%=============================================================================
n          = 5;  %Numerical Resolution
Resolution = 100;

%Definition Range (Radians)
theta1 = linspace(0, 2*pi ,Resolution*n);%Elevation Angle Range (theta)
phi1 = linspace(0, 2*pi ,Resolution*n);  %Azimuth Angle Range (phi)
[theta, phi] = meshgrid(theta1,phi1);

%Applied vertical force to axle of 3D KS  (Unit Force)
%  Note:  This is a constant funciton. While this code does not support a
%         variable vertical force funciton, it can be added.
Fv = 1000;

%Generating Desired Reaction Force Function in Theta (raidal) Direction
%  Note: This code only supports horizontal ground reaction forces in
%        exponential and sinosodial force functions, specifiying constants.
c1R = 100;       odrR = 0;
c2R = 5;         odr2R = 1;
c3R = 10;        freq1R = 1;
c4R = 0;         freq2R = 1;


%Fr = zeros(length(theta)); %Blank Vector
```

278

```matlab
Fr =    c1R*theta.^odrR       ...
     + c2R*phi.^odr2R       ...
     + c3R*sin(freq1R*theta) ...
     + c4R*sin(freq2R*phi);

%Generating Desired Reaction Force Function in Phi (tangential) Direction
c1T = 10;       odrT = 0;
c2T = 10;       odr2T = 0;
c3T = 0;        freq1T = 1;
c4T = 10;       freq2T = 1;

%FT = zeros(length(phi)); %Blank Vector
FT =  c1T*theta.^odrT        ...
    + c2T*phi.^odr2T         ...
    + c3T*sin(freq1T*theta) ...
    + c4T*sin(freq2T*phi);

%Specify coordinates where within Input force the shape will start
%     Coordinates = [Theta, Phi]
pThidx = 1*n;    %Starting Point Index in theta direction
pPhidx = 1*n;    %Starting Point Index in phi direction

%Initial Radius of 3D Kinetic Shape  (Unit Length)
Ri = 1;

%Integration direction values
%     A value of 1 is 2pi, 0.5 is pi, and so on...
ThetaPath = 1;
PhiPath   = 1;
%============================================================================


FTotal = Fr + FT;       %Total Force - Radial plus Tangential Force

%Direction of Integration (Rolling Movement)
%     In this code the integration direciton is linear and constantly
%     increasing, however one can reprogram this code such that the
%     integration path is over a non-linear theta and phi range.
position = [[pThidx, pPhidx], [theta1(pThidx), phi1(pPhidx)], ...
   FTotal(pPhidx, pThidx)];
for r = 8:(Resolution*n)
    %Direction travel
    %For each angle step, take one index step in theta direction
    pThidx = pThidx + ceil(ThetaPath*4);   %Index amount moved in theta ...
        direction
    pPhidx = pPhidx + ceil(PhiPath*4);    %Index amount moved in phi direction

    pThidx = ceil(r*ThetaPath);
    pPhidx = ceil(r*PhiPath);

    position = [position; pThidx pPhidx theta1(pThidx), phi1(pPhidx), ...
        FTotal(pPhidx, pThidx)];
end
```

279

```matlab
%==================================================================================
%                  Applying Three-Dimensional Kinetic Shape Equation
%==================================================================================
%Derivation of Shape (Curve)
[a, b] = size(theta);
r1(a,b) = 0;
firstRun = 0;
for j = 2:length(position)
    t     = position(j,   1);
    t_min1 = position(j-1, 1);

    p     = position(j,   2);
    p_min1 = position(j-1, 2);

    th  = phi(t,       p);
    th1 = phi(t_min1, p);

    ph  = theta(t, p);
    ph1 = theta(t, p_min1);


    if(firstRun==0)
        r1(t_min1,p_min1) =  Ri;
        firstRun = 1;
    end

    %==============  Theta Direction Integrals ================
    Int_Fr_dth = c1R*(th^(odrR+1))/(odrR+1) ...
        +       th*c2R*(ph^(odr2R))...
             - c3R*(1/freq1R)*cos(freq1R*th) ...
        +       th*c4R*sin(freq1R*ph);

    Int_Fr_dth1 = c1R*(th1^(odrR+1))/(odrR+1)  ...
          +  th1*c2R*(ph^(odr2R))...
             - c3R*(1/freq1R)*cos(freq1R*th1) ...
          +  th1*c4R*sin(freq1R*ph);
    C = log( r1(t_min1,p_min1) ); %Constant

    r1(t_min1,p) = exp(  (Int_Fr_dth / Fv) - (Int_Fr_dth1 / Fv)   +  C  );


    %==================  Phi Direction Integrals ====================
    Int_FT_dph =          ph*c1T*th^odrT + c2T*(ph^(odr2T+1))/(odr2T+1)...
             +  ph*c3T*sin(freq1T*th) - c4T*(1/freq2T)*cos(freq2T*ph);
    Int_FT_dph1 =         ph1*c1T*th^odrT + c2T*(ph1^(odr2T+1))/(odr2T+1)...
            +  ph1*c3T*cos(freq1T*th) - c4T*(1/freq2T)*cos(freq2T*ph1);

    Int_Fr_dph =          ph*c1R*th^odrR + c2R*(ph^(odr2R+1))/(odr2R+1)...
             + ph*c3R*sin(freq1R*th) - c4R*(1/freq2R)*cos(freq2R*ph);
    Int_Fr_dph1 =         ph*c1R*th1^odrR + c2R*(ph1^(odr2R+1))/(odr2R+1)...
            + ph1*c3R*sin(freq1R*th) - c4R*(1/freq2R)*cos(freq2R*ph1);
```

```matlab
    r1(t,p) = r1(t_min1,p)* exp(  (Int_FT_dph/Int_Fr_dph) ...
              - (Int_FT_dph1/Int_Fr_dph1)    );
end


%================================================================================
%                          Plotting Kinetic Shape
%================================================================================
%Converting Shape from spherical to cartesian coordiantes for plotting
[x1,y1,z1] = sph2cart(theta,phi,r1);
value = find(x1 ≠ 0);
noZigZag = [x1(value(2:2:end)),y1(value(2:2:end)),z1(value(2:2:end))];

%Plotting Derived 3D KS
figure(1);
plot3(0,0,0,'-mo','MarkerSize',10,'MarkerFaceColor','k')   %Origin point
hold on
plot3(x1(value(2:2:end)),y1(value(2:2:end)),z1(value(2:2:end)),...
      '.k','MarkerSize',10);
title('3D Kinetic Shape', 'FontSize',14, 'FontName','Times New Roman')
xlabel('X') ; ylabel('Y') ; zlabel('Z')
axis equal %tight
view(60, 30);
grid on

%Plotting Radial Force
figure(2);   %Input
contour(theta1, phi1, Fr, 18);
hold on
plot(position(:,3), position(:,4),'--k','Linewidth',4)
title('Radial Reaction Force', 'FontSize',14, 'FontName','Times New Roman')
xlabel('Theta (Radians)','FontSize',12, 'FontName','Times New Roman');
ylabel('Phi (Radians)','FontSize',12, 'FontName','Times New Roman'),
zlabel('Force','FontSize',12, 'FontName','Times New Roman');
set(gca,'xLim',[min(theta1),max(theta1)]);
set(gca,'yLim',[min(phi1),max(phi1)]);
colorbar
grid on

%Plotting Tangential Force - Input
figure(3);
contour(theta1, phi1, FT, 18);
hold on
plot(position(:,3), position(:,4),'--k','Linewidth',4)
title('Tangential Reaction Force', 'FontSize',14, 'FontName','Times New ...
   Roman')
xlabel('Theta (Radians)','FontSize',12, 'FontName','Times New Roman');
ylabel('Phi (Radians)','FontSize',12, 'FontName','Times New Roman'),
zlabel('Force','FontSize',12, 'FontName','Times New Roman');
set(gca,'xLim',[min(theta1),max(theta1)]);
set(gca,'yLim',[min(phi1),max(phi1)]);
colorbar
grid on

%Ploting Total Forces onto a contour plot
```

```matlab
figure(4);
C = contour(theta1, phi1, FTotal, 18);
hold on
plot(position(:,3), position(:,4),'--k','Linewidth',4)
title('TOTAL Reaction Force Input', 'FontSize',14, 'FontName','Times New ...
    Roman')
xlabel('Theta (Radians)','FontSize',12, 'FontName','Times New Roman');
ylabel('Phi (Radians)','FontSize',12, 'FontName','Times New Roman')
set(gca,'xLim',[min(theta1),max(theta1)]);
set(gca,'yLim',[min(phi1),max(phi1)]);
colorbar
grid on


%=============================================================================
%              Export 3D data points to text file and .STL File
%=============================================================================
%XYZ point coordinates to text file:
Data = noZigZag;
dlmwrite('3D_KS_XYZ.txt', Data, 'precision', '%g', ...
          'newline', 'pc');

%3D object to .stl file:
surf2stl('3D_KS_STL.stl',x1,y1,z1)

%Checking what was written to the .stl file file
check = stlread('3D_KS_STL.stl')
figure
patch(check,'FaceColor',       [0.5 0.8 1.0], ...
            'EdgeColor',        'none',        ...
            'FaceLighting',     'gouraud',     ...
            'AmbientStrength', 0.15);
view([-135 35]);
%NOTE: When rendering/loading in SolidWorks, use "point cloud" option
```

Appendix C: Kinetic Shape System Notation

Here I am presenting my kinetic shape system notation that I have invented, explaining the symbols used to describe a kinetic shape system. These are the symbols I came up with, however, other symbols and arrangements for the kinetic shape system may be possible.

Table C.1: Kinetic Shape System Notation

Name	Symbol	Variation / Application	Description
Force Transfer Connector			
Force Input			This symbol is used at the beginning of the kinetic shape system diagram or anywhere where new force is added into the system.
Force Output			This symbol represents any force that is an product or output force of the kinetic shape system
Kinetic Shape Force Left			This represents a kinetic shape that creates a radial ground reaction force in the left direction. "Left" is a arbritary designation dependent on the sign convention.
Kinetic Shape Force Right			This represents a kientic shape that creates a radial ground reaction force in the right direction. "Right" is a arbritary designation dependent on the sign convention.
Force Devision			This symbol represents applying a force to one or more kinetic shapes in series. This devides the force each time by a value greater than one.
Force Multiplication			This symbol represents pulling a kinetic shape by the rolling platform, while it reacts by pushing perpendicular and by the shape axle. This multiplies the force.
Force Addition			This symbol represents two kinetic shape forces adding in reaction forces.
Force Subtraction			This symbol represents two kinetic shape forces subtracting in reaction forces.
Spring Force			This symbol represents a spring-like mechanism attached between a kinetic shape and ground or other configuartions. Note that a spring is kinetic shape position dependent.
Redirection			This symbol represents a redirection or reorientation of force, by a gear, pulley, or sprocket.

Name	Symbol	Variation / Application	Description
Inline Torque Input	τ/r	10/0.1	This is an input torque, τ, inline with a force connection, which may represent a rotary actuator such as a motor. This torque has to be devided by the torque lever, r.
Torque Output	r (OUT)	0.3 (OUT)	This is an torque, τ, output from the kinetic shape system. This symbol must be defined with a torque lever, r.
Force Transfer Loss	N%	30%	This symbol is used as an indicator of force transfer loss within the kinetic shape system. This may be due to striction, friction, or misalignments.
Conditional Statement	- +	- + / + -	This symbol is used when a kinetic shape's ground reaction force definition can be positive or negative. When connected to two other kinetic shapes, it will engage one shape when it is positive and the other when it is negative. This symbol may also output or disipate force as an option.

Appendix D: Kinetic Board Drawings

In this appendix section, I am presenting more detailed computer aided drafting (CAD) drawings and other appropriate schematics for my invented kinetic board device. CAD drawings were produced in SolidWorks®.
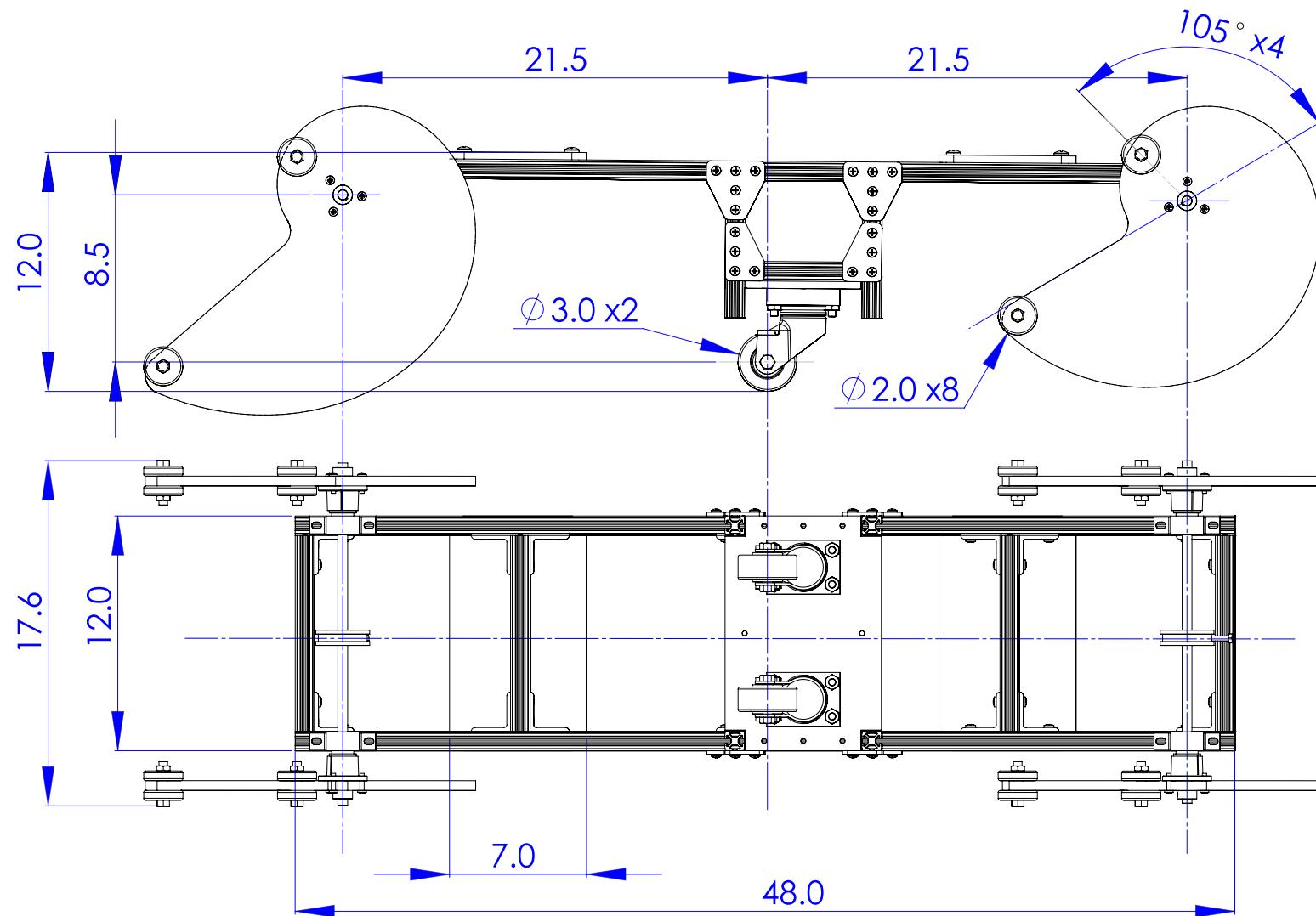
Figure D.1: The kinetic board dimensions, side and bottom view. All dimensions in inches.

Wheel Bushing (x4)
(1/2" Bore)

Ball Bearing (x4)
(1/2" Shaft, Base Mount)

Wooden Stepping Board (x2)

Reset Pulley (x2)

Aluminum Extrusion Framing (1"x 1")

Plastic Rollers Assembly (x8)

Spring Attachment (x2)

Kinetic Shape Wheel (Back)

Spring Loaded Rubber Caster Wheel (x2)

Kinetic Shape Wheel (Front)

L-Bracket (x16)
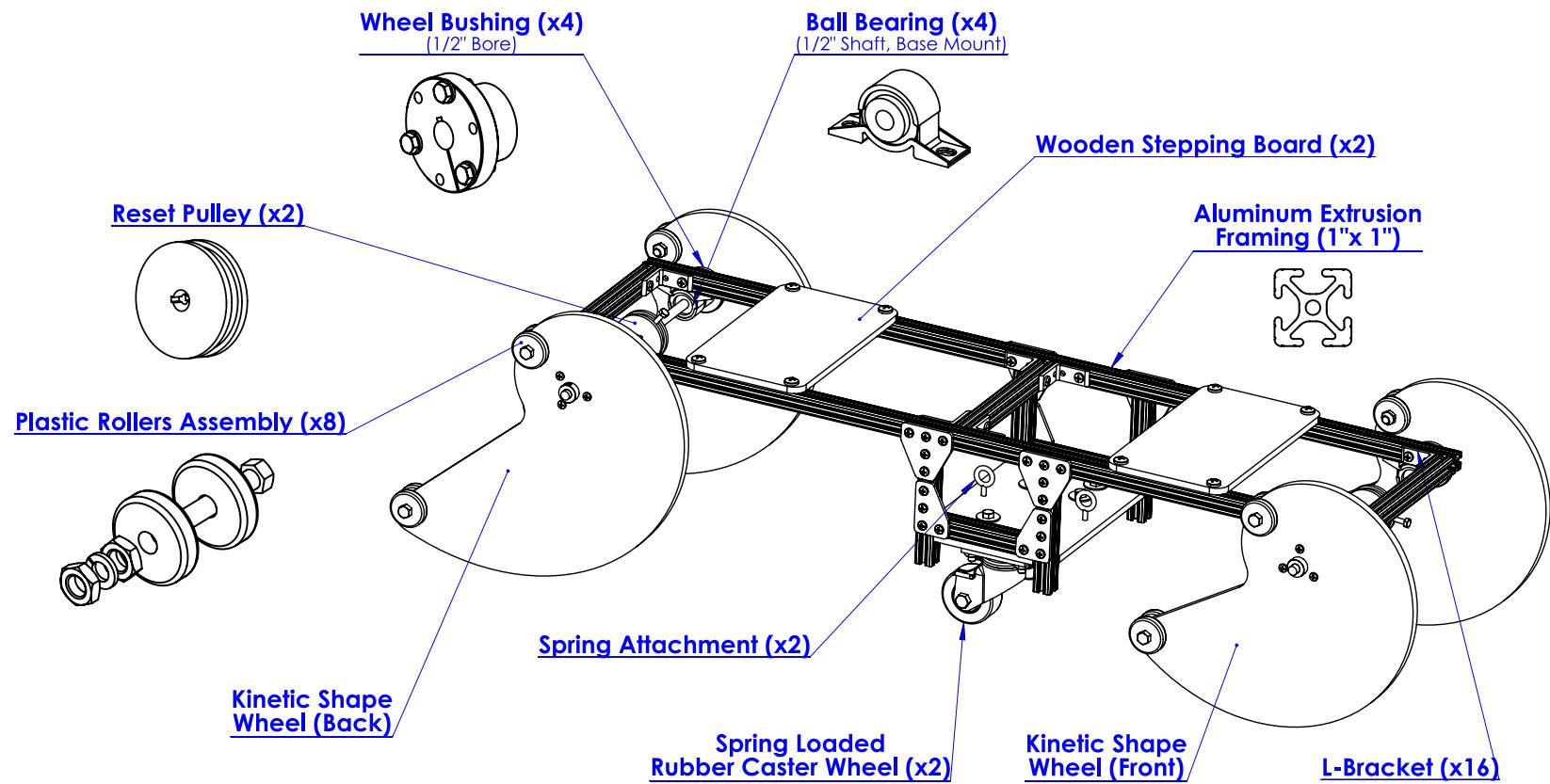
Figure D.2: Parts anatomy of the kinetic board
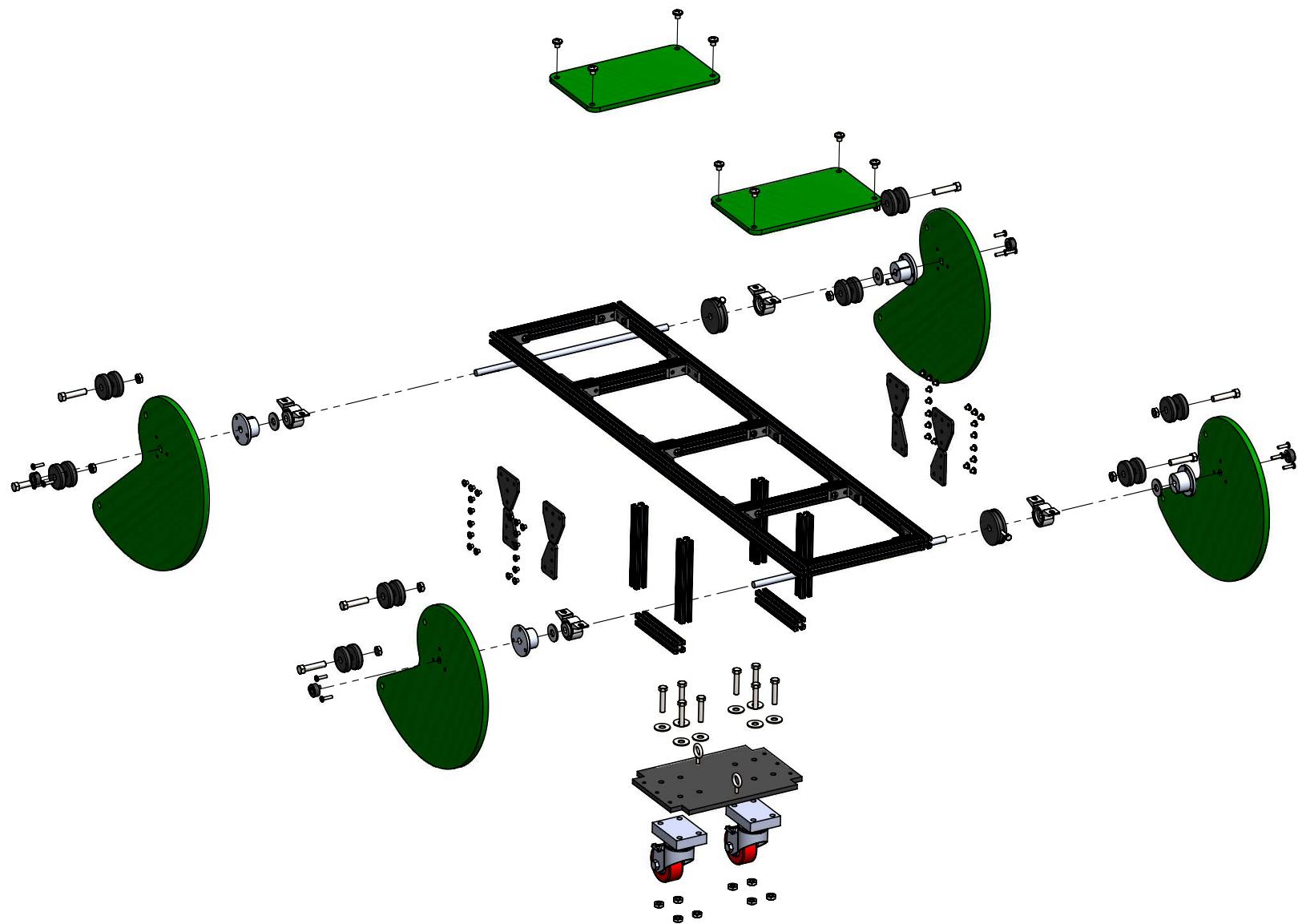
Figure D.3: The kinetic board exploded view

Appendix E: Passive Dynamic Walker Derivation Schematics

In this appendix section, I will present the derivation schematics for my point foot passive dynamic walker (PDW) model. These schematics are included in this dissertation to calrify and ease the derivation of the PDW models which I am presenting. Note that the schematics of the actual 9-mass PDW models are too cluttered to be presented as useful schematics. However, these simplified drawings are sufficient to be extrapolated for more masses on the walker. Note that I am including one mass per link, which again can be extrapolated for two or more masses per link.

E.1   PDW Schematic Notation

Here I am designating the stance leg parameters with the subscript "ST", while all swinging leg parameters are denoted by the subscript "SW". The stance and swing leg parameters may be renamed "L" for left side parameters, or "R" for right side parameters. This differentiating of PDW sides, allows for asymmetric PDW parameter definitions, such as asymmetric link lengths or link masses.

In the case of a three link PDW, the thigh masses are designated with the subscript "t', while a shank masses are designed by a subscript "s". The subscript "H" denotes the hip mass. For example, a designation of "m_{tSW}" represents a mass on the thigh of the swing leg. However, in my computer program the sides and mass numbers are differentiated. As such, the second mass on the left swinging thigh would be designated as "m_{tL2}", while the first mass on on the right leg would be designated as "m_{sR1}".

Simplified Parameters
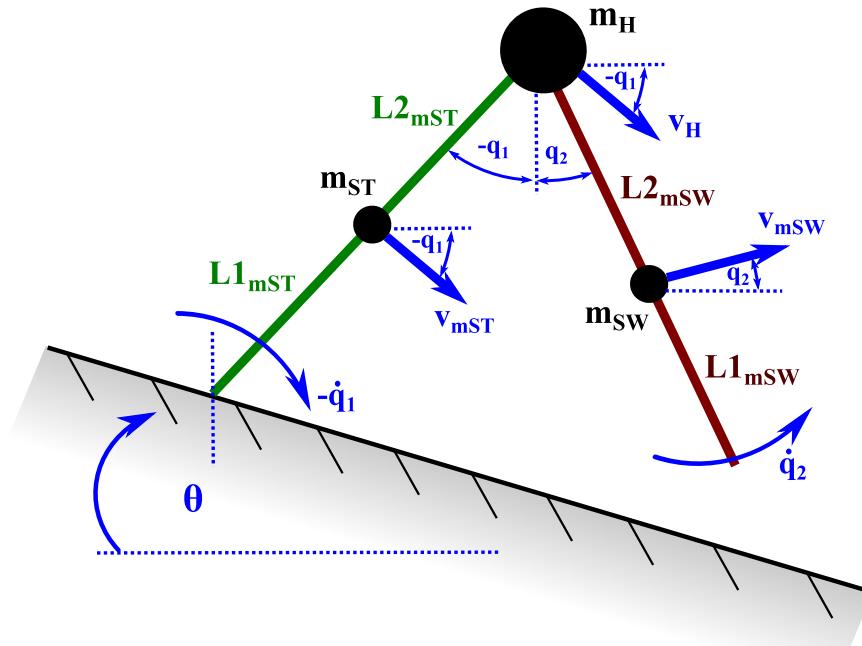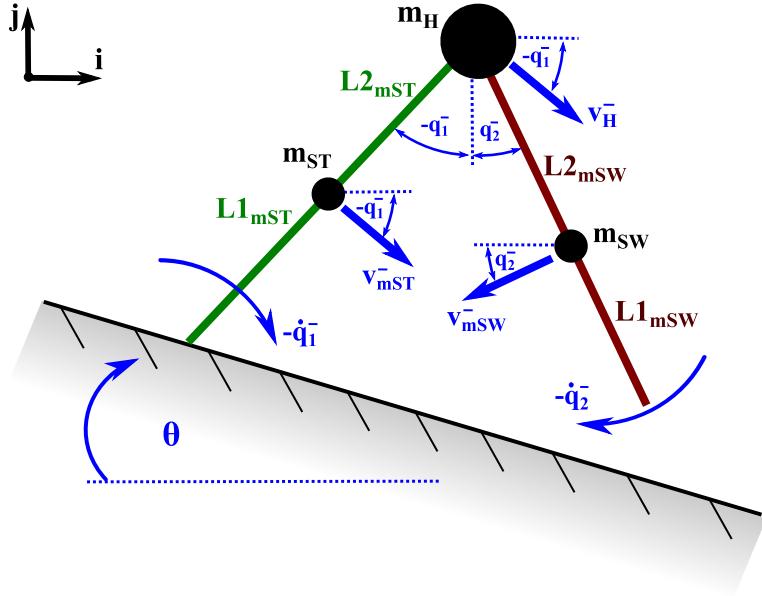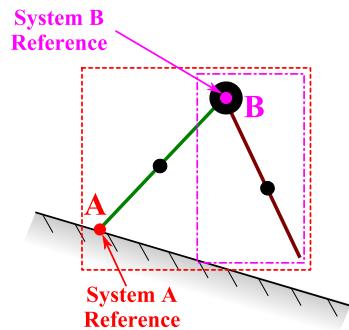
Figure E.1: Simplified 2-link point foot PDW kinematic parameters. This drawing may be used to define the potential and kinetic energy needed to derive the Lagrangian.
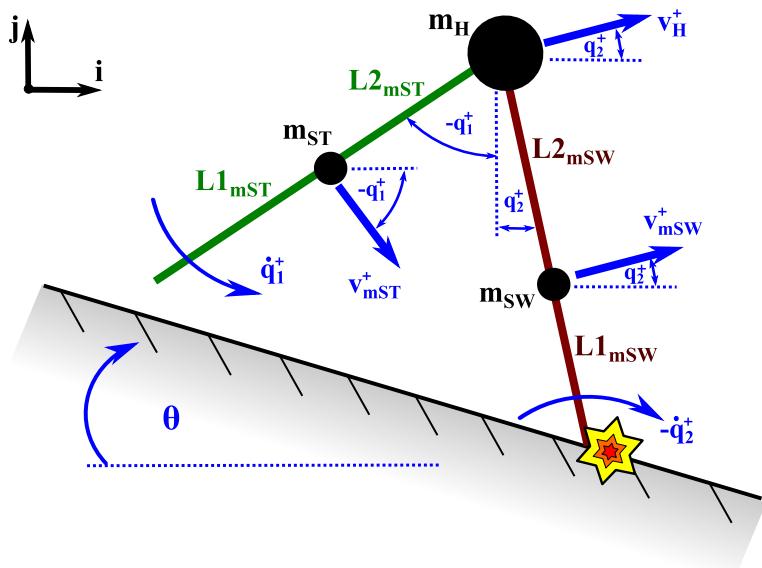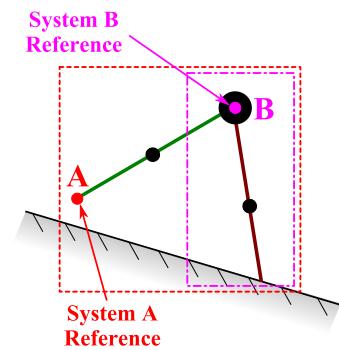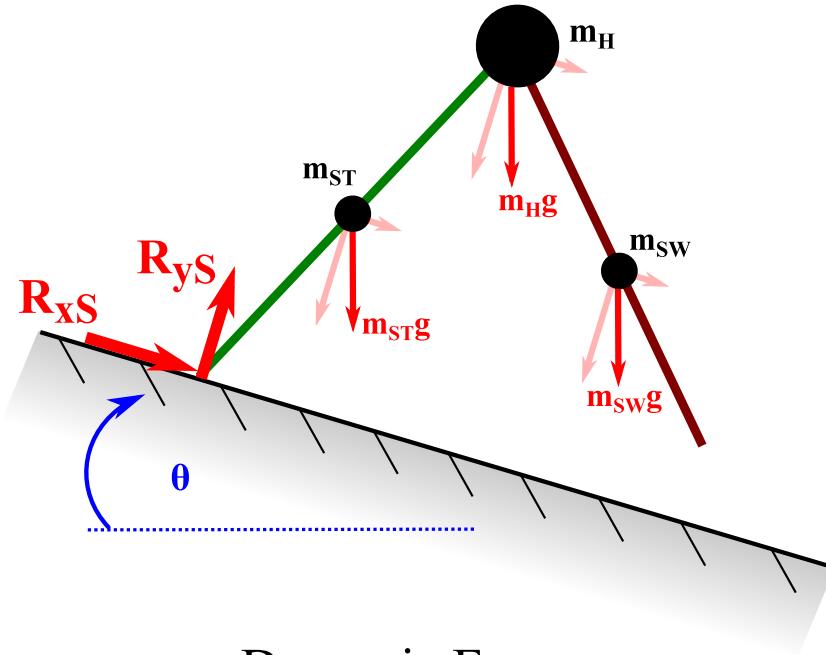
Figure E.2: Simplified 2-link point foot PDW collision event parameters and conserved systems before and after a heel strike. Two conserved systems will yield two conservation of angular momentum equations to be solved for the dynamics *prior* to heel strike. If the PDW subsequently goes into 3-link phase, three post-collision conservation of angular momentum equations are produced *after* the collision.
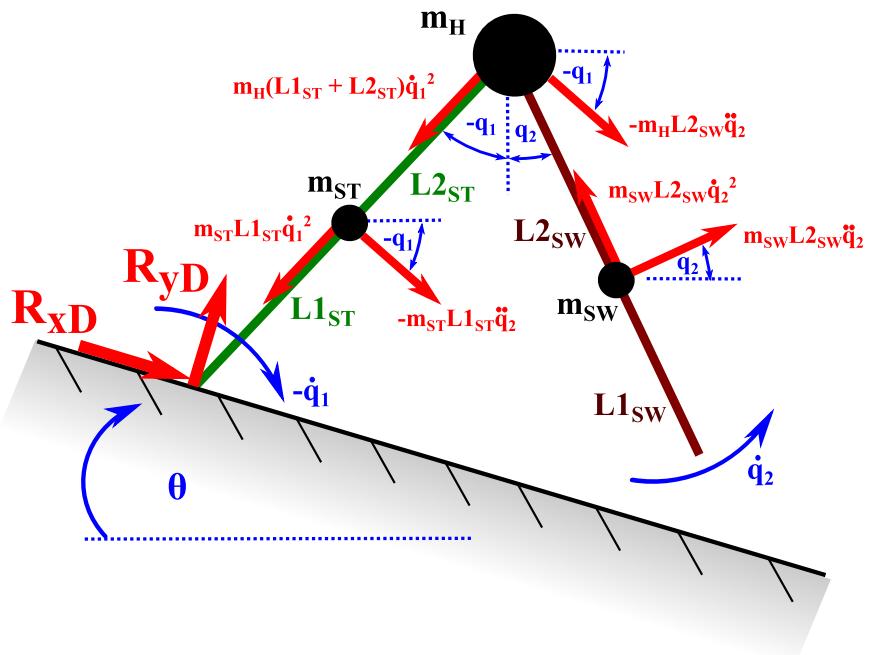
Figure E.3: 2-link point foot PDW kinetic diagram

Simplified Parameters
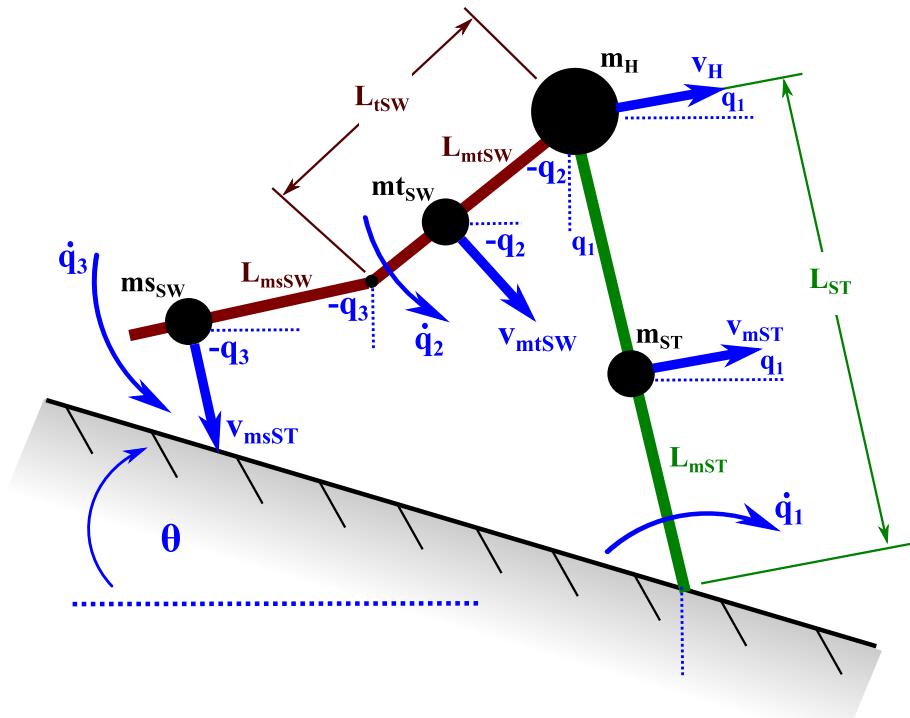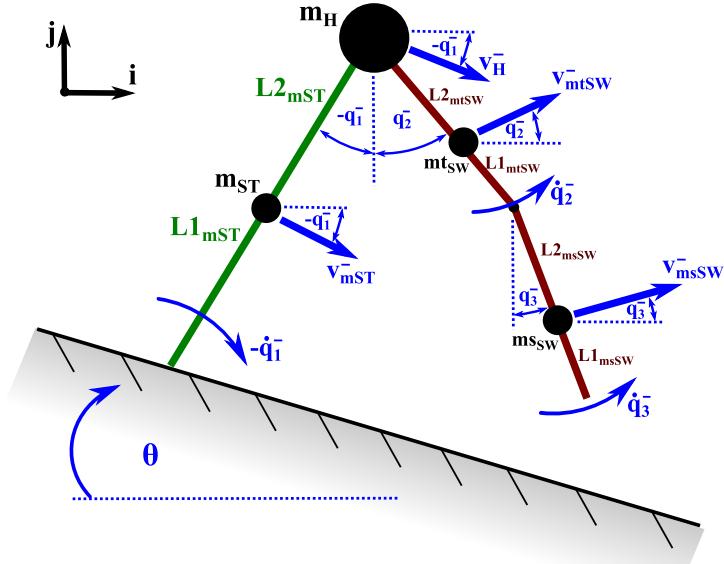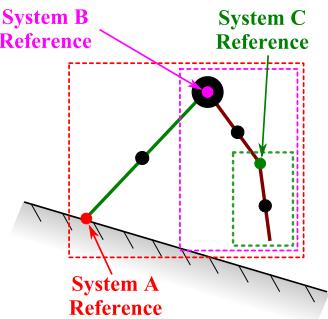
Figure E.4: Simplified 3-link point foot PDW kinematic parameters. This drawing may be used to define the potential and kinetic energy needed to derive the Lagrangian.
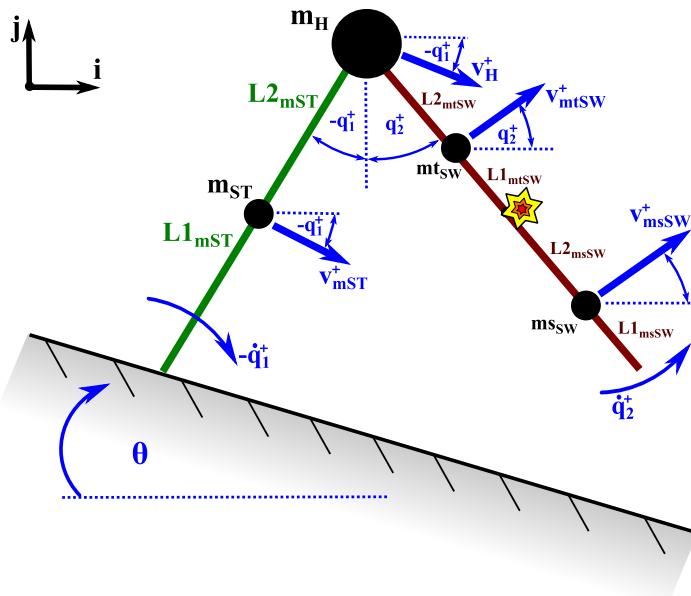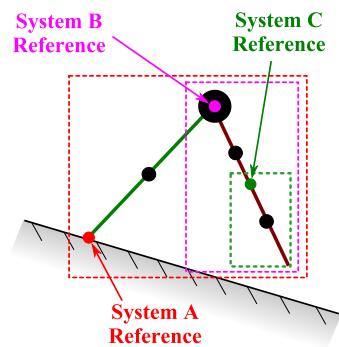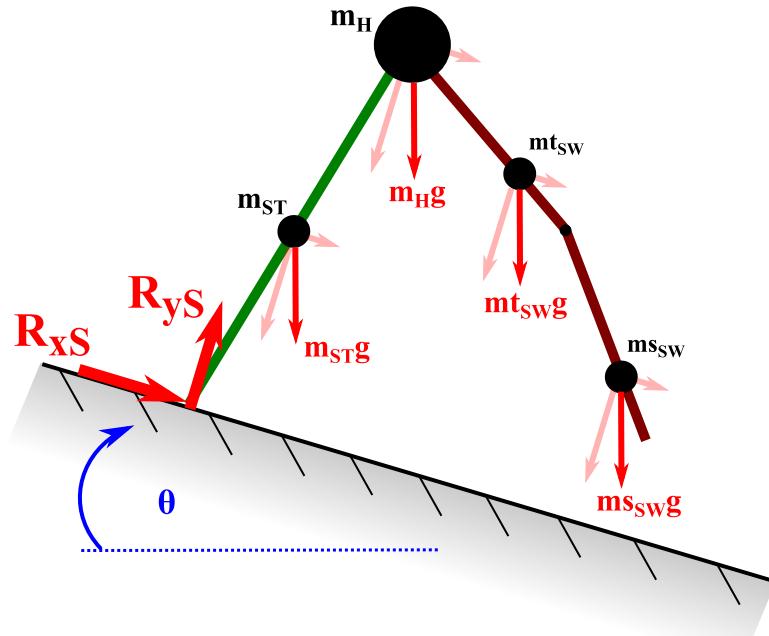
Figure E.5: Simplified 3-link point foot PDW collision event parameters and conserved systems before and after a heel strike. Three conserved systems will yield two conservation of angular momentum equations to be solved for the dynamics *prior* to heel strike. If the PDW subsequently goes into 2-link phase after knee strike, two post-collision conservation of angular momentum equations are produced *after* the collision.
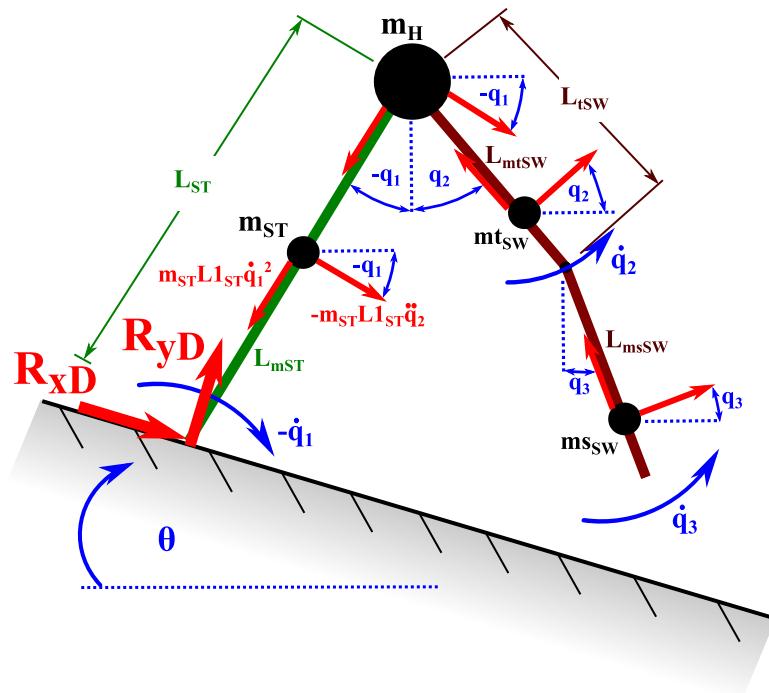
Figure E.6: 3-link point foot PDW kinetic diagram

Figure E.7: Simplified 2-link variable curve foot PDW kinematic parameters. This drawing may be used to define the potential and kinetic energy needed to derive the Lagrangian.
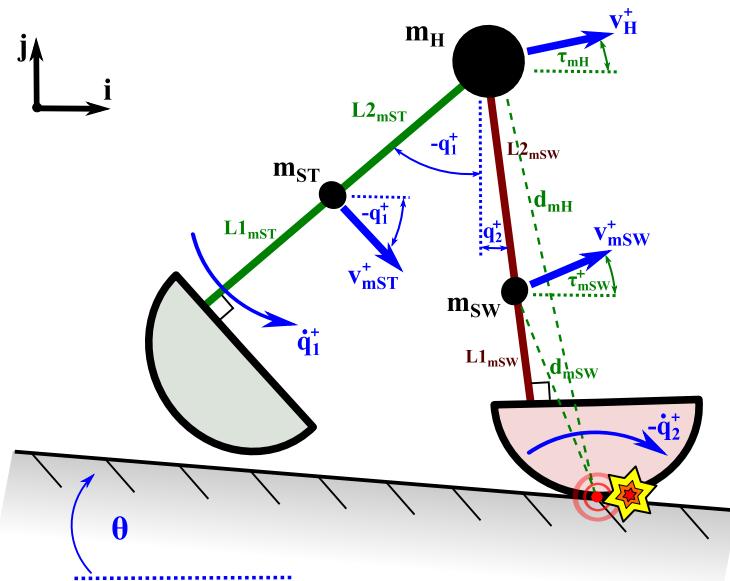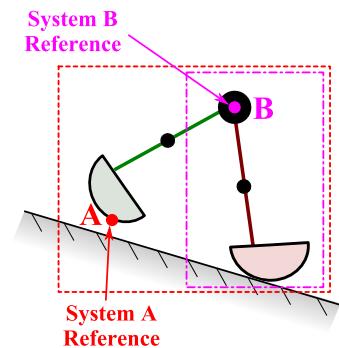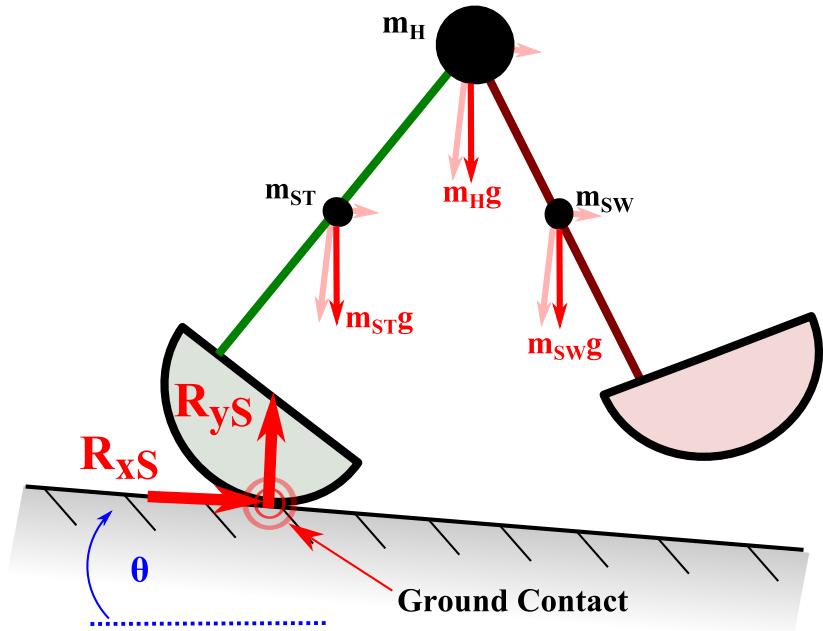
Figure E.8: Simplified 2-link curve foot PDW collision event parameters and conserved systems before and after a heel strike. Two conserved systems will yield two conservation of angular momentum equations to be solved for the dynamics *prior* to heel strike. If the PDW subsequently goes into 3-link phase, three post-collision conservation of angular momentum equations are produced *after* the collision.

Static Forces

Dynamic Forces
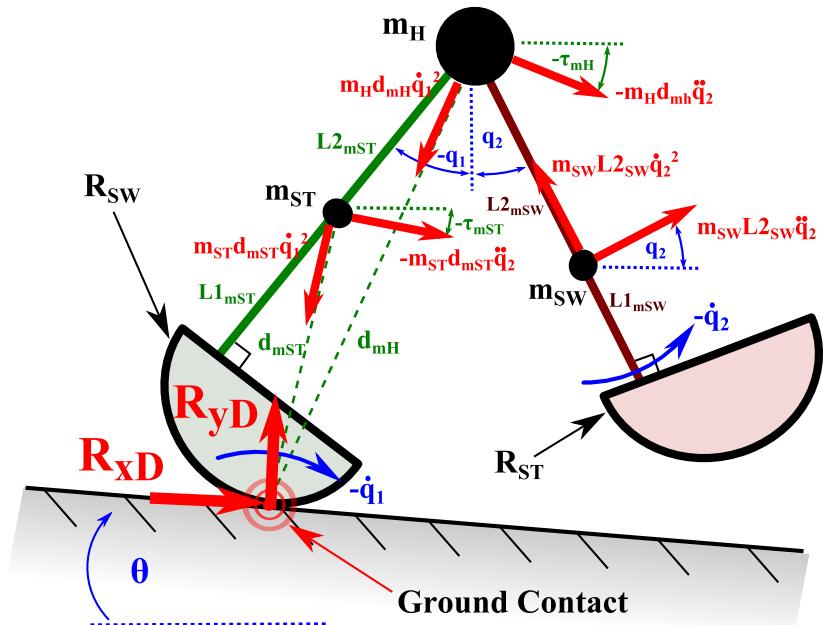
Figure E.9: 2-link curve-foot PDW kinetic diagram

Simplified Parameters
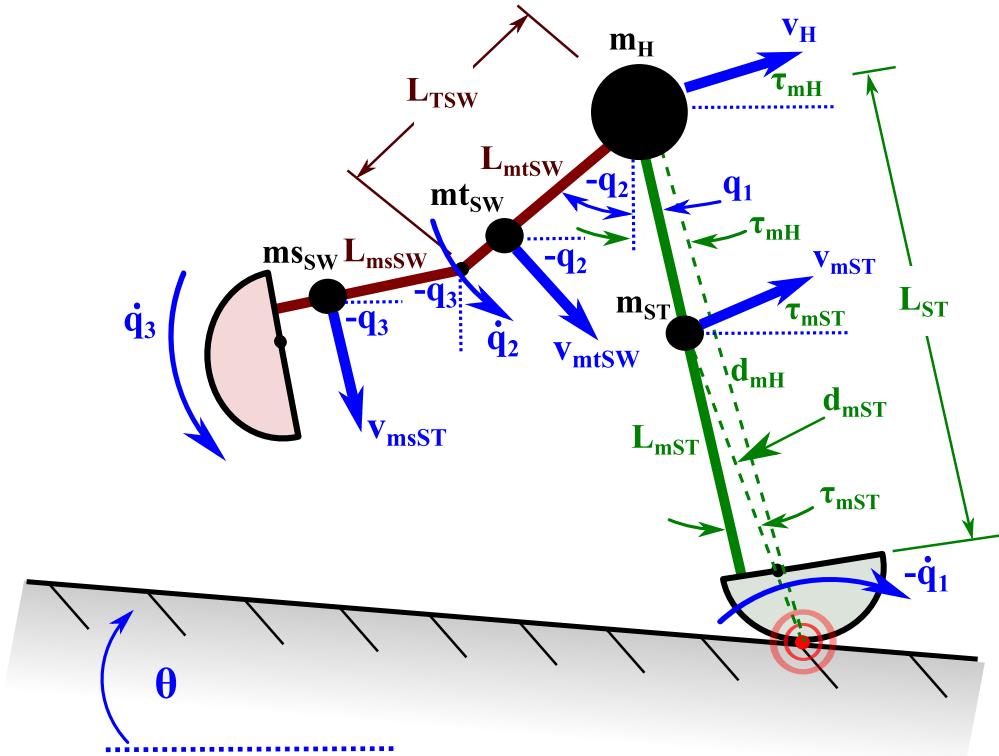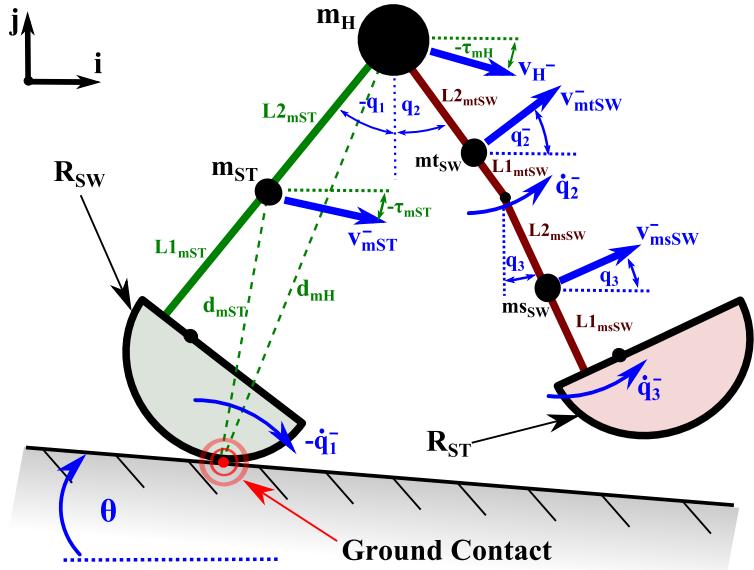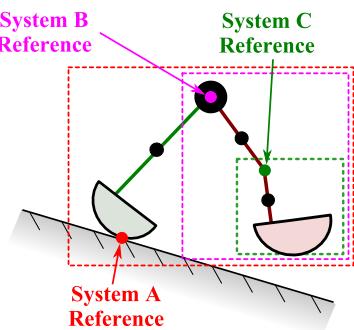
Figure E.10: Simplified 3-link curve-foot PDW kinematic parameters. This drawing may be used to define the potential and kinetic energy needed to derive the Lagrangian.
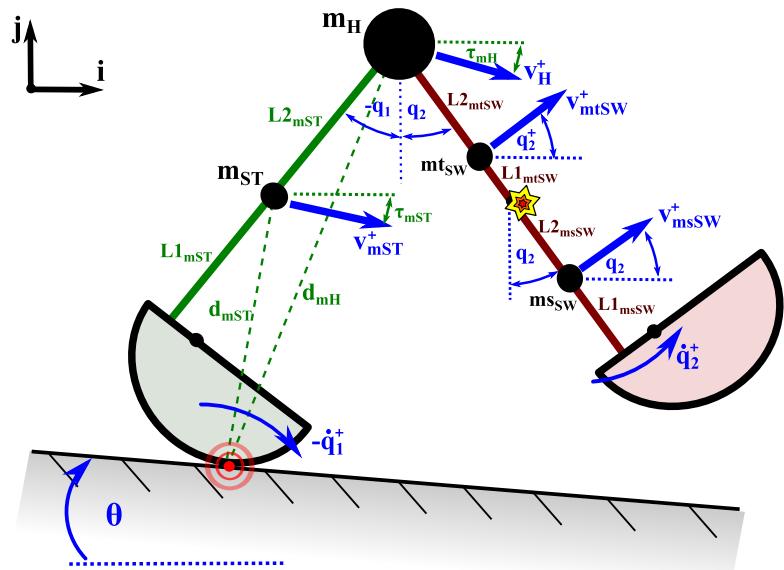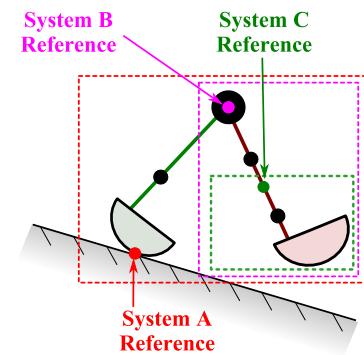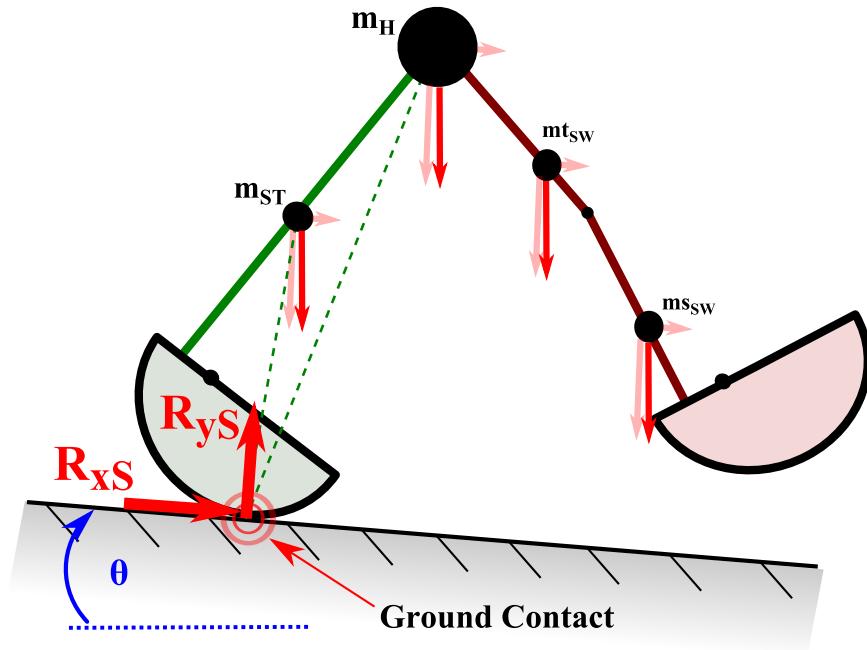
Figure E.11: Simplified 3-link curve-foot PDW collision event parameters and conserved systems before and after a heel strike. Three conserved systems will yield two conservation of angular momentum equations to be solved for the dynamics *prior* to heel strike. If the PDW subsequently goes into 2-link phase after knee strike, two post-collision conservation of angular momentum equations are produced *after* the collision.

Static Forces

Dynamic Forces
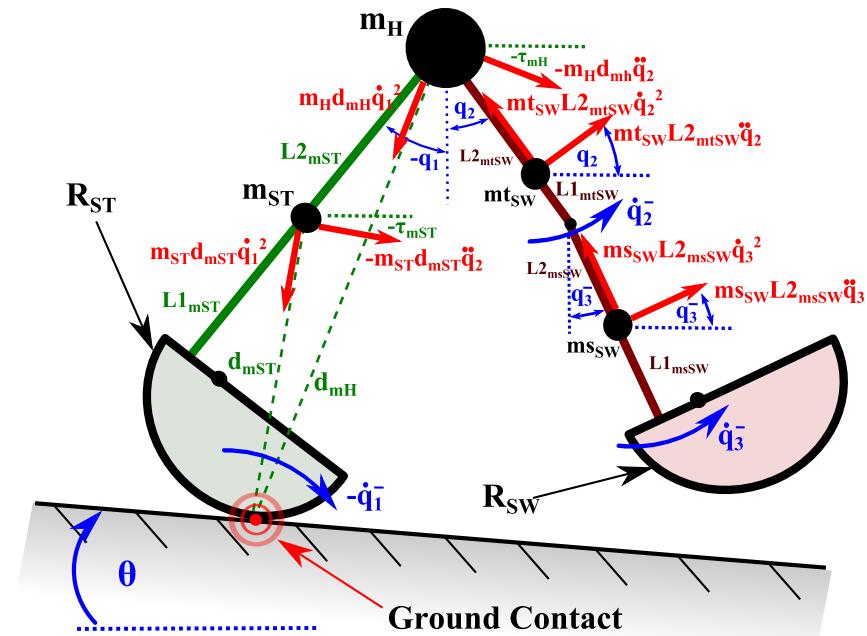
Figure E.12: 3-Link curve-foot PDW kinetic diagram

Appendix F: Research Progress, Setbacks, and Lessons Learned

In this appendix section, I am outlining and explaining my research from a subjective perspective. In the following three sections I am presenting my Gait Enhancing Mobile Shoe, kinetic shape, and passive dynamics research in terms of setbacks, progress, and lessons learned. These subjective views and explanations are traditionally only implied and often times not well understood to persons outside graduate studies or individuals beginning their graduate studies. I am writing this section in hope of illustrating that the path from research to results is often times not linear and can be a product of resources, experience, fundamental knowledge, common sense, and a little bit of luck.

F.1 Gait Enhancing Mobile Shoe

When I first started graduate school, my new advisor had offered me two different projects which I would be able to work on: Bimanual upper limb rehabilitation or the Gait Enhancing Mobile Shoe (GEMS). To be honest I did not a have vision for either one of them and at the time was only interested in getting my Master's degree, becoming a better engineer on the way, and finally getting a well paying job. Because the GEMS seemed to have a greater design and creativity aspect to it, I accepted the GEMS project.

My advisor was new to the university and at the time did not have a fully functioning laboratory. Within the first few months working on the GEMS, I mostly read related publications and research papers my advisor forwarded to me. I tried to soak up as much relevant information as I could to firmly grasp the methods and jargon related to this project topic which was asymmetric gait rehabilitation. Shortly after, I started designing my first redesign of the already existing GEMS. To place my skill as a researcher and design engineer at the time into perspective, I initially designed the GEMS wheel to be milled out of heavy carbon steel, greatly increasing the weight this rehabilitation shoe. In hind sight, I did not have the adequate experience that could have made any initial developments on this project a success, where to me success meant satisfying my advisor's design criteria. It also did not help that I spent most of my time preparing for and taking graduate

school classes, that were much more time consuming than any undergraduate engineering classes I had taken before. However, I still managed to start a reasonable GEMS design CAD model.

My advisor and I met every Monday to review my advancements in the GEMS design, tweaking details, discussing changes, and pitching ideas. I finally settled on one design and started sending drawings to, and working with, the machine shop at the engineering department. I visited and checked upon the machine shop every week or two, eventually taking and bringing the entire device with me as I came and went. As time went by, I took more pride in my design and really wanted it to be a success in any way. In theory, this first GEMS redesign could potentially have been a good design, however in practice it was never reliable, always too heavy, complicated, and needed a lot of unplanned tweaking. At the time I was the first and only graduate assistant to my advisor. Working individually on this project offered more control and creative freedom, however sometimes mistakes were overlooked only to be caught and corrected late in the design process.

Finally, during my final semester for my Master's degree my advisor and I set up an appointment to use a infrared motion capture system across campus to measure the kinematics of the completed GEMS. This motion capture would reveal if in fact the GEMS was moving in an controlled manner that it was designed for. This was my definite deadline to have the GEMS design fully and reliably functioning, however the night before our testing appointment, it just was not functional. The poorly aligned and unnecessarily complicated gear train within the device would constantly lock up, paralyzing the GEMS, while the wheels would randomly slide off the undersized axle and poor attachment method. The electronics needed to be re-soldered or diagnosed a lot, which required the top to be unscrewed each time. The thin chain that connected the two wheel axles would constantly snap, while the thin aluminum axles would slightly bend impeding the whole system. The list of last minute problems grew. Our appointment was at eleven the next morning and I spend the entire night in the laboratory still tinkering with the GEMS trying to get it to work. Finally, that very morning my advisor called the appointment off, which left me very disappointed and discouraged. It just was not possible to deliver a functioning design that

morning and I was disappointed that I was not able to properly conclude my GEMS project which I had started over a year ago.

We never did use the motion capture system on that version of the GEMS. Instead I recorded the GEMS' motion using a video camera, tracking its position with time. It wasn't much and I felt like I really didn't achieve anything with the design and construction of this GEMS prototype. I certainly did not think I achieved so much for my thesis to be accepted by a defense committee, however it eventually did get approved.

I decided to keep track of all my set-backs and solutions that were associated with the my first research project. Below is a list of mechanical and electrical issues I encountered while working on my first redesign of the GEMS during my first year and a half of my graduate school career.

1. Due to heavy work overflow, the machine shop took a long time to fabricate and modify things.

2. A prototype that used high gear ratio worm gear failed due to incorrect estimating torques of the system torques.

3. Steel wheels were too heavy, aluminum wheels were used instead.

4. Aluminum axles bend easily under applied torques and forces, steel axles were used instead.

5. Frame material and structure too stiff, heavy, and not easily manipulated.

6. Frame material was easily stripped when screws were repeatable taken in and out for things such as taking off the top cover.

7. Plastic Miter and spur gears were too weak for reaction forces during GEMS operation.

8. Plastic Miter and spur gears could not be fastened down using set screws, the plastic stripped. Steel gears used.

9. Steel gear train was too heavy. Attempted to lighten by drilling holes through the spur gears.

10. Bearings that were press fit into the fiberglass frame became loose and were slipping out.

11. Miter gears needed precise mesh to function smoothly or to not lock up, this was difficult to design and customize.

12. Gear train produced too much noise.

13. Set screwed Miter gears slipped easily and needed to be pinned to axles.

14. Gear reduction over estimated. Needed 44:1 but mistakenly ended up with 64:1 gear ratio.

15. Later found a vendor with higher gear ratio spur gear sets with same size and material.

16. Aluminum redirect pulley (part of the reset mechanism) was too weak and bend, needed to be redesigned twice, ending up with a with a steel pin design.

17. Constant force springs were too weak to reset the GEMS.

18. Constant force springs became entangled very easy without proper constraints.

19. After ordering new reset springs took eight weeks to arrive.

20. After trying numerous strings and wires, two braided nylon strings in parallel were the final solution. Considering their strength, it had the lowest friction and most flexibility.

21. Reset mechanism string continuously snapped after rubbing on attachment screw when it spun around.

22. Reset spring to string aluminum connection is unbalanced to where the spring had an asymmetric bend, needs to be redesigned to where the nylon string can be easily tied to this connection.

23. Top shoe cover needed to be constraint. Movement of the GEMS frame top cover offset the gear shafts, worsening the meshing between gears and in turn locking up any movement or increasing the system. friction and . Aluminum plates prevented front-back motion, various screws and brackets prevented side to side motion.

24. Rear miter gear bracket was bending due to large Miter gear reaction forces. Needed to be custom fabricated and restrained differently.

25. Various metal spaces were inserted in the gear train to obtain most efficient and smooth gear mesh.

26. Back Miter gear's reaction forces, pushed miter gear with axle up through the top cover causing the gear pair to lose mesh and skip gear teeth. Thick aluminum plate was fixed above the axleâĂŹs bearing.

27. Middle support torsion spring with roller assembly was removed due to instability/unpredictability/complication in current design.

28. Potentiometer bracket too bulky and weighed a lot.

29. Potentiometer bracket needed to be substantially filed down because the reset spring and it were colliding.

30. Frame to reset spring bracket had to be fabricated because forces exerted by the springs were too high.

31. Using a timing belt (with custom fabricated belt tensioner) to transfer torque from rear axle to front axle was too hight which caused severe belt slippage, replaced with chain and sprockets.

32. Chain slacked, could not be tightened fully due to discrete chain links and unavailable chain tools and methods. This gave front and back axle a lag.

33. Magnetic particle brake output shaft and last gear train output shaft that were in parallel while mated with a set of spur gears. Parallel shafts bent apart due to gear reaction forces lowering the meshing efficiency. Brake was slightly angled so that the gears meshed.

34. Shoe plastic strap clips were slipping, Velcro straps were used instead.

35. Opposite leg plastic platform had to be screwed together because hot glue was peeling off.

36. Rubber wheel cover for GEMS-ground traction could not be glued onto the wheel using super/krazy glue or hot glue.

37. Aluminum wheels could not be firmly and reliably attached to the steel axle by only using two set screws and a flat. LocTite helped but the attachment was still unreliable.

38. Two Parallex BSp24 microprocessors were broken and replaced.

39. BSp24 microprocessor only had pulse width modulation (PWM) output to create 0-5VDC.

40. BSp24 could only read a certain type of sensor signal.

41. Initial optical encoder was not compatible with BSp24 microprocessor, used a potentiometer instead.

42. Initial accelerometer was not compatible with BSp24, used an Parallex provided accelerometer.

43. One Parallex accelerometer was broken and replaced.

44. Op-Amp was not outputting predicted voltage, after an extensive diagnosis, an extra connection within op-amp pins was needed.

45. Electrical circuit made out of generic circuit board had weak and unclear connections. Soldering on it was a mess. A circuit board customized and ordered instead.

46. Soldering iron was not working for a bit.

47. 5V regulator found to be redundant since the BSp24 microcontroller has an build in regulator outputting constant 5V.

48. Battery pack connections had to be re-soldered during GEMS operation.

49. Finished battery pack was not used due to time constraints. A adjustable power source was used instead.

50. PCB boards did not have correct hole size for PCB terminals, had to be re-drilled.

51. PCB terminals soldered in redrilled holes lost connection randomly and needed to be either on the opposite side of the PCB board or connections had to be redirected around terminals.

52. Last minute, accelerometer suddenly did not read the right values. Design was reduced to using the potentiometer only.

53. Potentiometer-Gear shaft belt was loose and slipping, throwing off potentiometer readings. Belt remade three times.

Although I had encountered an extensive list of setbacks and problems, I was reluctant to start over, designing and constructing a subsequent GEMS prototype. At the time when I decided to continue my research as a PhD student, my advisor had advanced our laboratory by acquiring a complete machine shop and a laser cutter for rapid prototyping. I quickly set out to design and construct another GEMS prototype. Having learned numerous and valuable lessons from the previous design and having new tools available in the laboratory, it did not take long before I had a complete GEMS prototype that fit the design criteria I initially set out to fulfill. While the previous version was bulky, unreliable, and untestable, this version was lighter, simpler, and very reliable. Shortly after, we tested this version on healthy subjects yielding very promising results. After reporting our results in two conference papers and a journal publication, my advisor and I filed a patent that eventually was licensed to a medical device company. It finally seemed as if the GEMS research that once seemed so bleak had finally matured into a practical and effective innovation.

Functionally, the first GEMS design did not seem like a success, however it is only because of the numerous failures and lessons learned from this first iteration that it finally yielded a solid and positive end result. Working on this research project, with every failure came a piece of awareness that could be coupled with other pieces in my cognitive toolbox. During my work on the GEMS, I was faced with many technical problems I had never encountered or thought about before, however every unknown and uncomfortable problem I solved carried an addition to an array of tools to be used in subsequent problems. Moreover, the harder and more uncomfortable the solved problem was, the greater the addition, thus the greater the ability to solve further obstacles.

With this domino effect, an exceptional and interactive advisor, and an open working environment, research transformed from an assigned project to a personal passion.

Years before, when I initially entered graduate school and began the GEMS project with a shallow goal of potentially raising my future pay check, I was not aware of what research was, how it was generally conducted, or even how to feel about it. No one in my direct family and friends were ever involved in a any type of research or worked in any kind of research oriented environment, hence I knew *really* never what research in its essence was and was never able to appreciate it fully. It was not until a couple years into my PhD program and after some many failures and successes in the laboratory that I could confidently put my finger on what I called research. To me research was the ongoing accumulation of minuscule and broad lessons and achievements resulting from countless failures and successes that are focused into a particular, but yet unknown direction.

F.2   The Kinetic Shape

While the kinetic shape is my key innovation during my years as a PhD student and graduate assistant, it began as a wheel definition problem for the Gait Enhancing Mobile Shoe (GEMS) about two years into my PhD program.

In part of my first project as a graduate student, I started looking into designing the GEMS wheel so that it would produce a predicted and constant backward rolling force. Due to the lack of an exact wheel shape definition that would produce a predetermined rolling force, I was forced to use a numerical approach to approximate a force at each angel around the wheel. This approach was somewhat methodical and gave some insight into the wheel dynamics, however it wasn't very accurate and more of a rough approximation.

Other students attempted to somehow linearize the reaction force of the GEMS wheel shape but eventually ended up abandoning this project and moved on to other research. My advisor eventually suggested to pass the problem to an undergraduate student, Wuthipat Brink, who had been looking for a project in his calculus III class. Although initially enthusiastic, over time he

came to a halt with his project and I decided to sit down to see if I could help him and tried to solve it myself.

In the beginning, I attempted to fit various approximated wheel shape radius definitions into a differential equation I had come up with using the wheel shape's static equilibrium equation and the shape's polar tangential angle. Solving differential equations wasn't my strong point at the time and to me this differential equation solution approach *seemed* right at the time. These radial function approximations included radius definitions of the Archimedean spiral, logrithmic spiral, Cortes' spiral, Fermat's spiral, Hyperbolic spiral, an involute circle, and random guesses that formed spiral-like radial functions. The results were not obvious and there was nothing I could compare it to.

Each approximation and substitution yielded a different definition of a spiral-like curve, and when I checked the result by inserting an applied force definitions, each result produced a contrasting shape. To see which shapes came closest to a true value, that is, produced the given reaction forces, I was able to numerically apply the initially defined force function to the derived shapes and observe how close the force output of the derived shapes would come to the initially defined forces. I observed that some solution approximations generated shapes that in turn produced reaction forces that were close to the true value for some input ranges, while producing impossible values for other input ranges. At the time, my advisor and I decided this may be enough in that we may use some solutions for one type of input, while using another shape solution for another type of input.

While this was a reasonable approach, I was not satisfied and was more than ever determined to find a more complete "wheel shape" definition. A week went by and among other research I dug into my old undergraduate calculus and differential equation books in the hope to find any equations, equation pattern, or even something that esthetically looked like my differential equation. Anything I found either did not produce any realistic solution or I wasn't understanding the method well enough for me to apply to my problem at hand.

Then finally, it was around 10pm on a Saturday night. I had been sitting in front of the computer the whole day starring at Matlab code and getting lost in one of many open internet sites about multi-variable and differential calculus. I stayed late to spend some time on Woody's calculus III problem, when I glanced over some of my detailed notes for the PhD qualifying exam that I just had taken and failed. And there it was. It was so simple, that I didn't even think of it before. It was an elementary differential equation operation called separation of variables. It was so straightforward but seemed so elegant and perfect when applied to this problem.

I ecstatically jumped, pumped my fist, jump shot my soft drink can into the trash can, while repeating the words "That's it!". I quickly sat back down and translated my solution into programming code. After testing my new approach by sampling various functions, it worked! It worked for *any* force function definition input. I carefully compiled and nicely formatted a few good looking results, which I then send to my advisor.

My advisor was also very excited about this solution saying "That is definitely publishable in a journal!". After a discussion, he encouraged me to proceed and find a solution for the three dimensional version of my solution. Shortly after, I sat down again and derived the equations that defined a three dimensional shape which is able to react simultaneously with a predicted pushing and rolling forces. This three dimensional solution was now easier to solve in that I already figured out the steps to do so. Due to the kinetic properties of the kinetic shape, and because I was only able to find a music band with the same name, I suggested to name these definitions "kinetic shapes". It must have been close to two months after my discovery that I submitted a fully developed journal article which eventually was published.

These solutions were a breakthrough for my research and after this discovery, my research progressed rather quickly. Shortly after, I invented the kinetic board/transport, time dependent kinetic shapes, heterogeneous material slicer, kinetic shape self-stabilization, kinetic shape strain gages, and a musical kinetic shape string instrument. I eventually discovered the kinetic shape dynamics equations, which can predict kinetic shape's kinematics behavior as it rolls over ground or pushes an object. I then proceeded to invent a whole new type of force mathematics that utilize a

system of kinetic shapes used for systematic mechanical force manipulation. All these inventions, including a more efficient kinetic shape crutch tip, usually seemed to come to me while acutely focused in the laboratory late at night. Nonetheless, every time I had come up with one of these inventions, I experienced the same reaction of joy as I initially did when I found the solution to the kinetic shape equation.

It was impossible for me to say that these discoveries sprung out of thin air. It would also be dishonest or ignorant to claim that these ideas emerged out of nothing. Nothing breads nothing. One can never produce a new though or an idea with no exposure to new information that is external to the mind. Research and innovation at a micro or macro scale is fueled by the open exposure to information. The kinetic shape is no exception. A series of non-linear consciously and unconsciously related events and inflow of information all led to my kinetic shape discoveries. I could argue that the fuel for this innovation stemmed from my background and experience. However, events such as the invention of the GEMS, my advisor accepting me as a research assistant and teaching me invaluable thinking tools, working in a free and creative working environment, or even Woody's calculus class project all can also be seen as such innovation fuel. Hence, in my opinion, innovations such as the kinetic shape can be viewed as the product of my available and absorbed information deliberately directed onto a research problem over the right time period.

This entire kinetic shape research experience redefined my outlook on research itself and the path it may or may not take. This single realization of a kinetic shape solution on that one Saturday night has filled half of this dissertation with content and may very well be able to fill another half. Research and innovation are not linear. Good research perhaps is never linear, but rather a combination of organically flowing probable events captured only when one is entirely and sometimes a little too obsessively immersed into one's work, pondering every step, angle of approach, or an often times unrelated detail. Only then one is able to unexplainably and spontaneously compose, improvise, design, or create something that was not there before. In hind sight, some of the things and solutions I present in this dissertation may have been sheer

serendipity or even a "common sense grind", however I think that this may precisely be the beauty and power of good research and innovation. After spending (or rather earing) countless hours, days, or sometimes weeks in the laboratory, just purely and entirely immersed in a problem and its countless details, things tend to effortlessly and simply solve and discover themselves in a joyful realization. These moments may present themselves anywhere from resolving of some annoying compiling error in a programming code to a big "AHA! THAT'S IT!" moment that causes you to voluntarily lose sleep, disregard relationships, and ignore basic human necessities. Such moments become realized when least expected and over-saturated in relevant and irrelevant details, suddenly connecting old dots to new dots to completely unrelated dots. After devoting so much time on, around, and absorbed within a complicated problem, dots become lines become shapes.

F.3 Passive Dynamic Walking Model

Persistence is the main and essential ingredient to success. Although this may sound like a cliche slogan extensively used in motivational speeches and catchphrases, it carries a great truth in my personal development as a researcher and engineer and my development of the three-link variable radius foot passive dynamic walker (PDW) model.

A couple years into the doctoral program, my advisor asked me to adopt a numerical PDW computer model previously advanced by two graduating Master's students. This model was a modification of a common point-foot model. The fundamental code for this PDW model was forwarded to us by a graduate student from another university, hence we did not fundamentally understand how the core equations were derived. However, it was enough to manipulate it in such a way to systematically research unexplored asymmetric gait hypotheses.

Shortly after I was introduced to the PDW programming code, my advisor asked me if I could possibly modify this code such that the PDW walks on variable radius shape feet instead of point feet. Although this sounds like a minute change, it required some major changes within the PDW's non-linear dynamics and collision event equations. Additionally, I was completely puzzled on where and how to begin.

In order to fully grasp how to derive the PDW, I initially set out to derive and compare the exact same three-link point foot model that was forwarded to us. This available three-link point-foot model was relatively common among literature, therefore I speculated that it would not require much effort. As I dug into numerous published PDW articles and conference papers, one common and frustrating theme emerged: All the research I had found only showed either abbreviated and highly generalized end equations, had derivations for a narrow and specific PDW model used in a specific situation, or presented a derivation that was filled with jargon and mathematics which was well beyond my awareness at the time. To me it seemed as if all the publications were skipping some crucial steps that were fundamental to the PDW derivation, but thought to be too straightforward to be outlined.

From my literature review, I was able to understand the use of the Lagrangian dynamics to derive the kinematics of the PDW system, and I also understood the methods to derive the potential and kinetic energy of the PDW system for the the use of the Lagrangian. I understood the conservation of angular momentum method for deriving the post-collision angular velocities as the PDW progressed. However, time after time my solutions, and so the kinematics, did not match the original and available PDW code. I attacked the problem from different angles by defining the walker velocities from different reference points and even attempting to use the conservation of linear momentum, however the results repeatedly were not matching. There were numerous attempts where the resulting kinematics did not compare to the original PDW model kinematics, however the kinematics of my derived PDW model were reasonable and realistic. This had me questioning if our available code that was forwarded to us was in fact correct.

A couple weeks into the model derivation process I stumbled upon an interesting and more elaborate book chapter, which outlined the derivation of the simplest compass gait (2-link) point-foot model. This manuscript presented a more detailed blueprint for the derivation of the PDW dynamics and collision events. Over the next couple nights I carefully tried to replicate this work and eventually succeeding in modeling this simple PDW model. This was a breakthrough for me in that it showed the general derivation methods and path. I subsequently took the next step and

relatively quickly derived the three-link point foot model, which I compared to the PDW model we were using. It finally matched! All the terms in equations were finally clear and made tremendously more sense than ever. Although I was excited about this success, the extensively harder part of my PDW research still lay ahead.

I set out to define the point-foot PDW model ground reaction forces as the PDW progressed down a slope. In this case, I did not have any available sources to reference for guidance and only relied on my undergraduate statics and dynamics textbooks along with course notes. During my undergraduate studies, statics and dynamics seemed like challenging courses, and at the time I had started this derivation, these topics appeared very cloudy and porous in my mind. However, in order to solve the problem at hand, I needed to review, understand, and master these topics. I spend the next month drawing countless kinetic diagrams, applying numerous geometric and trigonometric methods, and contemplating and reassuring myself on the values of various angles and dimensions. As I translated and applied my derivations into programming code, I finally saw my grit pay off as this model was able to mimic the trends of the measured ground reaction forces of a human gait. Despite the correlation to actual values, considering that I was individually working on this project and the complexity of it, it was hard for me to confidently state that this computer model was entirely flawless, however after many diverse tests and hypothetical conditions, I was mostly confident.

The subsequent step was to apply all my acquired knowledge from this previously solved problem to finally tackle the derivation of a variable radius foot PDW model with a continous foot shape definition. To my knowledge and literature review, such a model has never been derived, however would be quite useful in human and robotic gait analysis.

I began to utilize the same derivation techniques used earlier for the point-foot model, however I quickly found that the assumption of a curved foot shape is far more complex in nature and decided to pursue the derivation of a slightly simplified 2-link curved foot model. I was committed and determined to solve this problem and completely submerged myself into the process. Week after week I drew detailed geometric drawings outlining every angle and distance

on countless blank printer paper. My laboratory desk was covered with scribbles, equations, and schematics of the PDW model in every size and orientation that would reveal more useful information. Because the PDW model was entirely passive, I knew that the correct dynamics would yield a constant total system energy, that is, as the PDW system moved, its kinetic and potential energy have to be constant. I used this information to check the dynamics and collision event equation I produced. During some instances the animated dynamics solution appeared to be undoubtedly correct, however with a detailed analysis of tests and a variation of initial condition inputs, I discovered that the fundamental equations were wrong. After many setbacks, I was finally able to produce a valid variable radius foot 2-link PDW model. When I found that my derivation of this model was valid, it was as if a distant and doubtful yet idle believe came to realization. Seeing that after all this effort, the model was finally working was simply awesome.

I felt as if I could push this accomplishment one step further and derive a 3-link PDW model with variable radius feet. Similar to the previous derivations, I immersed myself into the derivation process. This final step was not so much conceptually difficult as it was time consuming. I already had a firm understanding, system, and method to derive the kinematics and collision event equations for this PDW model, however with thousands of lines of programming code and hundreds of various variables, the process was long, detailed, and vulnerable to errors that were hard to troubleshoot. Nevertheless, after extensive hours of repeated drawing, deriving, testing, troubleshooting, and animating, the variable radius feet 3-link PDW model was finally complete and was ready to be used to analyze various gait patterns and rehabilitation methods.

One year prior to the completion of this model, I was completely baffled on how to derive even the simplest PDW model. I was confused and somewhat overwhelmed with the derivation process, uncomfortable even with the methods I apparently should have firmly learned and been comfortable with during my undergraduate studies.

In retrospect, although the entire PDW model derivation process was long, laborious, and at times plain tedious, I was eager, enthusiastic, and at the edge of my seat drawing, deriving, programming, solving, and learning. No matter how overwhelmingly large and frustrating the

setbacks were, I never viewed them as defeats or failures, rather as a good chance to expand my awareness and learn what went wrong so that I could correct it and move forward toward the greater goal. There were times where my research reached a plateau and it seemed as if no real progress emerged. For me, these sluggish periods could range from days to whole weeks. However, I considered these plateaus to be normal and natural. Given the variables that factor into researching and solving a problem that has never been solved or even attempted, it is absurd to think that progress can be constant and always positive on a global or a particular level. The process of finding a valuable solution to a good and relevant problem is supposed to be uncomfortable, frustrating, and flooded with setbacks and plateaus. While this is true in many ventures in life, I found it specifically true in scientific research. In research, it is not how much one knows that defines success, but rather how much one can learn without underscoring setbacks. Naturally, preceding knowledge and experience helps the problem solving process, but there is no substitute for a willing, excited, and persistent approach with a positive vision.

A good researcher acknowledges that the setbacks are frustrating and awful, however he/she knows that the failures are eclipsed by the meaningful successes and a joyful foresight. A good researcher is always slightly uncomfortable, unsure, and skeptical in the specifics, but strongly, confidently, and energetically strives towards some greater vision. A good researcher understands that innate intellect alone can never produce valuable results, and an underlying reliable and tenacious energy source is needed to fuel the progress. The main and essential trait to a good researcher is raw persistence.

Appendix G: Copyright Permissions

License Number	3424181162569
License date	Jul 08, 2014
Licensed content publisher	Springer
Licensed content publication	Paladyn
Licensed content title	Design and pilot study of a Gait Enhancing Mobile Shoe
Licensed content author	Ismet Handzic
Licensed content date	Jan 1, 2011
Volume number	2
Issue number	4
Type of Use	Thesis/Dissertation
Portion	Full text
Number of copies	1
Author of this Springer article	Yes and you are the sole author of the new work
Title of your thesis / dissertation	Analysis and Application of Passive Gait Rehabilitation

License Number	3424170719346
License date	Jul 08, 2014
Licensed content publisher	Elsevier
Licensed content publication	Applied Acoustics
Licensed content title	The musical kinetic shape: A variable tension string instrument
Licensed content author	Ismet Handžić,Kyle B. Reed
Licensed content date	November 2014
Licensed content volume number	85
Number of pages	7
Type of Use	reuse in a thesis/dissertation
Portion	full article
Format	electronic
Are you the author of this Elsevier article?	Yes
Will you be translating?	No
Title of your thesis/dissertation	Analysis and Application of Passive Gait Rehabilitation

About the Author

Ismet Handžić is a Bosnia and Herzegovina native and refugee who finished his Bachelor of Science in Mechanical Engineering at Western Kentucky University in Bowling Green Kentucky in 2009. During his undergraduate education he interned at Pan-Oston Co. conducting statistical time studies and developing prediction formulas for manufacturing process time. He worked three years at the General Motors Corvette/XLR assembly plant where he designed and analyzed multiple assembly line components. Ismet continued his education for a Masters of Science in Mechanical Engineering at the University of South Florida under Dr. Kyle B. Reed by designing, constructing, and testing a gait enhancing shoe for rehabilitation. After completion in 2011, he proceeded to pursue his Ph.D. in Mechanical Engineering under Dr. Kyle B. Reed. The contents of this dissertation portray his research at the University of South Florida.